UiT The Arctic University of Norway

Faculty of Science and Technology, Department of Geosciences

# Cracking into Cryoseismology

Seismological studies of frost quakes and floating ice sheets

Rowan Romeyn

A dissertation for the degree of Philosophiae Doctor Dec 2021

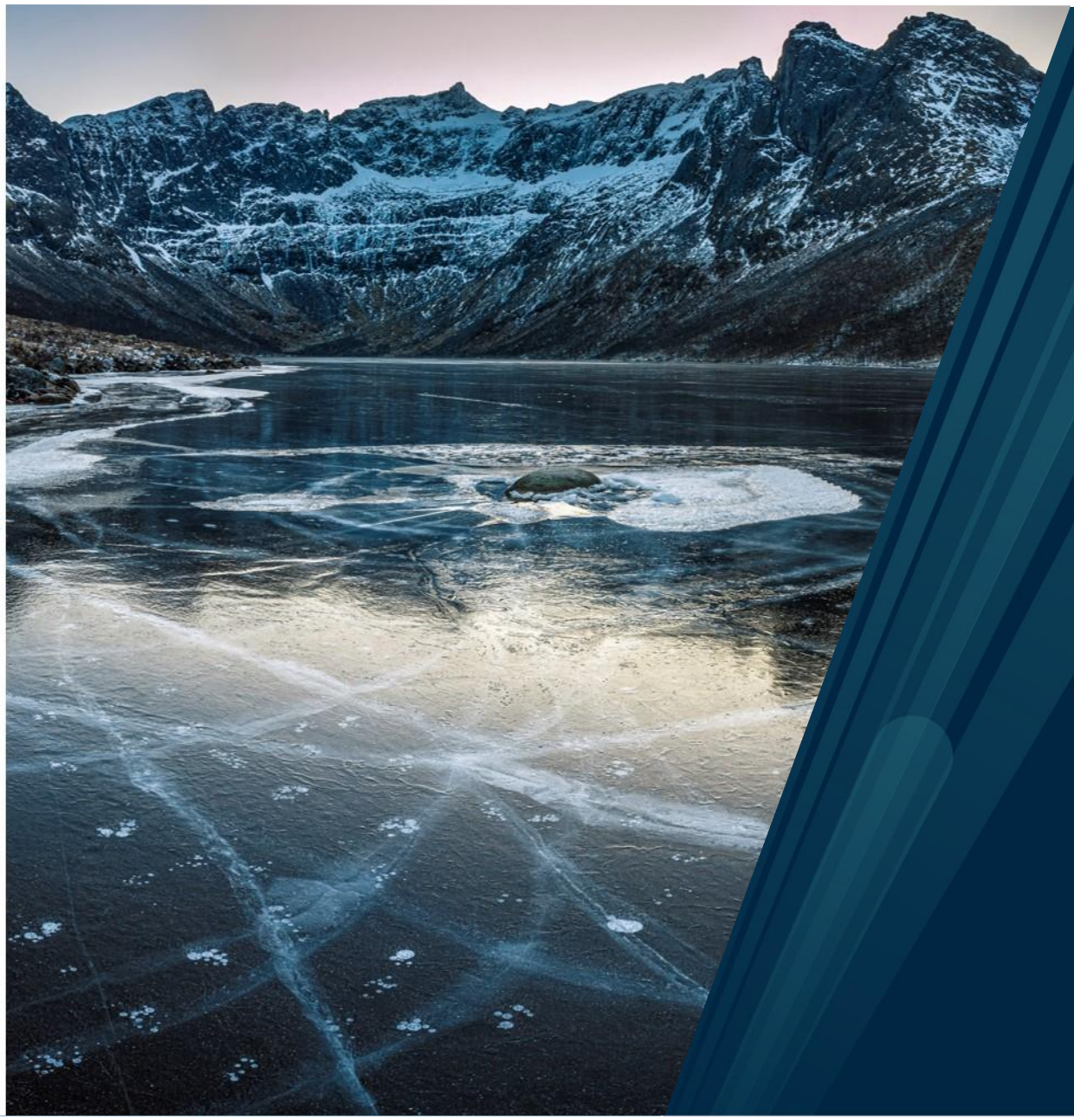

# Abstract

The cryosphere encompasses the seasonally and perennially frozen parts of the earth and its extent is both sensitive to and impacts upon the global climate through surface energy and moisture fluxes and feedbacks. The dynamics of ice and frozen ground also impact directly on, e.g., construction and maintenance of roads in cold regions or transportation across floating ice sheets. Environmental seismology is an emerging paradigm focussing on the excitation and propagation of seismic waves with a non-tectonic, natural origin. Cryoseismology is an important subdiscipline within this paradigm, due to the dynamic stresses associated with freezing and temperature changes in ice, in addition to contrasting elastic properties according to, e.g., ground ice content or ice sheet thickness. While cryoseismology is an emerging field, close analogues may be found with well-studied engineering materials like concrete slabs and pavements and the transfer of knowledge from these studies formed an important part of this thesis. The overarching aim of this thesis was to investigate the extent to which seismic methods can be used to study dynamic processes and longer-term changes in the cryosphere.

The thesis is structured around three case studies linking active- and passive-source seismic experiments with numerical models of thermal stress, seismic wave dispersion and propagation. Signal processing techniques such as beamforming and matched field processing were also elemental in connecting data with theory and tackling the important problem of estimating the source location for passive seismic experiments. In Paper 1, a temporary array of geophones with fine spatial sampling demonstrated that high ground-ice content in the near-surface during winter/spring produces a complex multimodal dispersion pattern analogous to asphalt pavements. A repeat deployment in the autumn demonstrated the potential to monitor seasonal ice content related stiffness changes in the subsurface using seismic surface waves excited by frost quakes. In Paper 2, the role of thermal stress in triggering frost quakes was further explored using borehole temperature measurements and multi-decadal continuous seismic recordings from the small-aperture Spitsbergen seismic array (SPITS). Thermal contraction cracking within the frozen active layer was shown to be a plausible mechanism contributing to frost quake seismicity. In Paper 3, a multi-annual catalogue of explosive source seismic experiments conducted on first-year sea-ice in Van Mijenfjorden, Svalbard, was used to demonstrate the usefulness of air-coupled flexural waves for estimating the thickness of a floating ice sheet. Within the context of the environmental seismology paradigm, we were also able to hypothesize and

demonstrate the potential to record air-coupled flexural waves produced by thermal-stress related ice-quakes with a simple microphone, raising the potential for low-tech, inexpensive, non-contact ice thickness monitoring. Viewed as a whole, the case studies developed in this thesis illustrate the ability of seismic methods to record and monitor dynamic processes in the cryosphere over a range of temporal scales. Continuous passive seismic recordings with high-temporal resolution provide a useful complement to other geophysical and remote sensing techniques used for monitoring the dynamics of the cryosphere.

# List of thesis papers

I. Romeyn, R., Hanssen, A., Ruud, B. O., Stemland, H. M., and Johansen, T. A. 2021. **Passive seismic recording of cryoseisms in Adventdalen, Svalbard**, The Cryosphere, 15, 283–302, https://doi.org/10.5194/tc-15-283-2021

II. Romeyn, R., Hanssen, A., and Köhler, A. **Long term analysis of cryoseismic events and associated ground thermal stress in Adventdalen, Svalbard**, The Cryosphere Discuss. [preprint], https://doi.org/10.5194/tc-2021-329, in review, 2021.

III. Romeyn, R., Hanssen, A., Ruud, B. O., and Johansen, T. A. 2021. **Sea ice thickness from air-coupled flexural waves**, The Cryosphere, 15, 2939–2955, https://doi.org/10.5194/tc-15-2939-2021.

# Supervision committee

Primary supervisor – Professor Alfred Hanssen, UiT The Arctic University of Norway

Co-supervisor – Professor Tor Arne Johansen, University of Bergen (UiB) and The University Centre in Svalbard (UNIS).

# Project funding

This research has been funded by the University of Tromsø - The Arctic University of Norway, by the ARCEx partners and by the Research Council of Norway through grant number 228107. The publication charges for the research papers, that constitute an important contribution of this study, were covered by a series of grants from the publication fund of UiT - The Arctic University of Norway.

# Acknowledgements

Field data was a crucial part of this thesis and a very special thanks go to Stig Monsen, Bent Ole Ruud, Helene Meling Stemland, Tor Arne Johansen, the UNIS field logistics staff and countless UNIS students for their fantastic efforts lugging heavy seismic equipment around in all sorts of weather conditions over the course of many years. I am also grateful to Andreas Köhler who has been a great source of inspiration and a true font of knowledge on all things related to seismology. Meandering discussions on physics, maths, research, life, everything in between and occasionally even geology, with my main supervisor, Alfred Hanssen, have truly shaped this thesis and ensured that it has been an exciting and most enlightening journey. Thanks also to Elisabeth Hansen, Kayak the puppy and Furman the cat for supporting me on the home front, on mountains, fjords and couches, under the midnight sun, the polar night and on grey rainy days. All of you as well as a great group of work colleagues and office mates here at the department of geosciences at UiT have really made Tromsø a wonderful place to live and write a PhD.

# Contents

# Introduction

## 1.1 Thesis motivation and objectives

Fundamentally, the objective of this thesis is to explore the connection between experimental data and theoretical modelling in order to advance the emerging field of cryoseismology. We set out to find the simplest possible dynamical or physical models that could explain observations derived from real cryoseismological data. The primary motivation was to improve our understanding of the complex physical dynamics of selected aspects of the cryosphere. These dynamics have both direct societal implications and application to change detection and monitoring within the broader context of climate warming and a rapidly changing cryosphere. The development of novel signal processing and data analysis techniques in order to best utilise available field data to derive information about cryospheric processes was also an important objective.

## 1.2 The cryosphere and its dynamics

Water is the only common substance that exists in gaseous (water vapor), liquid (water) and solid (ice) forms over the relatively small range of temperatures and pressures that exist on the surface of the Earth (Graham et al., 2010). The term “cryosphere” groups all portions of the Earth’s surface where water is in its frozen state, i.e., where it exists as ice or snow (Barry and Gan, 2011). Consequently, the cryosphere encompasses a wide variety of landforms and environments from icebergs to floating sea ice and ice shelves to ice sheets, glaciers and snow covers to permafrost and ground ice (see Figure i). The components of the cryosphere may be seasonally or perennially frozen so that its extent varies in phase with the seasons of the northern and southern hemispheres (Barry and Gan, 2011; Kotlyakov, 1999). The balance of water held in the atmosphere, hydrosphere and cryosphere plays a crucial role in regulating global climate due to, e.g., the high heat capacity of water, latent heat exchange during phase transitions and the rejection of salt that occurs when sea water freezes. These processes are important drivers of the global thermohaline circulation that redistributes solar energy from the equatorial belt towards the poles and is a primary contributor to the climate that we experience in all parts of the world (Rahmstorf, 2003). The high albedo of ice that reflects incoming shortwave

radiation, compared to the low albedo of water, is also an important factor in the surface energy balance, affecting how much solar energy the Earth absorbs (Curry et al., 1995).

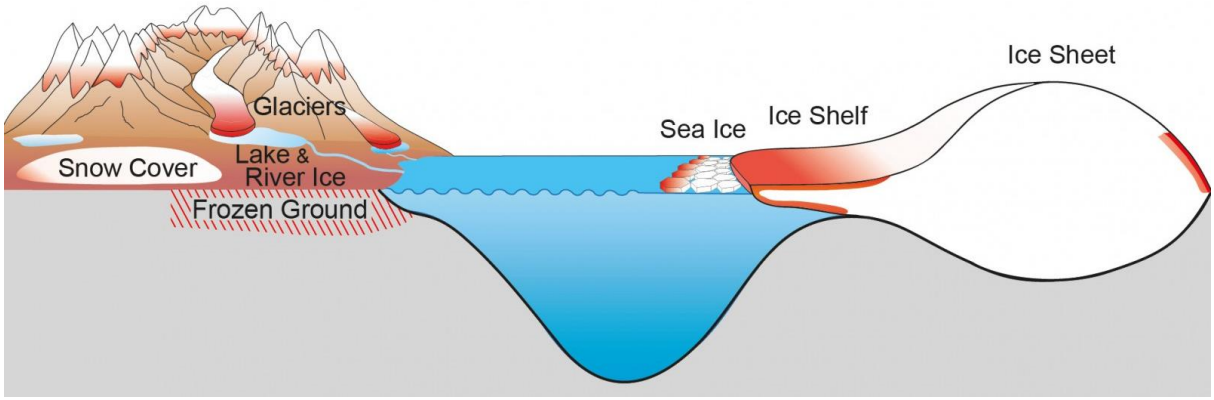


*Figure i – Cartoon illustrating the main components of the cryosphere (modified from Vaughan and Comiso (2014)). The red colour indicates the areas that are currently melting/thawing due to the anthropogenically driven long-term warming trend.*

The co-existence of water vapor, water and ice over the relatively narrow range of temperatures and pressures encountered at the surface of the Earth dictates that the extent of the cryosphere is highly sensitive to temperature. Under the presently warming climate, the extent of the cryosphere is decreasing and the melting of ice on land is a major contributor to global sea level rise (Nicholls and Cazenave, 2010; Rahmstorf, 2010), while thawing permafrost contributes to rapid erosion on up to 34% of the world's coastlines (Lantuit et al., 2013). Significantly, changes in the extent of the cryosphere also feedback on climate through, e.g., the albedo feedback mechanism where highly reflective snow/ice surfaces are replaced by less reflective water/land (McGehee and Lehman, 2012; Thackeray and Hall, 2019), or the release of methane (a greenhouse gas) to the atmosphere caused by thawing permafrost (Kohnert et al., 2017; Masyagina and Menyailo, 2020; Schuur et al., 2015). These feedbacks can increase the rate of climate change and further enhance the climatic forcing acting on the cryosphere.

While this thesis is mainly method driven, i.e., focused on the development of concepts that are not specific to a single geographical area, data examples from Svalbard have nonetheless prevailed. In addition to reasons of geographical proximity and administrative ties to mainland Norway, Svalbard is particularly well suited as a natural laboratory to study dynamic processes of the cryosphere. This is because the rate of temperature increases across the artic is significantly higher than the global average (Isaksen et al., 2016; Nordli et al., 2014). As Figure ii illustrates, if we focus on winter temperatures over the past decades, Svalbard has experienced the largest increase in temperature of anywhere on the planet. One may therefore expect changes to the cryosphere over interannual to

interdecadal timescales to be significantly magnified on Svalbard, compared to areas where climate warming has progressed at a slower rate (e.g. Isaksen et al., 2007).

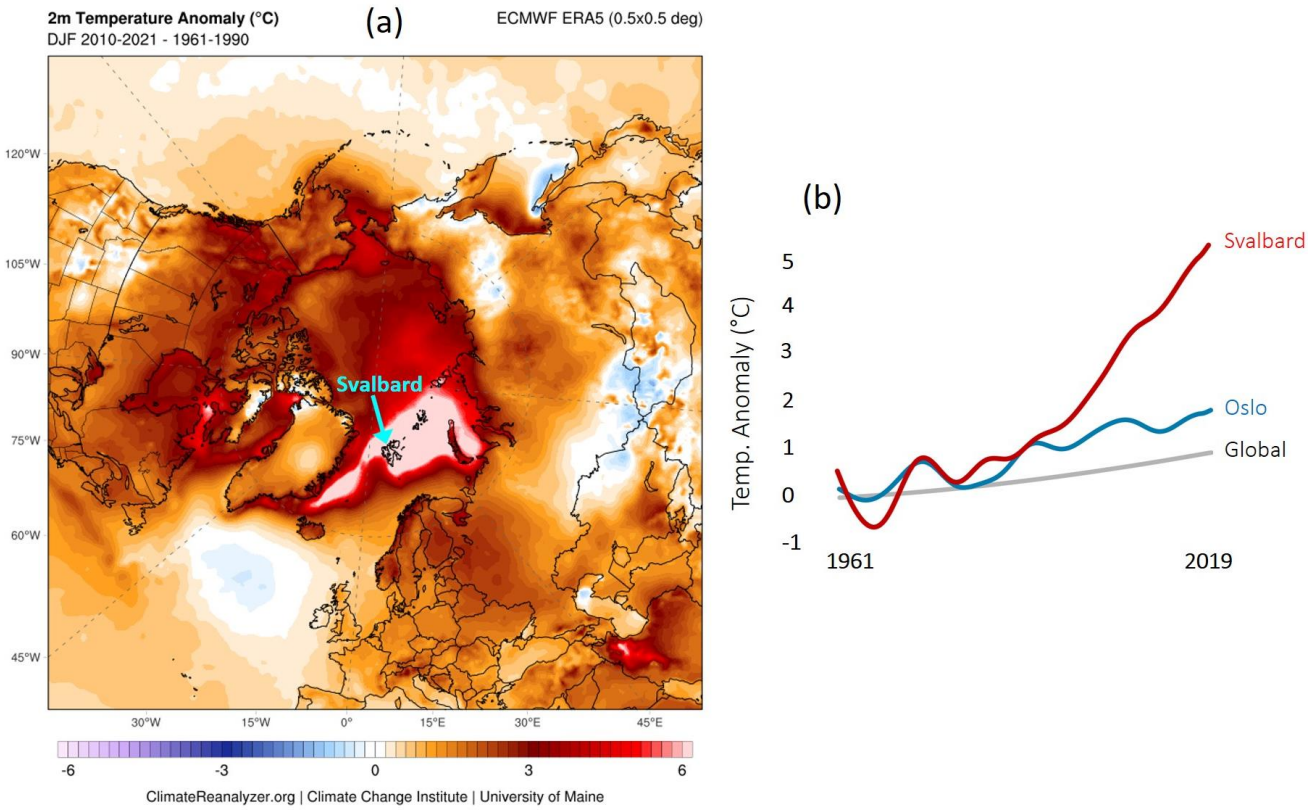


*Figure ii – (a) Winter (Dec-Feb) temperature anomalies according to the ERA5 global reanalysis (Hersbach et al., 2020) for the period 2010-2020 compared to the 1960-1990 baseline. (b) smoothed timeseries showing trends in temperature anomalies at select locations relative to the same 1961-1990 baseline period modified from Holm and Isaksen (2019).*

So far it has been outlined how the cryosphere is crucially important to the global climate and how it is both affected by and feeds back on the ongoing anthropogenic climate change, that is one of the most important factors impacting on human development in the 21st century (Calel et al., 2020; Lamb and Rao, 2015; Tanner and Horn-Phathanothai, 2014). However, it is important to highlight that it is not only the remote effects of a changing cryosphere that are important. The cryosphere encompasses vast land and sea areas (Barry and Gan, 2011) and the dynamics of ice and snow in these areas impacts directly on the life of all organisms inhabiting these areas. In this thesis, the focus is mainly on physical processes, giving some examples of the relevance of these processes to human activity. However, while not the main focus of this thesis, it is important to remember that the cryosphere also forms an integral part of critical ecosystems and impacts directly on others (Elser et al., 2020; Fountain et al., 2012; Hodson et al., 2015; Vincent et al., 2011).

Thawing permafrost poses a significant risk to Arctic infrastructure, which may be damaged, or be subject to costly maintenance or stringent construction requirements due to the loss of bearing

capacity and/or differential subsidence due to ground ice melt (Suter et al., 2019). Erosion of thawing permafrost coastlines may also necessitate the costly and socially complex relocation of entire communities (Farbotko et al., 2020; Gudmestad, 2020; Maldonado et al., 2014). While only ~0.15% of the global population live north of the Arctic circle, the circumpolar Arctic is rich in resources and contributes ~0.6% to global gross domestic product (Larsen and Fondahl, 2015; Larsen and Huskey, 2015; Laruelle, 2015). Infrastructure such as buildings, roads, railroads, ports and pipelines are vulnerable to damage due to degrading permafrost (Shiklomanov et al., 2017; Suter et al., 2019), potentially requiring costly mitigation strategies, increased maintenance, etc. (Larsen et al., 2008; Streletskiy et al., 2019). Thawing mountain permafrost has also been identified as a trigger of natural hazards such as rock avalanches (e.g. Frauenfelder et al., 2018). Limiting climate warming by reducing greenhouse gas emissions has been proposed as a plausible proactive adaption strategy that could significantly reduce damages to Arctic infrastructure (Melvin et al., 2017).

In addition to interannual long-term processes such as permafrost degradation, the short-term seasonal dynamics of the cryosphere can also be significant. Frost heave, the upward displacement of the ground surface due to the formation of ice lenses, and frost quakes, i.e., ground cracking due to ice formation or thermal contraction, contribute significantly to seasonal road damage (DiMillio, 1999; Fortier and Allard, 2005; Lai et al., 2012; Peppin and Style, 2013; Vel'sovskij et al., 2015). In this case, appropriate engineering and construction methods have proven to be effective in mitigating frost-related road damage (Lai et al., 2012; Lawrence et al., 2000; Vel'sovskij et al., 2015; Øvstedal, 2012), though initial road cost is increased and correspondingly not all roads are constructed in this way (Loranger et al., 2017).

The seasonal dynamics of the cryosphere are also important from a natural hazard and risk perspective. The probability of destructive snow avalanches or rockfalls are highly related to the physical dynamics of a layered snowpack (Schweizer et al., 2020), cornices (Vogel et al., 2012), or freeze-thaw dynamics in rock walls (Fischer et al., 2012; Hales and Roering, 2009). Further natural hazards like glacial lake outburst floods (Jökulhlaup) or lahars related to ice covered volcanoes are also important in some areas (Carey et al., 2021; Ding et al., 2021). The strength and thickness of floating sea or lake ice is also of critical importance for transport and recreational ice users such as: ice skaters (Rankin, 2018), vehicles from snow scooters to semi-trailers (Takizawa, 1988; Van der Sanden and Short, 2017), aircraft (Matiushina et al., 2016) and ice breakers including ships (Montewka et al., 2015), submarines (Kozin and Pogorelova, 2008) and hovercraft (Hinchey and Colbourne, 1995).

## 1.3 An introduction to cryoseismology

### 1.3.1 The emerging field of environmental seismology

Seismology is the study of elastic wave propagation through the solid earth, where earthquakes are the most commonly utilized seismic source (Stein and Wysession, 2009). By contrast, environmental seismology shifts the focus away from tectonic earthquakes and is defined as the study of seismic vibrations that either have a natural, non-tectonic origin or whose propagation is perturbed by modifications of environmental external parameters (Larose et al., 2015). Natural phenomena capable of exciting seismic waves that have been utilized in seismological studies include wind and storms (pressure disturbances or precipitation events) in the atmosphere or ocean, water flow and sediment transport in rivers, movement of glaciers and ice sheets, ice fracturing, landslides, debris flows, rock avalanches and rockfall (Ardhuin et al., 2011; Burtin et al., 2013; Dammeier et al., 2011; Favreau et al., 2010; Hibert et al., 2014; Larose et al., 2015).

Environmental seismology is providing new insights into dynamic processes at or near the earth surface, due to high temporal sampling compared to other techniques and the richness of information conveyed by seismic waveforms. For example, Dietze et al. (2017) used passive seismic recordings of alpine rockfalls in the Swiss Alps to resolve distinct dynamic phases of these events with millisecond precision. These phases included detachment, free fall, intermittent impact, fragmentation, arrival at the talus slope and subsequent slope activity. Efficiently locating and estimating the size of large populations of rockfalls has also been achieved using passive seismic recordings (Hibert et al., 2014). Similarly, other authors have used seismic recordings to constrain the force history and frictional processes of landslides (Moretti et al., 2015; Moretti et al., 2020). Generally speaking, environmental seismology represents a paradigm shift for seismic site surveys, away from active source experiments and in favour of passive methods. The focus on passive surveying brings wide reaching implications. It simultaneously simplifies the logistics of monitoring environmental changes over longer timescales (e.g. Gajek et al., 2017; Hibert et al., 2017; Köhler et al., 2016; Sergeant et al., 2019), allows the dynamics of natural seismic sources to be studied (e.g. Dietze et al., 2017; Moretti et al., 2020) and lessens the environmental impact of seismic surveying (e.g. Duncan, 2005; Stemland et al., 2019) by eliminating the need for artificial seismic sources.

### 1.3.2 What is cryoseismology?

Cryoseismology can be considered a sub-discipline within environmental seismology, focussed on the various components and dynamics of the cryosphere and how these excite or influence the propagation of seismic waves (e.g. Podolskiy and Walter, 2016). In this thesis, following the definition of Lacroix (1980), a cryoseism is considered as the general class of non-tectonic seismic events caused by freezing action in ice, ice-soil and ice-rock materials. Frost quake is correspondingly used to designate the sub-group of events relating to the formation of ice or its thermal expansion/contraction in ice-soil and ice-rock materials (e.g. Barosh, 2000; Okkonen et al., 2020). While somewhat arbitrary, this terminology is intuitive because frost quakes are typically associated with perma-"frost" or periglacial environments.

The designation "ice quake" then groups the events relating to ice in its more or less pure form, i.e., glaciers (e.g. Bonnet et al., 2020; Hudson et al., 2020; Köhler et al., 2015; Podolskiy et al., 2019), ice sheets (e.g. Barcheck et al., 2019; Lombardi et al., 2019), sea ice (e.g. Moreau et al., 2020a) and lake ice (e.g. Ruzhich et al., 2009). Ice quakes can be a result of thermal expansion or contraction stresses driven by temperature gradients in ice (e.g. Podolskiy et al., 2019), or a result of stresses that develop due to the movement of glaciers (e.g. Podolskiy et al., 2021). For completeness, the term "frost creep" is used to describe the slow inelastic deformation of ice or frozen ground (Andersen et al., 2015; Benedict, 1976). While there is some variation in the use of these terms in the literature, this terminology seems to be the most intuitive and consistent with common usage.

Cryoseismology is an interesting case because both the dynamics of the seismic source and the propagation of the seismic waves through near-surface media are in focus. For example, Okkonen et al. (2020) focused on thermal stress as trigger for frost quakes from the perspective that frost quakes may damage buildings and other infrastructure. Similarly, Köhler et al. (2015) used a long-term seismic record to study the temporal distribution of glacier ice quakes in order to infer glacial dynamics such as calving and surging. Podolskiy et al. (2021) used an ocean bottom seismometer deployed proximally in front of a tidewater glacier to study both basal sliding and calving dynamics. On the other hand, within the environmental seismology paradigm, these quakes can also be considered a useful source of environmental noise that can be leveraged in seismic studies of subsurface structure and elastic properties. For example, Moreau et al. (2020a) used guided waves from natural ice quakes to study sea ice thickness and elastic properties. Albaric et al. (2021) used Rayleigh waves from ice quakes to investigate permafrost shear wave velocity structure and found that changes in ice content could explain the observed trends over both seasonal and interannual timescales.

Seismic methods in general are highly complementary to other geophysical methods and this is also true of cryoseismology. This is partly because different geophysical methods are sensitive to different physical properties, such that combining information from contrasting methods can give a more complete picture. The propagation velocity of seismic surface waves is highly sensitive to, for example, variation in ice content of permafrost, which means that seismic methods have good potential to detect or monitor these variations (e.g. Dou and Ajo-Franklin, 2014; Stemland et al., 2020). However, combining both seismic and electromagnetic methods can give additional constraint on, for example, complex topics like the unfrozen water content in saline permafrost that exhibits hysteresis under freezing/thawing states (Wu et al., 2017). The high temporal resolution and potentially long record length of passive seismic data can also complement the high spatial resolution of methods such as airborne electromagnetics (Minsley et al., 2012), lidar scanning (Hubbard et al., 2013; Köhler et al., 2019), induced polarisation tomography (Banville et al., 2016), ground penetrating radar (Santin et al., 2019), synthetic aperture radar (Parsekian et al., 2021) and interferometric synthetic aperture radar (Rouyet et al., 2019; Rouyet et al., 2021).

## 1.4 Frozen materials as thermo-viscoelastic solids

Frozen materials containing a sufficient volume fraction of ice typically behave elastically on short timescales and viscously on long timescales under applied stress (e.g. Mangold et al., 2002; Schulson and Duval, 2009; Sinha, 1978; Weeks and Assur, 1967). The work done to deform a perfectly elastic material is entirely stored as recoverable elastic energy, while for a purely viscous material (a Newtonian fluid) the mechanical work required to deform the material is fully dissipated. Ice and frozen soil, like most materials, behave somewhere in between these end-members and can be considered viscoelastic materials. The flow of matter in these materials and their subsequent deformation falls under the field of rheology. Rheology translates literally from Greek as "the study of flow" and highlights the connection between gases, liquids and "soft" solids that may all be considered to flow under increasingly long periods of observation.

Time-dependent behaviour is a defining characteristic of viscoelastic materials (Bonfanti et al., 2020; Coleman and Noll, 1961). On the timescale of seismic wave propagation, the behaviour is dominantly elastic and cryoseisms are the result of elastic stresses that exceed the material strength (Maloof et al., 2002; Mellon, 1997; Podolskiy et al., 2019). As a result, cryoseismology is well suited to studying the elastic properties of frozen materials like sea ice and permafrost. Other geophysical techniques like InSAR may only resolve the sum of both elastic and inelastic creep deformations (e.g. Rouyet et al., 2019), since the satellite repeat cycle limits temporal resolution such that it is not possible to distinguish between the two.

The elastic, or Young's modulus, $E$, relates the amount of elastic deformation, or strain, $\varepsilon$, that a given material will experience under the application of a stress, $\sigma$, so that $\sigma = \varepsilon E$. Young's modulus may be measured dynamically by wave propagation experiments (Christ and Park, 2009; Kaplar, 1969; Langleben, 1962; Wang et al., 2006), or static loading experiments (Furnish, 1998; Timco and Weeks, 2010; Wang et al., 2019; Weeks and Assur, 1967). The results of these measurements are often termed the dynamic Young's modulus and the static or effective Young's modulus, respectively. The need to distinguish between the two stems from the fact that static loading experiments are typically conducted over varying timescales, with varying strain rates, where viscous creep plays a varying role in the observed deformation (e.g. Timco and Weeks, 2010). Consequently, measurement of the dynamic Young's modulus using seismic or ultrasonic wave methods is typically considered more reproducible, since the deformation is dominantly elastic at the timescale of seismic wave propagation (DiMarco et al., 1993; Timco and Weeks, 2010; Weeks and Assur, 1967).

Viscoelastic materials are typically modelled mathematically based on the identification of constitutive relationships that concisely describe the relationship between stress, strain and time (Bonfanti et al., 2020; Coleman and Noll, 1961). One of the simplest forms is the Maxwell model (Figure iii-a), composed of an elastic Hookean spring with spring constant, $k$, such that $\sigma(t) = k\varepsilon(t)$, and a viscous Newtonian dashpot with viscosity, $\eta$, such that $\sigma(t) = \eta\frac{d\varepsilon}{dt}$. In the Maxwell model, these are linked in series so that the stress response to a sudden deformation, $\varepsilon_0$, is given by, $\sigma(t) = \varepsilon_0 k e^{-t\frac{k}{\eta}}$.

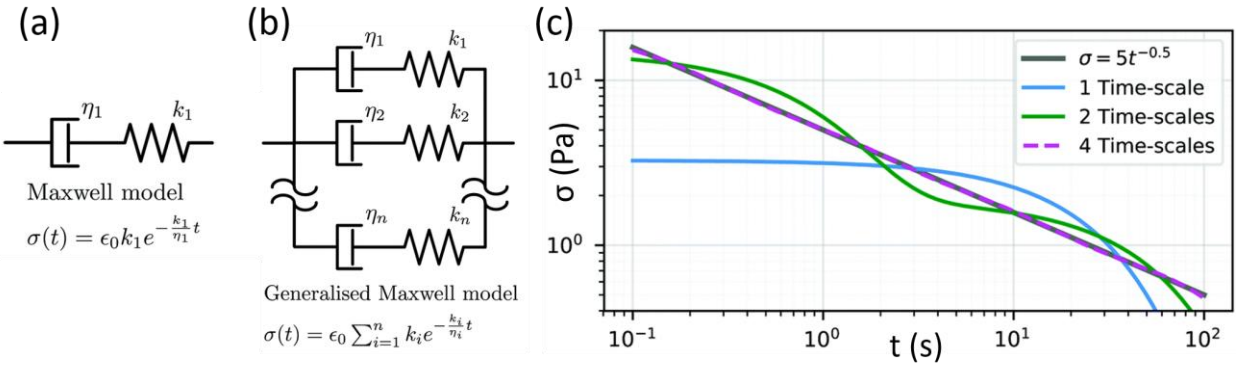


*Figure iii – Modified from Bonfanti et al. (2020). (a) the single spring and dashpot Maxwell model, (b) the generalised Maxwell model containing an arbitrary number of springs and dashpots, (c) stress response to a sudden deformation where the grey line is a power law relation, the blue line is the simple maxwell model and the green/purple lines contain two and four sets of springs and dashpots, respectively.*

The Maxwell model describes that stress generated when the material is deformed dissipates according to a characteristic relaxation time (Figure iii-c), falling to $1/e$ of its initial value after time $\tau = \eta/k$. More complex materials can be represented by incorporating additional springs and dashpots (Figure iii-b) with different relaxation times (Figure iii-c), although this comes at the cost of increasing computational expense and decreased model transparency (Bonfanti et al., 2020). Many real materials exhibit a broad range of relaxation/viscous creep timescales due to different modes of dissipation/deformation acting on different spatial and temporal scales (Bonfanti et al., 2020). Alternative constitutive forms that concisely describe this behaviour are therefore preferable in order to model the behaviour of these materials.

Power law relations have emerged as a popular parametrisation representing the viscous behaviour of a range of materials with complex microstructures such as ice (Schulson and Duval, 2009), gels (Ng and McKinley, 2008), polymers (Xu and Hou, 2011), concrete (Bouras et al., 2018), asphalt (Mino et al., 2016), biological cells/tissues (Desprat et al., 2005; Nicolle et al., 2010) and even cheese (Faber et al., 2017). Mathematically, these relations describe a continuous distribution of relaxation timescales (Bonfanti et al., 2020). For the case of ice, the experimental study of Glen (1955) has proved influential.

He identified the following empirical relation as a good representation of the observed stress-strain behaviour of polycrystalline ice;

$$\frac{d\varepsilon}{dt} = k\sigma^n,$$

where $k$ is a constant that varies with temperature and $n \approx 3$ is the "creep exponent". In order to relate the behaviour of ice to the more extensively studied problem of metals at high temperatures, Glen (1955) subsequently reformulated the mathematical form of the power law relation as,

$$\frac{d\varepsilon}{dt} = B\sigma^n \exp(-Q/RT) .$$

Here, $R$ is the universal gas constant, $B$ is an empirically determined constant, $Q$ is another empirical constant that is typically interpreted as an activation energy and $T$ is the temperature. Essentially, the temperature-dependent Arrhenius exponential term models the increasing ductility (the ease with which the material can be deformed) as temperature increases. This formulation has since gained popularity and a great number of studies have identified different values of the constants, $B$, $Q$ and $n$ corresponding to particular ice types, crystal structures and temperature ranges (e.g. Schulson and Duval, 2009; Weertman, 1983). While the power law representation of viscoelastic effects is empirical and cannot be interpreted based on a foundational derivation from fundamental physics, it at least gives a flexible and relatively concise representation of various forms of ice and other real-world materials.

Thermoviscoelastic models additionally incorporate the effect of temperature changes on the state of stress in a material. Here temperature plays a dual role. On one hand, temperature changes cause the material to deform via thermal expansion or contraction, a process that can be modelled by (e.g. Landau and Lifshitz, 1970),

$$\varepsilon = \alpha(T - T_0),$$

where $T_0$ is a reference temperature for the undeformed state, and $\alpha$ is the thermal expansion coefficient. Essentially, thermal loading due to temperature changes acts as an external driving agent on the system. On the other hand, the elastic and viscous parameters that describe the system may also be temperature dependent, such as through the temperature dependent Arrhenius behaviour discussed previously. A thermoviscoelastic model may therefore describe a system that is both forced by, and responds to changes in temperature (e.g. Mellon, 1997). The temperature dependence of ice saturation in a frozen soil is therefore also an important consideration that affects the thermoviscoelastic behaviour of the material. Freezing occurs over a relatively wide range of

temperatures due to both salinity (e.g. Dou et al., 2017; Wu et al., 2017) and capillary effects (e.g. Ma et al., 2015; Peppin and Style, 2013), such that predicting ice saturation as a function of temperature is far from trivial.

Within the scope of this thesis, we may consider thermoviscoelastic materials as examples of driven and damped dynamical systems, with temperature acting as the driver and viscosity as a damping factor. A driven undamped system is prone to instability, so the inclusion of damping through viscosity is important in order to ensure stable solutions of the dynamical models. For example, viscosity contributes to the attenuation of propagating waves in both time and space. It also contributes to material deformation over long timescales, significantly longer than the timescale over which seismic waves propagate. The slow release of accumulated elastic stress due to viscosity may also be envisaged as a simplified representation of the physical process of frost creep. The dynamical balance between the elastic and viscous components of the system then determines whether creep or fracture will dominate. For example, a key requirement for the initiation of a frost quake driven by thermal contraction is that stress accumulates elastically faster than it is dissipated until the tensile strength of the material has been exceeded.

## 1.5 Surface wave dispersion in layered media

Surface waves propagate along the free surface of an elastic solid (Stein and Wysession, 2009). Rayleigh waves (Rayleigh, 1885) involving elliptical wave motion in the vertical plane, are a specific class of surface waves that typically dominate when the earth-air interface is excited by a vertical seismic source. More than two thirds of the seismic energy produced by dynamite or vibroseis sources, for example, is propagated in the form of Rayleigh waves (Richart et al., 1970). The ground motion associated with Rayleigh waves decays exponentially with depth and becomes negligible within about one wavelength from the free surface in homogeneous media (Foti et al., 2018). As a result, lower frequency Rayleigh waves probe greater depths from the surface than higher frequencies, so that waves of different frequency are affected by the physical properties of the ground at different depths. This, in turn, means that Rayleigh waves of different frequency will propagate at different velocities for the typical case where the ground physical properties vary with depth, termed geometric dispersion (Foti et al., 2018). This property hints towards the general application that surface waves can be used to study variations of ground physical properties, particularly where flat, homogeneous, layered earth models may be reasonably assumed.

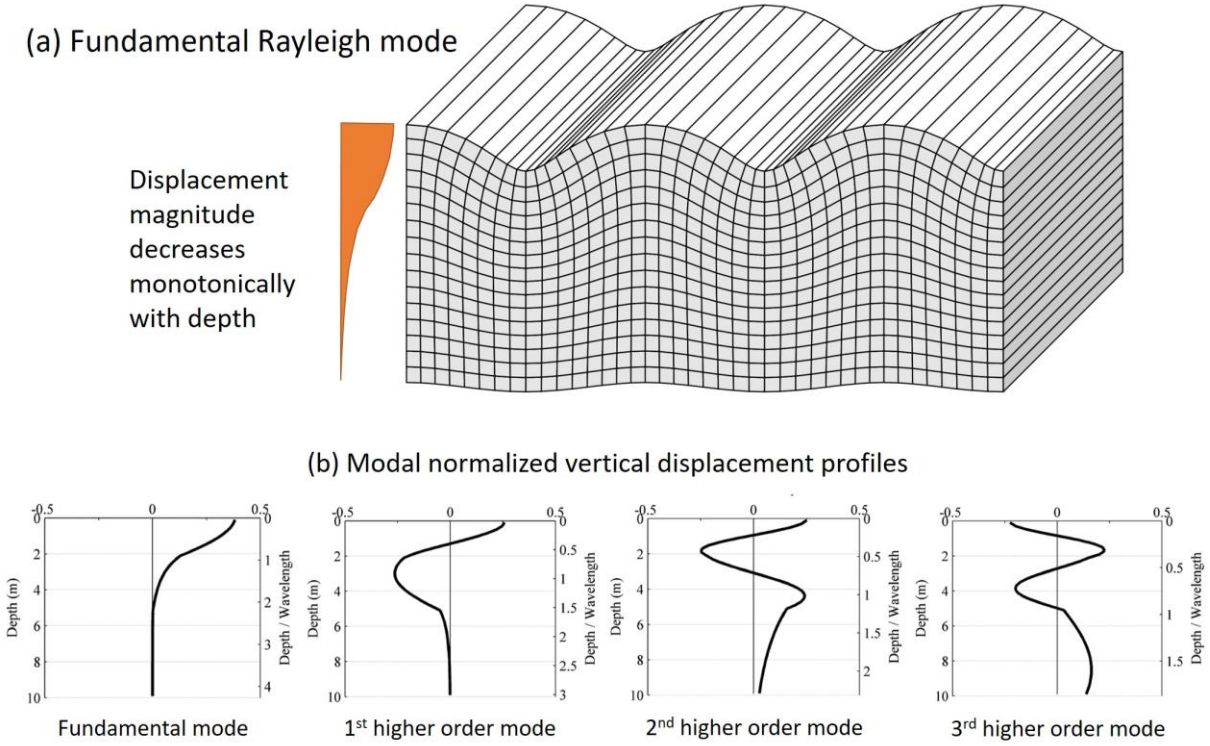


*Figure iv – (a) Illustration of the ground deformation of the fundamental mode Rayleigh wave, modified from Shearer (2009) and (b) normalized vertical displacement profiles corresponding to the fundamental and first three higher order Rayleigh modes at 60 Hz frequency for a normally dispersive layered earth model (S-wave velocity increasing monotonically with depth) modified from Lin and Ashlock (2014).*

An important point to clarify is that much like the harmonics of a plucked string, higher order modes of Rayleigh wave propagation are possible (see Figure iv). Whereas the ground displacement of the fundamental mode decreases monotonically with depth, the higher order modes are associated with more complex displacement profiles involving polarity reversals (Figure iv-b) and greater depth penetration (Pan et al., 2018). The amount of energy partitioned across the different modes depends on the specific variation of physical properties with depth. For the simple and common case where shear velocity and stiffness of the ground increase monotonically with depth (Figure v-a) due to compaction, Rayleigh wave phase velocities decrease with increasing frequency and the fundamental mode dominates (e.g. Naskar and Kumar, 2017; Thomson, 1950). The wavefield and its dispersion for a representative example of this case is illustrated in Figure v-b-c. The relatively straightforward relationship between frequency and penetration depth for the fundamental Rayleigh mode in this case, termed normal dispersion, has facilitated the successful inversion of ground physical properties using a range of techniques (e.g. Beaty et al., 2002; Foti et al., 2018; Naskar and Kumar, 2017; Park et al., 1999; Xia et al., 1999). The dispersion of surface waves is more sensitive to S-wave velocity, than P-wave velocity and density, so the S-wave velocity depth profile is typically the primary objective of inversion (e.g. Pan et al., 2018).

However, for cases where seismic velocity is not monotonically increasing with depth (Figure v-d), i.e., when a stiff layer lies above a soft stratum, the dispersion of surface waves becomes inherently multi-modal (Forbriger, 2003; Foti et al., 2003; Naskar and Kumar, 2017; Tokimatsu et al., 1992). The representative case illustrated in Figure v shows how simply varying the velocity of the surface layer has a dramatic effect on both the wavefield (Figure v-e) and on the wave dispersion (Figure v-f). Higher order Rayleigh modes (Tokimatsu et al., 1992) may contribute significantly to the ground motion and anomalously high velocity layers may act as partial waveguides that allow other types of waves to propagate (Ryden and Park, 2004). For example, a high velocity surface layer is associated with a multimodal dispersion pattern that approaches the Lamb waves of a plate in a vacuum (Lamb, 1917) if the shear velocity of the upper layer exceeds the compressional velocity of the underlying half-space (Ryden and Park, 2004). Inverting the multimodal wave dispersion for ground physical properties for inversely or irregularly dispersive media is a complex task that has shown some promising results but remains an active area of research (Naskar and Kumar, 2017; O'Neill et al., 2003; Pan et al., 2018; Pan et al., 2013; Yuen and Yang, 2020; Zhang and Alkhalifah, 2019).

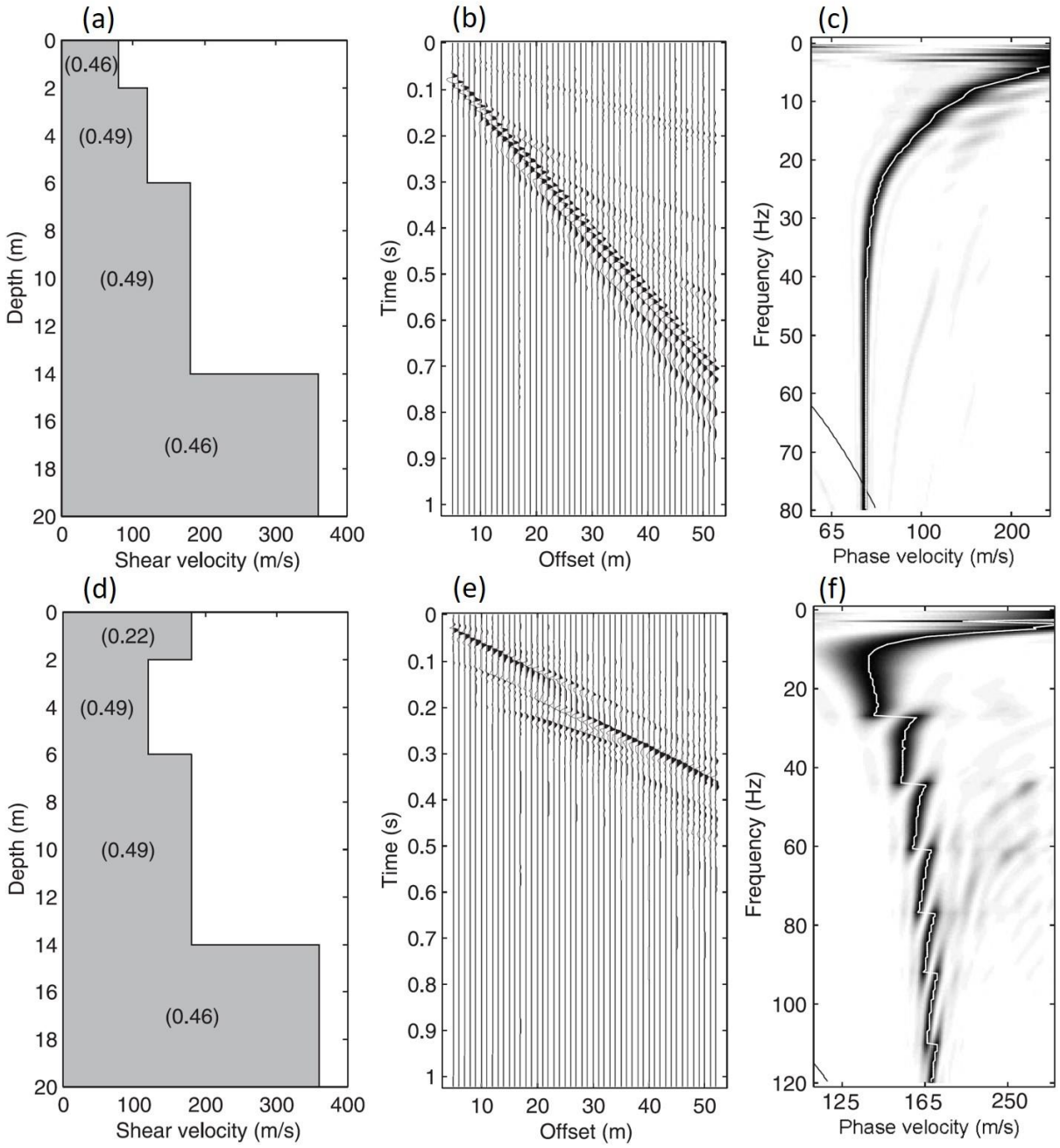


*Figure v – Modified from O'Neill et al. (2003). (a) and (d) are 1D shear velocity models where only the velocity of the top layer differs (numbers in brackets are Poisson's ratio for each layer). (b) and (e) are vertical component (P-SV) synthetic waveforms for a simulated linear array of receivers. (c) and (f) show the synthetic wavefields transformed to frequency-velocity space, i.e., the dispersion images of the wavefields (the white curves are the picked maxima of the dispersion spectra).*

## 1.6 The air-ice-water system

A sheet of ice, floating on water and in contact with the atmosphere above is a system of particular relevance to this thesis and deserving of further elaboration following the preceding description of frozen materials as thermo-viscoelastic solids. To give an introduction to the air-ice-water system, the physical properties in Table i will be assumed and the behaviour of representative systems of sea ice/air, sea ice/water and lake ice/water will be discussed. The air layer is an infinite halfspace, the ice thickness will be considered in proportion with frequency and the water layer has finite thickness.

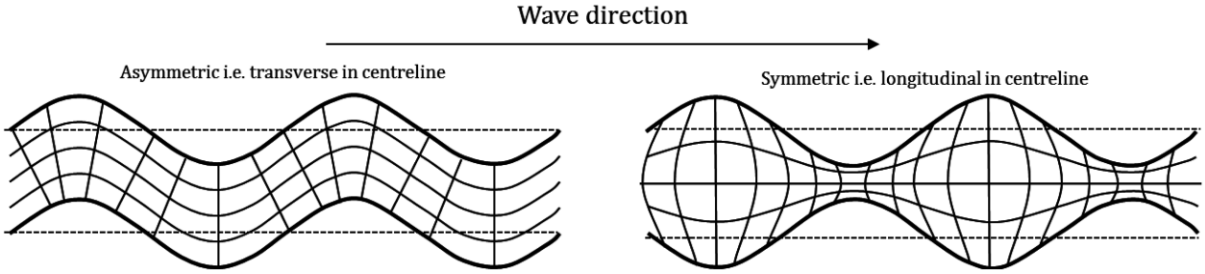


*Figure vi – illustration of antisymmetric and symmetric Lamb waves for a plate in a vacuum (from Marks et al., 2016).*

The floating ice sheet acts as a waveguide that behaves analogously to an elastic plate in a vacuum (also referred to as a free plate). A classic study by Lamb (1917), demonstrated that a series of symmetric and antisymmetric wave modes propagate in this system. The antisymmetric modes consist of bending or flexural motion, while the symmetric modes consist of longitudinal compression and dilation (see Figure vi). Fundamental modes propagate at all frequencies, while higher-order modes are restricted to high frequencies. A solid plate immersed in a light fluid, e.g., air, behaves similarly to a plate in a vacuum, though some energy can be lost from the plate to the fluid (Hayashi and Inoue, 2014; Kiefer et al., 2019). The designation “leaky Lamb waves” is consequently applied to describe the plate-fluid interaction and energy radiation into the fluid.

If the plate is heavily fluid loaded on one side, as for ice floating on water, the boundary condition is significantly modified. This results in a modification of the symmetric and antisymmetric Lamb wave modes as well as propagation of an additional mode analogous to a Scholte wave, a class of surface wave that propagates along the interface between solid and liquid half-spaces (Vinh, 2013; Zhu et al., 2004). The finite thickness of the ice sheet modifies the propagation of this Scholte wave (compared to the case of a solid elastic halfspace) and it is correspondingly referred to as a quasi-Scholte wave (Inoue and Hayashi, 2015). It is this quasi Scholte-wave that dominates the vertical component of surface displacement for a floating ice sheet excited by an impulsive source (Moreau et al., 2020a).

*Table i - Physical properties used to calculate dispersion curves shown in Figures vii and viii. Note that the fluid depth only affects the thin plate model calculations, the fluid in the Kiefer et al. (2019) model is infinite.*

| | *Sea ice/Air system* | *Sea ice/water system* | *Lake ice/water system* |
|---|---|---|---|
| *Young's Modulus (GPa)* | 2.5 | 2.5 | 8.5 |
| *Poisson's ratio (-)* | 0.33 | 0.33 | 0.33 |
| *Ice density (kg.m$^{-3}$)* | 931 | 931 | 917 |
| *Fluid density (kg.m$^{-3}$)* | 1.3 | 1027 | 1000 |
| *Fluid bulk velocity (m/s)* | 320 | 1500 | 1500 |
| *Fluid depth (m)* | 20 | 20 | 20 |

A common simplifying assumption is that the thickness of the ice sheet is small compared to the wavelength, the so-called thin plate approximation (e.g. Squire et al., 1996), such that the motion of the thin plate can be described by the partial differential equation

$$D\nabla^4\zeta + \rho_l h\frac{\partial^2\zeta}{\partial t^2} + \rho_w g\zeta = -\rho_w \frac{\partial\phi}{\partial t}\Big|_{z=b} - f(x,y,t). \quad \text{(I)}$$

The plate extends infinitely along the horizontal x and y axes and the vertical axis, z, is positive downwards with its origin at the upper undisturbed water surface and lower surface of the plate (its draught) lies at depth $b$. Here, $\zeta(x,y,t)$ is the vertical deflection of the plate's neutral surface and $\phi$ is the velocity potential in the fluid, $D = \frac{Eh^3}{12(1-\nu^2)}$ is the plate flexural stiffness, $E$ is Young's modulus, $h$ is the plate thickness, $\nu$ is Poisson's ratio, $\rho_w$ is the water density, $\rho_l$ is the plate density, $g$ is the acceleration due to gravity and $f(x,y,t)$ is the applied external spatiotemporal force. In essence, the first term on the LHS represents the bending forces in the plate, the second represents the plate acceleration and the third is the plate buoyancy. The terms on the RHS are due to the constraint of finite water depth and the driving external force. Upon excitation, the vertical deflection of the ice surface is dominated by a pure bending mode of plate motion that is commonly referred to as the flexural wave (e.g. Johansen et al., 2019; Stein et al., 1998). The validity of the thin plate approximation depends on the relationship between plate thickness and wave frequency and for frequency-thickness products less than 50 Hz·m where it holds, the flexural wave is approximately equivalent to the quasi-Scholte wave (Moreau et al., 2020a).

An important property of the air-ice-water system is wave dispersion, i.e., the variation of propagation velocity with frequency. For illustration, we will consider the wave dispersion using both the thin plate approximation and an exact guided wave theory using a spectral collocation scheme to solve the full leaky Lamb wave spectrum, including exact interaction with the fluid (Kiefer et al., 2019). This spectral

collocation method is chosen because it ensures that all possible wavemodes are found at a given frequency, in comparison to the challenging and numerically ill-conditioned characteristic root-finding process traditionally employed (Kiefer et al., 2019).

If we first consider the air-ice system as illustrated in Figure vii, the dispersion curves predicted according to Kiefer et al. (2019) are essentially those of the free plate (i.e., ice sheet in a vacuum), with the addition of an extra branch corresponding to the compressional bulk velocity in air. Where the fundamental antisymmetric mode (denoted A0) of the free-plate crosses the speed of sound in air, the dispersion curves split into two modes. The quasi-Scholte branch remains trapped in the plate with a phase velocity less than the speed of sound in air, while a leaky mode branch exists at higher frequencies and radiates energy into the air proportional to the imaginary part of the wavenumber (Figure vii-b). We observe that energy radiation into the air is concentrated over a narrow band of frequency-thickness and the spread that is observed is due to radiation at different angles satisfying the phase matching condition,

$$\cos\theta = c_{air}/c_{ice}, \qquad \text{(II)}$$

where $c_{air}$ is the phase velocity of inhomogeneous bulk waves radiated into the air, $c_{ice}$ is the phase velocity of flexural waves in the ice and $\theta$ is the angle between the horizontally propagating flexural waves and the bulk waves radiated into the liquid (Mozhaev and Weihnacht, 2002). Radiation is most efficient at the grazing angle, where the leaky mode branch crosses the bulk compressional velocity in air. In general, subsonic guided waves are fully trapped in the waveguide and can only excite evanescent waves in the fluid (e.g. Brower et al., 1979) although energy leakage into the fluid as low as ~98.5% of the bulk fluid velocity can be explained by radiation from inhomogeneous waves that travel slower than homogeneous waves (Kiefer et al., 2019; Mozhaev and Weihnacht, 2002).

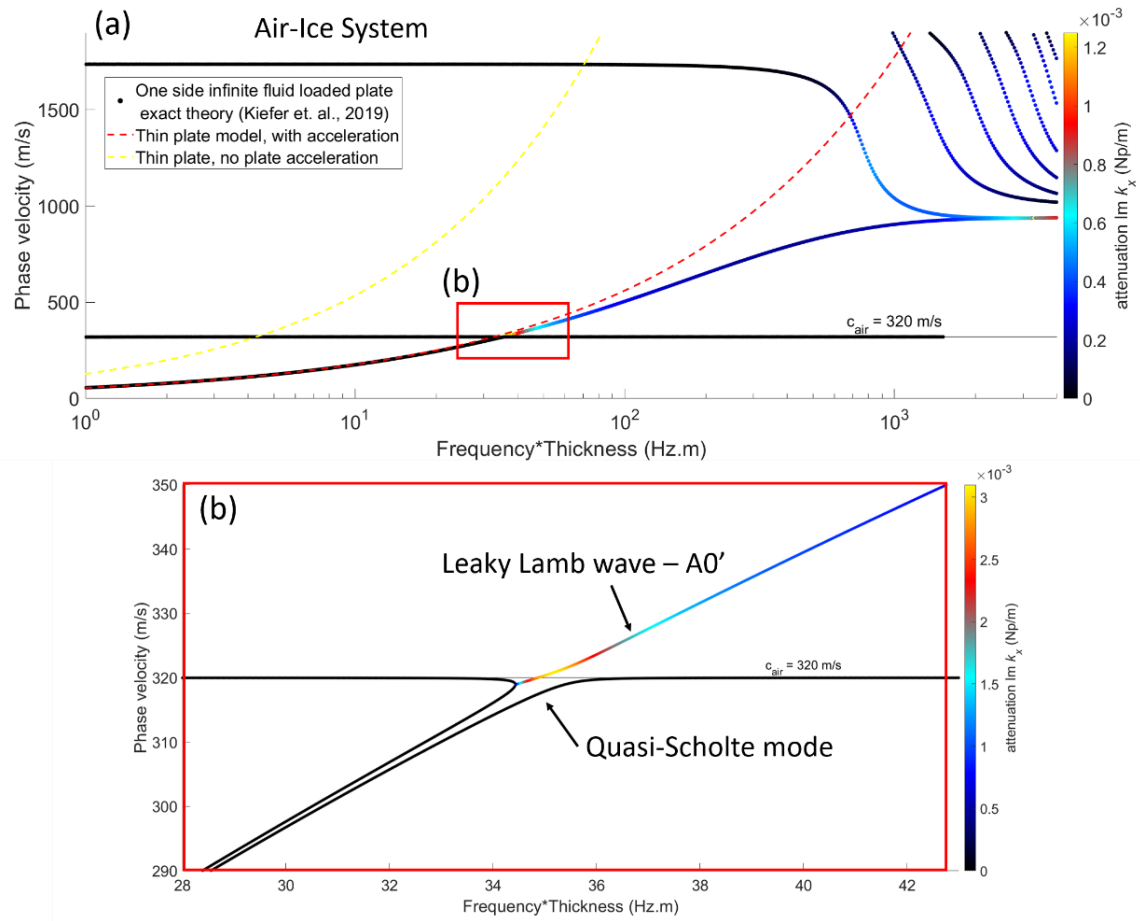


*Figure vii - (a) Dispersion curves for the air/sea ice system calculated by the exact spectral collocation method of Kiefer et al. (2019) compared to thin plate approximate model Eq. (I) shown with (dashed red line) and without (dashed yellow line) the inclusion of plate acceleration. (b) enlargement highlighting the dispersion curve splitting and transition to leaky behaviour at the phase velocity corresponding to the bulk compressional wave velocity in air.*

If we now consider the water-ice system as illustrated in Figure viii, the exact dispersion curves calculated according to Kiefer et al. (2019) differ substantially from the free plate (ice sheet in a vacuum), due to the heavy fluid loading. Interestingly, for the sea ice/water system the shear wave velocity in ice drops below the longitudinal wave velocity in water, leading to a multiplicity of trapped modes at high frequencies (Figure viii-a) compared to the lake ice/water system (Figure viii-b). Notably, this behaviour occurs in the ultrasonic range, far above the frequency range typically studied in environmental seismology. As discussed by Moreau et al. (2020a), the thin plate approximation of a floating ice-sheet (Eq. (I)) follows the quasi-Scholte mode branch of the ice-water waveguide and is a useful simplification maintaining accurate representation of the system for frequency-thickness products below 50 Hz·m.

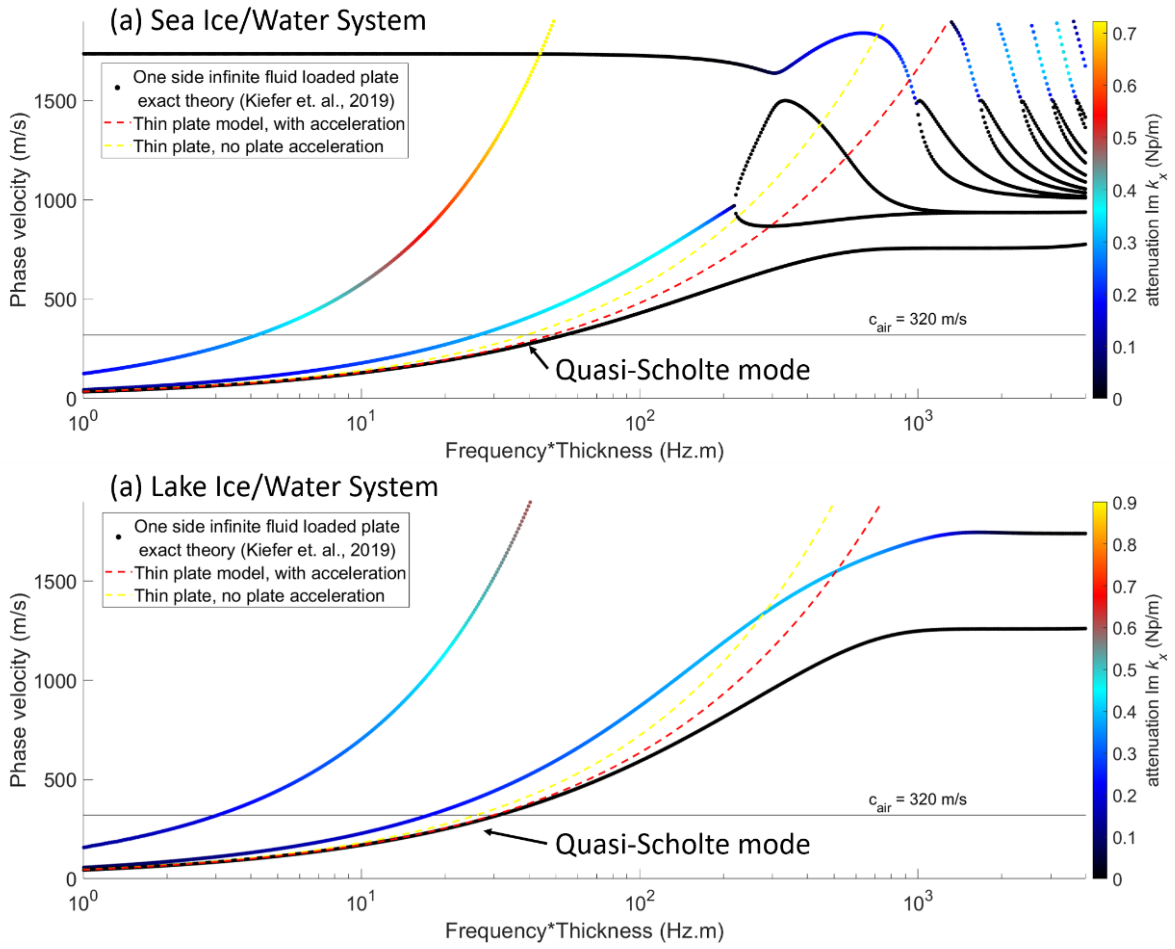


*Figure viii - (a) Dispersion curves for the sea ice/water system calculated by the exact spectral collocation method of Kiefer et al. (2019) compared to thin plate approximate model Eq. (I) shown with (dashed red line) and without (dashed yellow line) the inclusion of plate acceleration. (b) as in (a) but using elastic parameters corresponding to fresh water lake ice.*

The complete air-ice-water system can be expected to behave as a hybrid of Figure vii and Figure viii, i.e., the dispersion will be virtually identical to the ice-water system (Figure viii) with the addition of the mode splitting around the bulk compressional velocity in air as illustrated in Figure vii-b. Here, it is worth noting that choosing appropriate wave mode terminology for the air-ice-water system can be complicated, as it is a rather special example of a plate that is heavily fluid loaded on one side and lightly fluid loaded on the other side. As a result, there are formally two quasi-Scholte modes and two sets of leaky Lamb modes corresponding to the ice-air and ice-water interfaces. The air-ice-water system also deviates significantly from the free plate for which true Lamb waves are defined, and the one side fluid-loaded plate for which the quasi-Scholte mode is best defined. Apart from ultrasonic studies, the low frequency, thin plate approximation (Eq. (I)) where flexural waves are physically described by a pure bending mode of plate motion, remains an appropriate and attractive simplification within cryoseismology.

# 2 Thesis papers

## 2.1 Preface to paper 1

Romeyn, R., Hanssen, A., Ruud, B. O., Stemland, H. M., and Johansen, T. A. 2021. **Passive seismic recording of cryoseisms in Adventdalen, Svalbard**, The Cryosphere, 15, 283–302, https://doi.org/10.5194/tc-15-283-2021

Paper 1 focuses on a series of transient seismic signals that were recorded by a temporary seismic array deployed in Adventdalen on Svalbard. The spatial correspondence of the estimated source positions of these events with frost polygons/ice wedge areas and temporal correlation with rapidly decreasing temperature led to the interpretation that these seismic events were cryoseisms, or more specifically frost quakes.

One of the key results of this article was demonstrating that frost quakes can act as sources of surface waves that can be used to produce high-quality dispersion images. To give additional context to this result, Figure ix shows a comparison of different multichannel seismic experiments conducted in Adventdalen that were designed to record surface waves. Active source experiments were conducted using (a) sledgehammer blows on a steel plate and (b) explosive point charges consisting of detonating cord wrapped around a detonator. The vertical component of ground motion was recorded by a linear array of 60 geophones spaced 1 m apart and deployed in-line with the source. For comparison, Figure ix also shows an example of a frost quake recorded passively by the 2D geophone array reported on in Paper 1.

The dispersion images shown in Figure ix were produced according to the standard phase shift method of Park et al. (1998). The dispersion image from the sledgehammer experiment is relatively poorly resolved due to low signal to noise ratio and only the general trend of the apparent dispersion curve is resolvable. The signal to noise ratio is improved for the more powerful explosive point charge and a multimodal dispersion pattern begins to be discernible. However, the strong air wave produced by the explosive charge appears to interfere with and reduce the coherency of the surface waves at higher frequencies. By contrast, the frost quake recorded by the 2D geophone array produces a much-improved dispersion image where the multimodal dispersion pattern is well resolved. It is therefore

clear that frost quakes can be a useful source of surface wave energy. However, some of the improvement for the frost quake example compared to the active source experiments (Figure ix) may be attributable to the uneven spacing of the geophones along the 1D domain representing radial distance from the source (also known as offset). This irregular spacing may improve the sampling of surface waves of different wavelengths. Further controlled experiments would be required to determine whether the passive recordings of frost quakes gave high quality results because of the of the frost quake source characteristics, or because of the geometry of the geophone array. In this context, a buried explosive charge would be a useful point of comparison, since this should suppress the air wave and improve source-ground coupling, potentially giving a result more like the frost quake example. However, on Svalbard, seismic surveying may not leave a lasting environmental footprint and is only permitted on top of snow-covered ground. Use of buried explosive charges is therefore not permitted. Environmental considerations thereby also strengthen the attractiveness of utilizing naturally occurring frost quakes as a seismic source for near-surface seismic surveying.

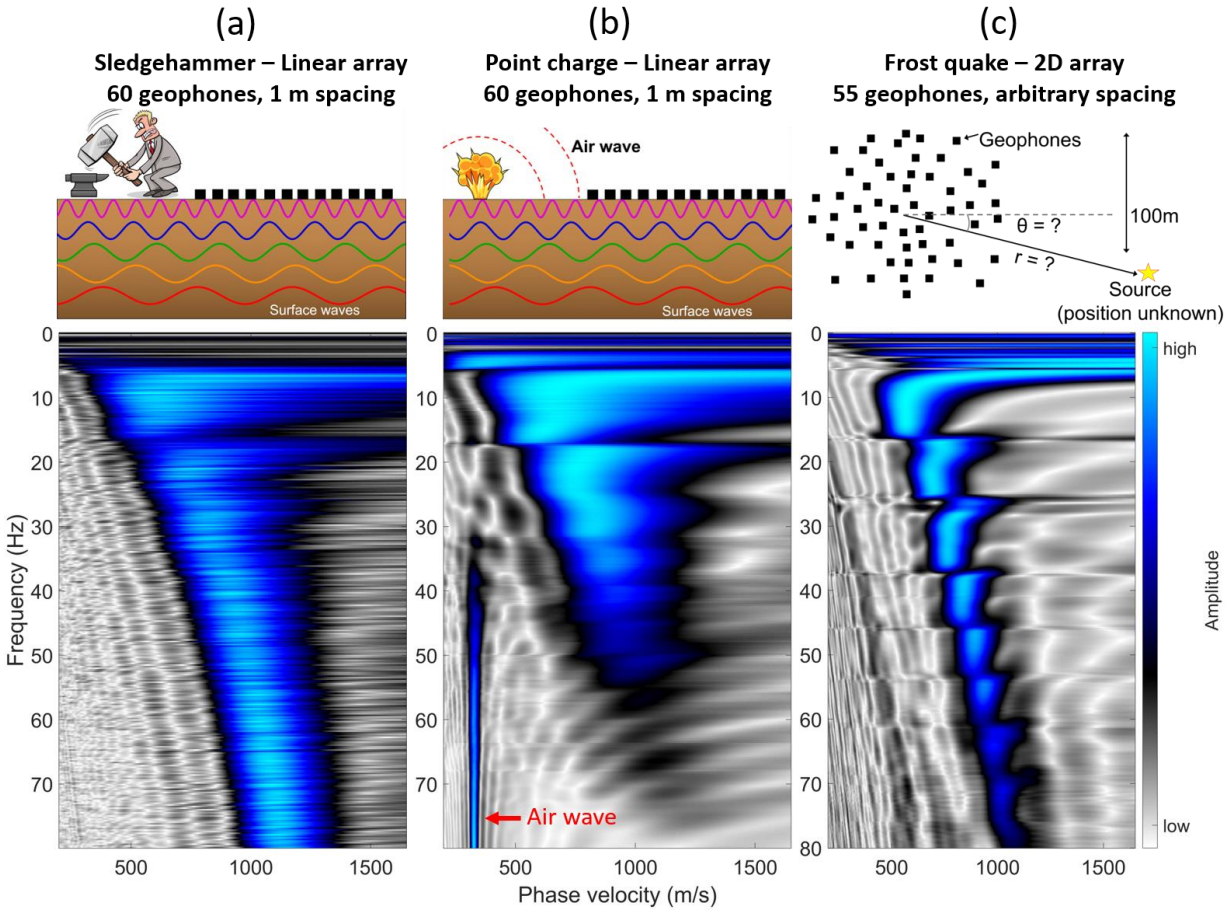


*Figure ix – Illustration of different multichannel seismic experiments conducted in Adventdalen on Svalbard. (a) Sledgehammer and (b) explosive point charge sources were located 25 m inline from the nearest geophone. (c) The frost quake source location was estimated to be ~190 m at a bearing of ~353° from the centre of the 2D geophone array.*

# Paper 1

The Cryosphere, 15, 283–302, 2021
https://doi.org/10.5194/tc-15-283-2021


The Cryosphere Open Access EGU

# Passive seismic recording of cryoseisms in Adventdalen, Svalbard

**Rowan Romeyn[1,2], Alfred Hanssen[1,2], Bent Ole Ruud[2,3], Helene Meling Stemland[2,3], and Tor Arne Johansen[2,3,4]**

[1]Department of Geosciences, University of Tromsø – The Arctic University of Norway, 9037 Tromsø, Norway
[2]Research Centre for Arctic Petroleum Exploration (ARCEx), 9037 Tromsø, Norway
[3]Department of Earth Science, University of Bergen, 5007 Bergen, Norway
[4]The University Centre in Svalbard (UNIS), 9171 Longyearbyen, Norway

**Correspondence:** Rowan Romeyn (rowan.romeyn@uit.no)

Received: 20 May 2020 – Discussion started: 25 June 2020
Revised: 30 October 2020 – Accepted: 7 December 2020 – Published: 20 January 2021

**Abstract.** A series of transient seismic events were discovered in passive seismic recordings from 2-D geophone arrays deployed at a frost polygon site in Adventdalen, Svalbard. These events contain a high proportion of surface wave energy and produce high-quality dispersion images using an apparent offset re-sorting and inter-trace delay minimisation technique to locate the seismic source, followed by cross-correlation beamforming dispersion imaging. The dispersion images are highly analogous to surface wave studies of pavements and display a complex multimodal dispersion pattern. Supported by theoretical modelling based on a highly simplified arrangement of horizontal layers, we infer that a ∼ 3.5–4.5 m thick, stiff, high-velocity layer overlies a ∼ 30 m thick layer that is significantly softer and slower at our study site. Based on previous studies we link the upper layer with syngenetic ground ice formed in aeolian sediments, while the underlying layer is linked to epigenetic permafrost in marine-deltaic sediments containing unfrozen saline pore water. Comparing events from spring and autumn indicates that temporal variation can be resolved via passive seismic monitoring. The transient seismic events that we record occur during periods of rapidly changing air temperature. This correlation, along with the spatial clustering along the elevated river terrace in a known frost polygon, ice-wedge area and the high proportion of surface wave energy, constitutes the primary evidence for us to interpret these events as frost quakes, a class of cryoseism. In this study we have proved the concept of passive seismic monitoring of permafrost in Adventdalen, Svalbard.

## 1 Introduction

Permafrost is defined as ground that remains at or below 0 °C for at least 2 consecutive years (French, 2017). On Svalbard, an archipelago located in the climatic polar tundra zone (Kottek et al., 2006), at least 90 % of the land surface area not covered by glaciers is underlain by laterally continuous permafrost (Christiansen et al., 2010; Humlum et al., 2003). A seasonally active layer, where freezing/thawing occurs each winter/summer, extends from the surface to a depth of 0.8–1.2 m (Christiansen et al., 2010) and overlies the permafrost. However, the purely thermal definition of permafrost means that the mechanical properties can vary widely depending on the actual ground-ice content. The ground-ice content varies spatially according to sediment texture, organic content, moisture availability and sediment accumulation rate (Gilbert et al., 2016; Kanevskiy et al., 2011; O'Neill and Burn, 2012). Because of the significant impact of ice content on mechanical strength, seismic velocities are a relatively sensitive tool to study the subsurface distribution of ground ice (Dou et al., 2017; Johansen et al., 2003).

The thermal dynamics of this permafrost environment lead to an interesting phenomenon called cryoseisms, sometimes referred to as frost quakes. Cryoseisms are produced by the sudden cracking of frozen material at the Earth's surface (Battaglia and Chagnon, 2016). They are typically observed in conjunction with abrupt drops in air and ground temperature below the freezing point, in the absence of an insulating snow layer and in areas where high water saturation is present in the ground (Barosh, 2000; Battaglia and Chagnon, 2016; Matsuoka et al., 2018; Nikonov, 2010). When the surface temperature drops well below 0 °C the frozen perme-

**Published by Copernicus Publications on behalf of the European Geosciences Union.**

able soil expands, increasing the stress on its surroundings, which can eventually lead to explosive pressure release and tensional fracturing (Barosh, 2000; Battaglia and Chagnon, 2016). Seismic waves from these events decay rapidly with distance from the point of rupture but have been felt at distances of several hundred metres to several kilometres and are usually accompanied by cracking or booming noises, resembling falling trees, gunshots or underground thunder (Leung et al., 2017; Nikonov, 2010). The zero focal depth of cryoseisms means that, relative to tectonic earthquakes, a larger proportion of the energy is distributed in the form of surface waves (Barosh, 2000).

Methods based on the analysis of surface waves are used extensively in engineering fields, such as the non-destructive testing of structures or assessment of the mechanical properties of soils relating to their use as a foundation for built structures (Chillara and Lissenden, 2015; Park et al., 1999, 2007; Rose, 2004). In a typical soil profile, the shear velocity and stiffness of the ground increase gradually with depth due to compaction, leading to a simple wave field dominated by fundamental mode Rayleigh waves (Foti et al., 2018). Mechanical properties of the ground are then estimated relatively simply from the geometrical dispersion of the recorded wave field, i.e. the measured pattern of phase velocity as a function of frequency, where lower frequencies interact with the ground to greater depths than higher frequencies.

By contrast, in permafrost environments, the surface layer freezes solidly during the winter, leading to an increase in the shear modulus of the upper layer (Johansen et al., 2003) and an inverse shear velocity with depth profile. This is similar to the case of pavement in civil engineering studies, where a thin, relatively stiff, high-velocity layer at the surface overlies softer and slower ground materials beneath. The high-velocity surface layer acts as a waveguide, permitting the excitation of higher-order wave modes, and the wave field becomes significantly more complicated due to the large number of simultaneously propagating wave modes (Foti et al., 2018; Ryden and Lowe, 2004). Such engineering applications have furthermore driven the development of wave propagation models capable of modelling these complicated wave fields. For example, the ground may be represented by a horizontally layered medium with partial wave balance at the interfaces, for which the dispersion spectrum and stress-displacement field is readily calculated using the global matrix method (Lowe, 1995).

## 2 Study area and seismic acquisition

Our study site is located in Adventdalen, near the main settlement Longyearbyen on the island Spitsbergen, within the Svalbard archipelago in the high Arctic, as shown in Fig. 1. The climate of this area, as recorded at Longyearbyen airport, is characterised by low mean annual precipitation of 192 mm and mean annual air temperature of −5.1 °C for the period 1990–2004, rising to −2.6 °C during the period 2005–2017. The maritime setting and alternating influence of low-pressure systems from the south and polar high-pressure systems means that rapid temperature swings are common during winter from above 0 °C down to −20 or −30 °C, while summer temperatures are more stable in the range of 5–8 °C (Matsuoka et al., 2018). Snow cover in the study area is typically shallow, due to the strong winds that blow along the valley, and varies according to local topography with 0–0.1 m over local ridges and 0.3–0.4 m in troughs. Positive temperature and snowmelt events also occur sporadically through the freezing season (October to May) and subsequently result in the formation of a thin ice cover. Both shallow snow cover and thin ice cover permit efficient ground cooling throughout the freezing season (Matsuoka et al., 2018).

Adventdalen has continuous permafrost extending down to ∼ 100 m depth (Humlum et al., 2003), but the highest ground-ice content is restricted to the uppermost ∼ 4 m in the loess-covered river terraces that bound the relatively flat, braided Adventelva river plain. The geological setting of the study site is illustrated in Fig. 2. The formation of permafrost in Adventdalen began around 3 ka, concurrent with the subaerial exposure and onset of aeolian sedimentation on valley-side alluvial terraces (Gilbert et al., 2018). Sediment cores studied by Cable et al. (2018) and Gilbert et al. (2018) show a consistent pattern of an increased ground-ice content over a ∼ 4 m thick interval (decreasing towards the coast), beneath a ∼ 1 m thick active layer. This interval was observed consistently in cores retrieved from alluvial and loess deposits and is interpreted as ice-rich syngenetic permafrost (Cable et al., 2018; Gilbert et al., 2018).

The underlying interval consists of marine-influenced deltaic sediments into which permafrost has grown epigenetically and where ground-ice content remains low (Gilbert et al., 2018). Unfrozen permafrost has been mapped in Adventdalen below the Holocene marine limit (which includes the entire study area as illustrated in Fig. 1) using nuclear magnetic resonance and controlled source audio-magnetotelluric data (Keating et al., 2018). This is again related to the presence of saline pore water in these marine-influenced deltaic sediments that causes the pore water to remain at least partially unfrozen despite sub-zero temperatures.

Ice-wedge polygons, one of the most recognisable landforms in permafrost environments (Christiansen et al., 2016), are present at the investigated site in Adventdalen. They form when freezing winter temperatures cause the ground to contract and crack under stress (Lachenbruch, 1962). Water later infiltrates the cracks and refreezes as thin ice veins that extend down into the permafrost. These veins have lower tensile strength compared to the surrounding ground (Lachenbruch, 1962; Mackay, 1984), so subsequent freeze-induced cracking occurs preferentially along this plane of weakness. The repeated cracking, infilling and refreezing causes the ice wedges to grow laterally, forcing the displaced ground up-

wards and resulting in a series of ridges in a polygonal arrangement that are the surface hallmark of the phenomenon (Christiansen et al., 2016; Lachenbruch, 1962).

Sudden ground accelerations corresponding to cryoseismic events have previously been observed at our study site in Adventdalen. Matsuoka et al. (2018) monitored three ice-wedge troughs within an area of polygonal patterned ground at the site, using a combination of extensometers, accelerometers and breaking cables connected to timing devices. Their study, which extended over the 12-year period 2005–2017, provides a valuable overview of the seasonality and correspondence between ground motion and environmental parameters. The related study of O'Neill and Christiansen (2018) further details the accelerometer results. Ice-wedge cracking was typically registered in late winter, when the top of the permafrost cooled to around −10 °C, resulting in large accelerations of 5 g to more than 100 g. However, O'Neill and Christiansen (2018) also report smaller magnitude accelerations throughout the freezing season, typically in conjunction with rapid surface cooling, that are thought to be caused by the initiation of cracks within the active layer or the horizontal and vertical propagation of existing ice-wedge cracks. Given the timing of the field campaigns for the present study, during spring and autumn of 2019, we expect it is rather the latter category of events that have been recorded.

In the present study ground motion was recorded using geophones deployed in 2-D arrays (the geometry of which is discussed in Sect. 3.3.1). During the spring field campaign, groups of eight gimballed vertical-component geophones connected in series (geophone type sensor SM-4/B 14 Hz, 0.7 damping and spurious frequency of 190 Hz) were deployed on the snow surface at each receiver location. During deployment for the autumn field campaign, geophones were embedded into the unfrozen ground surface as an assortment of spike geophones (Sercel SG-10 10 Hz) connected in series in strings of four geophones and 3C geophones (DT-Solo 3C with $z$ element HP301V 10 Hz) where only the vertical channel was used. Both of these geophone types have damping of 0.7, giving a flat response above the natural frequency up to the spurious frequency of 240 Hz. Data were recorded for defined time intervals as will be discussed in Sect. 4.1, mandated primarily by battery considerations.

## 3 Methods

In this study, we present a methodology to isolate transient seismic signals in passive seismic recordings from two-dimensional vertical-component geophone arrays. These transient signals contain surface wave energy with a relatively high signal-to-noise ratio. We implement a novel method to localise the unknown source position of these signals based on the 2-D receiver array geometry and subsequently recover dispersion spectra using a cross-correlation beamforming technique. In order to infer subsurface physical properties we generate theoretical dispersion curves using the global matrix method (Lowe, 1995) based on idealised horizontally layered media models. The forward model is manually tuned to achieve the best fit with the experimentally observed dispersion spectra. Similar experiments were conducted over two field campaigns in the spring and autumn in order to investigate temporal variation in permafrost mechanical strength.

### 3.1 Isolation of microseismic events in passive records

Our passive seismic recordings contain a significant amount of non-surface wave energy, including wind noise and air waves. As a result we find it more effective to isolate and analyse specific transient microseismic events rather than attempting to recover the Green's function from ambient noise cross-correlations as for example Sergeant et al. (2020) have done for passive recordings on glaciers. The periodic microseismic signals are isolated from background random noise based on permutation entropy, a nonlinear statistical measure of randomness in a time series (Bandt and Pompe, 2002), that produces local minima for coherent signals embedded in noise. We follow the implementation of Unakafova and Keller (2013) using ordinal patterns of third order extracted over successive samples and a sliding window size of 200 samples. We then apply a peak-finding algorithm to identify local minima in permutation entropy that meet peak prominence criteria defined by thresholds of peak value, height and width. An example of event detection is shown in Fig. 3 for real, noisy data recorded at the study site.

The isolated microseismic events were subsequently processed in a similar way to active source experiments, i.e. using well-established multichannel analysis of surface waves (MASW) methodologies, with modification due to the unknown source position.

### 3.2 MASW dispersion imaging with unknown source position

Several processing methods for multichannel analysis of surface waves (MASW) are possible depending on the acquisition setup. One of the most well known is the 1-D phase shift method of Park et al. (1998) that is straightforward to apply for line arrays of receivers and inline sources at known offsets. The dispersion image is built by scanning over frequency ($\omega$) and phase velocity ($v$) according to

$$E_{\text{1-D}}(\omega, v) = \left| \sum_{i=1}^{N} \mathrm{e}^{j\phi_i} R_i(\omega) \right|, \quad (1)$$

where $j = \sqrt{-1}$, $R_i(\omega)$ is the Fourier transform of the $i$th trace $r_i(t)$ of $N$ recorded traces, and $\phi_i = \omega x_i / v$ is the corresponding phase shift at known source–receiver offset $x_i$. On the other hand, processing of passively recorded microseismic events is complicated by the fact that the source position

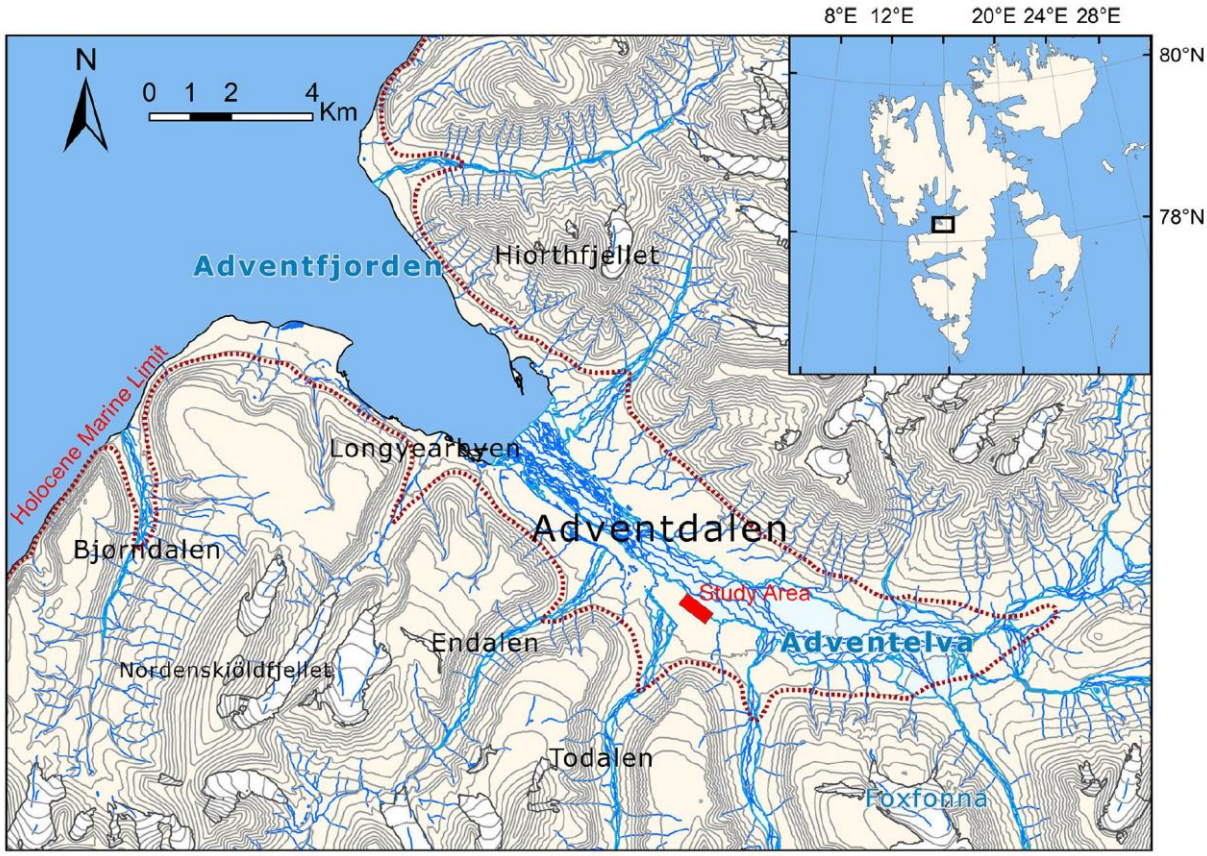


**Figure 1.** 1 : 100 000 scale map showing the location of the study area (red box) in Adventdalen. Inset map illustrates the location with respect to the Svalbard archipelago. The Holocene marine limit (red dashed line) is drawn according to Lønne (2005). Map data © Norwegian Polar Institute (http://npolar.no, last access: 3 September 2020).

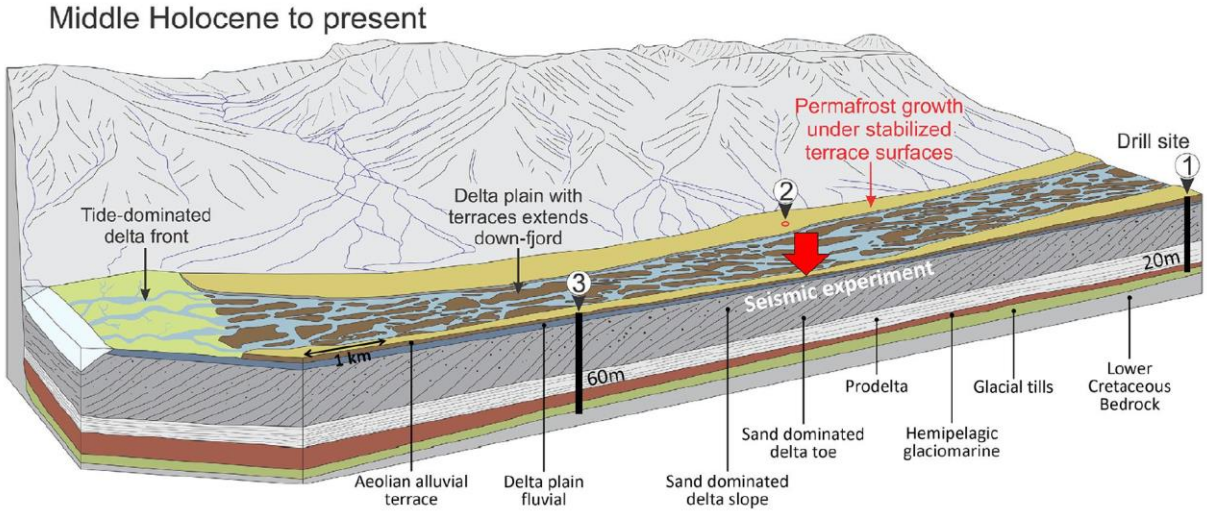


**Figure 2.** Geological model of Adventdalen, Svalbard, modified from Gilbert et al. (2018); the numbered sites mark the coring locations studied by Gilbert et al. (2018), and the red arrow marks the position of the seismic experiments described in this study.

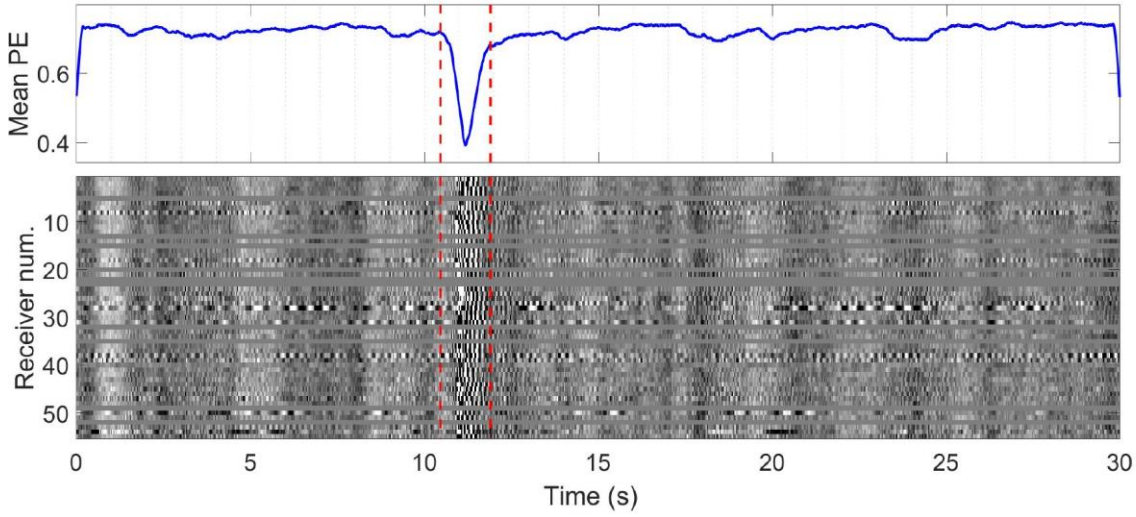


**Figure 3.** Detection of transient event based on mean permutation entropy (PE), a metric that peaks towards minima when coherent amplitudes are recorded across the array of receivers. Red dashed lines mark the temporal extent of the extracted event that is shown in greater detail in Fig. 4. This event was recorded on 30 March 2019 at 18:06 UTC+0.

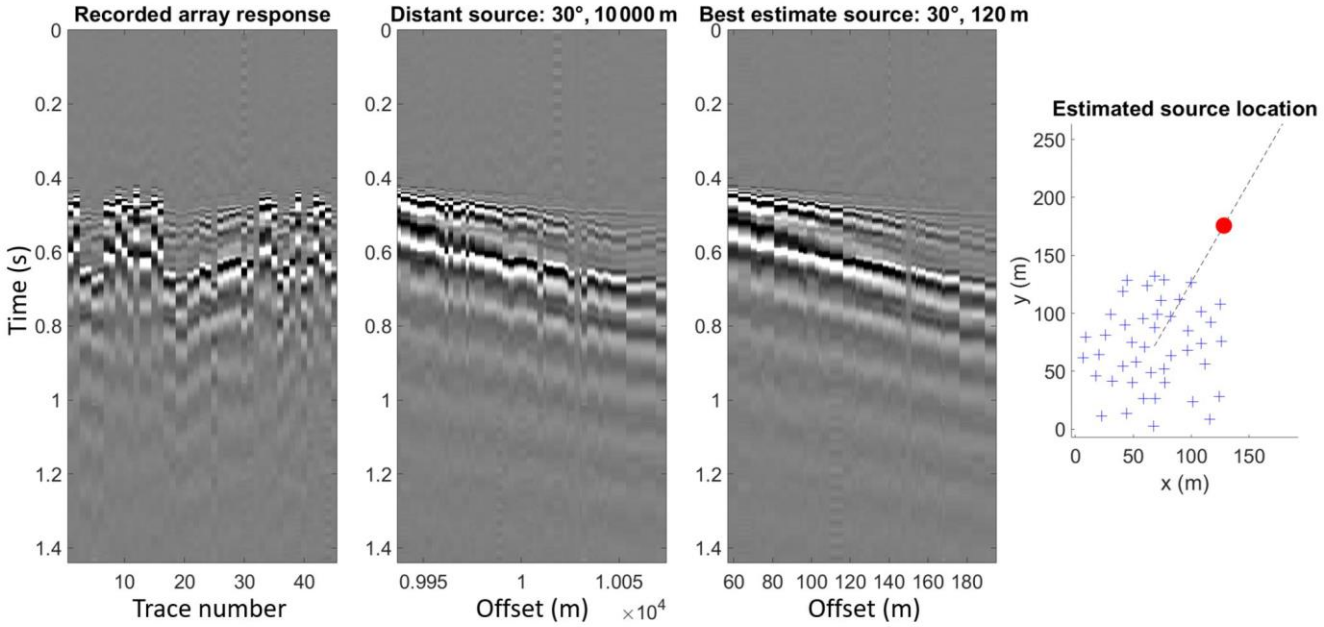


**Figure 4.** Field recording of a transient event, whose detection is highlighted in Fig. 3, demonstrates that re-sorting traces by apparent offset to a distant source produces a gather with poorer coherence than re-sorting by offset to the best-estimate source range at 120 m. Blue crosses denote geophones, while the red circle marks the best-estimate source position.

is unknown. We employed a 2-D receiver array that allows us to localise the unknown passive seismic sources. Again, there are several possibilities to process the 2-D array data. For example, Park et al. (2004) describe an azimuth scanning technique assuming far-field sources and utilising the plane-wave projection principle. The dispersion image is formed according to

$$E_{\text{2-D}}(\omega, v, \theta) = \left| \sum_{i=1}^{N} \mathrm{e}^{j\phi_x} \mathrm{e}^{j\phi_y} R_i(x, y, \omega) \right|, \tag{2}$$

where $R_i(x, y, \omega)$ is the Fourier transform of the $i$th trace $r_i(x, y, t)$, located at position $(x, y)$, of $N$ recorded traces, and $\phi_x = -\omega x \cos\theta / v$ and $\phi_y = -\omega y \sin\theta / v$ are the phase shifts corresponding to the $x$ and $y$ components of the phase

velocity, where $\theta$ denotes the source azimuth. We implement this approach by computing, for each combination of velocity and frequency, the azimuth that maximises the spectral magnitude. The source azimuth is thus estimated by calculating the modal azimuth across all frequencies and velocities, and the dispersion spectrum can be formed by fixing the azimuth and reiterating over frequency and velocity axes. The key drawback of forming the dispersion image according to Eq. (2) is that the source must be distant enough that the plane wave assumption is valid. In Fig. 4 we demonstrate that our experimental data are not consistent with the far-field source approximation, since moving the source position closer to the array simplifies the structure of the apparent offset sorted gather. This observation led us to develop an alternative processing approach.

### 3.3 Two-step MASW approach

We propose a two-step processing approach where the first step involves locating the unknown source position, permitting the dispersion image to be formed in the second step. Even the simplest 1-D phase shift method from Eq. (1) will give superior results to Eq. (2) if a nearby source can be reliably located. Our approach is based on the idea that if the source position was known, the seismic traces from the 2-D array could be arranged by their apparent offset from the source to form a shot gather that resembles the simple case of a line array with an inline source at known offset. Figure 4 shows that when we determine the source azimuth using Eq. (2) and re-sort the recorded traces by offset to a distant source lying along this azimuth we observe that the gather begins to resemble the response of a line array. However, when we shift the assumed source position closer to the array, the offset sorted gather resembles the simple linear array response even more closely. Thus, by formalising a metric that encodes the resemblance of an apparent offset sorted gather to a line array response, we can obtain a useful tool for source localisation that leverages the 2-D array geometry. This further avoids the problem of picking specific P- and S-phase arrivals, a traditional seismological method for source localisation, since these arrivals are difficult to detect reliably in our experimental data.

#### 3.3.1 Step 1 – source localisation

The source is located by re-sorting the seismic traces by offset to a series of test positions. The validity of a given test position is assessed by summing the magnitude of the delays between neighbouring traces in the re-sorted gather. The delays between neighbouring traces are estimated based on the lag that gives maximal value to the normalised cross-correlation between the two signals. The delays are estimated on a relatively narrowband-filtered copy of the seismic (10–15–30–45 Hz Ormsby filter), to minimise the influence of random noise and dispersion. After sorting, the source position is selected as the test position that produces the smallest magnitude sum of adjacent trace delays, corresponding to the simplest and most coherent offset sorted gather. To ensure unphysical velocities are avoided, for each pair of traces we subtract the delay corresponding to a wave travelling the inter-station distance at the maximum expected phase velocity (here we use $2000\,\mathrm{m\,s^{-1}}$). This simple approach works well in practice and is fast enough to allow a relatively large number of test positions to be evaluated.

In Fig. 5 we show that the source azimuths estimated using this technique are consistent with those estimated by picking maxima in azimuth scans using Eq. (2) but have the additional benefit that the source range is also estimated. Matched-field processing (MFP) is another localisation technique capable of resolving azimuth and range to an unknown source that we include for comparison. We follow the MFP implementation of Walter et al. (2015) but omit the ensemble averaging over multiple seismic noise windows since we are dealing with large-amplitude, distinct microseismic events. Similarly to Walter et al. (2015), we neglect amplitude information and match only the wave phase. The MFP method uses a model of the medium velocity as an additional constraint. We specify the medium velocity as the dominant A0 mode trend picked from the dispersion image formed with Eq. (2). For our catalogue of microseismic events, MFP and our trace re-sorting and delay minimisation method give source locations that we consider equivalent (Fig. 5), since dispersion images corresponding to these source locations were indistinguishable.

The reliability of our source localisation method was further investigated using synthetic gathers corresponding to a set of known source azimuths and ranges. We ran a 1-D noise-free forward model (that accounts for 3-D wave field divergence) using the OASES package for seismo-acoustic propagation in horizontally stratified waveguides, which employs a wave-number-integration solution method (Schmidt and Jensen, 1985). We model the wave field using the layer properties corresponding to the spring field conditions detailed in Table 1. We then specify the receiver positions as deployed in the field and form the synthetic gathers by selecting traces with appropriate offset from the 1-D pre-calculated wave field. The range and azimuth errors produced when attempting to recover the known source positions using the proposed source localisation approach are illustrated in Fig. 6.

The proposed method effectively recovers the direction to the source, regardless of azimuth, although uncertainties relating to the true receiver positions in the field are also important to consider (see Sect. 3.3.3). We also observe reliable estimation of source range within a radius of $\sim 500\,\mathrm{m}$ from the array centre, beyond which we observe an increasing tendency to underestimate the source range (Fig. 6). Further tests with a range of different array geometries indicate that the array aperture is the dominant factor controlling the maximum source range that can be estimated reliably.

### 3.3.2 Step 2 – dispersion imaging

Once the seismic traces from the 2-D array have been sorted by the apparent offset to the localised source, we are left with a gather that resembles a linear receiver array and an inline source, as seen in Fig. 4. At this point, the dispersion image may simply be formed by applying Eq. (1), i.e. the 1-D phase shift method of Park et al. (1998). However, more advanced processing methodologies have emerged over time, and we observe significantly improved dispersion imaging using the cross-correlation beamforming approach of Le Feuvre et al. (2015), as demonstrated in Fig. 7. This approach utilises the cross-correlations between all possible pairs of receivers, rather than the recorded traces themselves, to increase the effective spatial sampling of the array and thereby reduce aliasing and increase signal-to-noise ratio. In an adaption of this approach, we form the dispersion image, $D(\omega, v)$, a function of frequency ($\omega$) and phase velocity ($v$), according to the following equation using the source position, $r_s(x, y)$, estimated as described in Sect. 3.3.1:

$$D(\omega, v) = \left| \sum_{j=1}^{N_R-1} \sum_{k=j+1}^{N_R} \delta(\omega, v, r_s, r_j, r_k) \right|, \tag{3}$$

with $N_R$ the number of receivers and $r_j(x, y), r_k(x, y)$ denoting the positions of the receivers for the cross-correlation pair. Furthermore,

$$\delta\left(\omega, v, r_s, r_j, r_k\right) = \begin{cases} \tilde{C}_{jk}(\omega)\, e^{i\omega \frac{\|r_s - r_k\| - \|r_s - r_j\|}{v}} \\ \quad \text{if } \|r_s - r_j\| \leq \|r_s - r_k\|, \\ \tilde{C}_{kj}(\omega)\, e^{i\omega \frac{\|r_s - r_j\| - \|r_s - r_k\|}{v}} \\ \quad \text{if } \|r_s - r_j\| > \|r_s - r_k\|. \end{cases} \tag{4}$$

Here, the causal cross-correlations $\tilde{C}_{jk}$ and $\tilde{C}_{kj}$ between the receivers located at $r_j$ and $r_k$ are selected according to the direction of propagation, determined by comparing the two source-to-receiver distances, while the propagation distance is given by the difference between the two. In practice, we do not compute the cross-correlation $\tilde{C}_{kj}$ directly, but instead use the equivalent time-reversed acausal part (negative time delays) of $\tilde{C}_{jk}$ (Le Feuvre et al., 2015). It is important that the seismic traces are pre-whitened prior to computing the cross-correlations, as whitening effectively removes the autocorrelation of the signals that can blur the cross-correlation (El-Gohary and McNames, 2007). We find that a simple first-order backward differencing scheme is an effective method to whiten the recorded traces. We furthermore find it convenient to normalise the frequency response of the dispersion spectrum so that the maximum amplitude along a given frequency is unity.

It should also be noted that it is possible to localise the source by searching for source positions that produce dispersion images with maximum amplitude, as the correct source location is expected to produce the most coherent high-amplitude dispersion modes (Le Feuvre et al., 2015). This approach was tested in the present study. However, we find this method slow and inefficient compared to the trace re-sorting approach we implement, even though maximising dispersion image magnitude does appear to be a valid approach for locating an unknown source.

### 3.3.3 Influence of receiver position errors

During the field campaigns, we recorded GPS positions at the recording nodes that the receivers are connected to rather than at the receivers themselves. The positions of the receivers were subsequently assigned based on approximate dead reckoning and therefore have a degree of uncertainty associated with them. We estimate that this positional uncertainty lies in the range of $\sim$ 2–3 m. The impact of receiver position errors was investigated using an OASES 1-D seismo-acoustic propagation model (Schmidt and Jensen, 1985) for the horizontally stratified waveguide corresponding to the spring field conditions detailed in Table 1. We extracted a reference gather assuming a source range of 200 m, azimuth of 100° and receiver geometry corresponding to the spring field campaign. We then ran 1000 iterations adding flat-spectrum random perturbations to the receiver positions. In this way we effectively define a circle with a defined radius, where there is equal probability that the receiver is positioned at any given point within this circle. We then measure the impact of these perturbations on both source localisation and dispersion spectra. The dispersion spectrum error ($\varepsilon^2$) is given by the sum of squared differences for a given noise-perturbed trial $S_{test}$, compared to a noise-free reference spectrum $S_{ref}$ over $n$ frequencies ($\omega$) and $m$ velocities ($v$):

$$\varepsilon^2 = \sum_{i=1}^{n} \sum_{j=1}^{m} \left(S_{test}(\omega_i, v_j) - S_{ref}(\omega_i, v_j)\right)^2. \tag{5}$$

In Fig. 8 we show that positional errors up to 4–5 m have a very minor impact on source azimuth estimation and dispersion spectra in the frequency range of interest, i.e. up to 100 Hz. Range estimation is somewhat more sensitive (but less important to dispersion spectrum quality), and we see a general trend that the source range tends to be overestimated rather than underestimated. This indicates that the estimated positional uncertainty for the field campaigns ($\sim$ 2–3 m) should not significantly affect our experimental results, although we may expect some minor overestimation of source range. As the positional error magnitude increases further, Fig. 8 demonstrates that the source localisation becomes progressively more imprecise, while Fig. 9 shows that the maximum frequency imaged coherently in the dispersion spectra progressively decreases. We can formalise this trend by observing the relation that coherent dispersion spectra are recovered for wavelengths of approximately 2–3 times the maximum positional error magnitude.

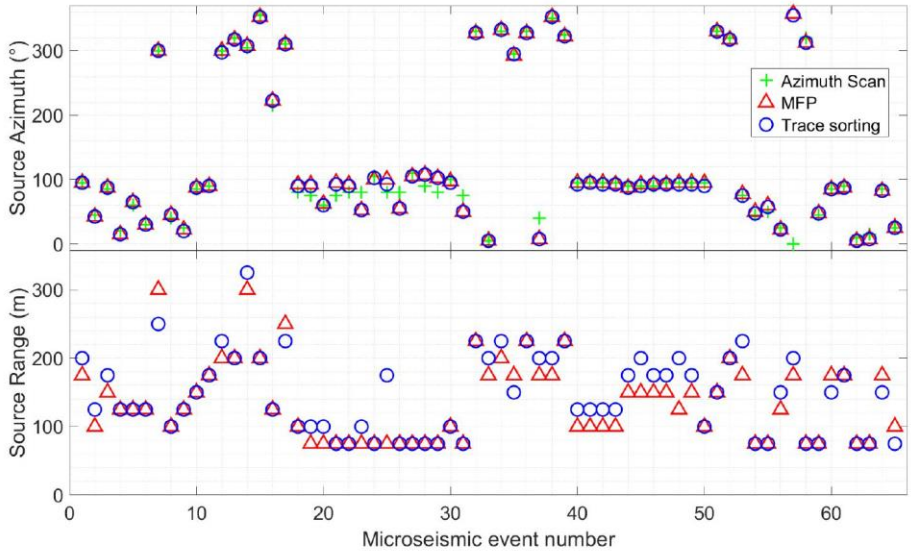


**Figure 5.** Comparison of source localisation using azimuth scanning (i.e. Eq. 2), matched-field processing (MFP), and our trace re-sorting and delay minimisation method. Azimuths are given as compass bearings.

**Table 1.** Physical properties of homogeneous, horizontally layered media used to calculate theoretical dispersion curves shown in Fig. 16. The key feature of the model is a high-velocity surface layer overlying a layer with lower velocity and high Poisson ratio.

| Layer | $h$ (m) | | $V_s$ (m s$^{-1}$) | | $V_p$ (m s$^{-1}$) | | Poisson's ratio | | $\rho$ (kg m$^{-3}$) |
|---|---|---|---|---|---|---|---|---|---|
| | Spring | Autumn | Spring | Autumn | Spring | Autumn | Spring | Autumn | |
| 1 | 4.5 | 3.5 | 1700 | 1520 | 3180 | 3164 | 0.30 | 0.35 | 2000 |
| 2 | 31 | 29 | 500 | 525 | 1837 | 1929 | 0.46 | 0.46 | 2000 |
| Half-space | $\infty$ | $\infty$ | 2000 | 2000 | 3742 | 3742 | 0.30 | 0.30 | 2000 |

### 3.4 Theoretical dispersion curve modelling

The global matrix method was introduced by Knopoff (1964), further elaborated by Lowe (1995) and again by Ryden and Lowe (2004). It involves the assembly of a system matrix **S** that describes the interaction of displacement and stress fields across interfaces between horizontal layers described by a series of interface matrices. The propagating wave modes are characterised by combinations of frequency ($\omega$) and wave number ($k$) that satisfy all boundary conditions such that the determinant vanishes:

$$f(\omega, k) = \det[\mathbf{S}] = 0. \tag{6}$$

We abstain from providing a full derivation but give a specific case study that illustrates our implementation and may serve as a simple practical reference point for the reader interested in further exploration of the method. The layer models used in this study contain two discrete layers ($i = 2, 3$) bounded by an infinite vacuum half-space above ($i = 1$) and a solid half-space below ($i = 4$), giving the system matrix the following form:

$$\mathbf{S} = \begin{bmatrix} \mathbf{D}_{1b}^{-} & -\mathbf{D}_{2t} & & \\ & \mathbf{D}_{2b} & -\mathbf{D}_{3t} & \\ & & \mathbf{D}_{3b} & -\mathbf{D}_{4t}^{+} \end{bmatrix}, \tag{7}$$

where the matrices describing the top interfaces $\mathbf{D}_t$ and the bottom interfaces $\mathbf{D}_b$ for each layer are given by the following expressions (noting that the minus superscript denotes taking only the upward travelling partial waves given by columns two and four, while the plus superscript denotes selecting only the downward travelling partial waves given by columns one and three):

$$[\mathbf{D}_{it}] = \begin{bmatrix} k & kg_\alpha & C_\alpha & -C_\alpha g_\alpha \\ C_\beta & -C_\beta g_\beta & -k & -kg_\beta \\ i\rho_i B & i\rho_i B g_\alpha & 2i\rho_i kB^2 C_\alpha & -2i\rho_i kB^2 C_\alpha g_\alpha \\ -2i\rho_i kB^2 C_\beta & 2i\rho_i kB^2 C_\beta g_\beta & i\rho_i B & i\rho_i B g_\beta \end{bmatrix}, \tag{8}$$

$$[\mathbf{D}_{ib}] = \begin{bmatrix} kg_\alpha & k & C_\alpha g_\alpha & -C_\alpha \\ C_\beta g_\beta & -C_\beta & -kg_\beta & -k \\ i\rho_i B g_\alpha & i\rho_i B & 2i\rho_i kB^2 C_\alpha g_\alpha & -2i\rho_i kB^2 C_\alpha \\ -2i\rho_i kB^2 C_\beta g_\beta & 2i\rho_i kB^2 C_\beta & i\rho_i B g_\beta & i\rho_i B \end{bmatrix}, \tag{9}$$

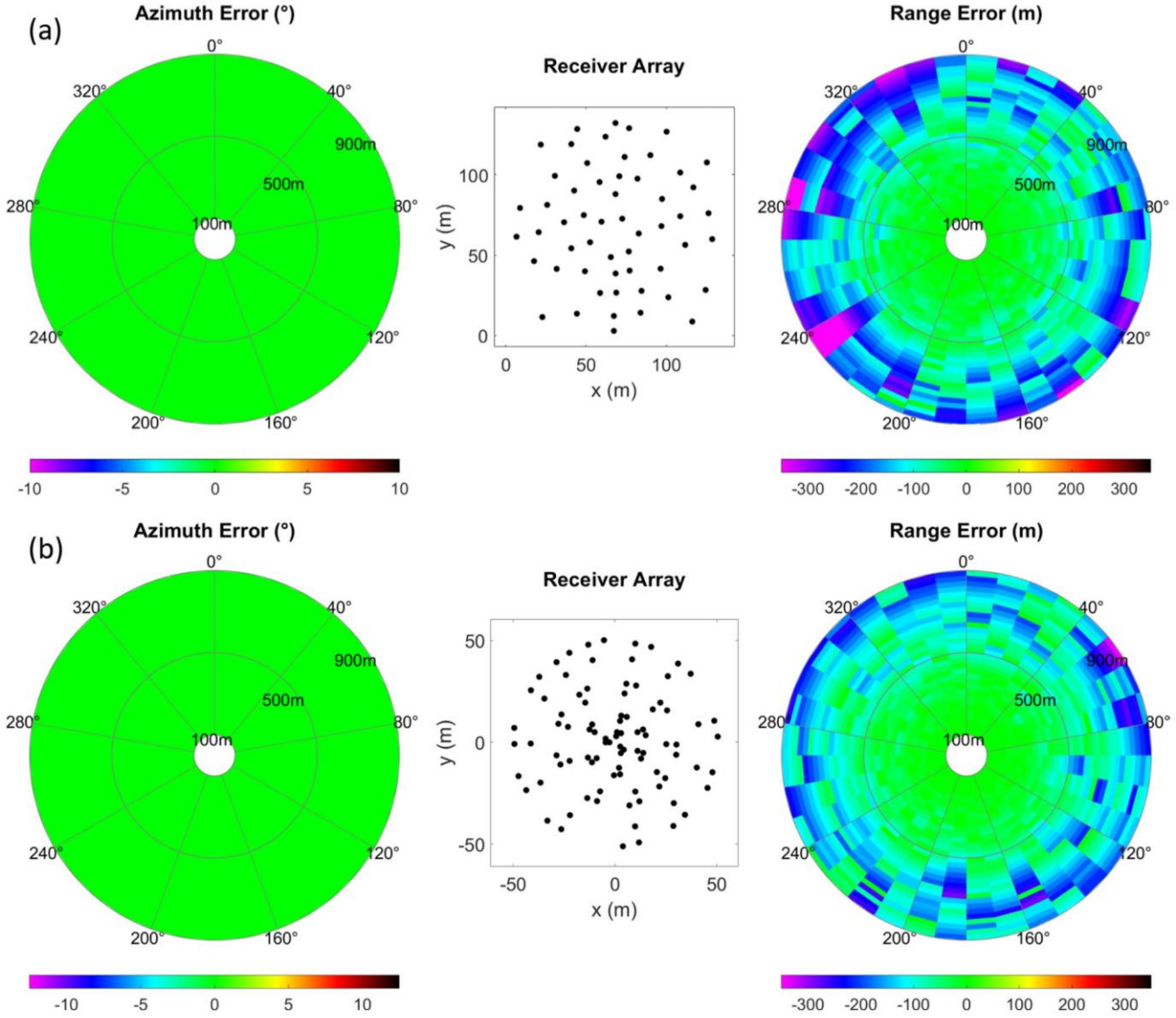


**Figure 6.** Predicted source localisation azimuth and range errors based on forward modelling with known source positions and receiver geometry corresponding to **(a)** spring and **(b)** autumn field campaigns.

with

$$g_\alpha = \mathrm{e}^{iC_\alpha h_i}, g_\beta = \mathrm{e}^{iC_\beta h_i}, \tag{10}$$

$$C_\alpha = \left(\frac{\omega^2}{\alpha_i^2} - k^2\right)^{\frac{1}{2}}, C_\beta = \left(\frac{\omega^2}{\beta_i^2} - k^2\right)^{\frac{1}{2}}, \tag{11}$$

$$B = \omega^2 - 2\beta_i^2 k^2, \tag{12}$$

and the physical properties of the system enter as

$h_i =$ thickness of layer $i$, set to zero for the half-spaces;

$\rho_i =$ density of layer $i$, set to zero for the upper vacuum half-space;

$\alpha_i =$ bulk compressional velocity of layer $i$, an arbitrary non-zero value for upper vacuum half-space; and

$\beta_i =$ bulk shear velocity of layer $i$, an arbitrary non-zero value for upper vacuum half-space.

We are also interested in the magnitude of displacement at the ground surface (top interface of layer $i = 2$) for the different wave modes so that we may predict which are most likely to be excited and subsequently recorded in the field. To this end, we proceed by assuming the amplitudes of the incoming waves in the two half-spaces, setting a unitary amplitude entering the system at the top ($\{A_1^+\} = 1$) and zero amplitude entering the system from below ($\{A_4^-\} = 0$), allowing us to specify the right-hand side of the following system and solve

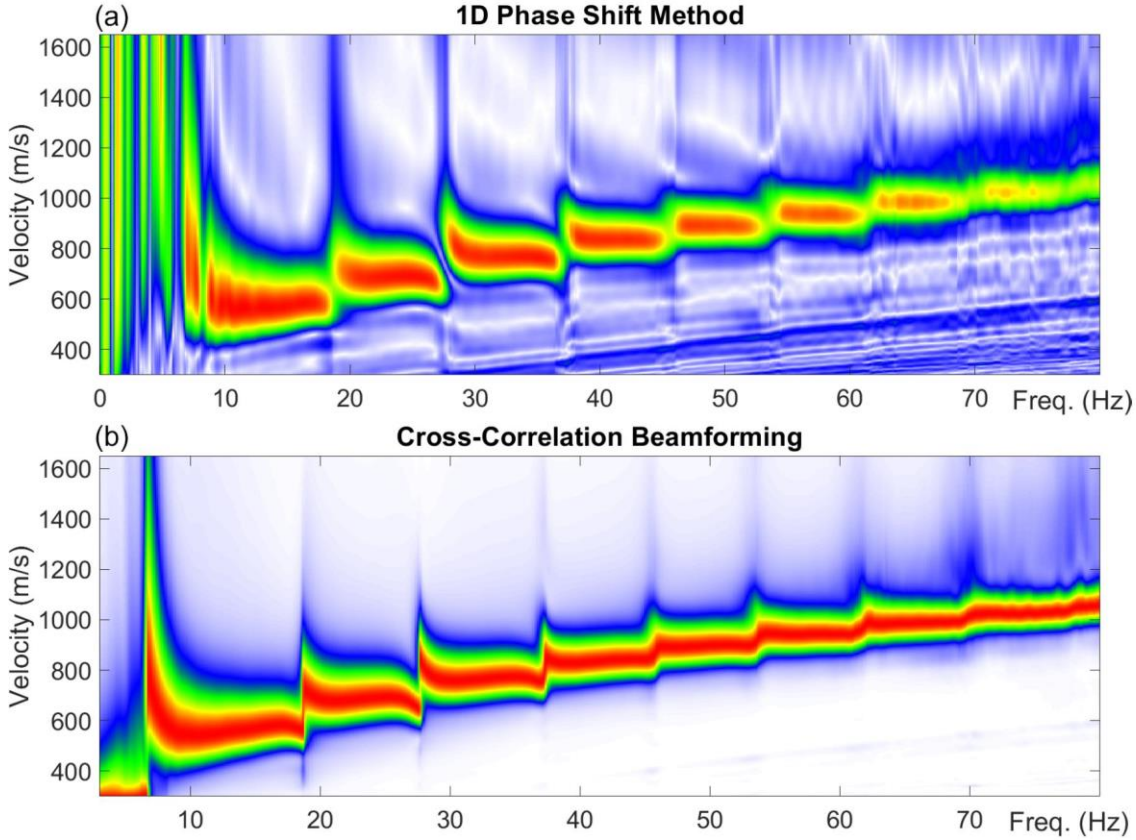


**Figure 7.** Dispersion spectra with linear colour scaling using the 1-D phase shift method **(a)** and Le Feuvre et al. (2015) cross-correlation beamforming **(b)**. The microseismic event was recorded on 2 May 2019 at 10:01 UTC+0 at assumed azimuth of 120° and range of 140 m.

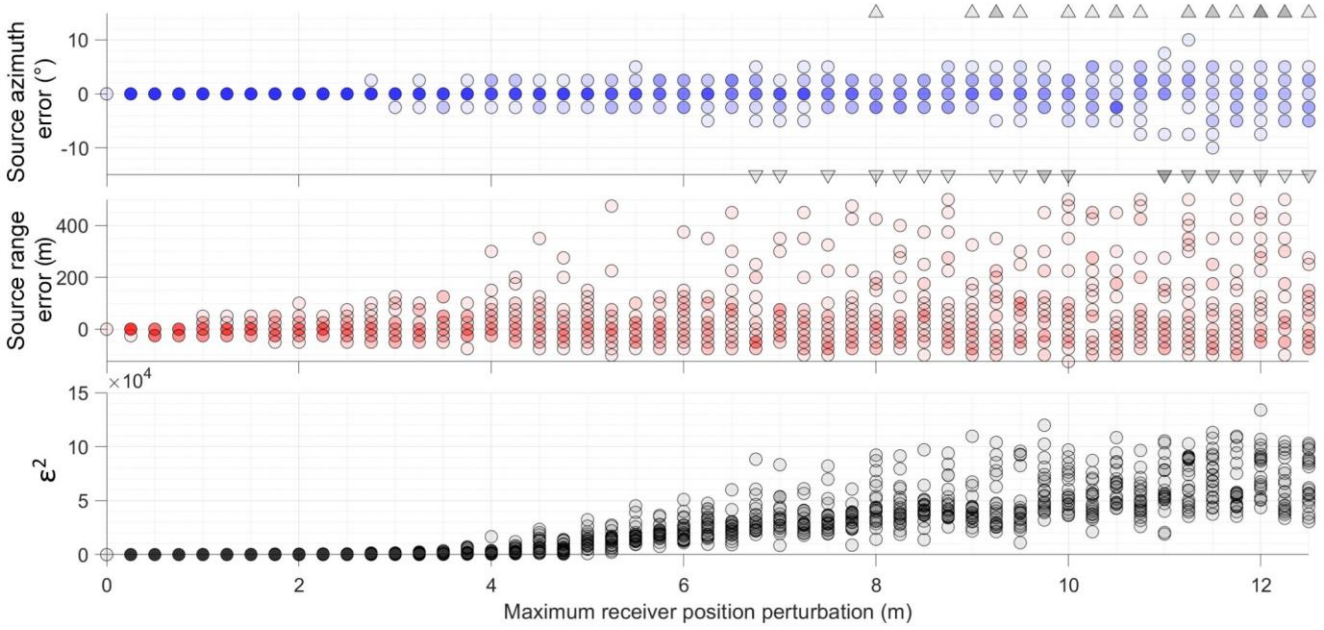


**Figure 8.** Summary of results of 1000 modelling iterations with random white noise perturbation to receiver positions. Grey triangles denote outliers, i.e. iterations that result in large azimuth errors outside the plotted range. Higher colour density denotes overlap, i.e. multiple iterations with the same result. $\varepsilon^2$ denotes dispersion spectrum error Eq. (5).

for the unknown interface amplitudes using a least-squares approach:

$$\begin{bmatrix} \mathbf{D}_{1b}^{-} & -\mathbf{D}_{2t} & & \\ & \mathbf{D}_{2b} & -\mathbf{D}_{3t} & \\ & & \mathbf{D}_{3b} & -\mathbf{D}_{4t}^{+} \end{bmatrix} \begin{Bmatrix} \{A_1^-\} \\ \{A_2\} \\ \{A_3\} \\ \{A_4^+\} \end{Bmatrix} = \begin{bmatrix} \mathbf{D}_{1b}^{-} & \\ & -\mathbf{D}_{4t}^{+} \end{bmatrix} \begin{Bmatrix} \{A_1^+\} \\ 0 \\ 0 \\ \{A_4^-\} \end{Bmatrix}. \quad (13)$$

Here we substitute the system matrix $\mathbf{S}$ for the combinations of frequency and wave number that correspond to the propagating wave modes. The vectors of amplitudes are arranged in the following way:

$$\{A\} = \begin{Bmatrix} A_{(L+)} \\ A_{(L-)} \\ A_{(S+)} \\ A_{(S-)} \end{Bmatrix}, \quad \{A^+\} = \begin{Bmatrix} A_{(L+)} \\ A_{(S+)} \end{Bmatrix}, \quad \{A^-\} = \begin{Bmatrix} A_{(L-)} \\ A_{(S-)} \end{Bmatrix}, \quad (14)$$

where $L$ and $S$ denote longitudinal and shear waves respectively, while $-$ and $+$ symbols denote upward and downward travelling partial waves. Having solved for the unknown amplitudes in Eq. (13) we then calculate the displacements and stresses at the ground surface according to the following equation:

$$\begin{Bmatrix} u_x \\ u_z \\ \sigma_{zz} \\ \sigma_{xz} \end{Bmatrix}_{2t} = [\mathbf{D}_{2t}]\{A_2\}, \quad (15)$$

where $u_x$ and $u_z$ denote the complex valued in-plane and vertical displacements, while $\sigma_{zz}$ and $\sigma_{xz}$ denote the complex valued vertical and lateral stresses and the calculation is made at the top interface of layer 2.

In Fig. 10, we show an example of the dispersion curves produced by this approach for the spring layer properties listed in Table 1. Since we measured the vertical component of ground motion in the field, we plot the magnitude of the vertical displacement ($u_z$) as an indicator of the relative likelihood of exciting and subsequently recording specific wave modes. We also highlight, for a given frequency, the wave mode giving the largest displacement at the surface that is considered most likely to dominate the ground response and contribute to the apparent dispersion curve produced by the superposition of multiple modes observed in experimental data.

#### 3.4.1 Numerical root finding method

To recover the dispersion curves it is necessary to find the roots of the system matrix (Eq. 6). In this study, we assume a half-space with higher velocity than the overlying layers, which reflects the presence of compacted sediments and bedrock at depth in Adventdalen. The implication of this choice is that the propagating surface wave modes do not leak energy into the half-space and are much simpler to search for numerically. The permitted surface wave modes are given by combinations of frequency and phase velocity (or wave number) that minimise the determinant of the system matrix. We localise these minima by conducting a simple 2-D numerical search over a regular grid of frequency and real wave number (the imaginary part of the wave number is zeroed since we consider only non-leaky modes). The local minima in the matrix sampling the determinant of the system matrix are found by morphological image processing techniques rather than the more traditional method of curve tracing using bisection algorithms favoured by for example Lowe (1995). Specifically, we use the *imregionalmax* routine in MATLAB on the negative of the determinant matrix, applying a series of linear connectivity kernels for detection of local maxima ridges. We then mask out non-dispersive body waves that appear as horizontal ridges in frequency-phase velocity space and use morphological closing operations to fill in the gaps that this creates. We further apply skeletonisation to the binary image of dispersion curves. The non-zero elements of the binary matrix then define the combinations of frequency and velocity that represent the dispersive wave modes and that are subsequently used to calculate surface wave amplitudes with Eq. (13).

## 4 Results and discussion

### 4.1 Interpretation of cryoseisms

A series of transient seismic events were isolated from passive seismic recordings of 2-D geophone arrays deployed at our study site in Adventdalen. The estimated source positions for these events are shown in Fig. 11, while their temporal occurrence is illustrated in Fig. 12. The events cluster primarily around frost polygons along the raised river terrace. A small number of events fall just beyond the raised riverbank and plot within the Adventelva river valley. While these events may be correctly located, we also cannot rule out the possibility that they occurred on the raised terrace and the source range has been overestimated as discussed in Sect. 3.3.3. Figure 12 shows that the transient events were all recorded during periods of rapidly changing air temperature as recorded at a nearby weather station. This observation together with the spatial clustering around frost polygons and on the raised river terrace, which is known to have high ground-ice content within the upper $\sim 4$ m (Gilbert et al., 2018), leads us to infer

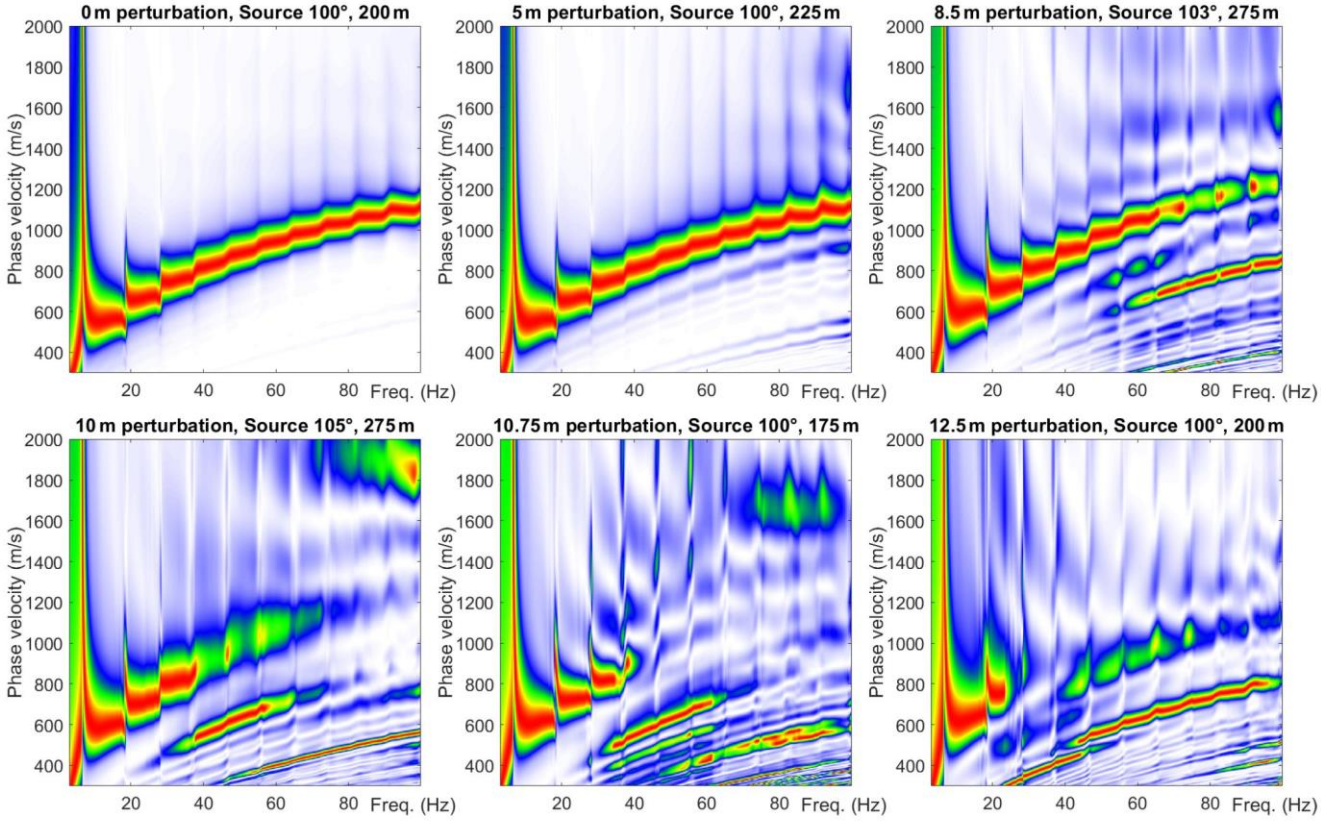


**Figure 9.** Dispersion spectra calculated from forward model with receiver positions perturbed by white random noise of indicated magnitude illustrating how the maximum frequency that is coherently imaged decreases with increasing uncertainty in receiver position. The true source position is at 100°, range 200 m. Colour scale is linear.

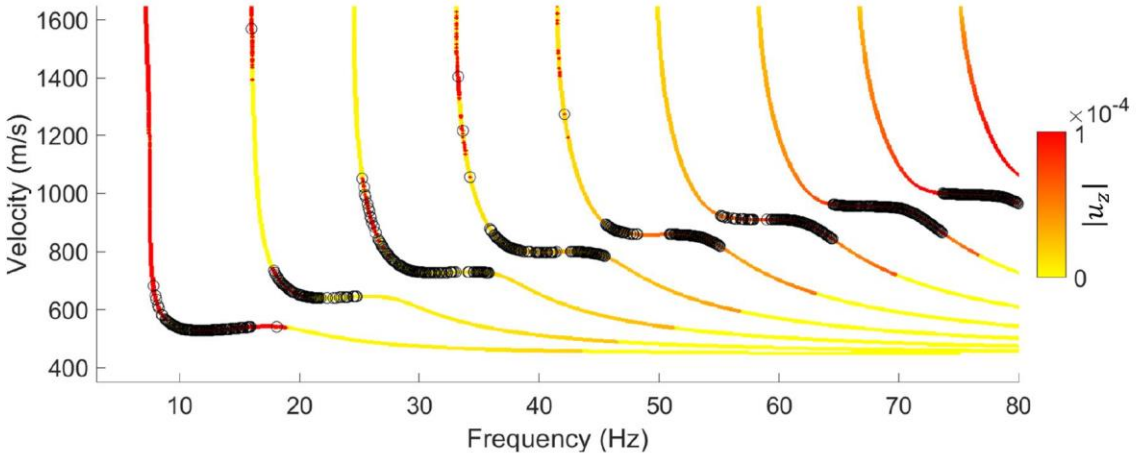


**Figure 10.** Example of theoretical dispersion curves coloured by magnitude of vertical displacement at the ground surface. Black circles denote the wave mode with largest displacement for a particular frequency.

that these events are most likely cryoseisms, or frost quakes. The fact that these events consist dominantly of surface wave energy is also consistent with a shallow source and previous descriptions of cryoseisms (Barosh, 2000). Similarly, the fact that the source range for all of the recorded events was in the order of hundreds of metres is also consistent with the distance over which previously observed cryoseisms have propagated (Leung et al., 2017; Nikonov, 2010), and we are unaware of any other likely seismic sources within this range. Other possible seismic sources include an operational coal

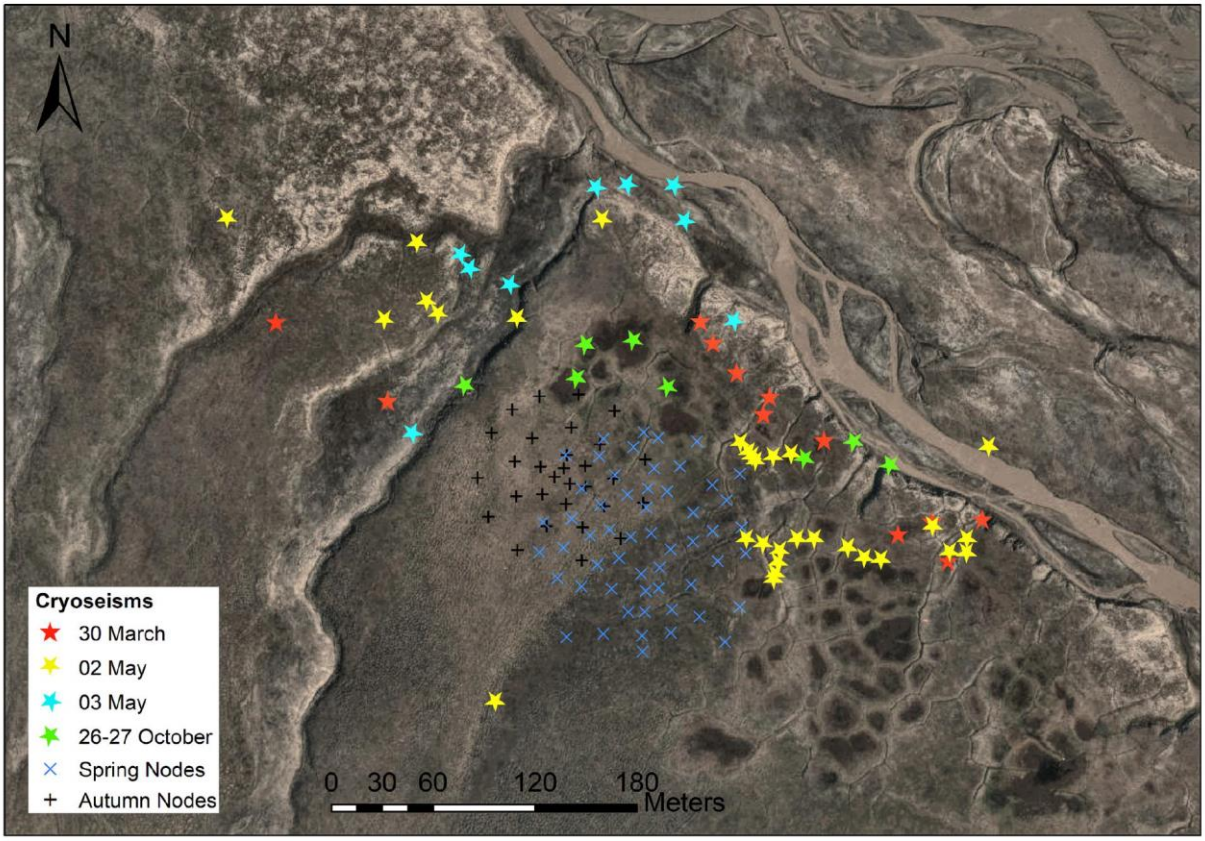


**Figure 11.** Localised source positions (coloured stars) and receiver positions for spring (cross symbols) and autumn (plus symbols) field campaigns; background is a contrast-enhanced version of an orthophoto © Norwegian Polar Institute (http://npolar.no).

mine, Gruve 7, that conducts blasting operations ∼ 5 km to the SE. Road traffic ∼ 650–850 m S–SW and snowmobile traffic along the Adventelva river valley N–E of the study site are also possible sources. However, these sources do not explain the spatial distribution and character of the recorded events. Known examples of snowmobile and vehicle traffic contain strong air wave arrivals with non-dispersive velocity of ∼ 320–330 m s$^{-1}$ that was not observed for the class of events attributed to cryoseisms.

The temporal resolution of this study is limited due to the fact that data were recorded during specific intervals rather than continuously (see Fig. 12). This means that additional cryoseisms may have occurred under rapid cooling events during the field campaigns for which no data were recorded. However, we can observe that the recording windows for which no cryoseisms were detected were associated with temperatures that were either too high or changing slowly in comparison to the periods when cryoseisms were detected. The frequency of cryoseisms was greater during the spring compared to the autumn, probably owing to the increased progression of ground freezing in the aftermath of cold winter air temperatures. It is interesting to note that the highest frequency of cryoseisms was recorded on 2 May 2019 during a period when the air temperature was rapidly increasing and following a sharp cold snap down from above-freezing temperatures 3 d prior. It is unclear whether these events are a delayed effect of the preceding cold snap, where the subsurface stress continues to increase for some time after the drop in air temperature, or if the events are caused by the sharp temperature rise itself and associated with cracking driven by thermal expansion rather than contraction. We also note that snow cover on the raised river terrace was thin or absent during the field campaigns, due to relatively low precipitation and strong prevailing winds. The lack of an insulating snow layer increases the plausibility of correlating air temperature at 5 m above ground with cryoseismic events in the shallow subsurface and has been recognised as a necessary condition facilitating sufficiently rapid ground cooling to generate cryoseisms in previous studies (Barosh, 2000; Battaglia and Chagnon, 2016; Matsuoka et al., 2018; Nikonov, 2010).

### 4.2 Dispersion images and temporal variation

Dispersion images from the isolated cryoseisms resemble the complex multimodal dispersion of Lamb–Rayleigh waves that is relatively well known from pavement studies (Ryden and Lowe, 2004; Ryden et al., 2004). This complexity

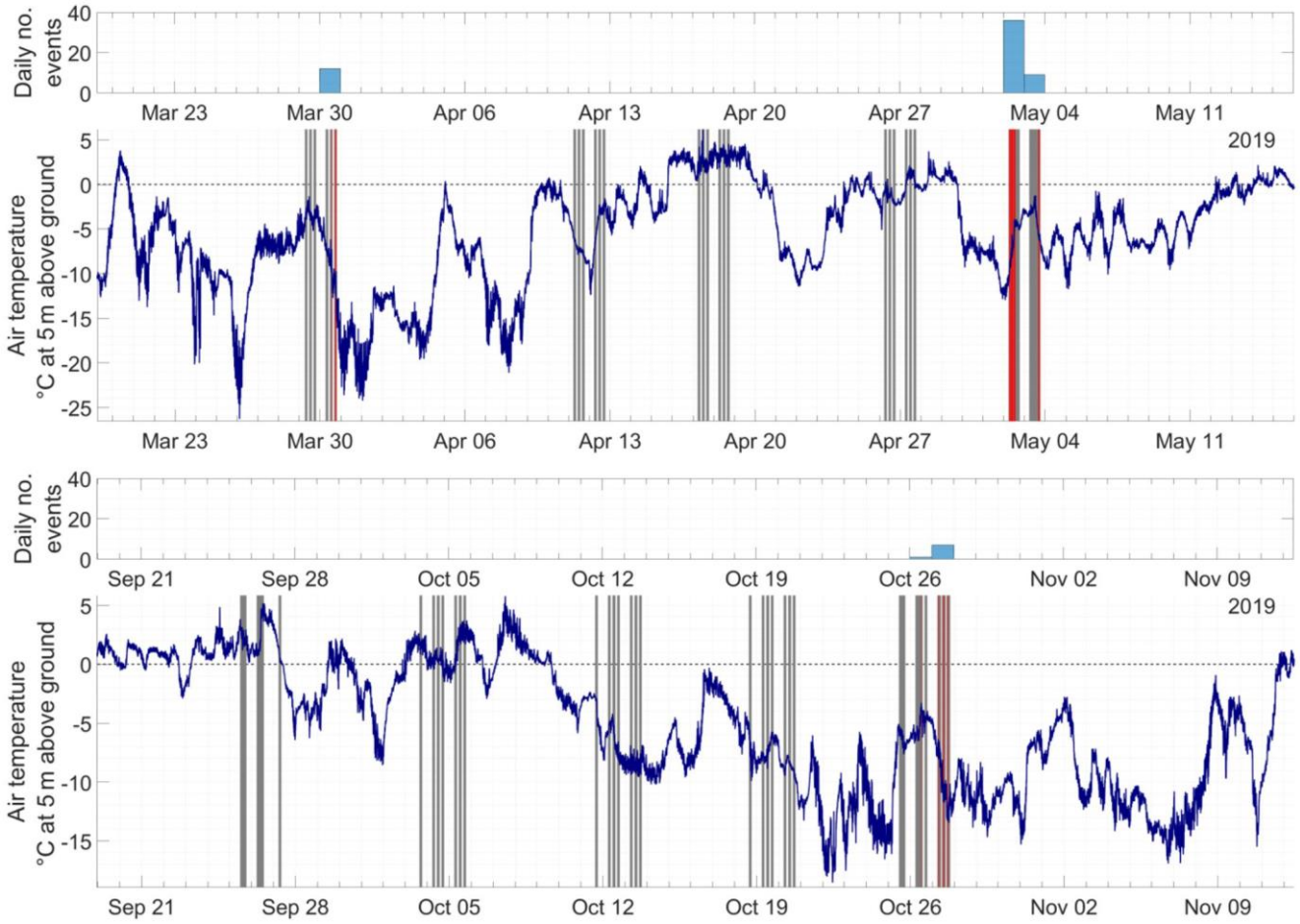


**Figure 12.** Temperature at 5 m above ground at nearby weather station in Adventdalen. Grey bars denote periods when passive seismic data were recorded, and red bars denote periods where transient seismic events producing multimodal dispersion spectra were detected.

emerges when a stiff high-velocity layer overlies a softer layer producing an inversion in the shear velocity profile and acting as a waveguide. Some examples of estimated dispersion spectra are shown in Fig. 13 spanning both spring and autumn field campaigns. We observe that the number of wave-mode branches imaged in the spring records was higher than in the autumn over the investigated range of frequencies. In Fig. 14, we compare individual events from spring and autumn, and we observe that the apparent dispersion curve is shifted towards lower velocities in the autumn and that transitions between successive modes are shifted to higher frequencies with larger spacing between modes. This trend is robust across the catalogue of cryoseisms giving well-resolved dispersion images, as shown in Fig. 15, displaying the time-frequency-traced ridges of dispersion images corresponding to multiple records from spring and autumn field campaigns. MATLAB's built-in routine *tfridge* was found to be effective for ridge tracing in this study.

In addition to temporal variation in ground structure, one might anticipate that the varying receiver footprint or lateral variation in ground structure could also contribute to the observed variation in dispersion spectra. Based on dispersion imaging of synthetic test data, we are confident that the varying receiver footprint does not play a significant role for a laterally homogenous, horizontally layered medium. Further, we observe that dispersion images for spatially dispersed events over short time windows (24–48 h) are highly consistent, which points towards a ground structure that is relatively consistent laterally. On the other hand, events that cluster spatially while being dispersed temporally show significant variation. The dominant trend is well illustrated in Fig. 15, i.e. events within a given season are quite similar despite variation in source location, but there is significant variation between events occurring at different times of the year. These observations are consistent with the interpretation that the variation in surface wave dispersion is mainly caused by temporal variation in ground structure.

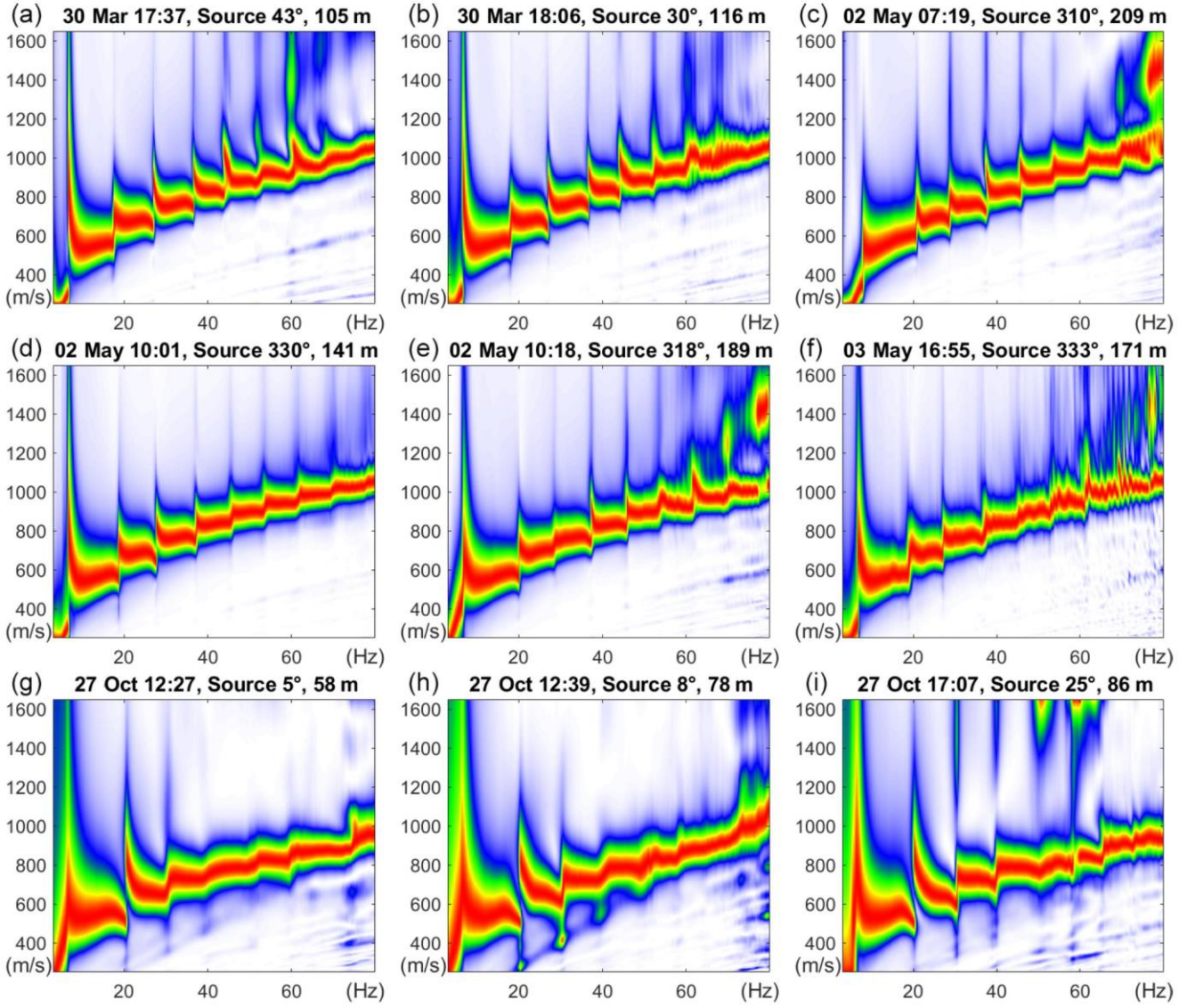


**Figure 13.** Examples of dispersion spectra for selected cryoseismic events from spring **(a–f)** and autumn **(g–i)** field campaigns; source azimuths are given as compass bearings and colour scaling is linear.

### 4.3 Inferring subsurface structure from dispersion images

To further investigate what the structure of the dispersion images tells us about the subsurface permafrost structure and its variation between spring and autumn field campaigns, we ran a series of theoretical models using the global matrix approach discussed in Sect. 3.4. These models were optimised manually by qualitatively fitting the resulting dispersion curves with experimental dispersion images and manually adjusting the physical parameters to achieve a best possible fit. We focussed our attention on the simplest possible models that give a good approximation of the experimental data, which in this case meant two discrete layers with an inverse velocity profile sandwiched between infinite vacuum (above) and solid (below) half-spaces. The physical properties of the best-estimate models corresponding to spring and autumn conditions are listed in Table 1.

The primary property of the models that allows us to fit the experimental data is the high velocity of the uppermost part of the ground, overlying relatively low velocity material beneath. We also see evidence that the Poisson ratio in the low-velocity layer is relatively high (0.46), consistent with a softer material that transmits shear stress less effectively. The physical manifestation of the high-velocity surface layer is likely to be the zone of elevated ground-ice content of $\sim 4$ m thickness observed in the Adventdalen boreholes of Gilbert et al. (2018). This zone is rich in void-filling ice, lentic-

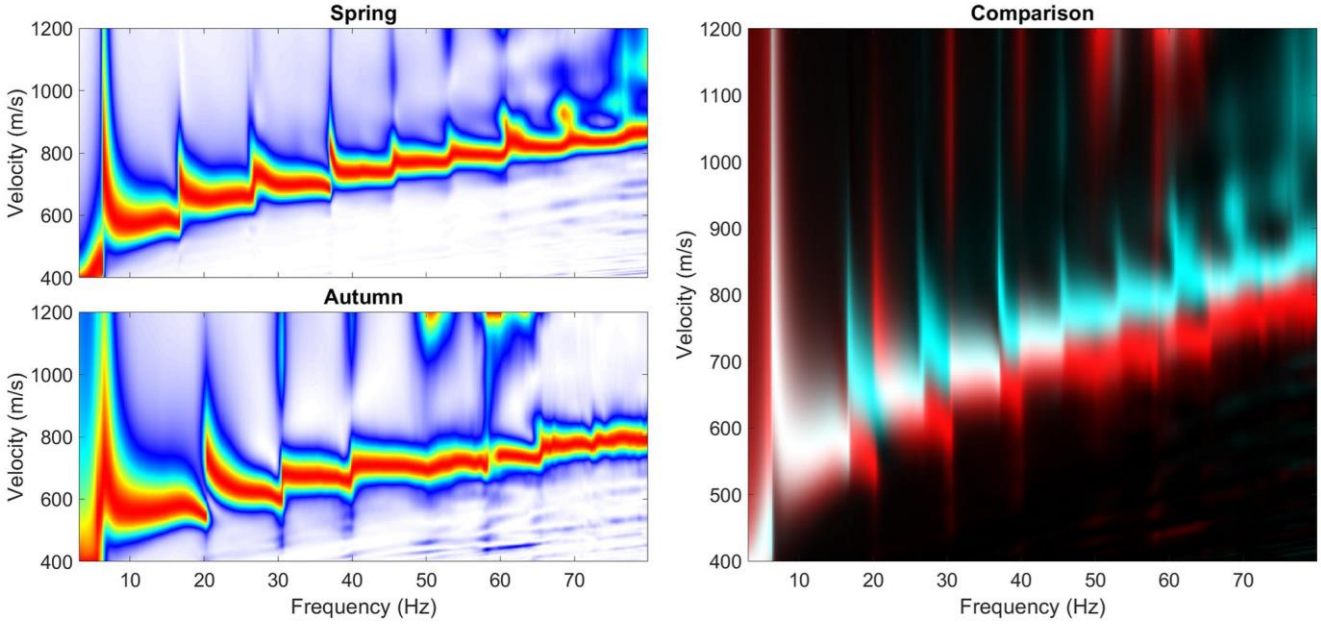


**Figure 14.** Comparison of records from spring and autumn; in the right panel the spring record is shown in cyan and the autumn record is shown in red, and areas where the two spectra overlap appear white.

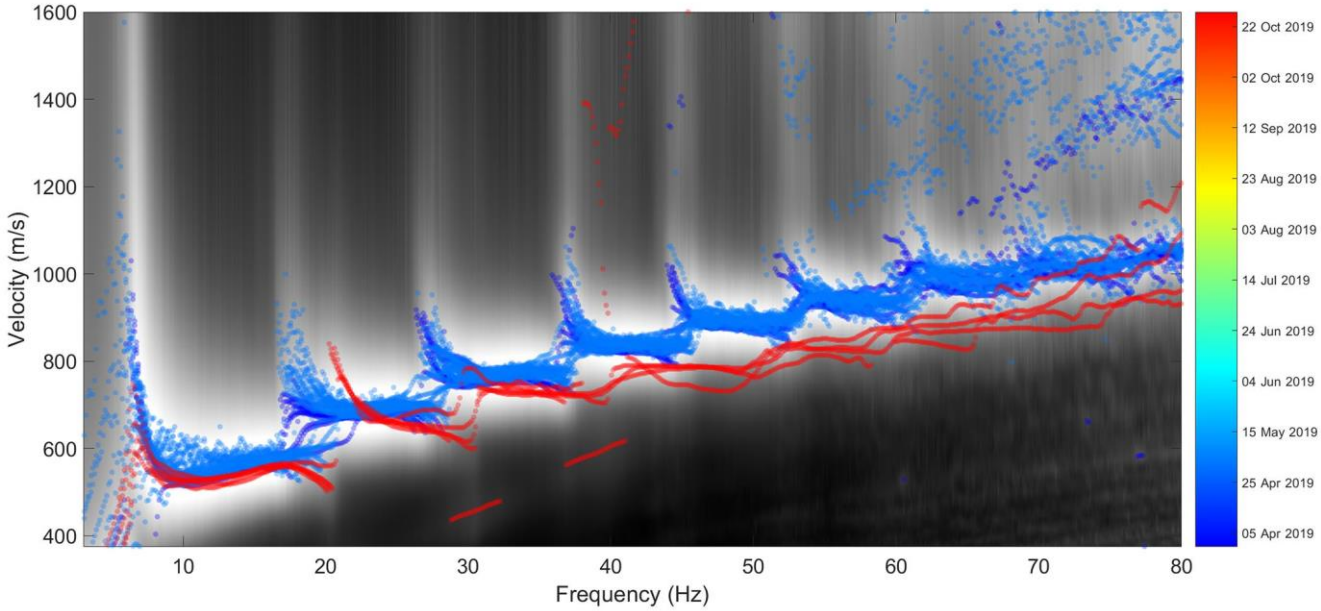


**Figure 15.** Illustration of temporal variation. Greyscale background image shows the mean dispersion spectrum for all displayed transient events. Coloured circles denote time frequency ridges picked from individual dispersion spectra and coloured according to date of recording.

ular and massive solid bodies of ice that macroscopically strengthen the dominantly loess sediments (Gilbert et al., 2018), leading to relatively high shear wave velocity and a relatively low Poisson ratio.

The low-velocity layer may simply reflect the absence of these stiffening ice bodies and subsequently decreased shear strength in the porous medium. However, the low-velocity zone may also indicate the presence of unfrozen permafrost due to elevated salinity, recalling that permafrost is defined simply as ground that remains below 0 °C over at least 2 consecutive years, but does not imply that the ground is in fact frozen. This interpretation is supported by the high Poisson ratio of the lower layer, since according to Skvortsov et al. (2014) a Poisson ratio of 0.45–0.46 represents a thresh-

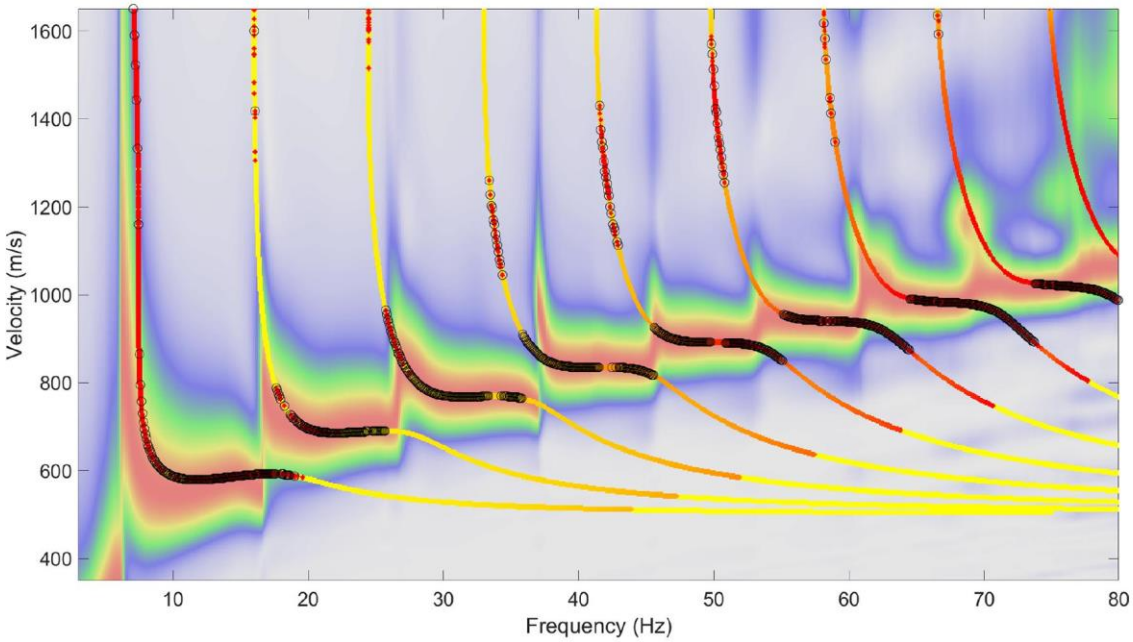


**Figure 16.** Spring field campaign best-qualitative-fit theoretical dispersion curves, based on a simple three-layer horizontal model (see Table 1). Dispersion spectrum corresponds to event recorded on 2 May at 06:51 UTC+0, displayed with linear colour scaling.

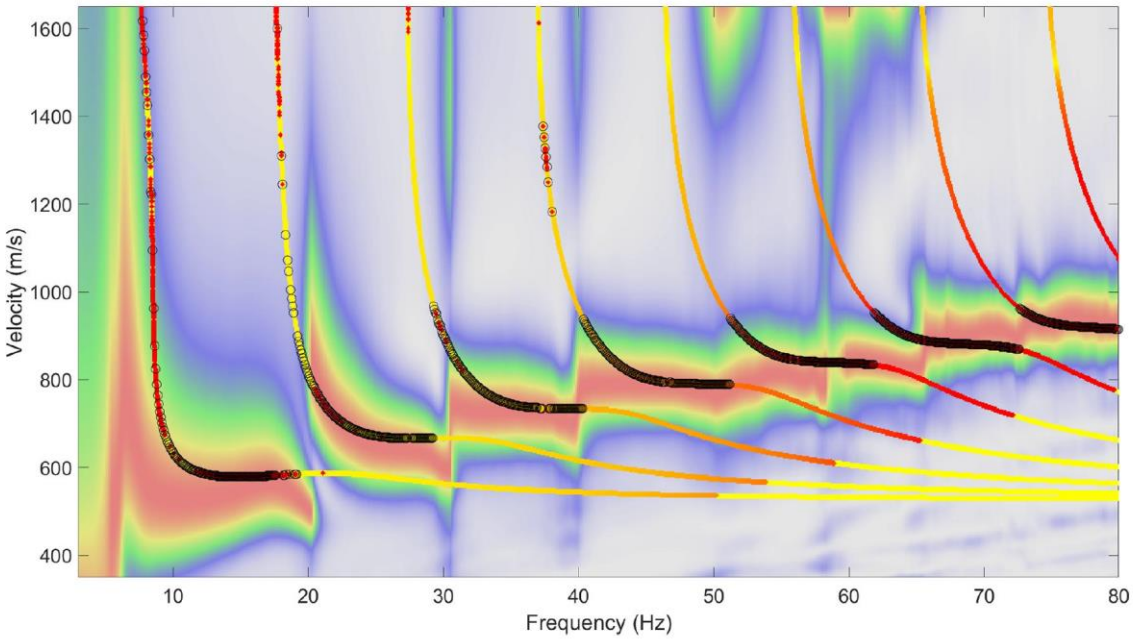


**Figure 17.** Autumn field campaign best-qualitative-fit theoretical dispersion curves, based on a simple three-layer horizontal model (see Table 1). Dispersion spectrum corresponds to event recorded on 27 October at 12:27 UTC+0, displayed with linear colour scaling.

old between frozen and unfrozen states for water-saturated soils, irrespective of composition, temperature and salinity. Furthermore, nuclear magnetic resonance and controlled source audio-magnetotelluric data suggest the presence of unfrozen saline permafrost below the Holocene marine limit in Adventdalen (Keating et al., 2018). On balance, we conclude that unfrozen saline permafrost is the most likely explanation for the observed low-velocity zone.

In Fig. 16 we see that the theoretical dispersion curves fit the experimental data recorded in spring remarkably well, given our simplistic layer model. Figure 17 illustrates that the fit between model and experimental data is somewhat

poorer for the autumn, although good overall fit was still achieved. Reasons for this contrast may include that the cryoseisms were stronger in spring due to colder temperatures and a more advanced state of freezing, leading to a more broadband source signal. Alternately, the ground may have been more heterogeneous in the autumn, as indicated by interspersed ponds of unfrozen water and ice observed at the study site when deploying geophones in September compared with a relatively homogeneous frozen landscape with thin snow cover in March. This increased heterogeneity may affect the experimentally recorded events either via attenuation of the surface waves between source and receiver or by heterogeneities across the geophone array itself, leading to decreased coherency.

It was difficult to fit the steep phase velocity gradients at the frequencies where the ground response transitions from one wave mode to another using our simplistic layer model (particularly noticeable for modes 3–6 in Fig. 16). We have not investigated this phenomenon in detail but hypothesise that some additional degree of freedom such as allowing for velocity gradients within layers may be required to improve this aspect of the fit. In general, it would be advantageous to develop an inversion scheme capable of robustly selecting the physical model(s) that best fits the observed dispersion spectra. However, we anticipate that this would be a complex task due to the non-uniqueness and non-linearity of the problem, exacerbated by the complex multimodal dispersion structure. These factors make it difficult to optimise inversion parameters by exploiting partial derivatives. While developing a suitable inversion scheme fell outside the scope of this study, we direct the interested reader towards the study of Ryden and Park (2006). They implemented a global optimisation approach based on the fast-simulated annealing algorithm to invert multimodal surface waves recorded in pavement. Their scheme appears capable of dealing with the problems of cost-function local minima and correlated parameters, assuming that the parameter perturbation size and cooling schedule of the simulated annealing can be adequately tuned for the specific set of dispersion spectra.

## 5 Conclusions

We present a methodology designed to isolate transient seismic events in passive records and thereby estimate their unknown source location and image their phase velocity dispersion. The spatial association of the source positions with a well-known frost polygon area along an elevated river terrace in Adventdalen, together with temporal correlation with periods of rapidly changing air temperature, indicates that these events are likely cryoseisms. The phase velocity dispersion of these cryoseisms furthermore allows us to infer the subsurface structure of the permafrost and detect changes between seasons. A high-velocity solid-frozen surface layer overlying a slower and softer layer leads to a complex multimodal dispersion pattern that is familiar from previous studies of pavements. The uppermost part of the permafrost appears to be measurably softer during the autumn than the spring, implying that this methodology may also have the potential to detect changes in an inter-annual monitoring context. A future field campaign recording continuously over an entire freeze season would, for example, give a more complete picture of the spatio-temporal occurrence of cryoseisms. Alternatively, our methodology could be applied for other locations with suitable seismic sources, such as on or adjacent to glaciers.

*Code and data availability.* Data and code used to produce this research can be shared upon request to the authors.

*Author contributions.* The field campaigns were administered by TAJ and carried out by RR, BOR, HMS and TAJ. Initial data collation and processing was carried out by BOR. Exploratory data analysis was conducted by RR and HMS. The data processing methodology was developed and implemented by RR in collaboration with AH. Finite difference modelling was carried out by BOR and dispersion curve models by RR and AH. RR was responsible for analysing and visualising the data and writing the manuscript with contributions from all authors.

*Competing interests.* The authors declare that they have no conflict of interest.

*Financial support.* This research has been supported by the University of Tromsø – The Arctic University of Norway, ARCEx partners and the Research Council of Norway (grant no. 228107).

*Review statement.* This paper was edited by Adam Booth and reviewed by Aurélien Mordret and one anonymous referee.

## References

Bandt, C. and Pompe, B.: Permutation entropy: a natural complexity measure for time series, Phys. Rev. Lett., 88, 174102, https://doi.org/10.1103/PhysRevLett.88.174102, 2002.

Barosh, P. J.: Frostquakes in New England, Eng. Geol., 56, 389–394, 2000.

Battaglia, S. M. and Changnon, D.: Frost Quakes: Forecasting the Unanticipated Clatter, Weatherwise, 69, 20–27, https://doi.org/10.1080/00431672.2015.1109984, 2016.

Cable, S., Elberling, B., and Kroon, A.: Holocene permafrost history and cryostratigraphy in the High Arctic Adventdalen Valley, central Svalbard, Boreas, 47, 423–442, 2018.

Chillara, V. K. and Lissenden, C. J.: Review of nonlinear ultrasonic guided wave nondestructive evaluation: theory, numerics, and experiments, Opt. Eng., 55, 011002, https://doi.org/10.1117/1.OE.55.1.011002, 2015.

Christiansen, H. H., Etzelmüller, B., Isaksen, K., Juliussen, H., Farbrot, H., Humlum, O., Johansson, M., Ingeman-Nielsen, T., Kristensen, L., and Hjort, J.: The thermal state of permafrost in the Nordic area during the International Polar Year 2007–2009, Permafrost Periglac., 21, 156–181, 2010.

Christiansen, H. H., Matsuoka, N., and Watanabe, T.: Progress in understanding the dynamics, internal structure and palaeoenvironmental potential of ice wedges and sand wedges, Permafrost Periglac., 27, 365–376, 2016.

Dou, S., Nakagawa, S., Dreger, D., and Ajo-Franklin, J.: An effective-medium model for P-wave velocities of saturated, unconsolidated saline permafrost, Geophysics, 82, EN33–EN50, 2017.

El-Gohary, M. and McNames, J.: Establishing causality with whitened cross-correlation analysis, IEEE T. Bio.-Med.-Eng., 54, 2214–2222, 2007.

Foti, S., Hollender, F., Garofalo, F., Albarello, D., Asten, M., Bard, P.-Y., Comina, C., Cornou, C., Cox, B., and Di Giulio, G.: Guidelines for the good practice of surface wave analysis: A product of the InterPACIFIC project, B. Earthq. Eng., 16, 2367–2420, 2018.

French, H. M.: The periglacial environment, 4th edn., John Wiley and Sons, Hoboken, New Jersey, USA, 2017.

Gilbert, G. L., Kanevskiy, M., and Murton, J. B.: Recent advances (2008–2015) in the study of ground ice and cryostratigraphy, Permafrost Periglac., 27, 377–389, 2016.

Gilbert, G. L., O'neill, H. B., Nemec, W., Thiel, C., Christiansen, H. H., and Buylaert, J. P.: Late Quaternary sedimentation and permafrost development in a Svalbard fjord-valley, Norwegian high Arctic, Sedimentology, 65, 2531–2558, 2018.

Humlum, O., Instanes, A., and Sollid, J. L.: Permafrost in Svalbard: a review of research history, climatic background and engineering challenges, Polar Res., 22, 191–215, 2003.

Johansen, T. A., Digranes, P., van Schaack, M., and Lønne, I.: Seismic mapping and modeling of near-surface sediments in polar areas, Geophysics, 68, 566–573, 2003.

Kanevskiy, M., Shur, Y., Fortier, D., Jorgenson, M., and Stephani, E.: Cryostratigraphy of late Pleistocene syngenetic permafrost (yedoma) in northern Alaska, Itkillik River exposure, Quaternary Res., 75, 584–596, 2011.

Keating, K., Binley, A., Bense, V., Van Dam, R. L., and Christiansen, H. H.: Combined geophysical measurements provide evidence for unfrozen water in permafrost in the adventdalen valley in Svalbard, Geophys. Res. Lett., 45, 7606–7614, 2018.

Knopoff, L.: A matrix method for elastic wave problems, B. Seismol. Soc. Am., 54, 431–438, 1964.

Kottek, M., Grieser, J., Beck, C., Rudolf, B., and Rubel, F.: World map of the Köppen-Geiger climate classification updated, Meteorol. Z., 15, 259–263, 2006.

Lachenbruch, A. H.: Mechanics of thermal contraction cracks and ice-wedge polygons in permafrost, Geol. Soc. Am., The Waverly Press, Baltimore, Maryland, USA, 1962.

Le Feuvre, M., Joubert, A., Leparoux, D., and Cote, P.: Passive multi-channel analysis of surface waves with cross-correlations and beamforming. Application to a sea dike, J. Appl. Geophys., 114, 36–51, 2015.

Leung, A. C., Gough, W. A., and Shi, Y.: Identifying frostquakes in Central Canada and neighbouring regions in the United States with social media, in: Citizen Empowered Mapping, Springer, Cham, Switzerland, 2017.

Lønne, I.: Faint traces of high Arctic glaciations: an early Holocene ice-front fluctuation in Bolterdalen, Svalbard, Boreas, 34, 308–323, 2005.

Lowe, M. J.: Matrix techniques for modeling ultrasonic waves in multilayered media, IEEE T. Ultrason. Ferr., 42, 525–542, 1995.

Mackay, J. R.: The direction of ice-wedge cracking in permafrost: downward or upward?, Can. J. Earth Sci., 21, 516–524, 1984.

Matsuoka, N., Christiansen, H. H., and Watanabe, T.: Ice-wedge polygon dynamics in Svalbard: Lessons from a decade of automated multi-sensor monitoring, Permafrost Periglac., 29, 210–227, 2018.

Nikonov, A.: Frost quakes as a particular class of seismic events: Observations within the East-European platform, Izvestiya, Phys. Solid Earth, 46, 257–273, 2010.

O'Neill, H. B. and Christiansen, H. H.: Detection of ice wedge cracking in permafrost using miniature accelerometers, J. Geophys. Res.-Earth, 123, 642–657, 2018.

O'Neill, H. B. and Burn, C. R.: Physical and temporal factors controlling the development of near-surface ground ice at Illisarvik, western Arctic coast, Canada, Can. J. Earth Sci., 49, 1096–1110, 2012.

Park, C., Miller, R., Laflen, D., Neb, C., Ivanov, J., Bennett, B., and Huggins, R.: Imaging dispersion curves of passive surface waves, in: SEG technical program expanded abstracts 2004, Society of Exploration Geophysicists, Tulsa, Oklahoma, USA, 1357–1360, https://doi.org/10.1190/1.1851112, 2004.

Park, C. B., Miller, R. D., and Xia, J.: Imaging dispersion curves of surface waves on multi-channel record, in: SEG Technical Program Expanded Abstracts 1998, Society of Exploration Geophysicists, Tulsa, Oklahoma, USA, 1377–1380, https://doi.org/10.1190/1.1820161, 1998.

Park, C. B., Miller, R. D., and Xia, J.: Multichannel analysis of surface waves, Geophysics, 64, 800–808, 1999.

Park, C. B., Miller, R. D., Xia, J., and Ivanov, J.: Multichannel analysis of surface waves (MASW) – active and passive methods, Leading Edge, 26, 60–64, 2007.

Rose, J. L.: Ultrasonic Guided Waves in Structural Health Monitoring, Key Engineering Materials, 11th Asian Pacific Conference on Nondestructive Testing (llth-APCNDT), Jeju island, Korea, 3–7 November 2003, Trans Tech Publications, Ltd., 270–273, 14–21, https://doi.org/10.4028/www.scientific.net/kem.270-273.14, 2004.

Ryden, N. and Lowe, M. J.: Guided wave propagation in three-layer pavement structures, J. Acoust. Soc. Am., 116, 2902–2913, 2004.

Ryden, N. and Park, C. B.: Fast simulated annealing inversion of surface waves on pavement using phase-velocity spectra, Geophysics, 71, R49–R58, 2006.

Ryden, N., Park, C. B., Ulriksen, P., and Miller, R. D.: Multimodal approach to seismic pavement testing, J. Geotech. Geoenviron., 130, 636–645, 2004.

Schmidt, H. and Jensen, F. B.: A full wave solution for propagation in multilayered viscoelastic media with application to Gaussian beam reflection at fluid–solid interfaces, J. Acoust. Soc. Am., 77, 813–825, 1985.

Sergeant, A., Chmiel, M., Lindner, F., Walter, F., Roux, P., Chaput, J., Gimbert, F., and Mordret, A.: On the Green's function emergence from interferometry of seismic wave

fields generated in high-melt glaciers: implications for passive imaging and monitoring, The Cryosphere, 14, 1139–1171, https://doi.org/10.5194/tc-14-1139-2020, 2020.

Skvortsov, A., Sadurtdinov, M., and Tsarev, A.: Seismic Criteria for Identifying Frozen Soil, Kriosfera Zemli, 18, 75–80, 2014.

Unakafova, V. and Keller, K.: Efficiently measuring complexity on the basis of real-world data, Entropy, 15, 4392–4415, 2013.

Walter, F., Roux, P., Roeoesli, C., Lecointre, A., Kilb, D., and Roux, P.-F.: Using glacier seismicity for phase velocity measurements and Green's function retrieval, Geophys. J. Int., 201, 1722–1737, 2015.

## 2.2 Preface to paper 2

Romeyn, R., Hanssen, A., and Köhler, A. **Long term analysis of cryoseismic events and associated ground thermal stress in Adventdalen, Svalbard**, The Cryosphere Discuss. [preprint], https://doi.org/10.5194/tc-2021-329, in review, 2021.

Paper 2 developed as a complementary study to Paper 1, with primary focus on the temporal distribution of frost quakes and how they are triggered. These topics were difficult to address in Paper 1 since battery life constraints meant that the temporary seismic array reported on in that study could only record relatively short windows of time. By contrast, the SPITS seismic array on Janssonhaugen in Adventdalen is part of the permanent seismic monitoring infrastructure (Gibbons et al., 2011), has been in continuous operation since the 1990's and was very well suited to this task. The source positions for a catalogue of automatically detected seismic events were estimated using matched field processing and this proved to be an effective means of distinguishing between events that could be interpreted as frost quakes from those attributable to underground mining activities at the Gruve 7 coal mine. We were also able to identify spatial clustering of the frost quakes that was interpretable in terms of periglacial landforms visible on orthophotographic imagery.

The study also focuses on consideration of thermal stress as a trigger for frost quakes, following the typical observation that frost quakes are associated with rapidly decreasing air temperatures and the absence of an insulating snow layer (Barosh, 2000; Battaglia et al., 2016; Matsuoka et al., 2018; Nikonov, 2010). A key novelty of this paper is that we model thermal stress based on measured ground temperatures. Several previous studies (e.g. Okkonen et al., 2020; Podolskiy et al., 2019) have modelled thermal stress on the basis of ground temperatures that are, in turn, modelled based on measured air temperature (plus other environmental parameters that are estimated or known to a limited extent). To illustrate the implications of this, we tested the popular ground temperature model of Rankinen et al. (2004) that is applicable to snow-covered and seasonally frozen soils. This is also the ground temperature model that underpins the thermal stress model used by Okkonen et al. (2020) to investigate a frost quake swarm recorded in Finland. The Rankinen et al. (2004) ground temperature model is popular because of its simplicity and small set of input parameters and can be expressed as,

$$\frac{\partial T}{\partial t} = \frac{\partial}{\partial z}\left(\frac{K_T}{C_A}\frac{\partial T}{\partial z}\right) e^{-f_S D_S}.$$

Here $T(z,t)$ is the ground temperature at depth $z$ and time $t$, $K_T(z)$ is the ground thermal conductivity ($Wm^{-1}°C^{-1}$), $C_A(z)$ is the apparent volumetric heat capacity ($Jm^{-3}°C^{-1}$), $D_S$ is the snow depth (m) and $f_S$ is an empirical damping parameter related to the thermal conductivity of snow ($m^{-1}$). For a uniform layer with thickness of $2z$, the temperature in the middle of the layer, i.e., at depth $z$, is found by applying the explicit finite difference equation,

$$T(z,t+1) = T(z,t) + \frac{D(z)\Delta t}{(2z)^2}\big(T_{air}(t) - T(z,t)\big)e^{-f_S D_S},$$

where $T(z,t)$ is the ground temperature at depth $z$ and the previous time step $t$, $\Delta t$ is the time increment in seconds, $D(z) = K_T(z)/C_A(z)$ is the effective ground thermal diffusivity ($m^2s^{-1}$) at depth $z$ and $T_{air}(t)$ is the air temperature at the previous time step.

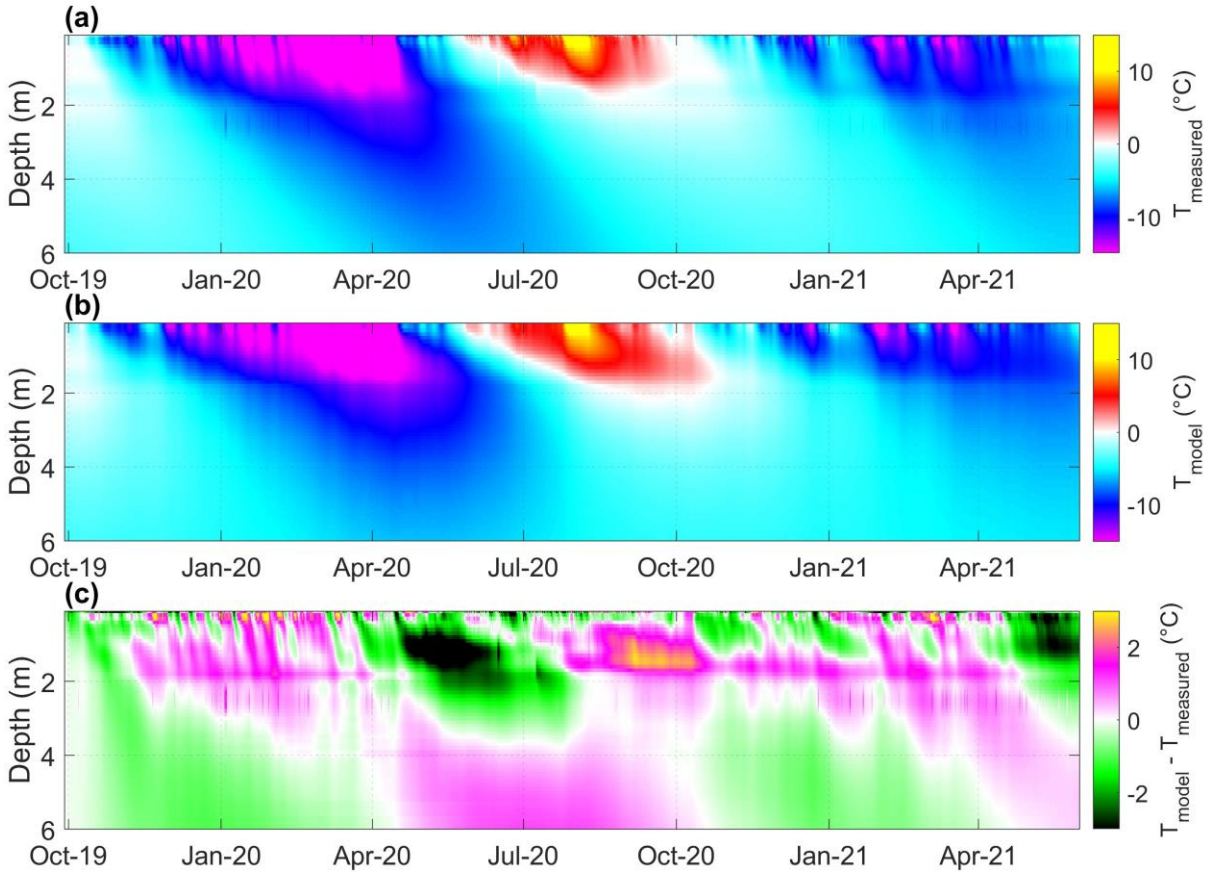


*Figure x – comparison of (a) ground temperature field measured by thermistors installed in the PACE P11 borehole, (b) ground temperatures modelled based on Rankinen et al. (2004) assuming the best fit thermal diffusivity profile illustrated in Figure xi and empirical damping parameter $f_S = 1.0\ m^{-1}$. (c) Subtraction of the measured from the modelled temperature field.*

We used air temperatures and snow depths measured at the Janssonhaugen meteorological station to model ground temperatures and ran a brute force optimization to find the thermal diffusivity depth

profile and empirical snow damping parameter which minimized the L2 norm described fit with borehole temperatures measured in the PACE P11 borehole at Janssonhaugen. The measured and modelled ground temperature fields are shown in Figure x and the best fit effective thermal diffusivity depth profile is shown in Figure xi. The empirical damping parameter value that best fit the observed data was $f_S = 1.0\ m^{-1}$.

We observe that the Rankinen et al. (2004) model gives a reasonable approximation of the measured ground temperature field (see Figure x), but that significant deviations are present when the difference between measured and modelled temperatures are examined in detail (see Figure x-c). Figure xii illustrates the timeseries of temperature at selected depths and further illustrates that while the model gives a reasonable approximation of the ground temperature, it remains at best a limited representation of the measured temperature field. In particular, high-frequency discrepancies of ± 3°C in the shallow subsurface (e.g., z=0.3 m) as illustrated in Figure xii-d are likely to have significant implications for thermal stress and modelled frost quake likelihood.

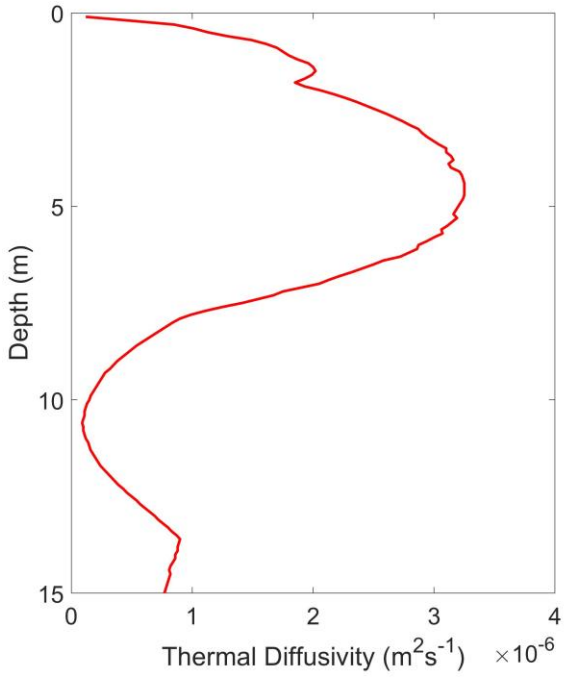


*Figure xi – Effective thermal diffusivity depth profile that gave best model fit compared with borehole measured temperatures.*

It is not a surprising result that our ability to model ground temperature based on air temperatures and additional environmental parameters is inherently limited. Ground temperature is a function of the site-specific energy balance and depends on conductive, convective and latent heat transport that are in turn governed by processes like moisture transport, soil freezing/melting, snow cover at the ground surface and the thermal properties of the ground (Chalhoub et al., 2017; Gisnås et al., 2016;

Xing and Spitler, 2017). Modelling ground temperature is always a trade-off between accuracy on the one hand and constraint data availability on the other (Droulia et al., 2009). A model which perfectly replicates observed ground temperatures would require such detailed knowledge of soil moisture, porosity, composition, thermal diffusivity of the components and snow depth that it would not be feasible in practice and would ultimately be more involved than measuring the ground temperature directly.

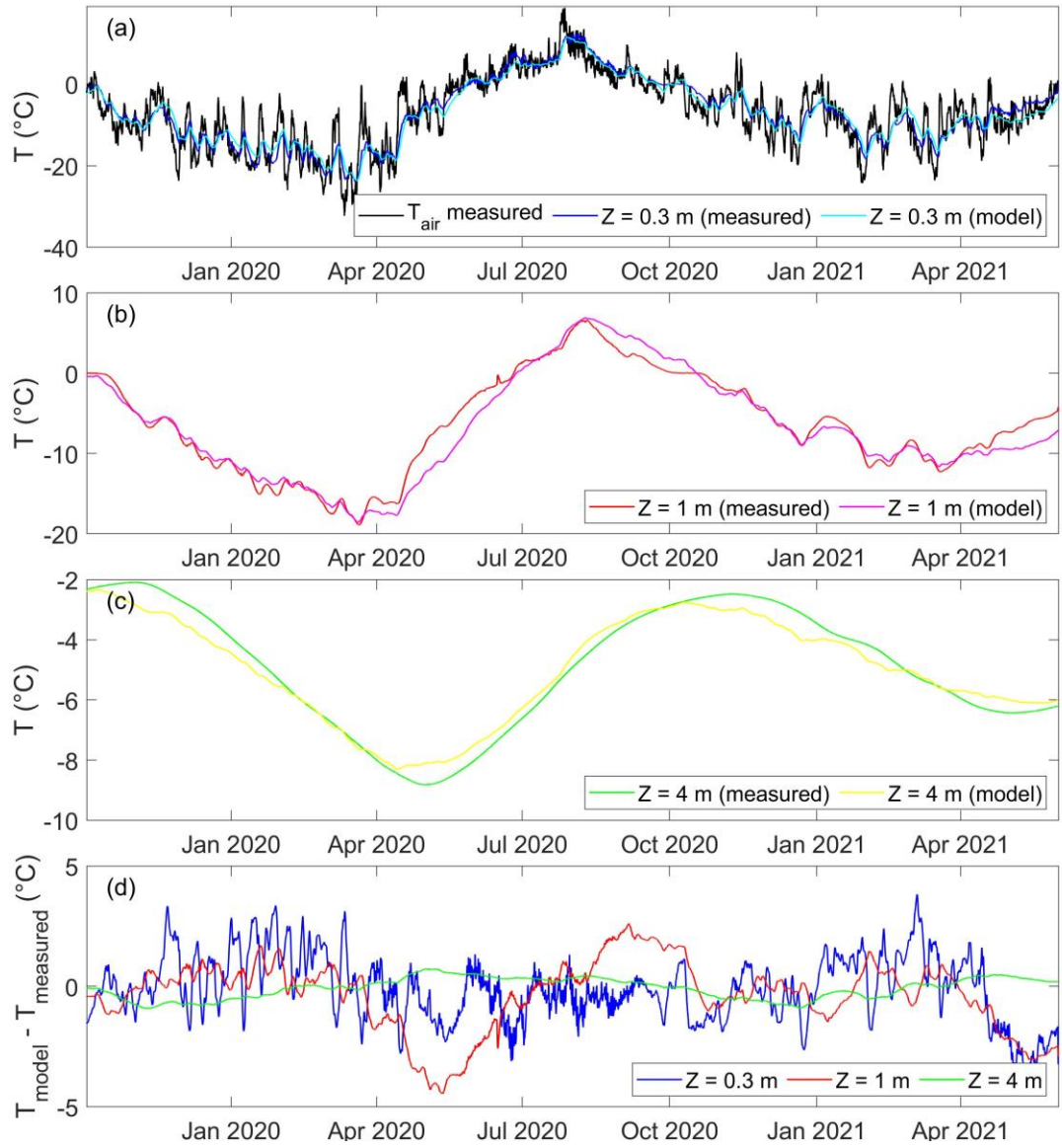


*Figure xii – (a) Air temperature, measured and modelled temperatures in the shallow subsurface at 0.3 m, (b) 1 m and (c) 4 m depths. (d) difference between measured and modelled temperatures at 0.3 m, 1 m and 4 m depths.*

# Paper 2

https://doi.org/10.5194/tc-2021-329
Preprint. Discussion started: 25 October 2021


The Cryosphere Discussions

# Long term analysis of cryoseismic events and associated ground thermal stress in Adventdalen, Svalbard

Rowan Romeyn[1], Alfred Hanssen[1], Andreas Köhler[1,2]

[1]Department of Geosciences, University of Tromsø – The Arctic University of Norway, 9037 Tromsø, Norway
[2]NORSAR, Gunnar Randers vei 15, 2007 Kjeller, Norway

*Correspondence to*: Rowan Romeyn (rowan.romeyn@uit.no)

**Abstract.** The small-aperture Spitsbergen seismic array (SPITS) has been in continuous operation at Janssonhaugen for decades. The high Artic location in the Svalbard archipelago makes SPITS an ideal laboratory for the study of cryoseisms, a nontectonic class of seismic events caused by freeze processes in ice, ice-soil and ice-rock materials. We extracted a catalogue of >100 000 events from the nearly continuous observation period between 2004 and 2021, characterized by short duration ground shaking of just a few seconds. This catalogue contains two main subclasses where one subclass is related to underground coal mining activities and the other is inferred to be dominated by frost quakes resulting from thermal contraction cracking of ice wedges or other segregated ice bodies. This inference is supported by the correspondence between peaks in observed seismicity with peaks in modelled ground thermal stress, based on a Maxwellian thermo-viscoelastic model constrained by borehole observations of ground temperature. The inferred frost quakes appear to be dominated by surface wave energy and SPITS proximal source positions, with three main areas that are associated with dynamic geomorphological features; boulder producing scarps and solifluction lobes. Seismic stations providing year-round, high temporal resolution measurements of ground motion may be highly complementary to satellite remote sensing methods, such as InSAR, for studying the dynamics of periglacial environments. The long-term observational record presented in this study, containing tens of thousands of cryoseismic events, in combination with a detailed record of borehole ground temperature observations, provides a unique insight into the spatiotemporal patterns of cryoseisms. The observed patterns may guide the development of models that can be used to understand future changes to cryoseismicity based on projected temperatures.

## 1 Introduction

Cryoseisms are a nontectonic class of seismic events caused by freeze processes in ice, ice-soil and ice-rock materials (Lacroix, 1980). For example, the buildup of thermal stress in frozen soils during intense periods of cooling can lead to tensional fracturing and explosive pressure release (Barosh, 2000; Battaglia et al., 2016). Since this pressure release triggers the propagation of seismic waves, these events are sometimes referred to as frost quakes (e.g. Okkonen et al., 2020). Observations of frost quakes are limited because seismic amplitudes decay rapidly with distance from the point of rupture, but they have been felt at distances of several hundred meters to several kilometers and are usually accompanied by cracking or booming

https://doi.org/10.5194/tc-2021-329
Preprint. Discussion started: 25 October 2021


noises, resembling falling trees, gunshots or underground thunder (Leung et al., 2017; Nikonov, 2010). Cracking typically occurs in response to rapid air and ground cooling, in the absence of an insulating snow layer and where sufficient moisture is present for ice to form (Barosh, 2000; Battaglia et al., 2016; Matsuoka et al., 2018; Nikonov, 2010). The resulting fractures may potentially cause damage to buildings and other infrastructure in cold regions (Okkonen et al., 2020). Frost heave (e.g. Rempel, 2010) can be understood as a combination of slow creep and rapid elastic (frost quakes) deformation of frozen ground and causes damage to roads requiring billions of dollars annually to repair in the United States alone (DiMillio, 1999).

Ice-wedge or sand-wedge polygons are a widespread manifestation of a dynamic cryosphere observed in the periglacial environment (e.g. Black, 1976; Matsuoka et al., 2004). These structures form when water infiltration and thermal contraction, or wind transported sand grains, hold open fractures which become planes of weakness (Lachenbruch, 1962; Mackay, 1984; Matsuoka et al., 2004; Sørbel and Tolgensbakk, 2002). Repeated cracking, infilling and refreezing along these planes causes the ice wedges to grow laterally, forcing the displaced ground upwards and resulting in a series of ridges in a polygonal arrangement that are one of the most recognizable landforms in permafrost environments (Christiansen et al., 2016; Lachenbruch, 1962; Matsuoka et al., 2018). For this reason, sand-wedge polygons, that were formed at sea level on the paleo-equator during late Neoproterozoic glacial episodes, have been used as evidence supporting the snowball Earth hypothesis (Maloof et al., 2002). Small-scale polygonal features observed on the surface of Mars have also been inferred to result from thermal contraction cracking (Mellon, 1997).

Frost cracking driven by segregation ice growth is also an important agent of bedrock erosion in cold mountainous areas, where active screes and high headwall erosion rates are observed in areas where frost erosion is most intense (Hales and Roering, 2009; Hales and Roering, 2007; Scherler, 2014). Rockfall driven by frost cracking may be the primary mechanism in cold and dry mountain climates (Hales and Roering, 2009). Progressive crack growth is driven by the migration of water to ice bodies in cracks that is similar to the mechanism by which ice lenses develop in freezing soil (Hallet et al., 1991; Murton et al., 2006; Peppin and Style, 2013; Walder and Hallet, 1985). Frost cracking and creep on slopes leads to the development of solifluction lobes and sheets (Cable et al., 2018; Matsuoka, 2001). Solifluction is broadly defined as the slow mass wasting resulting from freeze-thaw action in fine-textured soils (French, 2017; Matsuoka, 2001) and occurs due to the asymmetry between the heaving forces, which are perpendicular with the ground surface and subsequent vertical subsidence under the force of gravity.

Interferometric synthetic aperture radar (InSAR) is a satellite remote sensing technique capable of resolving down to millimeter scale ground surface displacements at a spatial scale of tens of meters (Hanssen, 2001; Rosen et al., 2000). Consequently, InSAR has used to resolve seasonal patterns of frost heave and thaw subsidence (Chen et al., 2020; Rouyet et al., 2021; Wahr et al., 2008). The broad spatial coverage and high spatial resolution of InSAR has also been used to show that the spatial patterns of ground displacement are related to specific geomorphological units, consisting of specific frost prone sediment types and periglacial landforms (Liu et al., 2018; Rouyet et al., 2019). On the other hand, the temporal resolution is determined

https://doi.org/10.5194/tc-2021-329
Preprint. Discussion started: 25 October 2021


by the repeat cycle of the satellite (~6 days for Sentinel-1), which means that it is not possible to distinguish between slow frost creep and rapid elastic deformation (frost quake) processes. In addition, snow cover causes a loss of radar coherence between repeat satellite passes that limits InSAR to snow free areas and times of year. As a result, InSAR is more suited to studying thaw subsidence than frost heave in areas such as Svalbard that are snow covered for the majority of the freezing season (e.g. Rouyet et al., 2019). Seismic stations providing year-round, high temporal resolution measurements of ground motion, at the expense of more limited spatial source resolution and coverage, may be highly complementary to InSAR methods for studying the dynamics of periglacial environments.

This study was motivated by the sporadic observation of clusters of events recorded by the small-aperture Spitsbergen seismic array (SPITS), with durations of just a few seconds and peak amplitudes significantly above the background noise level. For comparison, regional tectonic earthquakes are typically associated with >30 s shaking duration. SPITS has previously been used to study a class of cryoseismic signals associated with iceberg calving at the termini of grounded tidewater glaciers at local to near-regional distances of up to 200 km (Köhler et al., 2015). These calving related seismic signals occurred most frequently during the melt season and the ground motion lasts ~15-20 s. Signals with intermediate durations have also been observed at SPITS, originating from nearby mountain glaciers (Albaric et al., 2021) and coal mining operations (Gibbons and Ringdal, 2006). Based on previous work further down-valley in Adventdalen, e.g. Matsuoka et al. (2018) and Romeyn et al. (2021), we hypothesized that the short duration events at SPITS might be dominated by frost quakes initiated by thermal contraction cracking in the vicinity of the array. The aim of this study was to test this hypothesis by analyzing the spatial and temporal occurrence of these events. This study is highly complementary to the previous work of Romeyn et al. (2021). While the spatial and temporal wavefield sampling of the SPITS array is much coarser than the temporary array they deployed, a much longer and nearly continuous record is available. This allows a more rigorous investigation of the temporal correlation of these events with ground cooling and thermal stress accumulation.

## 2 Study area and data

The small-aperture Spitsbergen seismic array (SPITS) is located on Janssonhaugen, in the Adventdalen valley on the island of Spitsbergen, part of the Svalbard archipelago (Figure 1). The SPITS array has been in operation since 1992, maintained by the research foundation NORSAR. At present, it consists of 9 CMG-3T seismometers with an aperture of 1 km and interstation distances >250 m (e.g. Gibbons et al., 2011; Köhler et al., 2015) installed in shallow boreholes below the permafrost active layer. The standard frequency response of the CMG-3T seismometer is flat (within -3dB) for the range from 0.0083 to 50 Hz. We chose to limit the present study to the period following August 2004 when the SPITS array was upgraded to a full broadband array with an increase in sampling rate from 40 to 80 Hz for all seismometers (Schweitzer et al., 2021). The waveform data following the upgrade is of high quality and well suited to source localization using broadband, coherent

https://doi.org/10.5194/tc-2021-329
Preprint. Discussion started: 25 October 2021


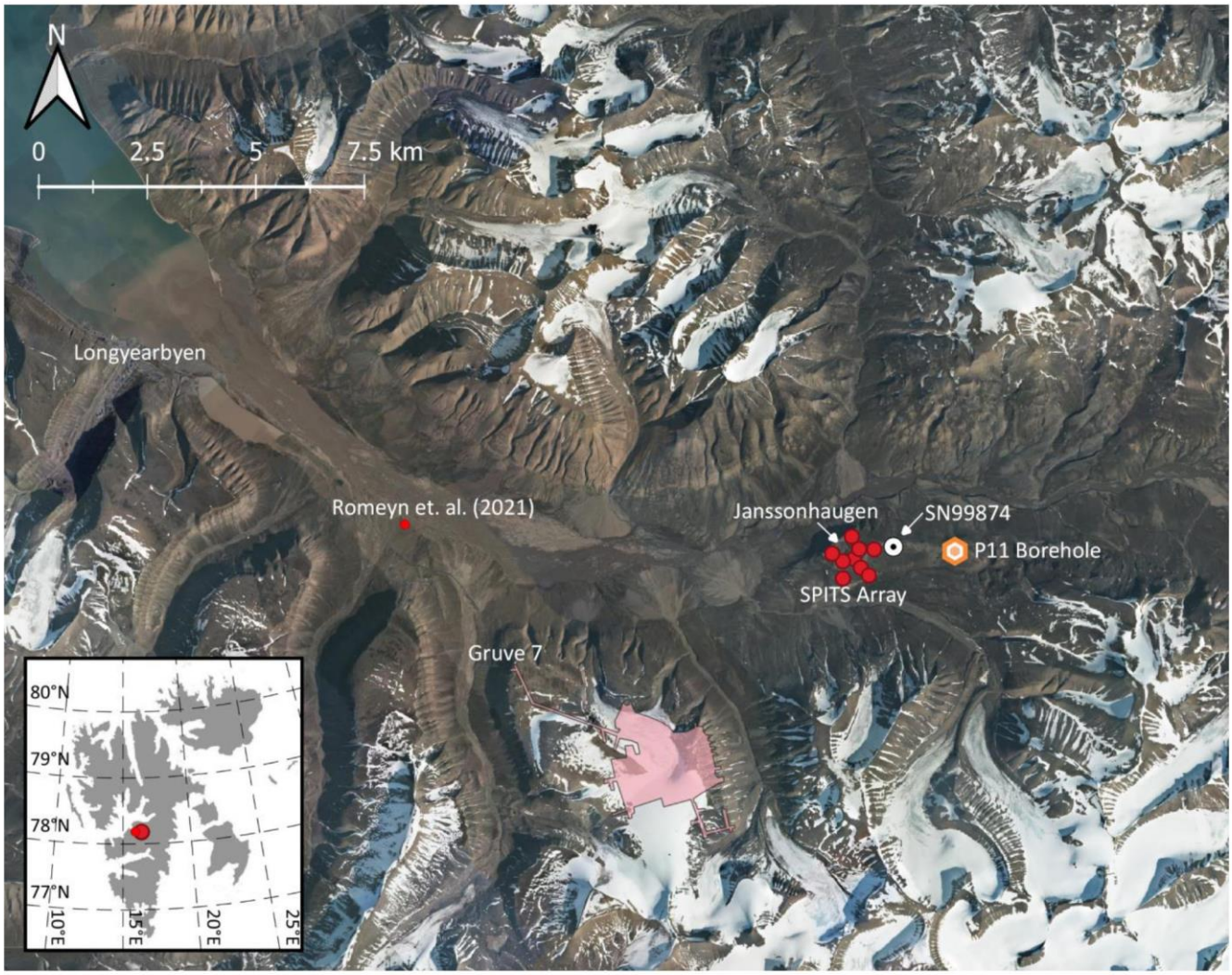


**Figure 1 – Overview of the location of the SPITS array located on Janssonhaugen in Adventdalen, up-valley from the settlement of Longyearbyen and the temporary seismic array of Romeyn et al. (2021). The P11 temperature logging borehole and the underground mining areas and tunnels of the operational coal mine, Gruve 7, are also shown. The met.no weather station "Janssonhaugen Vest" is marked by its station number, SN99874. Orthophoto © Norwegian Polar Institute (npolar.no).**

Janssonhaugen is a bedrock remnant located in the middle of the Adventdalen valley, with a ~0.2-0.3 m thick weathered sediment crust overlying homogeneous sand-/siltstone bedrock (density 2280kg.m$^{-3}$, porosity 20-25 %, >96.5 % $SiO_2$) corresponding to the Ullaberget Member of Lower Cretaceous Rurikfjellet Formation (Dypvik et al., 1991; Isaksen et al., 2001). The bedrock at Janssonhaugen has been drilled to a depth of 102 m and the permafrost zone is estimated to extend down

https://doi.org/10.5194/tc-2021-329
Preprint. Discussion started: 25 October 2021


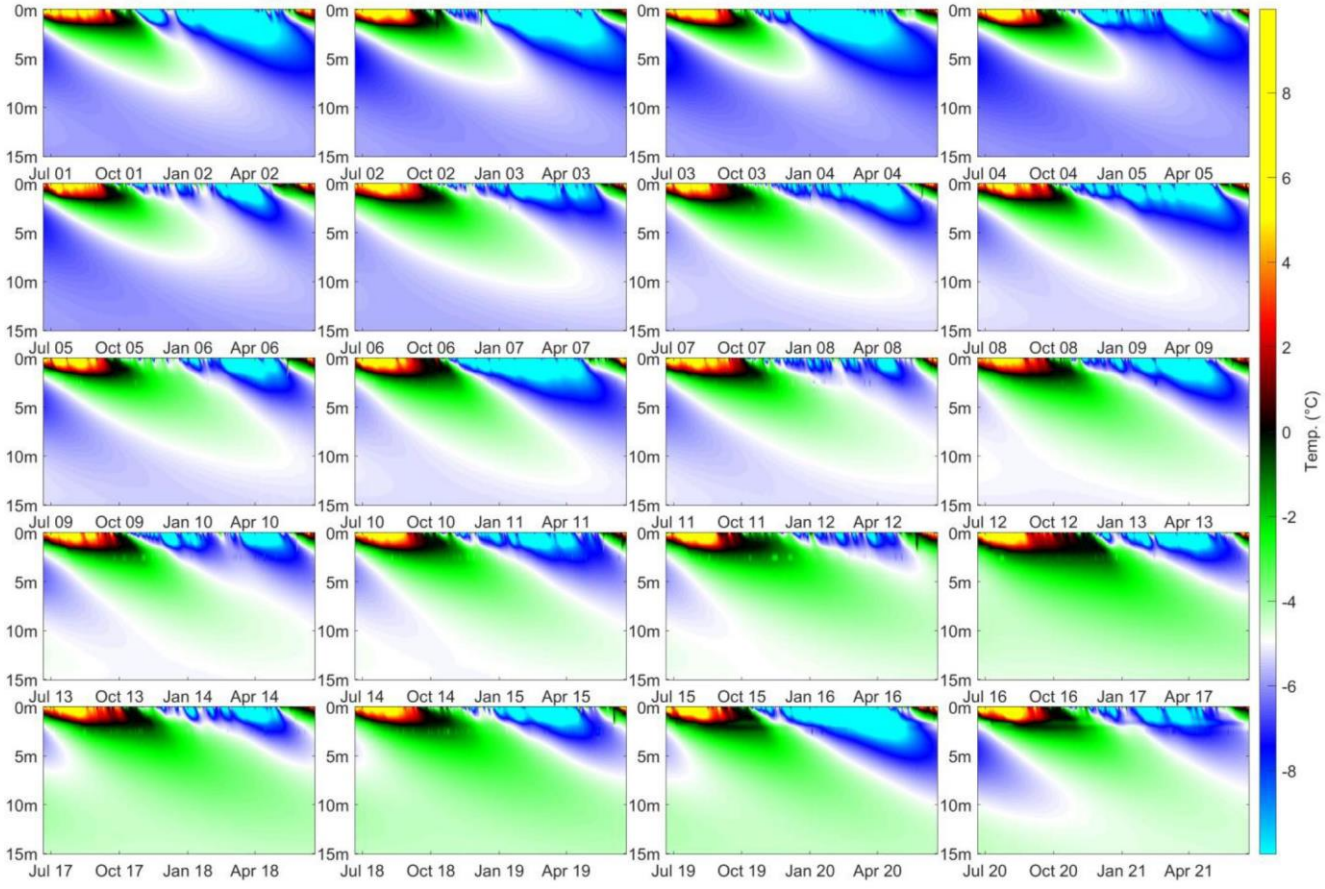


**Figure 2 – Illustration of borehole temperature history recorded at the PACE P11 borehole on Janssonhaugen. A long-term warming trend is observed below the active layer that is subject to seasonal freeze-thaw.**

Temperature monitoring boreholes installed at Janssonhaugen are critical to our ability to accurately model the subsurface buildup of thermal stress. Thermistors installed in the GTN-P (Global Terrestrial Network for Permafrost) boreholes P10 (102 m deep) and P11 (15 m deep) provide a continuous record of the subsurface temperature field at Janssonhaugen, with a sampling interval of 6 hours extending from April 1999 to the present (Isaksen et al., 2001). We focus on the P11 borehole (see Figure 1), which gives the most detailed record of the near-surface temperature field and is least disturbed by installations

to 220 m, based on downward extrapolation of the measured temperature gradient (Isaksen et al., 2001). Despite annual precipitation of 300-500 mm/yr., the snow cover on Janssonhaugen is typically thin or completely absent due to the scouring effect of the prevailing winds (Isaksen et al., 2001). The surface topography is generally flat but loose surface material is sorted into polygons (Isaksen et al., 2001), indicating the presence of sand/ice-wedges. The homogeneous geology at Janssonhaugen, it's flat topography, limited snow cover, relatively large distance to glaciers, rivers, ocean, human activity such as coal mining and position well above the Holocene marine limit make it a good location to study permafrost processes (Isaksen et al., 2000).

https://doi.org/10.5194/tc-2021-329
Preprint. Discussion started: 25 October 2021


at the ground surface. The temperature field measured by the P11 borehole is illustrated in Figure 2. The ~2 m thick active layer (Christiansen et al., 2020) is sampled by thermistors at 0.2, 0.4, 0.8, 1.2, 1.6 and 2 m and there is significant inter-annual variability in the magnitude of summer warming and winter cooling. A long-term warming trend is observed in the permafrost beneath the active layer (Figure 2). Furthermore, the Janssonhaugen Vest weather station (see Figure 1), which was installed in September 2019, provides an hourly sampled record of ground temperature at 0.1 m depth and provides a basis to compare depth and temporal sampling effects against the longer duration P11 record.

## 3 Methods

### 3.1 STA/LTA detection of short duration seismic events

The purpose of the event detector is to make a first-pass automatic identification of short duration seismic signals, which should be distinguished from both background noise and longer duration local and regional seismic events that may be high amplitude. The raw data from each seismometer was first de-trended, corrected according to the calibrated instrument sensitivity and bandpass filtered to the range 2.5-20 Hz using a delay-compensated minimum phase filter with a stopband attenuation of 60 dB (see Figure 3a).

Events are detected based on anomalous values of short-time-averaged amplitude divided by long-time-averaged amplitude, i.e., the classic STA/LTA approach (e.g. Trnkoczy, 2009). In our implementation, the short-term average (STA) from the trace envelope for each seismogram, given by the magnitude of the Hilbert transform and smoothed by taking the one-second moving average. Since we have an array of stations, we represent the array-STA by taking the $80^{th}$ percentile station-STA across all stations at a given time. By visual inspection of test periods, we found that this emphasizes very local events with large amplitude variation across the array, while still ensuring that there is at least some coherency across the array. If we had chosen the maximum array STA, we may detect arbitrary noise spikes with large amplitudes registered on a single seismometer. If the mean or median array STA were chosen, we would preferentially detect larger regional events with more consistent amplitudes across the array and suppress smaller local events with high amplitudes limited to a small subset of seismometers.

We calculate the long-term average (LTA) by simply smoothing the short-time average according to its moving average over a time-span of 20 seconds. This time-span is significantly longer than the events we seek to detect but shorter than the typical duration of the more regional scale seismic events that we want to ignore. We further reject epochs with LTA more than 2.5x the 2-hourly mean LTA in order to filter out large regional events. Events are then detected by applying a peak finding routine to the STA/LTA ratio. The STA/LTA peaks must have amplitude ≥10 and occur at least 5 seconds apart from one another. An example of event detection based on STA/LTA peaks is shown in Figure 3b, which illustrates that short duration events are selected while a longer high-amplitude event is not detected as intended.

https://doi.org/10.5194/tc-2021-329
Preprint. Discussion started: 25 October 2021


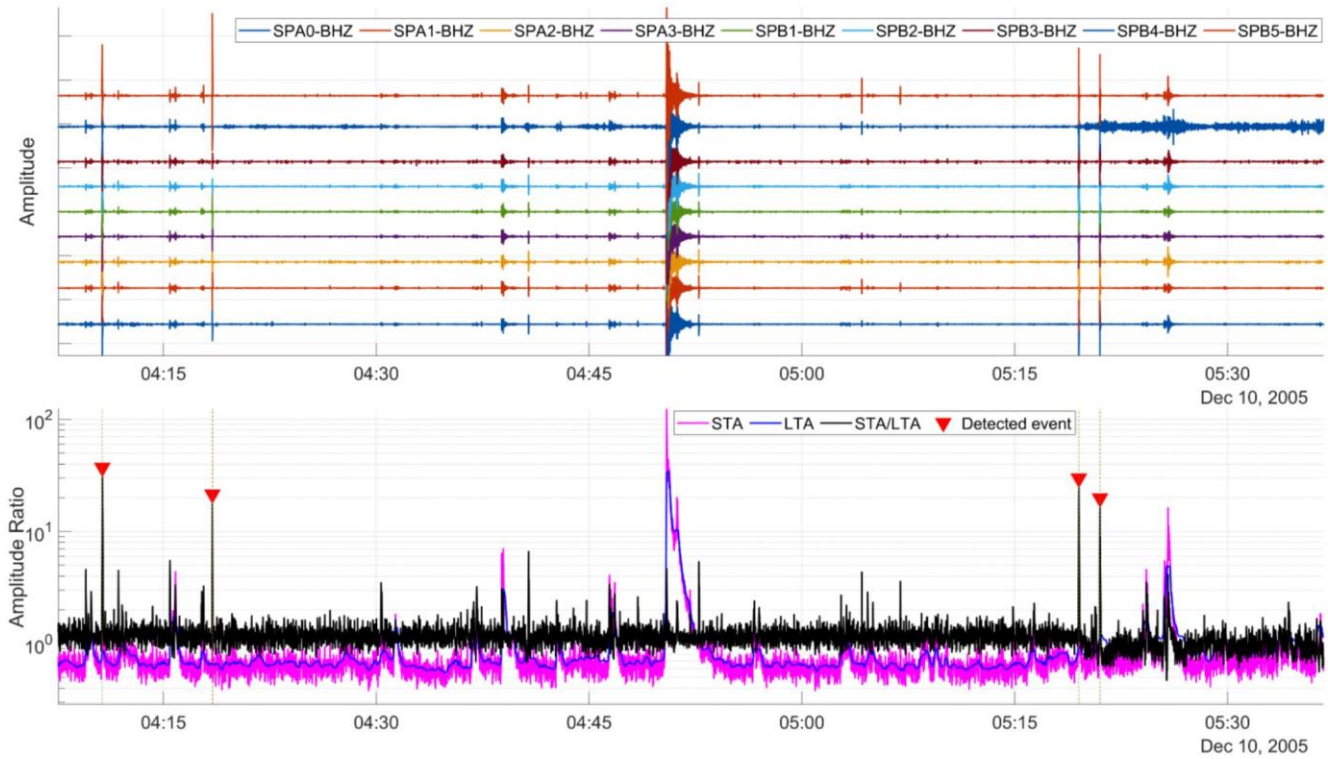


155 **Figure 3 – Example of event detection using the STA/LTA (short term/long term average) detector. Short duration events with sufficient amplitude and array coherence are selected while longer events such as the high amplitude example at 04:50 are ignored.**

### 3.2 Source localization by coherent MFP

Matched-field processing (MFP) is an established technique for localizing the position of seismic sources recorded by passive seismic arrays (Chmiel et al., 2016; Cros et al., 2011; Harley and Moura, 2014; Sergeant et al., 2020; Walter et al., 2015). MFP
160 proceeds via an evaluation of the similarity between the wavefield recorded at a receiver array and a series of predicted wavefields calculated for a grid of test source locations and a theoretical model of the source-receiver wave propagation. The MFP coherence is estimated by comparing the recorded data vector with a "replica" vector, which is a model representation of wave propagation within the medium. We assume a simple homogeneous medium with amplitude decay according to spherical divergence where the replica column vector, $\boldsymbol{R}'$ is represented by the theoretical harmonic wave emitted from a test
165 point $p(x, y)$ according to

$$\boldsymbol{R}'(\omega, \boldsymbol{d}) = \left[\frac{1}{d_1} e^{i\omega d_1/c(\omega)}, \frac{1}{d_2} e^{i\omega d_2/c(\omega)}, \ldots, \frac{1}{d_N} e^{i\omega d_N/c(\omega)}\right]^T / \eta. \quad (1)$$

Here, $i = \sqrt{-1}$, $\omega$ is the angular frequency, $\boldsymbol{d} = [d_1, d_2, \cdots, d_N]^T$ is an $N \times 1$ vector containing the absolute Euclidean distances between $p(x, y)$ and the $N$ recording stations where superscript $T$ denotes a transpose, $c(\omega)$ is the medium phase

https://doi.org/10.5194/tc-2021-329
Preprint. Discussion started: 25 October 2021


The Cryosphere Discussions

velocity at frequency $\omega$ and the vector is normalised to unit length by dividing by the factor $\eta = \sqrt{\sum_{j=1}^{N}(1/d_j^2)}$. The column

170 data vector is given by

$$\boldsymbol{R}(\omega) = [R_1(\omega), R_2(\omega), \ldots, R_N(\omega)]^T, \quad (2)$$

where $R_j(\omega)$ is a frequency transform of the $j$-th trace $r_j(t)$ of $N$ traces recording a specific seismic event. We then form the complex-valued $N \times N$ cross-spectral density matrix (CSDM) by

$$\mathbf{K}(\omega) = \boldsymbol{R}(\omega)\boldsymbol{R}^H(\omega), \quad (3)$$

175 where $(\cdot)^H$ denotes the Hermitian (conjugate transpose) operator. The frequency domain transform was implemented via the chirp z-transform (Rabiner et al., 1969), which provides a convenient means to evaluate the band limited transform (we select the 5-35 Hz band) with a specific frequency sampling interval (1 Hz). This allows us to efficiently and compactly represent the CSDM, whose size is a significant factor in the speed of computation, in addition to the number of test source points, $p(x, y)$. Conventionally, the MFP coherence is estimated using the linear Bartlett processor

180 $$G = \sum_{\omega} \boldsymbol{R}'^H(\omega, \boldsymbol{d})\mathbf{K}(\omega)\boldsymbol{R}'(\omega, \boldsymbol{d}) \quad (4)$$

which evaluates the inner product between the recorded and predicted wavefields before summing incoherently across frequency.

In this study we implement the coherent MFP scheme developed by Michalopoulou (1998), which is an elegant addition to the

185 conventional approach allowing cross-frequency spatial coherence structures to be exploited to give improved robustness and accuracy. In this scheme, measurement vectors at $L$ discrete frequencies are concatenated to form the $NL \times 1$ measurement super-vector

$$\boldsymbol{\mathcal{R}}(\boldsymbol{\omega}) = [\boldsymbol{R}(\boldsymbol{\omega_1}), \boldsymbol{R}(\boldsymbol{\omega_2}), \cdots, \boldsymbol{R}(\boldsymbol{\omega_L})]^T, \quad (5)$$

where $\boldsymbol{\omega} = [\omega_1, \omega_2, \cdots, \omega_L]^T$ is a frequency vector, and the replica vectors are concatenated to form the $NL \times 1$ replica super-

190 vector

$$\boldsymbol{\mathcal{R}}'(\boldsymbol{\omega}, \boldsymbol{d}) = [\boldsymbol{\mathcal{R}}'(\boldsymbol{\omega_1}, \boldsymbol{d}), \boldsymbol{\mathcal{R}}'(\boldsymbol{\omega_2}, \boldsymbol{d}), \cdots, \boldsymbol{\mathcal{R}}'(\boldsymbol{\omega_L}, \boldsymbol{d})]^T. \quad (6)$$

The super-CSDM $\boldsymbol{\mathcal{K}}(\boldsymbol{\omega}) = \boldsymbol{\mathcal{R}}(\boldsymbol{\omega})\boldsymbol{\mathcal{R}}^H(\boldsymbol{\omega})$ is then composed of $NL \times NL$ elements and the generalized MFP coherence is given by

$$\mathcal{G} = \boldsymbol{\mathcal{R}}'^H(\boldsymbol{\omega}, \boldsymbol{d})\, \boldsymbol{\mathcal{K}}(\boldsymbol{\omega})\, \boldsymbol{\mathcal{R}}'(\boldsymbol{\omega}, \boldsymbol{d}). \quad (7)$$

195 The estimated source position, $p(x, y)$, and phase velocity, $c(\omega)$, are those which maximize the coherence measure $\mathcal{G}$. Since some of the seismic events we wish to locate are dominated by surface waves and others are dominated by body waves, we simply assume that phase velocity is a constant and scan over the range 250-6000 m/s.

https://doi.org/10.5194/tc-2021-329
Preprint. Discussion started: 25 October 2021


The Cryosphere Discussions

### 3.3 Ground thermal stress model

Previous studies such as Mellon (1997), Maloof et al. (2002), Schulson and Duval (2009) and Podolskiy et al. (2019) have demonstrated that ice and frozen soil deform elastically on short timescales and viscously on long timescales. Thermal loading due to temperature changes acts as an external driving agent, and the resulting dynamical balance between the elastic and viscous response governs whether creep or fracture become dominant. Following Mellon (1997), we model the frozen soil as a Maxwellian viscoelastic solid augmented with thermal expansion and contraction. This allows us to decompose the total strain tensor $\varepsilon_{ij}$ into three components: an elastic ($\varepsilon_{ij}^{e}$), a thermal ($\varepsilon_{ij}^{T}$), and a viscous ($\varepsilon_{ij}^{V}$) component,

$$\varepsilon_{ij} = \varepsilon_{ij}^{e} + \varepsilon_{ij}^{T} + \varepsilon_{ij}^{V}, \tag{8}$$

where subscripts $ij$ indicate tensor components, $i, j = 1,2,3$, where 1 and 2 denote horizontal components, and 3 is the vertical component. The elastic strain tensor is related to the stress tensor $\sigma_{ij}$ by (e.g., Landau and Lifshitz, 1970)

$$\varepsilon_{ij}^{e} = \frac{1+\nu}{E}\,\sigma_{ij} - \frac{\nu}{E}\,\sigma_{kk}\,\delta_{ij}\,, \tag{9}$$

where $\nu$ is Poisson's ratio, $E$ is Young's modulus, $\delta_{ij}$ is the Kronecker delta, and Einstein's summation convention is applied throughout this paper.

The thermal strain tensor is a measure of the change in volume caused by the thermally driven deformation, and it is expressed as (e.g., Landau and Lifshitz, 1970)

$$\varepsilon_{ij}^{T} = \alpha(T - T_0)\,\delta_{ij}\,, \tag{10}$$

where $T$ is the temperature, $T_0$ is a reference temperature for the undeformed state, and $\alpha$ is the linear thermal expansion coefficient. The viscous strain tensor is a complicated topic in itself, and a wide range of phenomenological and heuristic parametric models for the viscous strain rate exist (e.g. Bingham, 1922; Carreau, 1972; Glen, 1955; Herschel, 1926; Saramito, 2007). To encompass this generality, we formulate the viscous strain rate as

$$\frac{\partial \varepsilon_{ij}^{V}}{\partial t} = \Gamma_N\{s_{ij}\}, \tag{11}$$

where $\Gamma_N\{\cdot\}$ is a nonlinear operator acting on the deviatoric stress $s_{ij} = \sigma_{ij} - \sigma_{kk}/3$. The chosen parametric form of $\Gamma_N\{\cdot\}$ determines how induced stress relaxes in the medium, and both Newtonian and non-Newtonian behavior can be incorporated in this formulation.

Following Mellon (1997), we assume $\sigma = \sigma_{11} = \sigma_{22}$ and $\partial\varepsilon_{11}/\partial t = \partial\varepsilon_{22}/\partial t = 0$. We assume that Poisson's ratio, $\nu = \nu(T)$, Young's modulus, $E = E(T)$, and the coefficient of linear thermal expansion, $\alpha = \alpha(T)$ are all temperature dependent, and thus, implicitly time dependent since $T = T(z,t)$ is the temperature at depth $z$ and time $t$. By direct evaluation of $\partial\varepsilon_{ij}/\partial t$ and collecting terms, we find that the temporal dynamics of horizontal stress $\sigma(z,t)$ in a Maxwellian viscoelastic solid driven

https://doi.org/10.5194/tc-2021-329
Preprint. Discussion started: 25 October 2021


The Cryosphere Discussions

by thermal expansion and contraction is governed by the following first-order nonlinear and nonhomogeneous differential equation

$$\frac{\partial \sigma}{\partial t} + \beta(t)\sigma + \Gamma\{\sigma\} = \kappa(t). \quad (12)$$

The time-dependent coefficients are found to be

$$\beta(t) = -\left(\frac{1}{E}\frac{\partial E}{\partial T} + \frac{1}{1-\nu}\frac{\partial \nu}{\partial T}\right)\frac{\partial T}{\partial t}, \quad (13)$$

$$\kappa(t) = -\frac{E}{1-\nu}\left[\alpha + \frac{\partial \alpha}{\partial T}(T - T_0)\right]\frac{\partial T}{\partial t}, \quad (14)$$

and $\Gamma\{\cdot\} = \frac{E}{1-\nu}\,\Gamma_N\{\cdot\}$. The scientific literature devoted to the rheology of frozen materials favor power-law parametrizations for the viscous term (e.g., Schulson and Duval, 2009). In this paper, we apply the heuristic temperature dependent power-law proposed by Glen (1955) in the form used by Mellon (1997) and Maloof et al. (2002):

$$\Gamma\{\sigma\} = \frac{E}{1-\nu} A_0 \left|\frac{\sigma}{2}\right|^n \mathrm{sign}(\sigma)\exp(-Q/RT). \quad (15)$$

In Glen's flow law, $R$ is the universal gas constant, and $A_0$, $Q$, and $n$ are empirical parameters that need to be chosen. The temperature-dependent Arrhenius exponential term in this particular choice of $\Gamma\{\cdot\}$ is included to model the increasing ductility as the temperature increases (e.g. Glen, 1955). To sum up, the first two terms on the left-hand side in Eq. (12) are connected to the elastic response of the solid, the third term models viscous relaxation, and the right-hand side is the thermal driving term. In order to solve Eq. (12) for $\sigma(z,t)$, we specify the initial condition $\sigma_0(z) = \sigma(z, t = 0) = 0$.

If we assume $\partial\nu/\partial T = 0$, Eq. (12) reduces to the model proposed by Mellon (1997). By contrast, if we assume $\partial\nu/\partial T = \partial E/\partial T = \partial\alpha/\partial T = 0$, Eq. (12) reduces to the model proposed by Podolskiy et al. (2019). Finally, if we assume $\partial\nu/\partial T = \partial E/\partial T = \partial\alpha/\partial T = A_0 = 0$, Eq. (12) reduces to the Timoshenko and Goodier (1951) model for thermal stress as applied by Okkonen et al. (2020), excluding the boundary correction terms that represent compressive stresses at the free surfaces of the finite thickness plate assumed by the latter authors.

We solved Eq. (12) numerically using the standard Matlab solver ode45, based on the well-known fifth-order Runge-Kutta method (Dormand and Prince, 1980). Notably, most previous studies of subsurface thermal stress have relied on thermal conduction models in order to infer subsurface temperature variation from measurements of air temperature. A significant novelty of this study is that the ground temperature profile, $T(z,t)$, at Janssonhaugen has been logged by a series of thermistors installed in the 15 m deep P11 borehole at 6 hr intervals since April 1999. We assume the stress at a given depth is decoupled from the stress at adjacent depths (Mellon, 1997) and solve Eq. (12) for the temperature timeseries at the selected depth of investigation. The set of physical parameters that we assume is described in Table 1.

https://doi.org/10.5194/tc-2021-329
Preprint. Discussion started: 25 October 2021


The Cryosphere Discussions

**Table 1 - Physical parameters used in thermal stress model**

| Parameter | Symbol, Unit | Value or Equation | Note or reference |
|---|---|---|---|
| $T$ at zero stress state | $T_0, °C$ | 0 | Initial reference temperature |
| Poisson's ratio | $\nu, -$ | $\begin{cases} 0.3 & T \geq 0 \\ 0.008T + 0.3 & -10 \leq T < 0 \\ 0.00067T + 0.23 & T < -10 \end{cases}$ | Generalized from Hu et al. (2013) alluvium, Istomin and Nazarov (2019) and Zhankui et al. (1998) |
| Young's modulus | $E, GPa$ | $\begin{cases} 0.7 & T \geq 0 \\ -0.73T + 0.7 & -10 \leq T < 0 \\ -0.047T + 7.5 & T < -10 \end{cases}$ | Generalized from Draebing and Krautblatter (2012); Timur (1968); Weeks and Assur (1967); Wu et al. (2017) small-strain dynamic elastic modulus of ice, permafrost and frozen rock measured by seismic waves |
| Linear thermal expansion coefficient | $\alpha, °C^{-1}$ | $\begin{cases} 10^{-6}\begin{pmatrix} -0.000237T^3 \\ +0.00885T^2 \\ -0.1852T + 52.52 \end{pmatrix} & T \leq 0 \\ 10^{-6}\begin{pmatrix} -0.0621T^2 \\ +5.78T - 22.3 \end{pmatrix} & T > 0 \end{cases}$ | Butkovich (1959) gives 3rd order polynomial for ice and a 2nd order polynomial was fitted to Kell (1967) water thermal expansion data |
| Viscous pre-factor | $A_0, s^{-1}Pa^{-n}$ | $1 \times 10^{-9}$ | Glen's non-Newtonian power law viscous flow (Behn et al., 2021; Glen, 1955; Weertman, 1983) |
| Viscous activation energy | $Q, J\ mol^{-1}$ | $1.34 \times 10^5$ | |
| Viscous exponent | $n, -$ | 3.2 | |
| Gas constant | $R, J\ mol^{-1}K^{-1}$ | 8.314 | $T$ converted to Kelvin when evaluating $RT$ |
| Tensile strength | $\sigma_T, MPa$ | 1.0 (range from 0.8-1.3 given in reference) | Currier and Schulson (1982), varies according to grain size for randomly oriented polycrystalline ice (finer grained ice stronger). |

### 3.3.1 Fracture model

We apply a simplistic model of fracturing by considering the modelled thermal stress as the potential stress. When the potential stress exceeds the tensile strength of the ground (see Table 1), a frost quake is assumed to occur and dissipate stress corresponding to 100% of the tensile strength. We keep a tally of the number of frost quakes over time and assume that multiple frost quakes occur if the tensile strength is exceeded by an integer factor greater than one. In reality, a fraction of the stress would be redistributed elastically rather than completely lost to friction as in this simple model. Since ground temperature is a measured quantity, we do not account for warming by frictional heat as a result of frost quake movement. Our aim is to model simple thermal tensional cracking of existing ice wedges or segregated ice bodies and not the initiation or propagation of new cracks into previously undamaged soil/bedrock, where pore scale fluid migration and stress localisation at crack tips become important (e.g. Walder and Hallet, 1985).

https://doi.org/10.5194/tc-2021-329
Preprint. Discussion started: 25 October 2021


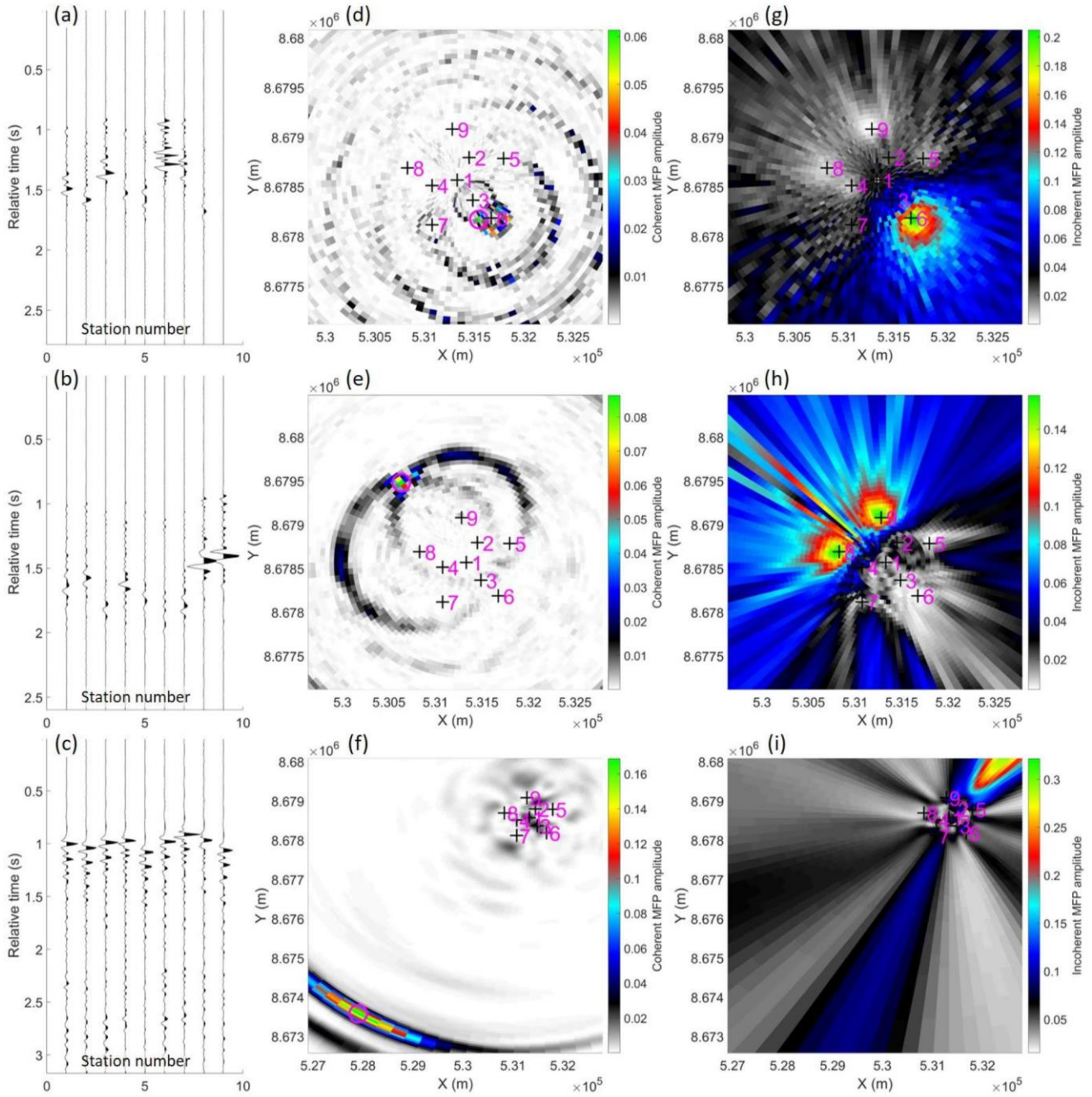


**Figure 4 – (a), (b) Examples of Class I events with significant amplitude variation across the array and relatively close source position inferred by (d), (e) coherent MFP. (c) Example of a Class II event with little amplitude variation across the array and a more distal (f) coherent MFP inferred source position. (g), (h) & (i) show corresponding incoherent MFP results, Eq. (4), demonstrating the improvement gained by coherent MFP. Station numbers in (a), (b) & (c) correspond to the labels annotated on the MFP panels where the seismometer locations are marked with black crosses.**

https://doi.org/10.5194/tc-2021-329
Preprint. Discussion started: 25 October 2021


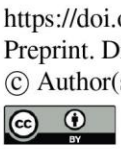

The Cryosphere Discussions
Open Access
EGU

## 4 Results and discussion

A total of 137,532 short duration seismic events were detected by our STA/LTA detector between July 2004 and June 2021. In order to improve the precision of the source localisation by coherent MFP, only events recorded by at least five seismometers were located for a total of 137,456 located short duration events. The estimated source locations were subsequently used to identify subclasses of events, as detailed in the following section.

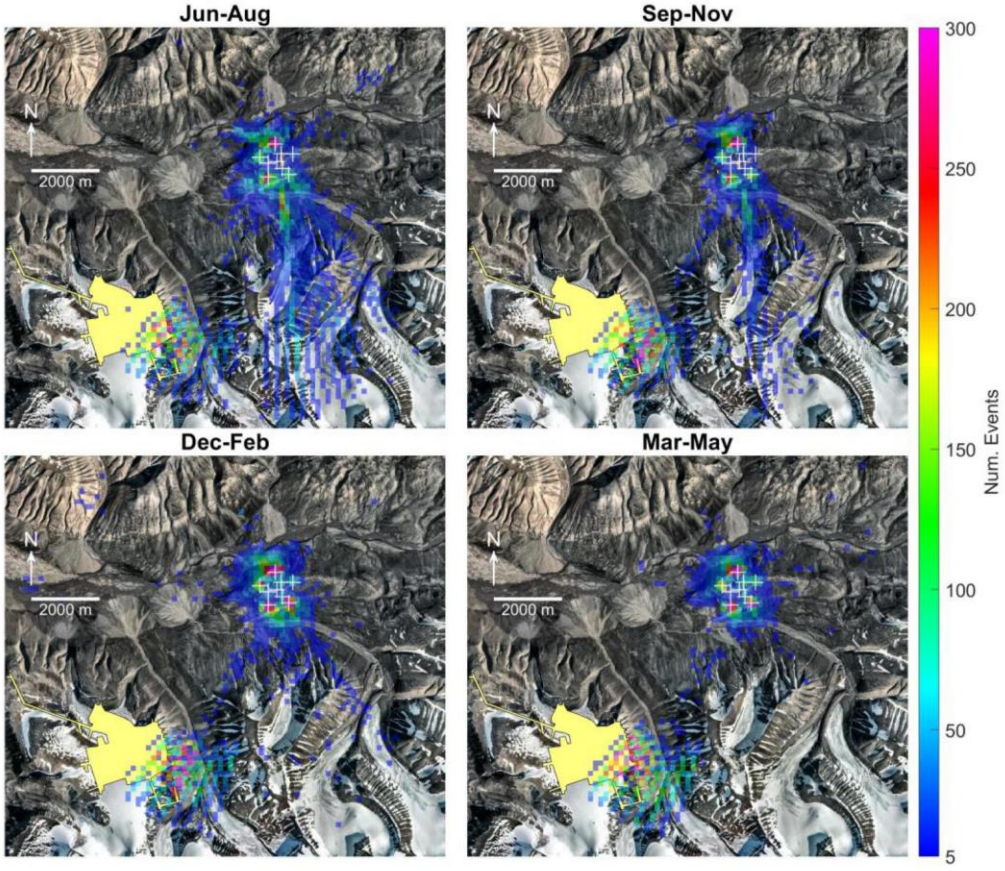


**Figure 5 – Spatially binned (150×150 m) distribution of coherent MFP inferred seismic source positions plotted by season for events recorded between August 2004 and July 2021. Positions of SPITS seismometers are indicated by white crosses. The distal event cluster corresponds with the location of underground mining operations at Gruve 7 (yellow polygon). Orthophoto © Norwegian Polar Institute (npolar.no).**

### 4.1 Subclasses of short duration seismic events

We find that there are two main sub-classes of short duration events recorded by the SPITS array. Event class I is characterised by significant amplitude variation and arrival time differences across the array seismometers, as illustrated in Figure 4a,b. Using coherent MFP to infer the source positions of these events, shows that they occur in relatively close proximity, within about 1500 m of the centroid of the array (Figure 4d,e). By contrast, Event class II is characterised by similar amplitudes across the array elements and smaller relative arrival time differences, as illustrated in (Figure 4c). Using coherent MFP, we find not

https://doi.org/10.5194/tc-2021-329
Preprint. Discussion started: 25 October 2021


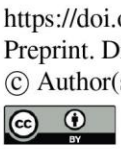

The Cryosphere Discussions

only are these events associated with more distant sources (Figure 4f), they also have a consistent azimuth. Figure 4 also illustrates the property that coherent MFP decreases source localisation ambiguity for arrays that coarsely sample the spatial domain when compared to the incoherent scheme (Michalopoulou, 1998). In Figure 4i, we see that incoherent averaging (Eq. 4) has enhanced a sidelobe and produced an incorrect source position that is not consistent with the relative arrival times observed in Figure 4c.

The mean MFP inferred propagation velocities for Class I events was 1150 m/s with a standard deviation of 1100 m/s, indicating that they are dominated by surface waves. The large standard deviation may indicate the surface waves are dispersive with different frequencies propagating at different phase velocities. By contrast, the mean MFP inferred propagation velocity for Class II events was 5750 m/s with a standard deviation of 400 m/s, indicating that this event class is dominated by P-wave energy.

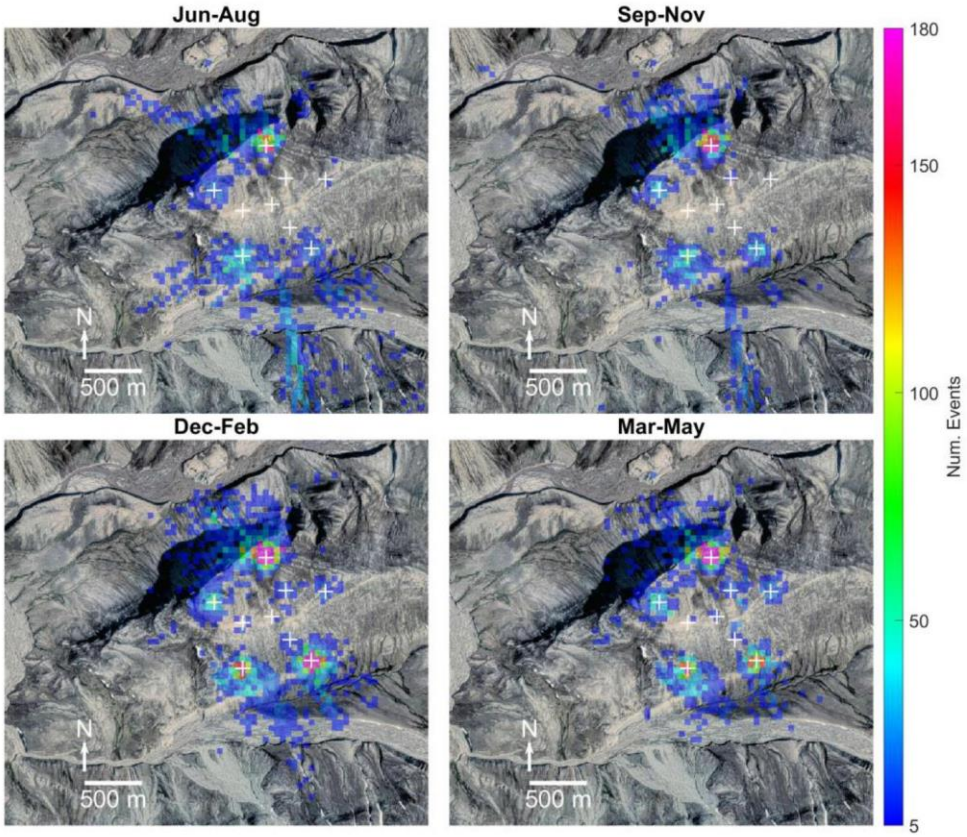


**Figure 6 – Detail view of Janssonhaugen overlaid with spatially binned (50×50 m) distribution of coherent MFP inferred seismic source positions plotted by season for events recorded between August 2004 and July 2021. Positions of SPITS seismometers are indicated by white crosses. Orthophoto © Norwegian Polar Institute (npolar.no).**

Mapping the inferred source positions, as in Figure 5, it is clear that Class II events are spatially coincident with the underground mining areas of Gruve 7. Furthermore, we observe that Class II events occur frequently during all seasons (see

https://doi.org/10.5194/tc-2021-329
Preprint. Discussion started: 25 October 2021




The Cryosphere Discussions
Open Access
EGU

310 Figure 5). We infer that Event class II is a result of mining operations and human activity in the underground coal mine, Gruve 7. These events are essentially unwanted noise from the environmental seismology perspective, although they do give a useful indication of the localisation performance of the coherent MFP algorithm as applied in this study.

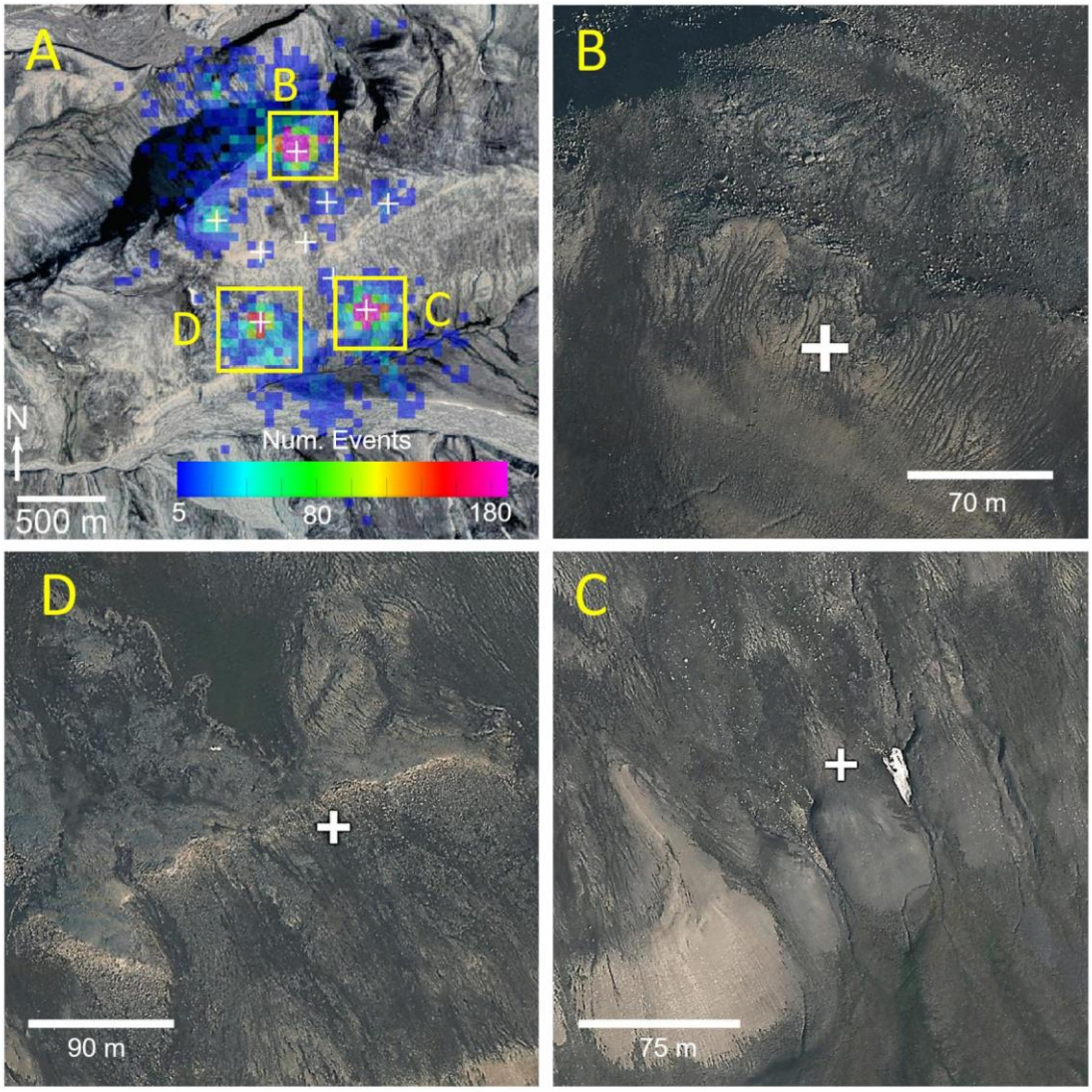


315 **Figure 7 – (a) Dec-Feb events as plotted in Figure 6 with orthophotograph details illustrating the geomorphologic features associated with the most seismically active areas i.e. boulder producing scarps (b), (d) and solifluction lobes (b), (c). Orthophoto © Norwegian Polar Institute (npolar.no).**

We observe a distinct seasonality for Class I events, with the highest detection rates occurring in the winter months (Dec-Feb) as illustrated in Figure 6. Detection rates are also high during the cold high-Arctic spring (Mar-May) and are lowest during the summer (Jun-August). We also observe a cluster of events due south of SPITS, with highest activity in the summer months, 320 decreasing in the autumn (Sep-Nov) and absent during the winter and spring. These events may be rockfalls related to fluvial

https://doi.org/10.5194/tc-2021-329
Preprint. Discussion started: 25 October 2021




undercutting of steep river cliffs, rockfalls from steep mountain flanks or glacier/rock glacier movements. Using InSAR, Rouyet et al. (2019) measured high summer subsidence rates in the river valley, glacier/rock glacier and mountain flank areas south of Janssonhaugen corresponding to the inferred source locations of these seismic events. However, since the dynamics of these processes are not represented by our model, we were careful to exclude these events when spatially isolating Class I events. By selecting the subset of events with inferred source positions within ~1500 m of the array centroid and excluding the cluster of summer-autumn events due south of the array, we isolated a total of 42,432 class I events recorded between July 2004 and July 2021. Class I events occur most frequently during the cold winter and spring seasons, suggesting a relation to freezing processes.

Locally, the Class I seismicity is dominated by three source areas (see Figure 7) corresponding to areas with boulder producing scarps and solifluction lobes. These areas may be associated with enhanced ground heat loss, thin or absent snow cover or elevated ground moisture/ice content (e.g. Abolt et al., 2018; Matsuoka, 2008), though we lack the field observations necessary to support this explanation for the anomalous seismicity of these areas. The boulder producing scarps, particularly the one on the northern side of the array (Figure 6), in addition to the steep NW flank of Janssonhaugen, were also active during the summer thaw season. These thaw season events may be rockfalls due to melting of ice causing loss of strength or joint lubrication (Matsuoka, 2019; Weber et al., 2017).

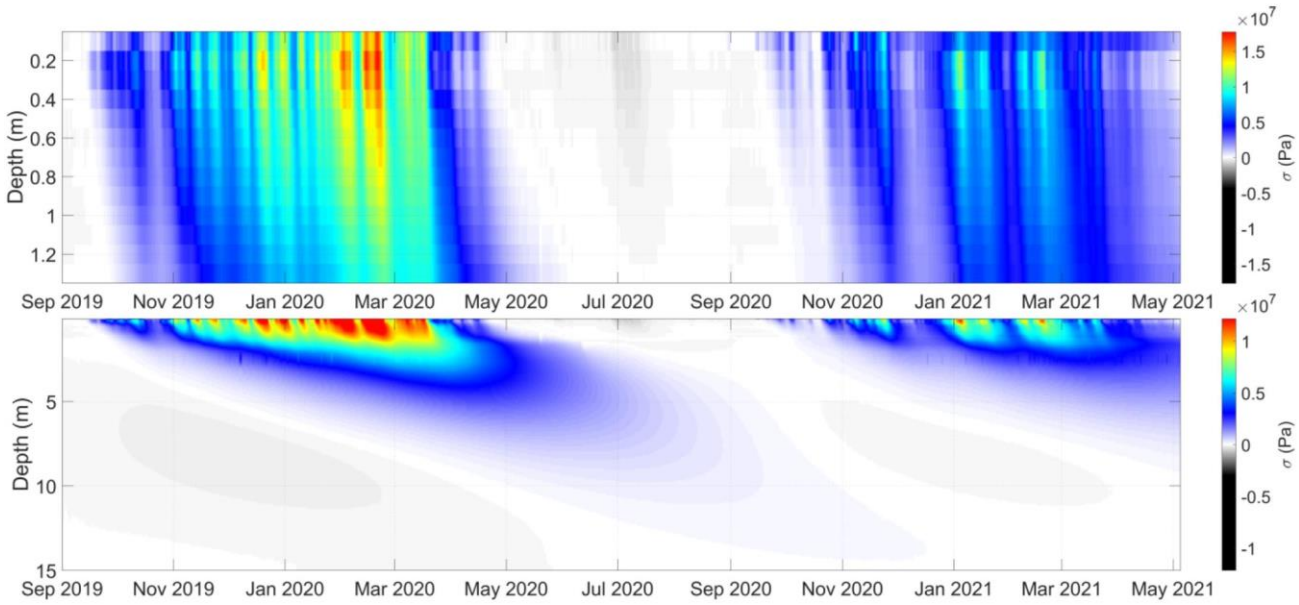


**Figure 8 – Illustration of spatiotemporal thermal stress field modelled according to Eq. (12) and constrained by temperature measurements recorded by sensors installed at Janssonhaugen Vest (0.1 m) and in the P11 borehole (0.2-15 m).**

https://doi.org/10.5194/tc-2021-329
Preprint. Discussion started: 25 October 2021




340 **4.2 Modelled thermal stress**

Figure 8 illustrates the spatiotemporal thermal stress field that was modelled by solving Eq. (12) using the parameters listed in Table 1 and a combination of the 0.1 m ground temperature timeseries recorded at the Janssonhaugen Vest meteorological station and the 0.2-15 m temperatures recorded in the P11 borehole. The largest thermal stresses occur in the active layer, which is subject to large amplitude winter cooling cycles. Since the peak annual stresses occur at 0.2 m depth and we have a 345 much longer record from the P11 borehole compared to the Janssonhaugen Vest meteorological station, we focus on this horizon as the dominant frost cracking depth throughout the rest of the study. That peak thermal stress is modelled at 0.2 m is interesting as it corresponds with the 20-30cm thick regolith layer at Janssonhaugen (Isaksen et al., 2001), suggesting that in-situ frost cracking may have weathered the bedrock to produce the surficial layer. Frost polygons in this region are interpreted to be very old (Sørbel and Tolgensbakk, 2002) so there has likely been sufficient time to reach a steady state condition. If frost 350 cracking extended much deeper, we would expect that repeated cracking over thousands of years would have produced a thicker regolith layer than that which is observed.

**4.3 Thermal stress associated with seismic events**

Figure 9 illustrates the shallowest measured temperature profiles and corresponding thermal stress for the Sep 2019 to Jun 2021 period. The Class II events, corresponding to mining activities at Gruve 7, have source ranges of 6000-7000 m with a 355 consistent azimuth of ~210° and no correspondence with thermal stress. On the other hand, Class I events have variable azimuths but source ranges <1500 m and tend to be associated with peaks in thermal stress.

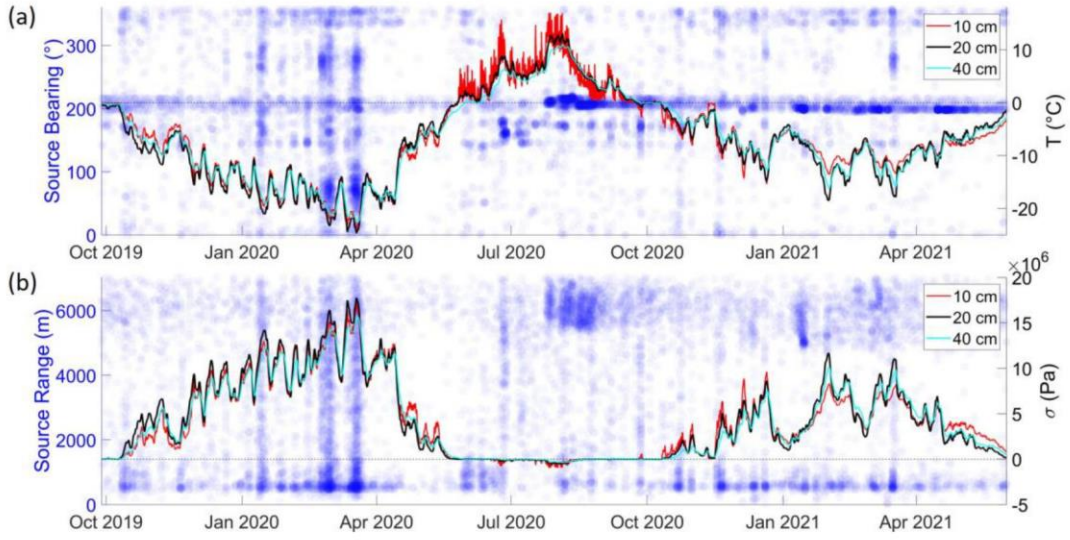


**Figure 9 – (a) Ground temperature profiles (solid lines) and bearing (clockwise from North) to coherent MFP localised source** 360 **positions from centre of SPITS array (blue circles). (b) modelled ground thermal stress from Eq. (12) (solid lines) and ranges to**

https://doi.org/10.5194/tc-2021-329
Preprint. Discussion started: 25 October 2021


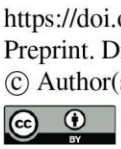



**coherent MFP localised sources (blue circles). Source ranges and azimuths are transparent such that denser colours represent clusters of events.**

Figure 10 shows a detailed comparison of the Class I seismicity and the modelled frequency of tensile fracturing due to thermal stresses exceeding the assumed tensile strength of the medium (as described in Section 3.3.1). Given that seismicity is a complex, stochastic process in time and space, our simple thermal stress-based fracture model does a reasonably good job of capturing the time periods and approximate frequency of the Class I events. This leads us to infer that thermal contraction cracking of segregated ice bodies, as modelled by Eq. (12) is a significant process contributing to event Class I seismicity. The clusters of events recorded June-August, when thermal stress is low (see Figure 6 and Figure 10), are most likely rockfalls on the steep boulder producing scarps (see Figure 7) initiated by melting of fracture-filling ice leading to loss of strength or joint lubrication (Matsuoka, 2019; Weber et al., 2017).

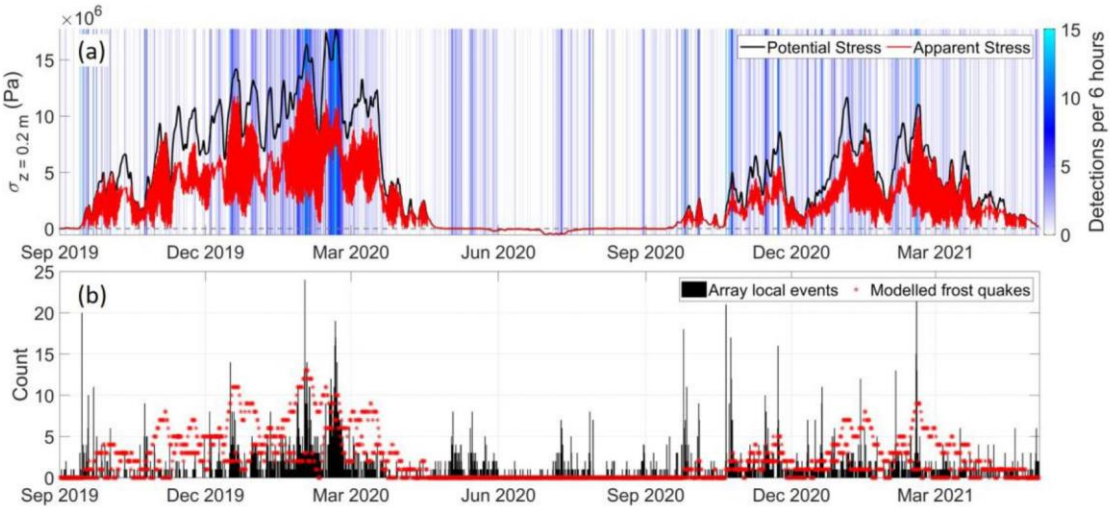


**Figure 10 – (a) Potential thermal stress (black) given by the solution to Eq. (12) and apparent thermal stress accounting for stress release by frost cracking (red) with blue colour gradient indicating the detection rate of Class I events. (b) modelled number of frost quakes (red) and frequency histogram of Class I events (black).**

A similar association between Class I events and peaks in thermal stress persists over the entire study period, from 2004-2021 (see Figure 11). Figure 12 shows that the modelled and observed frost quake seismicity also matches quite well over the study period (the normalised cross correlation is 0.61), though the observed seismicity has a tendency to occur in more defined periods than predicted by the model, resulting in a relatively spiky frequency histogram. Examples of anomalous seismicity not explained by the model are the periods 17-26 Feb 2010, 7-16 Feb, 2012 and 8-17 Jan 2016 (see Figure 12). While these periods of enhanced seismicity are still associated with peaks in thermal stress, our simple model is unable to explain the intensity of seismicity in these periods relative to, e.g., earlier periods in the same seasons with similar thermal stress but fewer Class I events (see Figure 11). There are likely multiple factors for this deviation, including the inherently stochastic nature of seismicity. However, there are likely also systematic factors that are simply not accounted for in our model like the spatial redistribution of stress between multiple fractures and across multiple depths. In addition, the mild temperatures preceding

https://doi.org/10.5194/tc-2021-329
Preprint. Discussion started: 25 October 2021


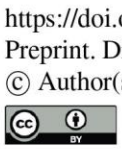



these episodes of enhanced seismicity (seen as pronounced drops in stress in Figure 11) may have produced unfrozen water and conditions favourable for the formation of new ice lenses (Hallet et al., 1991; Murton et al., 2006; Peppin and Style, 2013; Walder and Hallet, 1985). That is, there are other processes that can drive frost cracking in addition to the thermal contraction cracking of segregated ice bodies and ice wedges that is favoured by our model. We speculate that the inability of the thermal contraction model to explain the anomalously high levels of seismicity in the periods 17-26 Feb 2010, 7-16 Feb, 2012 and 8-17 Jan 2016 provides evidence that capillary and frozen-fringe effects are also important (Peppin and Style, 2013).

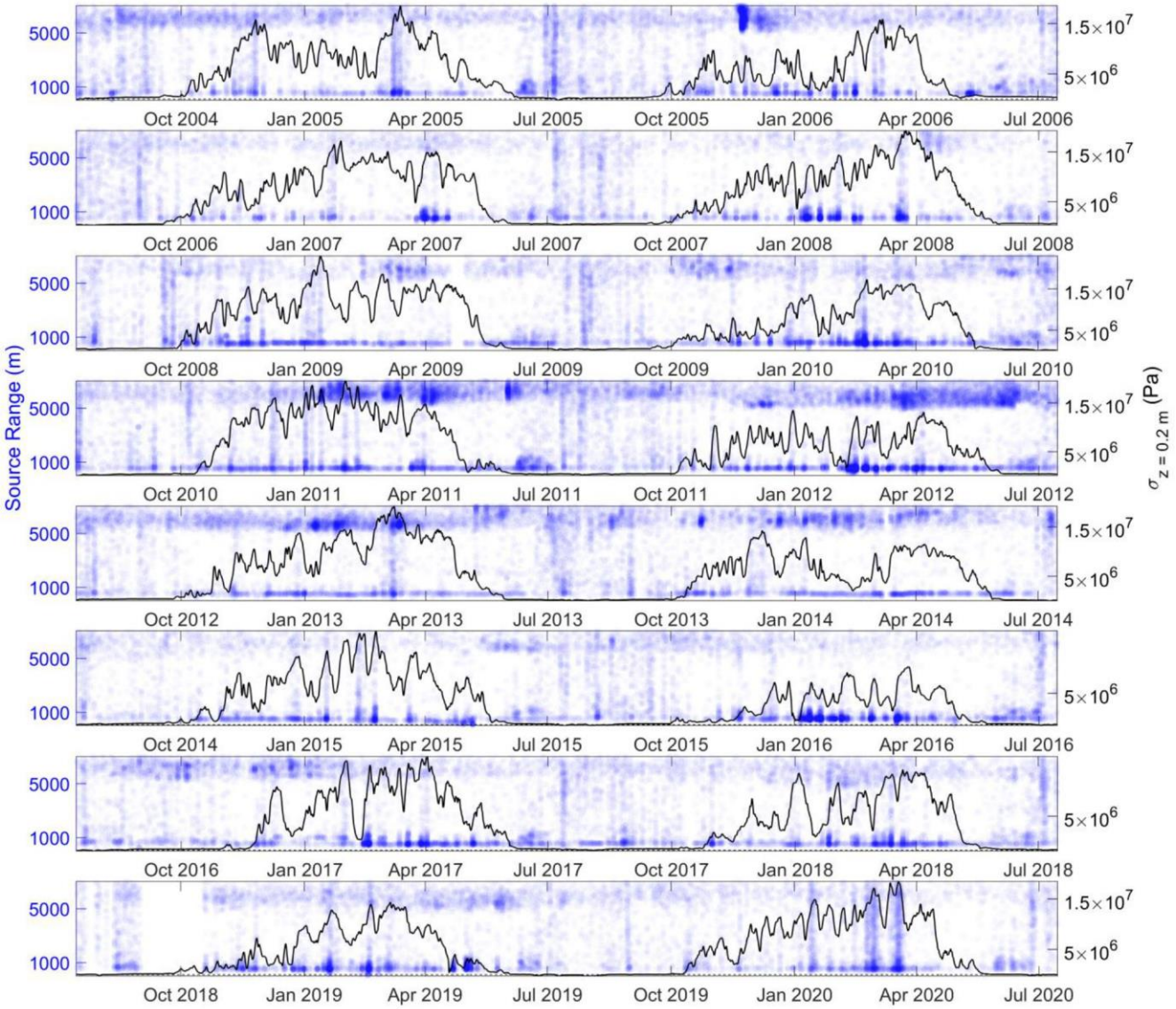


**Figure 11 – Modelled thermal stress from Eq. (12) at 0.2 m depth (black lines) and ranges to coherent MFP localised sources (blue circles). Source ranges and azimuths are plotted as transparent points such that denser colours represent clusters of events. Event class I & II are associated with small (<1500 m) and large (>5000 m) source ranges, respectively.**

https://doi.org/10.5194/tc-2021-329
Preprint. Discussion started: 25 October 2021


The Cryosphere Discussions

395 We consider the use of real ground temperature measurements a strength of this study, since the subsurface temperature field is a complex product of sensible, latent and convective heat fluxes, depending on matrix and pore-filling material properties as well as surface properties like the thermal conductivity of snow (e.g. Badache et al., 2016; Rankinen et al., 2004). However, it is important to recognize that the P11 borehole and Janssonhaugen Vest ground temperature measurements are point samples of a temperature field that may vary spatially according to local geomorphology and variation in snow cover. For example, 400 Abolt et al. (2018) have demonstrated that ground under the elevated rims of frost polygons cools significantly faster than the depressed centres due to decreased snow cover. Accounting for variation on the local scale fell outside the scope of the present study, but extending the model framework to allow stochastic temperature variation via stochastic differential equations may give additional insight into the significance of local scale variability.

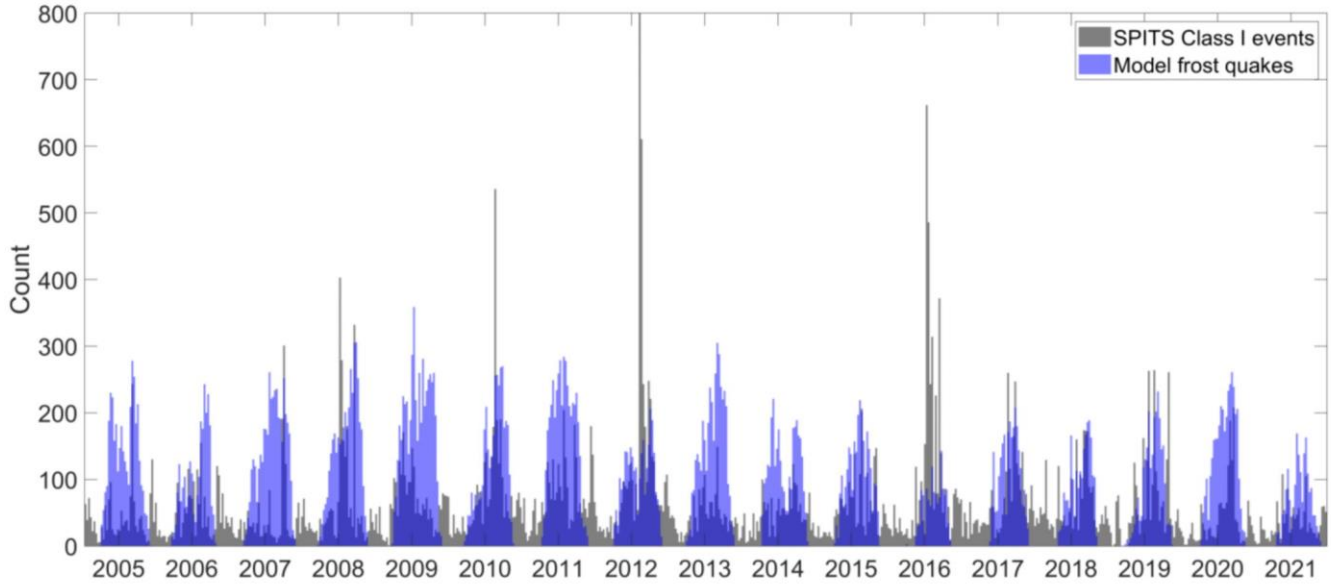


405 **Figure 12 – Histogram binned to 9-day intervals comparing the modelled frost quake frequency (blue) with the recorded frequency of Class I events (black).**

## 5 Conclusion

We studied the spatial and temporal patterns of the class of seismicity that lead to short duration ground shaking at the SPITS 410 array in Adventdalen, based on a catalogue of >100 000 events recorded between 2004 and 2021. To the best of our knowledge, this is a uniquely large and long spanning event catalogue amongst studies with a focus on cryoseisms. We find that these short duration seismic events, with ground motion lasting just a few seconds, can be grouped into two main subclasses. One class is clearly associated with mining activities at the underground coal mine, Gruve 7 and is mostly useful as an indicator of the performance of the coherent-MFP source localisation algorithm. The other subclass of short duration seismic events is 415 interpreted to be dominated by frost quakes produced by thermal contraction cracking of ice wedges or other sub-surface

https://doi.org/10.5194/tc-2021-329
Preprint. Discussion started: 25 October 2021


segregated ice bodies. These events appear to be dominated by surface wave energy and source positions that are proximal to the SPITS array, particularly three areas that are associated with dynamic geomorphological features; boulder producing scarps and solifluction lobes. Temporally these events are associated with peaks in ground thermal stress as modelled by a simple dynamical thermo-viscoelastic model constrained by borehole measurements of ground temperature. The long term continuous observational record, containing tens of thousands of inferred cryoseismic events, in proximity to high-quality borehole temperature observations, provides a unique insight into the spatiotemporal patterns of cryoseismicity.

## 6 Acknowledgments

This research is funded by the University of Tromsø - The Arctic University of Norway, by the ARCEx partners and by the Research Council of Norway through grant number 228107. The publication charges for this article have been funded by a grant from the publication fund of UiT The Arctic University of Norway.

## 7 References

Abolt, C. J., Young, M. H., Atchley, A. L., and Harp, D. R.: Microtopographic control on the ground thermal regime in ice wedge polygons, The Cryosphere, 12, 1957-1968, 2018.

Albaric, J., Kühn, D., Ohrnberger, M., Langet, N., Harris, D., Polom, U., Lecomte, I., and Hillers, G.: Seismic monitoring of permafrost in Svalbard, Arctic Norway, Seismological Society of America, 92, 2891-2904, 2021.

Badache, M., Eslami-Nejad, P., Ouzzane, M., Aidoun, Z., and Lamarche, L.: A new modeling approach for improved ground temperature profile determination, Renewable Energy, 85, 436-444, 2016.

Barosh, P. J.: Frostquakes in New England, Engineering Geology, 56, 389-394, 2000.

Battaglia, S. M., Changnon, D., Changnon, D., and Hall, D.: Frost quake events and changing wintertime air mass frequencies in southeastern Canada, Working Paper, Northern Illinois University. doi: 10.13140/RG. 2.2. 22351.48803, 2016.

Behn, M. D., Goldsby, D. L., and Hirth, G.: The role of grain size evolution in the rheology of ice: implications for reconciling laboratory creep data and the Glen flow law, The Cryosphere, 15, 4589-4605, 2021.

Bingham, E. C.: Fluidity and plasticity, McGraw-Hill, 1922.

Black, R. F.: Periglacial features indicative of permafrost: ice and soil wedges, Quaternary Research, 6, 3-26, 1976.

Butkovich, T.: Thermal expansion of ice, Journal of Applied Physics, 30, 350-353, 1959.

Cable, S., Elberling, B., and Kroon, A.: Holocene permafrost history and cryostratigraphy in the High-Arctic Adventdalen Valley, central Svalbard, Boreas, 47, 423-442, 2018.

Carreau, P. J.: Rheological equations from molecular network theories, Transactions of the Society of Rheology, 16, 99-127, 1972.

https://doi.org/10.5194/tc-2021-329
Preprint. Discussion started: 25 October 2021


445 Chen, J., Wu, Y., O'Connor, M., Cardenas, M. B., Schaefer, K., Michaelides, R., and Kling, G.: Active layer freeze-thaw and water storage dynamics in permafrost environments inferred from InSAR, Remote Sensing of Environment, 248, 112007, 2020.

Chmiel, M., Roux, P., and Bardainne, T.: Extraction of phase and group velocities from ambient surface noise in a patch-array configuration, Geophysics, 81, KS231-KS240, 2016.

450 Christiansen, H. H., Gilbert, G., Demidov, N., Guglielmin, M., Isaksen, K., Osuch, M., and Boike, J.: Permafrost temperatures and active layer thickness in Svalbard during 2017/2018 (PermaSval), SESS Report 2019-The State of Environmental Science in Svalbard, 2020. 2020.

Christiansen, H. H., Matsuoka, N., and Watanabe, T.: Progress in understanding the dynamics, internal structure and palaeoenvironmental potential of ice wedges and sand wedges, Permafrost and Periglacial Processes, 27, 365-376, 2016.

455 Cros, E., Roux, P., Vandemeulebrouck, J., and Kedar, S.: Locating hydrothermal acoustic sources at Old Faithful Geyser using matched field processing, Geophysical Journal International, 187, 385-393, 2011.

Currier, J. and Schulson, E.: The tensile strength of ice as a function of grain size, Acta Metallurgica, 30, 1511-1514, 1982.

DiMillio, A. F.: A quarter century of geotechnical research, Turner-Fairbank Highway Research Center, 1999.

Dormand, J. R. and Prince, P. J.: A family of embedded Runge-Kutta formulae, Journal of computational and applied

460 mathematics, 6, 19-26, 1980.

Draebing, D. and Krautblatter, M.: P-wave velocity changes in freezing hard low-porosity rocks: a laboratory-based time-average model, The Cryosphere, 6, 1163-1174, 2012.

Dypvik, H., Nagy, J., Eikeland, T., Backer-Owe, K., and Johansen, H.: Depositional conditions of the Bathonian to Hauterivian Janusfjellet subgroup, Spitsbergen, Sedimentary Geology, 72, 55-78, 1991.

465 French, H. M.: The periglacial environment, John Wiley & Sons, 2017.

Gibbons, S. J. and Ringdal, F.: The detection of low magnitude seismic events using array-based waveform correlation, Geophysical Journal International, 165, 149-166, 2006.

Gibbons, S. J., Schweitzer, J., Ringdal, F., Kværna, T., Mykkeltveit, S., and Paulsen, B.: Improvements to seismic monitoring of the European Arctic using three-component array processing at SPITS, Bulletin of the Seismological Society of America,

470 101, 2737-2754, 2011.

Glen, J. W.: The creep of polycrystalline ice, Proceedings of the Royal Society of London. Series A. Mathematical and Physical Sciences, 228, 519-538, 1955.

Hales, T. and Roering, J.: A frost "buzzsaw" mechanism for erosion of the eastern Southern Alps, New Zealand, Geomorphology, 107, 241-253, 2009.

475 Hales, T. and Roering, J. J.: Climatic controls on frost cracking and implications for the evolution of bedrock landscapes, Journal of Geophysical Research: Earth Surface, 112, 2007.

Hallet, B., Walder, J., and Stubbs, C.: Weathering by segregation ice growth in microcracks at sustained subzero temperatures: Verification from an experimental study using acoustic emissions, Permafrost and Periglacial Processes, 2, 283-300, 1991.

https://doi.org/10.5194/tc-2021-329
Preprint. Discussion started: 25 October 2021


Hanssen, R. F.: Radar interferometry: data interpretation and error analysis, Springer Science & Business Media, 2001.

Harley, J. B. and Moura, J. M.: Data-driven matched field processing for Lamb wave structural health monitoring, The Journal of the Acoustical Society of America, 135, 1231-1244, 2014.

Herschel, W.: Measurement of consistency of rubber-benzene solutions, Kolloid-zeitschrift, 39, 291-298, 1926.

Hu, X.-d., Wang, J.-t., and Yu, R.-z.: Uniaxial compressive and splitting tensile tests of artificially frozen soils in tunnel construction of Hong Kong, Journal of Shanghai Jiaotong University (Science), 18, 688-692, 2013.

Isaksen, K., Holmlund, P., Sollid, J. L., and Harris, C.: Three deep alpine-permafrost boreholes in Svalbard and Scandinavia, Permafrost and Periglacial Processes, 12, 13-25, 2001.

Isaksen, K., Mühll, D. V., Gubler, H., Kohl, T., and Sollid, J. L.: Ground surface-temperature reconstruction based on data from a deep borehole in permafrost at Janssonhaugen, Svalbard, Ann Glaciol, 31, 287-294, 2000.

Istomin, A. and Nazarov, T.: Numerical studies of reinforced concrete pile foundations on permafrost soils at low climatic temperatures, 2019, 012082.

Kell, G.: Precise representation of volume properties of water at one atmosphere, Journal of Chemical and Engineering data, 12, 66-69, 1967.

Köhler, A., Nuth, C., Schweitzer, J., Weidle, C., and Gibbons, S. J.: Regional passive seismic monitoring reveals dynamic glacier activity on Spitsbergen, Svalbard, Polar Research, 34, 26178, 2015.

Lachenbruch, A. H.: Mechanics of thermal contraction cracks and ice-wedge polygons in permafrost, Geological Society of America, 1962.

Lacroix, A. V.: A short note on cryoseisms, Earthquake Notes, 51, 15-21, 1980.

Landau, L. and Lifshitz, E.: Theory of Elasticity, 2nd Edition. Pergamon Press, Oxford, 1970.

Leung, A. C., Gough, W. A., and Shi, Y.: Identifying frostquakes in Central Canada and neighbouring regions in the United States with social media. In: Citizen Empowered Mapping, Springer, 2017.

Liu, L., Rouyet, L., Strozzi, T., Lauknes, T. R., and Christiansen, H. H.: Seasonal Thaw Settlement and Frost Heave in Permafrost Regions in the Arctic: A Synthesis of InSAR Observations Using Sentinel-1 SAR Images, 2018, GC31B-05.

Mackay, J. R.: The direction of ice-wedge cracking in permafrost: downward or upward?, Canadian Journal of Earth Sciences, 21, 516-524, 1984.

Maloof, A. C., Kellogg, J. B., and Anders, A. M.: Neoproterozoic sand wedges: crack formation in frozen soils under diurnal forcing during a snowball Earth, Earth and Planetary Science Letters, 204, 1-15, 2002.

Matsuoka, N.: Frost weathering and rockwall erosion in the southeastern Swiss Alps: Long-term (1994–2006) observations, Geomorphology, 99, 353-368, 2008.

Matsuoka, N.: A multi-method monitoring of timing, magnitude and origin of rockfall activity in the Japanese Alps, Geomorphology, 336, 65-76, 2019.

Matsuoka, N.: Solifluction rates, processes and landforms: a global review, Earth-Science Reviews, 55, 107-134, 2001.

https://doi.org/10.5194/tc-2021-329
Preprint. Discussion started: 25 October 2021


Matsuoka, N., Christiansen, H. H., and Watanabe, T.: Ice-wedge polygon dynamics in Svalbard: Lessons from a decade of automated multi-sensor monitoring, Permafrost and Periglacial Processes, 29, 210-227, 2018.

Matsuoka, N., Sawaguchi, S.-i., and Yoshikawa, K.: Present-day periglacial environments in central Spitsbergen, Svalbard, Geographical Review of Japan, 77, 276-300, 2004.

Mellon, M. T.: Small-scale polygonal features on Mars: Seasonal thermal contraction cracks in permafrost, Journal of Geophysical Research: Planets, 102, 25617-25628, 1997.

Michalopoulou, Z. H.: Robust multi-tonal matched-field inversion: A coherent approach, The Journal of the Acoustical Society of America, 104, 163-170, 1998.

Murton, J. B., Peterson, R., and Ozouf, J.-C.: Bedrock fracture by ice segregation in cold regions, Science, 314, 1127-1129, 2006.

Nikonov, A.: Frost quakes as a particular class of seismic events: Observations within the East-European platform, Izvestiya, Physics of the Solid Earth, 46, 257-273, 2010.

Okkonen, J., Neupauer, R., Kozlovskaya, E., Afonin, N., Moisio, K., Taewook, K., and Muurinen, E.: Frost Quakes: Crack Formation by Thermal Stress, Journal of Geophysical Research: Earth Surface, 125, e2020JF005616, 2020.

Peppin, S. S. and Style, R. W.: The physics of frost heave and ice-lens growth, Vadose Zone Journal, 12, 2013.

Podolskiy, E. A., Fujita, K., Sunako, S., and Sato, Y.: Viscoelastic Modeling of Nocturnal Thermal Fracturing in a Himalayan Debris-Covered Glacier, Journal of Geophysical Research: Earth Surface, 124, 1485-1515, 2019.

Rabiner, L. R., Schafer, R. W., and Rader, C. M.: The chirp z-transform algorithm and its application, Bell System Technical Journal, 48, 1249-1292, 1969.

Rankinen, K., Karvonen, T., and Butterfield, D.: A simple model for predicting soil temperature in snow-covered and seasonally frozen soil: model description and testing, Hydrology and Earth System Sciences, 8, 706-716, 2004.

Rempel, A. W.: Frost heave, Journal of Glaciology, 56, 1122-1128, 2010.

Romeyn, R., Hanssen, A., Ruud, B. O., Stemland, H. M., and Johansen, T. A.: Passive seismic recording of cryoseisms in Adventdalen, Svalbard, The Cryosphere, 15, 283-302, 2021.

Rosen, P. A., Hensley, S., Joughin, I. R., Li, F. K., Madsen, S. N., Rodriguez, E., and Goldstein, R. M.: Synthetic aperture radar interferometry, Proceedings of the IEEE, 88, 333-382, 2000.

Rouyet, L., Lauknes, T. R., Christiansen, H. H., Strand, S. M., and Larsen, Y.: Seasonal dynamics of a permafrost landscape, Adventdalen, Svalbard, investigated by InSAR, Remote Sensing of Environment, 231, 111236, 2019.

Rouyet, L., Liu, L., Strand, S. M., Christiansen, H. H., Lauknes, T. R., and Larsen, Y.: Seasonal InSAR Displacements Documenting the Active Layer Freeze and Thaw Progression in Central-Western Spitsbergen, Svalbard, Remote Sensing, 13, 2977, 2021.

Saramito, P.: A new constitutive equation for elastoviscoplastic fluid flows, Journal of Non-Newtonian Fluid Mechanics, 145, 1-14, 2007.

Scherler, D.: Climatic limits to headwall retreat in the Khumbu Himalaya, eastern Nepal, Geology, 42, 1019-1022, 2014.

https://doi.org/10.5194/tc-2021-329
Preprint. Discussion started: 25 October 2021


Schulson, E. M. and Duval, P.: Creep and fracture of ice, Cambridge university press, 2009.

Schweitzer, J., Köhler, A., and Christensen, J. M.: Development of the NORSAR Network over the Last 50 Yr, Seismological Society of America, 92, 1501-1511, 2021.

Sergeant, A., Chmiel, M., Lindner, F., Walter, F., Roux, P., Chaput, J., Gimbert, F., and Mordret, A.: On the Green's function emergence from interferometry of seismic wave fields generated in high-melt glaciers: implications for passive imaging and monitoring, The Cryosphere, 14, 1139-1171, 2020.

Sørbel, L. and Tolgensbakk, J.: Ice-wedge polygons and solifluction in the Adventdalen area, Spitsbergen, Svalbard, Norsk Geografisk Tidsskrift-Norwegian Journal of Geography, 56, 62-66, 2002.

Timoshenko, S. and Goodier, J.: Theory of Elasticity, McGraw-Hill book Company, New York, 1951.

Timur, A.: Velocity of compressional waves in porous media at permafrost temperatures, Geophysics, 33, 584-595, 1968.

Trnkoczy, A.: Understanding and parameter setting of STA/LTA trigger algorithm. In: New Manual of Seismological Observatory Practice (NMSOP), Deutsches GeoForschungsZentrum GFZ, 2009.

Wahr, J., Liu, L., and Zhang, T.: InSAR measurements of ground surface deformation due to thaw settlement and frost heave over permafrost on the North Slope of Alaska, 2008, C13B-02.

Walder, J. and Hallet, B.: A theoretical model of the fracture of rock during freezing, Geological Society of America Bulletin, 96, 336-346, 1985.

Walter, F., Roux, P., Roeoesli, C., Lecointre, A., Kilb, D., and Roux, P.-F.: Using glacier seismicity for phase velocity measurements and Green's function retrieval, Geophysical Journal International, 201, 1722-1737, 2015.

Weber, S., Beutel, J., Faillettaz, J., Hasler, A., Krautblatter, M., and Vieli, A.: Quantifying irreversible movement in steep, fractured bedrock permafrost on Matterhorn (CH), The Cryosphere, 11, 567-583, 2017.

Weeks, W. F. and Assur, A.: The Mechanical Properties of Sea Ice, Cold Regions Research & Engineering Laboratory, Hanover, New Hampshire, 1967.

Weertman, J.: Creep deformation of ice, Annual Review of Earth and Planetary Sciences, 11, 215-240, 1983.

Wu, Y., Nakagawa, S., Kneafsey, T. J., Dafflon, B., and Hubbard, S.: Electrical and seismic response of saline permafrost soil during freeze-thaw transition, J Appl Geophys, 146, 16-26, 2017.

Zhankui, Y., Yuanling, Z., and Ping, H.: Experimental study of Poisson's ratio for frozen soil, 1998, 1185-1186.

## 8 Code/Data availability

All data used in this study is publicly available, seismic waveform data may be downloaded via http://eida.geo.uib.no. The Janssonhaugen P11 temperature monitoring borehole is part of the GTN-P database (Global Terrestrial Network for Permafrost) and data is available upon request to the custodian. Meteorological data (including ground temperature) from the

https://doi.org/10.5194/tc-2021-329
Preprint. Discussion started: 25 October 2021


Janssonhaugen Vest weather station is available via the Norwegian Centre for Climate Services https://seklima.met.no/. The code used to produce this research can be shared upon request to the authors.

## 9 Author contribution

The study was conceptualised by AK and RR. The model, theory and methodology were developed by RR and AH. RR carried out the data collation and processing and was responsible for analysing and visualising the data. RR drafted the initial manuscript with contributions from all authors, with AH contributing significantly to the development and drafting of the theory sections. AH and AK also provided project supervision.

## 10 Competing interests

The authors of this article declare that they have no conflict of interest.

## 2.3 Preface to paper 3

Romeyn, R., Hanssen, A., Ruud, B. O., and Johansen, T. A. 2021. **Sea ice thickness from air-coupled flexural waves**, The Cryosphere, 15, 2939–2955, https://doi.org/10.5194/tc-15-2939-2021.

Paper 3 was conceived around the objective of using the flexural wavefield of a floating ice sheet to estimate its physical properties. Initially we focused on the distinctive, highly dispersive, ice flexural waves whose dispersion is well known to be controlled by the ice physical properties (e.g. Moreau et al., 2020a; Stein et al., 1998; Yang and Yates, 1995). However, upon examination of field data collected on sea-ice in Van Mijenfjorden, Svalbard, over four different field seasons, we consistently observed a prominent high-amplitude wave component with monochromatic frequency arriving in advance of the direct air wave. This wave component matched the description of the air-coupled flexural wave given by Press et al. (1951), although this topic has received strikingly little research attention since the 1950's. We recognized that the air-coupled flexural wave is convenient from a data analysis perspective because its phase velocity is constrained by the speed of sound in air. The study involved developing a theoretical framework that is more compatible with modern numerical computation techniques than the original, heavily analytical theoretical description of Press and Ewing (1951), and that aids conceptual understanding.

We found good agreement between ice thicknesses estimated from air-coupled flexural waves and those measured in boreholes drilled through the ice. The study focused on active source seismic experiments, using detonating cord to excite seismic waves. However, we were also able to demonstrate that air-coupled flexural waves are recordable in other settings, where they were excited by ice skates striking or cracking the ice, or natural ice quakes triggered by thermal stresses. The latter observation in particular, led us to hypothesize that air-coupled flexural waves could facilitate non-contact, passive monitoring of ice thickness, although the detailed practicalities of such an application remain a topic for further study.

It is important to highlight that Paper 3 has particular application, beyond the main scope presented in the article, to the estimation of ice thickness from a community safety perspective. Accidents where ice users fall through ice having insufficient load bearing capacity occur with unfortunate regularity. Tragically, some of these accidents also lead to fatalities. Figure xiii provides a summary of incidents in Norway reported in the period 2006-2021, where we should also note that persons falling through thin ice who were well prepared with the appropriate knowledge and equipment required to enact effective self-rescue are not included in these reports. All of these fatalities should be considered

avoidable, had timely and accurate information on ice thickness and bearing capacity been available. In this context, the fact that air-coupled flexural waves can be recorded with simple and inexpensive microphones could provide a possible avenue to develop more convenient and widespread means to estimate ice thickness and avoid travel on unsafe ice.

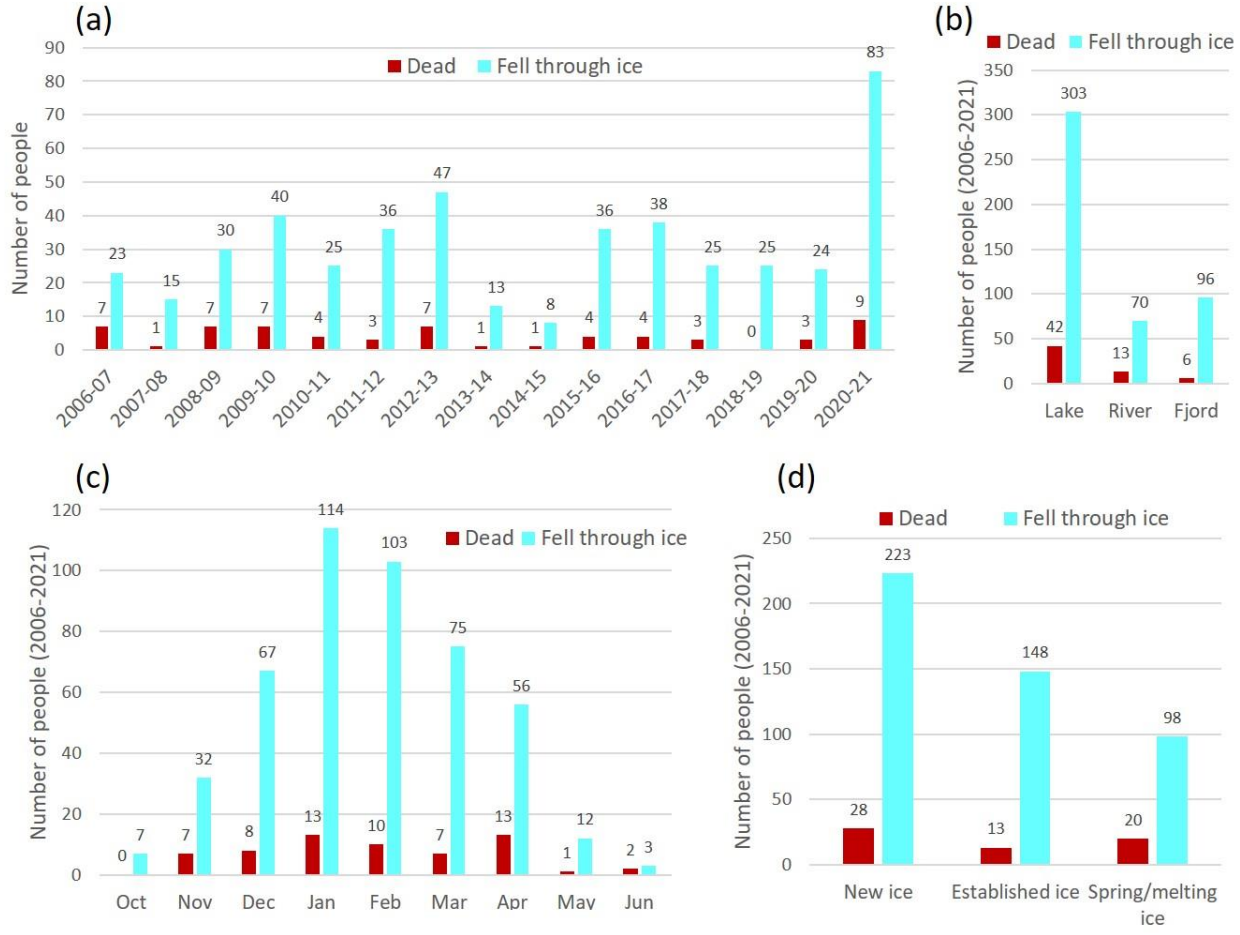


*Figure xiii – (a) Number of people involved in reported accidents on floating ice in Norway between 2006 and 2021, (b) the type of water body involved, (c) summary of accident seasonality and (d) the type of ice involved. Data from NVE (2021) based on collated reports published in traditional and social medias and incidents registered in the "Varsom Regobs" database (regobs.no).*

# Paper 3

The Cryosphere, 15, 2939–2955, 2021
https://doi.org/10.5194/tc-15-2939-2021


The Cryosphere Open Access EGU

# Sea ice thickness from air-coupled flexural waves

**Rowan Romeyn[1], Alfred Hanssen[1], Bent Ole Ruud[2], and Tor Arne Johansen[2,3]**

[1]Department of Geosciences, University of Tromsø – The Arctic University of Norway, 9037 Tromsø, Norway
[2]Department of Earth Science, University of Bergen, 5007 Bergen, Norway
[3]Department of Arctic Geology, The University Centre in Svalbard (UNIS), 9171 Longyearbyen, Norway

**Correspondence:** Rowan Romeyn (rowan.romeyn@uit.no)

Received: 25 February 2021 – Discussion started: 4 March 2021
Revised: 27 May 2021 – Accepted: 1 June 2021 – Published: 28 June 2021

**Abstract.** Air-coupled flexural waves (ACFWs) appear as wave trains of constant frequency that arrive in advance of the direct air wave from an impulsive source travelling over a floating ice sheet. The frequency of these waves varies with the flexural stiffness of the ice sheet, which is controlled by a combination of thickness and elastic properties. We develop a theoretical framework to understand these waves, utilizing modern numerical and Fourier methods to give a simpler and more accessible description than the pioneering yet unwieldy analytical efforts of the 1950s. Our favoured dynamical model can be understood in terms of linear filter theory and is closely related to models used to describe the flexural waves produced by moving vehicles on floating plates. We find that air-coupled flexural waves are a real and measurable component of the total wave field of floating ice sheets excited by impulsive sources, and we present a simple closed-form estimator for the ice thickness based on observable properties of the air-coupled flexural waves. Our study is focused on first-year sea ice of ∼20–80 cm thickness in Van Mijenfjorden, Svalbard, that was investigated through active source seismic experiments over four field campaigns in 2013, 2016, 2017 and 2018. The air-coupled flexural wave for the sea ice system considered in this study occurs at a constant frequency thickness product of ∼48 Hz m. Our field data include ice ranging from ∼20–80 cm thickness with corresponding air-coupled flexural frequencies from 240 Hz for the thinnest ice to 60 Hz for the thickest ice. While air-coupled flexural waves for thick sea ice have received little attention, the readily audible, higher frequencies associated with thin ice on freshwater lakes and rivers are well known to the ice-skating community and have been reported in popular media. The results of this study and further examples from lake ice suggest the possibility of non-contact estimation of ice thickness using simple, inexpensive microphones located above the ice sheet or along the shoreline. While we have demonstrated the use of air-coupled flexural waves for ice thickness monitoring using an active source acquisition scheme, naturally forming cracks in the ice are also shown as a potential impulsive source that could allow passive recording of air-coupled flexural waves.

## 1 Introduction

The term “air-coupled flexural wave” (ACFW) was coined by Press et al. (1951) to describe wave trains of constant frequency, varying with the flexural stiffness of a floating ice sheet, that arrive in advance of the pressure waves produced by an explosive source. The coupling in the case of air-coupled flexural waves is set up between pressure waves in air and flexural waves in the solid that have phase velocity equal to the speed of sound in air. Flexural waves propagating in a floating ice sheet are a class of guided elastic waves analogous to bending waves in rods or beams and the Lamb waves of a free plate. Greenhill (1886) published one of the earliest mathematical descriptions of flexural waves in a floating ice sheet and also discussed the concept of coupling between waves in air and water, which was further developed in Greenhill (1916). Several studies have used the dispersion of ice flexural waves (IFWs) to estimate ice elastic parameters; of these we highlight in particular the early work of Ewing and Crary (1934) and the study of Yang and Yates (1995) that advanced the use of transform methods in this field. Passive seismic studies of flexural wave dispersion are also emerging as an effective means to continuously monitor sea ice properties using array-based wave field trans-

**Published by Copernicus Publications on behalf of the European Geosciences Union.**

form methods (Moreau et al., 2020a) and noise interferometry and Bayesian inversion of dispersion curves (Moreau et al., 2020b).

Despite their commendable efforts to develop a theoretical foundation for the air-coupled flexural wave (Press and Ewing, 1951), the term has not been widely used since the initial investigation period in the 1950s and the study of Hunkins (1960). This may be because the theory developed by Press and Ewing (1951) is cumbersome, being built-up using demanding analytical integration methods at a time when computing power to handle more convenient numerical methods did not exist. We think this is unfortunate since the term "air-coupled flexural wave" gives a concise description of the physical mechanism that produces these waves. Furthermore, their monochromatic frequency is attractive from an experimental standpoint since it can be estimated from a single time series more readily than the precise time-frequency evolution of the highly dispersive ice flexural wave. Air-coupled flexural waves may therefore provide a simple and effective means to estimate the flexural rigidity of a floating ice sheet and to study variation in ice thickness, for the case when the elastic properties of the ice sheet are assumed or independently estimated.

### 1.1 A convergence of fields

Coupling between air and surface or guided waves is not limited to the case of a floating ice sheet and can be anticipated in all cases when the phase velocity of the medium below the air can attain the speed of sound in air (Haskell, 1951; Novoselov et al., 2020; Press and Oliver, 1955). For example, one of the strongest air waves ever recorded was produced by the volcanic eruption of Krakatoa in 1883, which travelled around the globe three times. It was not until the concept of air-coupled surface waves emerged that the extent of tidal waves associated with the eruption could be adequately explained, in which previous explanations had to invoke multiple coincidental local earthquakes at different locations to explain the observed arrivals of gravity waves in the ocean (Ewing and Press, 1955). The correlation of the major tide-gauge disturbances with the arrival of the first or second air-wave from the Krakatoa eruption has since been explained by waves propagating in a realistically coupled atmosphere–ocean system (Garrett, 1970; Harkrider and Press, 1967).

The idea of coupling between air and surface waves also exists in other fields under different terminological guises. In the field of structural acoustics, the frequency at which the free bending wave becomes equal to the speed of sound in air is called the critical frequency and is closely related to the coincidence frequency at which the speeds of the free and forced bending waves are equal (Renji et al., 1997). An understanding of the coupling between air waves and bending waves in structures therefore permits the design of advanced components like the honeycomb sandwich composite panels that are used in aerospace applications when one may wish to minimize the vibration response of the panels to acoustic excitation (Renji et al., 1997). Coupling between air and guided waves in engineered structures, like concrete slabs, is also relevant to non-contact applications of non-destructive testing (e.g. Harb and Yuan, 2018; Zhu, 2008).

At the coincidence frequency, a plate excited to vibration by travelling acoustic waves is acoustically transparent and maximally transmitting (Bhattacharya et al., 1971). A fascinating manifestation of this property is well known in the world of wild ice skating. Chasing perfectly smooth, newly frozen ice, typically in the $\sim$4–5 cm thickness range, these skaters flex the ice with their body weight and crack it with their skates. The acoustic waves produced by this cracking propagate over the ice surface and are maximally transmitted due to constructive interference with ice flexural waves at the frequency where the phase velocity of the flexural waves in the ice is equal to the speed of sound in air. When the ice is thin, this occurs in the audible frequency range and produces distinctive tones that have captured significant media attention (Griffin, 2018; Rankin, 2018). This phenomenon is analogous to the air-coupled flexural waves of Press et al. (1951), occurring within a different part of the frequency–flexural-stiffness spectrum.

### 1.2 A general theory – moving loads on floating plates

We now consider the closely related topic of moving vehicles travelling over floating ice sheets. The topic of moving loads on floating plates has received considerable attention due to the importance of roads on floating sea, river and lake ice that are traversed by vehicles from snow scooters to semi-trailers (Takizawa, 1988; Van der Sanden and Short, 2017; Wilson, 1955). Aircraft take-off and landing on floating ice (Matiushina et al., 2016; Yeung and Kim, 2000) or large man-made floating structures (Kashiwagi, 2004) have also received significant attention. A major focus of many of these studies is the so-called critical load speed, at which vehicle speed coincides simultaneously with the flexural phase and group velocities, and the ice deflection can grow very large over time (Wilson, 1955). In general, these studies are geared towards understanding the critical load speed so that vehicular transit at that speed may be avoided (e.g. Schulkes and Sneyd, 1988). Further studies have shown that the build-up of large enough deflections to break the ice may be limited by two-dimensional spreading (Nugroho et al., 1999), viscous effects (Wang et al., 2004), acceleration/deceleration through the critical speed (Miles and Sneyd, 2003) and/or non-linearities (Dinvay et al., 2019). Interestingly, a complementary field of study also exists that focuses on leveraging the resonant flexural waves produced by moving hovercraft to enhance their effectiveness as icebreakers (Hinchey and Colbourne, 1995; Kozin et al., 2017). Submarines surfacing in ice-covered waters may also seek to weaken or break the ice before surfacing by creating flexural gravity waves (Kozin and Pogorelova, 2008), which has been studied via

an adaption of the theoretical framework to include moving loads in the water column under a floating plate.

We propose that the air-coupled flexural wave phenomenon can be understood as a special case of the more general paradigm of moving loads on floating plates, in which the load speed is equal to the speed of sound in air. Furthermore, we hope to highlight the close physical relationship between phenomena spanning from Arctic seismic experiments to wild ice skating, ice roads, floating runways, structural acoustics and the eruption of Krakatoa. Our study was also motivated from the pragmatic standpoint that the monochromatic air-coupled flexural wave frequency is readily estimated from single sensor time series and can be related directly to ice thickness and rigidity. While other studies have focussed on measuring the dispersion of ice flexural waves in order to estimate ice physical properties (e.g. DiMarco et al., 1993; Moreau et al., 2020a; Yang and Yates, 1995), we present an additional alternative that is straightforward to implement and effective for both point and line explosive seismic sources.

## 2 Study area and data acquisition

In this study we investigate a series of active-source seismic experiments conducted in the innermost part of Van Mijenfjorden, on the island of Spitsbergen, in the high-Arctic Svalbard archipelago. The experiments were conducted during the spring season, when sea ice is best developed, in 2013, 2016, 2017 and 2018, as illustrated in Fig. 1. Detonating cord of the type "Nobelcord", containing 40 g Pentrit (PETN) per metre, was laid on the ice surface in various lengths or coiled into point-like charges to provide the seismic source. An example of the detonation of a point charge is shown in Fig. 2. These explosive charges produce a strong air wave that propagates radially over the ice surface, in addition to energy that travels horizontally through the ice, or downwards through the water column where it may be reflected back to the surface by layers of contrasting acoustic impedance. The sum of all of these modes of propagation gives the complex seismic wave field that was recorded using line arrays of geophones installed on the ice surface. For the majority of the experiments, the geophones were arranged in-line with the source, but we also include oblique arrangements from the 2013 campaign that employed a cross-type array (see Fig. 1).

The main purpose of these experiments was to test different acquisition designs for reflection seismic surveying of sub-seabed sediments, as reported by Johansen et al. (2019), an objective which is made difficult by the flexural wave energy propagating through the ice. Various source and receiver arrangements were tested including airguns, hydrophones and ocean bottom seismometers. However, in this study we focus on the subset of experiments employing explosive sources and vertical-component gimballed geophones deployed on top of the ice. This acquisition setup is operationally the simplest under field conditions but leads to the strongest recordings of ice flexural waves. While the flexural wave energy is regarded as bothersome coherent noise from the context of sub-seabed reflection surveying, it constitutes the primary signal in the present study and is used to estimate the ice thickness.

## 3 Theory

### 3.1 General wave field solution

In this study we approximate the air–ice–water system by a thin elastic plate resting on an incompressible inviscid fluid of finite depth, $H$, that corresponds to the widely used "simplest acceptable" mathematical model advocated by Squire et al. (1996). The plate extends infinitely along the horizontal $x$ and $y$ axes, and the vertical axis, $z$, is positive downwards with its origin at the upper undisturbed water surface. We impose the constraint that the fluid must satisfy the Laplace equation, $\nabla^2\phi = 0$, where $\phi$ is the velocity potential in the fluid. In addition, we impose a non-cavitation condition at the ice–water interface, $\left.\frac{\partial\phi}{\partial z}\right|_{z=b} = \frac{\partial\zeta}{\partial t}$, where $b$ is the draught of the ice and a normal flow condition at the sea bottom, $\left.\frac{\partial\phi}{\partial z}\right|_{z=H} = 0$, where $\zeta\,(x, y, t)$ is the vertical deflection of the plate's neutral surface. The linear spatio-temporal dynamics of the system is described by the partial differential equation (e.g. Squire et al., 1996)

$$D\nabla^4\zeta + \rho_\mathrm{I} h\frac{\partial^2\zeta}{\partial t^2} + \rho_\mathrm{w} g\zeta = -\rho_\mathrm{w}\left.\frac{\partial\phi}{\partial t}\right|_{z=b} - f(x, y, t). \quad (1)$$

Here, $D = \frac{Eh^3}{12(1-\sigma^2)}$ is the plate flexural stiffness, $E$ is Young's modulus, $h$ is the plate thickness, $\sigma$ is Poisson's ratio, $\rho_\mathrm{w}$ is the water density, $\rho_\mathrm{I}$ is the plate density, $g = 9.81\,\mathrm{m\,s^{-2}}$ is the acceleration due to gravity, and $f(x, y, t)$ is the applied external spatio-temporal force. The solution to Eq. (1) gives useful insight into the dynamics of the air-coupled flexural wave, and an illustrative example is given in Sect. 5.1.

In order to solve for the spatio-temporal deflection of the ice surface, we apply the three-dimensional Fourier transform (FT), defined as

$$P\left(k_x, k_y, \omega\right) = \iiint p\,(x, y, t)\, e^{i\left(k_x x + k_y y - \omega t\right)}\,\mathrm{d}x\,\mathrm{d}y\,\mathrm{d}t, \quad (2)$$

for an arbitrary spatio-temporal function $p\,(x, y, t)$. The wave number vector $\boldsymbol{k} = \begin{bmatrix} k_x \\ k_y \end{bmatrix}$ is decomposed in the $x$ and $y$ directions, $k^2 = |\boldsymbol{k}|^2 = k_x^2 + k_y^2$, and $i$ denotes the imaginary unit. By applying the FT defined in Eq. (2) to the spatio-temporal fields in Eq. (1), we find that the solution for the deflection in Fourier space is given by

$$Z\left(k_x, k_y, \omega\right) = -\frac{F\left(k_x, k_y, \omega\right)}{G\left(k_x, k_y, \omega\right)}, \quad (3)$$

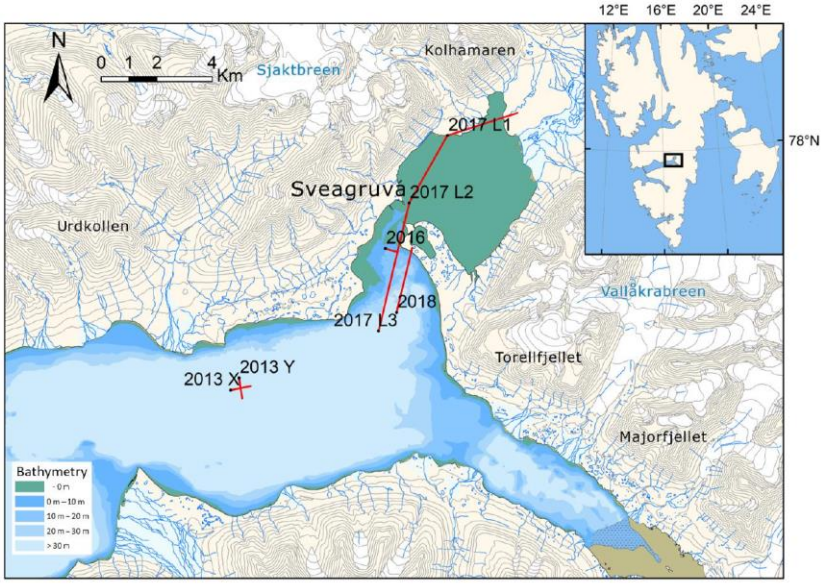


**Figure 1.** A 1 : 100 000 scale map of the innermost part of Van Mijenfjorden, Spitsbergen, showing the geophone arrays (red lines) deployed during field campaigns in 2013, 2016, 2017 and 2018. Inset map indicates the position relative to the Svalbard archipelago. Land contour interval is 50 m. Map data © Norwegian Polar Institute (https://npolar.no, last access: 25 June 2020).

**Figure 2.** Photo taken during the 2013 field campaign showing the explosive seismic source. The line of seismic receivers is marked with red poles (photo: Robert Pfau).

where $G\left(k_x, k_y, \omega\right) = Dk^4 + \rho_w g - \rho_i h\omega^2 - \left(\frac{\rho_w \omega^2}{k}\right) \coth\left(kH\right)$. Recalling linear filter theory, the form of Eq. (3) highlights that the floating ice plate simply acts as a linear filter on an arbitrary spatio-temporal input signal. This formulation is also attractive because the physical significance of the different terms in the denominator are clearly preserved: $Dk^4$ expresses the bending forces in the plate, $\rho_w g$ is due to the plate buoyancy, $\rho_i h\omega^2$ is the plate acceleration, and $\left(\frac{\rho_w \omega^2}{k}\right) \coth\left(kH\right)$ arises due to the constraint of finite water depth.

The general solution for the resulting spatio-temporal deflection wave field, $\zeta\left(x, y, t\right)$, is then given by the full three-dimensional inverse FT of $Z\left(k_x, k_y, \omega\right)$ as

$$\zeta\left(x, y, t\right) = -\frac{1}{\left(2\pi\right)^3} \iiint \frac{F\left(k_x, k_y, \omega\right)}{G\left(k_x, k_y, \omega\right)} \cdot e^{-i\left(k_x x + k_y y - \omega t\right)} \mathrm{d}k_x \, \mathrm{d}k_y \, \mathrm{d}\omega. \quad (4)$$

### 3.2 Ring delta function source for radial symmetry

To exploit spatial symmetry and reduce the dimensionality of the problem, we approximate the explosive source as a ring-shaped Dirac delta pulse expanding outwards from the origin with radial symmetry. This allows us to reduce the spatial dimensionality of the problem by using the radial coordinate $r = \sqrt{x^2 + y^2}$ and representing the propagating air wave source using the ring delta function,

$$f\left(r, t\right) = -\frac{1}{2\pi r} \delta\left(r - c_{\mathrm{air}} t\right), \quad (5)$$

where $c_{\mathrm{air}}$ is the speed of sound in air. By performing a partial Fourier transform of Eq. (5) with respect to time, $t$, we obtain the spatio-frequency representation of the source as

$$F\left(r, \omega\right) = \int_{-\infty}^{\infty} f\left(r, t\right) e^{-i\omega t} \mathrm{d}t = -\frac{1}{2\pi r c_{\mathrm{air}}} e^{-i\omega r / c_{\mathrm{air}}}, \quad (6)$$

so the spatio-frequency deflection wave field can be written as

$$Z\left(r, \omega\right) = -\frac{F\left(r, \omega\right)}{G_0\left(\omega\right)}, \quad (7)$$

where

$$G_0\left(\omega\right) = D\left(\frac{\omega}{c_{\mathrm{air}}}\right)^4 + \rho_w g - \rho_i h\omega^2 - \left(c_{\mathrm{air}} \rho_w \omega\right) \coth\left(\frac{\omega H}{c_{\mathrm{air}}}\right). \quad (8)$$

The spatio-temporal deflection wave field in radial coordinates then becomes

$$\zeta(r,t) = -\frac{1}{2\pi}\int_{-\infty}^{\infty}\frac{F(r,\omega)}{G_0(\omega)}e^{i\omega t}\mathrm{d}\omega. \quad (9)$$

When evaluating Eq. (9) numerically, we substitute $G_0(\omega) \rightarrow G_0(\omega + i\gamma)$, where $\gamma > 0$, which avoids dividing by zero and gives a tuneable heuristic damping parameter for wave attenuation and dissipation.

### 3.3 Dispersion relation

The dispersion relation for the propagating wave field in the ice sheet is given by the wavenumber and frequency pairs that satisfy the equation

$$G(k,\omega) = 0. \quad (10)$$

The solution of Eq. (10) gives the general dispersion relation (e.g. Squire et al., 1996)

$$\omega^2 = \frac{\left(Dk^5/\rho_\mathrm{w}\right) + gk}{kh\frac{\rho_\mathrm{i}}{\rho_\mathrm{w}} + \coth(kH)}. \quad (11)$$

This dispersion relation is complete in the sense that it retains all physical mechanisms included in the dynamical model Eq. (1), and it is well known from previous studies (e.g. Greenhill, 1886; Squire et al., 1996). At typical vehicle speeds and wavelengths that have been the main focus of moving load on floating plate studies, the plate acceleration may be safely neglected (e.g. Schulkes and Sneyd, 1988; Wang et al., 2004) giving the approximate dispersion relation

$$\omega^2 \approx \left(\frac{Dk^4}{\rho_\mathrm{w} g} + 1\right) gk\tanh(kH). \quad (12)$$

Another common assumption is to assume infinite water depth, $H$, which causes the hyperbolic tangent term to approach unity. However, when the load moves at the speed of sound in air, plate flexural waves with much shorter wavelengths are resonant, and it becomes important to retain the plate acceleration term. The common approximations that are valid at typical vehicle speeds may lead to significant inaccuracies when estimating physical properties of the floating ice sheet from estimates of air-coupled flexural wave frequency.

Figure 3 compares the full dispersion relation (Eq. 11) with the approximation that neglects water depth and plate acceleration (Eq. 12). Air-coupled waves are excited when the phase velocity is equal to the speed of sound in air, shown as the horizontal red line in Fig. 3. With finite water depth $H$ (black line in Fig. 3), we see that only flexural waves are coupled to the air wave. Gravity waves have been observed in landfast sea ice (Sutherland and Rabault, 2016) and may

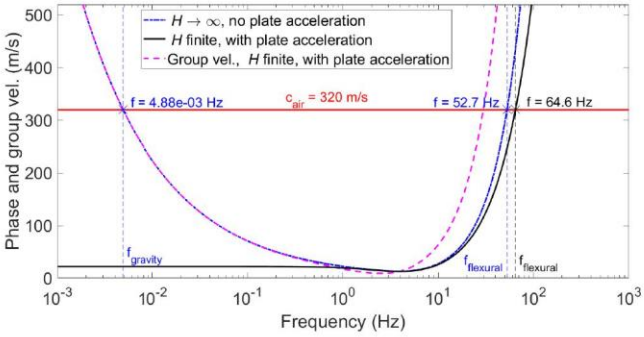


**Figure 3.** Comparison of simplified dispersion relation neglecting water depth and plate acceleration (blue, Eq. 12) with the full dispersion relation including these effects (black, Eq. 11) for $h = 0.74$ m and sea ice physical properties from Table 1.

theoretically couple to the air wave for the case of an infinite fluid (dashed blue line in Fig. 3), but the coupled wave is likely unobservable in practice. The air-coupled flexural waves arrive in advance of the air wave because the group velocity, $\partial\omega/\partial k$, is larger than the phase velocity for a given frequency (dashed magenta line in Fig. 3). The air-coupled flexural frequency is insensitive to water depths $> 3.2$ m, in this example, but is significantly affected by the plate acceleration term. Including the effect of plate acceleration increases the air-coupled flexural frequency by $\sim 23$ % using physical properties relevant to our field data (see Table 1). While studies of moving vehicles on floating plates may safely ignore the effect of plate acceleration, we show that it is important to include it when the considered load is moving at the speed of sound in air.

## 4 Methodology

A key attraction of air-coupled flexural waves is the ability to use the time series recorded by a single sensor to estimate ice thickness. This is possible because, as illustrated by our dynamical model, the phase velocity of the air-coupled flexural wave is equal to the speed of sound in air. This is similar to studies of ice roads and runways, in which the fact that the speed of the vehicle is known raises the potential for routine monitoring of ice flexural rigidity using a single sensor (Squire et al., 1988). The frequency of the air-coupled flexural wave is estimated from the high amplitude, monochromatic segment of the time series that directly precedes the air wave arrival. The air-coupled flexural frequency can then be directly related to the physical properties of the floating ice sheet using the dispersion relation introduced in the previous section.

### 4.1 Air wave arrival and velocity estimation

Since the arrival time of the air wave increases linearly with horizontal offset between the seismic source and receiver,

we can estimate its arrival time and velocity using the linear Radon transform, also referred to as the slant-stack or $\tau$-$p$ transform (Yilmaz, 2001). When the independent variable is source-to-receiver offset, energy with a constant velocity follows a linear trajectory. Under the linear Radon transform, energy corresponding to a specific velocity and origin time is stacked along this trajectory to form a single point in the transform space. For a given explosive charge (see Fig. 4a), we compute the linear Radon transform for offset-sorted geophone signals and estimate the velocity ($c_{\mathrm{air}}$) and intercept ($t_{\mathrm{int}}$) that correspond to the air wave by picking the local maximum of the transform magnitude (see Fig. 4b). The estimated arrival time of the air wave at a given geophone, $t_{\mathrm{air}}$, is then given by $t_{\mathrm{air}} = \frac{d}{c_{\mathrm{air}}} + t_{\mathrm{int}}$, where $d$ is the source-to-receiver offset.

### 4.2 Thomson multitaper estimation of air-coupled flexural frequency

The frequency of the air-coupled flexural wave is estimated from segments of the recorded time series which precede the arrival of the air wave (see Fig. 4c). We take the derivative of the time series to suppress low frequencies and linearly increase the gain of high frequencies and apply a Hamming window taper. For each time series, the Thomson multitaper power spectral density (Thomson, 1982) is then estimated using a time-half-bandwidth product of 2 and a zero-padded Fourier transform length of 4096 samples. Thomson's estimator utilizes a set of orthonormal data tapers called discrete prolate spheroidal sequences to control spectral leakage and stabilize the estimate through an inherent variance reduction (Hanssen, 1997). The air-coupled flexural frequency (see Fig. 4d) is then estimated from the multitaper power spectral density maximum. We only estimate the air-coupled flexural frequency for source-to-receiver offsets $> 125$ m because higher-velocity sub-seabed reflections arrive around the same time as the air wave and create too much interference at nearer offsets (see Fig. 5).

### 4.3 Closed-form estimator of ice thickness

Once we have estimated the frequency of the air-coupled flexural wave ($\omega_{\mathrm{f}}$) we can estimate the ice thickness using the dispersion relation (Eq. 11) rearranged as

$$\frac{Eh^3k_{\mathrm{f}}^5}{12\rho_{\mathrm{w}}\left(1-\sigma^2\right)} + gk_{\mathrm{f}} = \omega_{\mathrm{f}}^2\left[k_{\mathrm{f}}h\frac{\rho_{\mathrm{l}}}{\rho_{\mathrm{w}}} + \coth\left(k_{\mathrm{f}}H\right)\right], \tag{13}$$

where $k_{\mathrm{f}} = \omega_{\mathrm{f}}/c_{\mathrm{air}}$ is the wavenumber corresponding to the air-coupled flexural wave. The inclusion of the plate acceleration term means that we are left with a non-linear relation for the plate thickness, $h$, in terms of the plate elastic properties and the constant flexural frequency and wavenumber. We may either estimate the ice thickness by the non-linear numerical optimization of Eq. (13), using, for example, the bisection method, or we may rearrange Eq. (13) to give the cubic polynomial form

$$\left(\frac{Ek_{\mathrm{f}}^5}{12\rho_{\mathrm{w}}\left(1-\sigma^2\right)}\right)h^3 - \left(\omega_{\mathrm{f}}^2k_{\mathrm{f}}\frac{\rho_{\mathrm{l}}}{\rho_{\mathrm{w}}}\right)h + gk_{\mathrm{f}} - \omega_{\mathrm{f}}^2\coth\left(k_{\mathrm{f}}H\right) = 0, \tag{14}$$

which has one real, positive root corresponding to the plate thickness, $h$. Since Eq. (14) has a standard cubic form, a closed-form analytical solution can be derived. We followed the modified Cardan's solution method outlined by Nickalls (1993) to derive the following estimator,

$$h = 2\sqrt{\frac{b}{3a}}\cos\left[\frac{1}{3}\cos^{-1}\left(\frac{-3\sqrt{3}}{2}a^{1/2}b^{-3/2}c\right)\right], \tag{15}$$

where $a = \frac{Ek_{\mathrm{f}}^5}{12\rho_{\mathrm{w}}(1-\sigma^2)}$, $b = \omega_{\mathrm{f}}^2k_{\mathrm{f}}\frac{\rho_{\mathrm{l}}}{\rho_{\mathrm{w}}}$ and $c = gk_{\mathrm{f}} - \omega_{\mathrm{f}}^2\coth\left(k_{\mathrm{f}}H\right)$. We have confirmed that non-linear numerical optimization of Eq. (13), polynomial root finding of Eq. (14) and the closed form of Eq. (15) all give identical results.

## 5 Results

Air-coupled flexural waves appear to be a robust part of the wave field excited by explosive sources on floating sea ice and were observed for all four field campaigns, in spite of thin, variable snow covers. Furthermore, Fig. 5 illustrates that since the air-coupled flexural wave precedes the arrival of the air wave, it is recorded equally well for both point and line sources. This is significant because much of our field data employed line sources in order to attenuate the trailing low-frequency ice flexural waves that are an unwanted noise component from the perspective of reflection seismic surveying (Johansen et al., 2019).

### 5.1 Solution of the full dynamical model

It is only strictly necessary to consider the solution to the dispersion relation in order to estimate ice properties from flexural wave observations. However, it is also beneficial to consider the solution to the dynamical equation (Eq. 1) in order to demonstrate that the key physics involved in the propagation of air-coupled flexural waves are represented by the model. To this end, we evaluated Eq. (9) numerically using an inverse fast Fourier transform (IFFT) with $N = 2^{19}$ discrete points, a temporal sampling interval, $\mathrm{d}t = 2.5 \times 10^{-4}$ s, and a numerical attenuation/damping parameter, $\gamma = 25$. Figure 6 shows a portion of the modelled radially symmetric expanding wave field produced by a propagating ring delta loading that we use as an approximation of the air wave expanding outwards from a point explosive charge and pushing downwards on the ice sheet. We see that the ice sheet is deflected downwards underneath and behind the air wave. The negative deflection decays smoothly and extends to a position

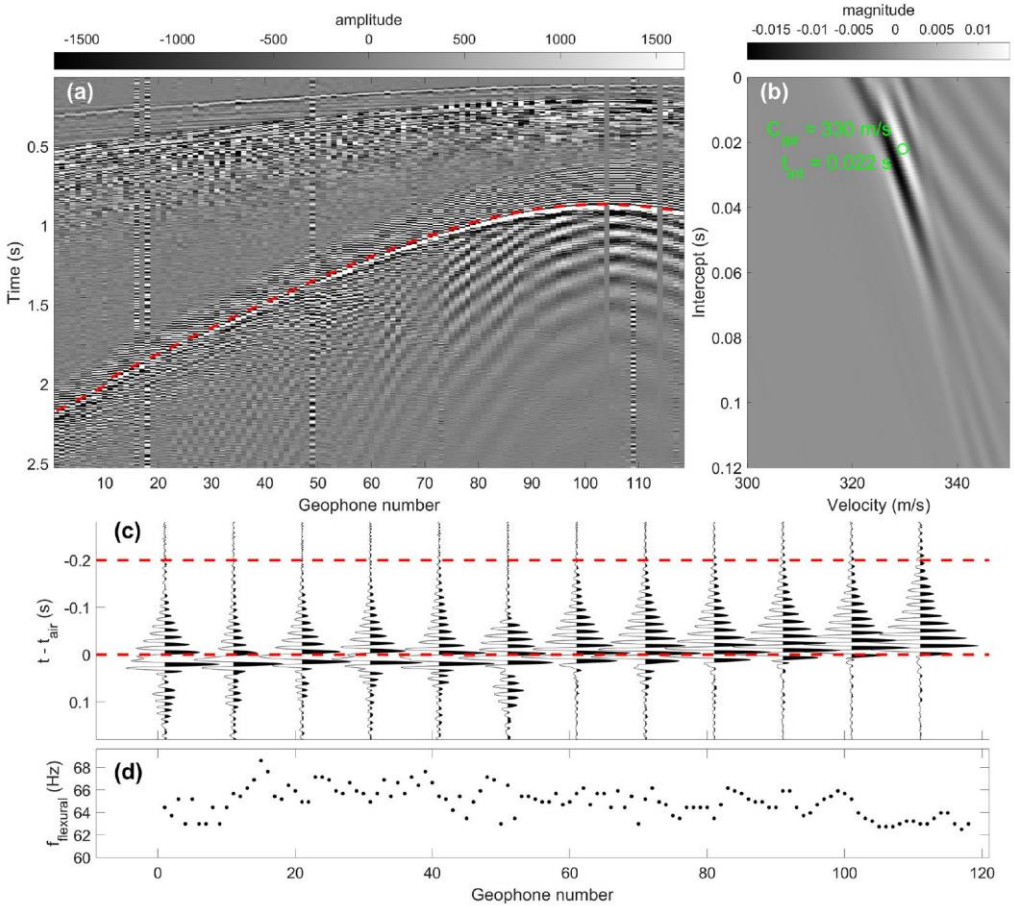


**Figure 4.** Example of air-coupled flexural wave frequency estimation. **(a)** Geophone records with dashed red line indicating the air wave arrival, **(b)** air wave arrival time and velocity is estimated by picking the local maximum of the linear radon transform, **(c)** waveform plot for every 10th geophone indicating the frequency estimation window (dashed red lines), and **(d)** air-coupled flexural frequency estimated by the multitaper method.

around 300 m behind the load, although this is outside the figure view. Ahead of the air wave, the ice surface is elevated, and we see a high amplitude, constant frequency wave train that corresponds to the air-coupled flexural wave, which decays gradually with distance ahead of the load due to the inclusion of numerical damping in the model.

To compare the solutions of the full dynamical model result with field data, we calculate the velocity response of the plate at a given offset by numerical time differentiation of the output from Eq. (9) and compare that directly to the recorded geophone time series at the same offset. We find that local velocity estimates calculated from our solutions to the dynamical model are very similar to the real waveforms recorded by geophones, as illustrated by the example in Fig. 7. This increases our confidence that we understand the underlying physics that describe the excitation of air-coupled flexural waves in floating ice sheets.

### 5.2 Ice thickness estimation from air-coupled flexural waves

As summarized in Table 1, ice thicknesses calculated using Eq. (15) from the estimated air-coupled flexural frequencies and air wave velocities show very good agreement with ice thicknesses measured in boreholes. Notably, this good agreement was achieved across all four field seasons with a single set of elastic properties that are realistic for sea ice. This is partly because ice thickness is an extrinsic property that has a dominant effect on the air-coupled flexural frequency (stemming from the fact that $D \propto h^3$); i.e., the 20–80 cm thickness range from this study corresponds to a 400 % variation in air-coupled flexural frequency. By contrast, variation of intrinsic material properties, i.e., Young's modulus (1.7–5.7 GPa) and Poisson's ratio (0.33–0.39) as reported by Timco and Weeks (2010), for first-year sea ice would give $\sim 60$ % and $\sim 2$ % variation in air-coupled flexural frequency, respectively. The combined effects of water and ice density variation over the ranges given in Table 1 would only

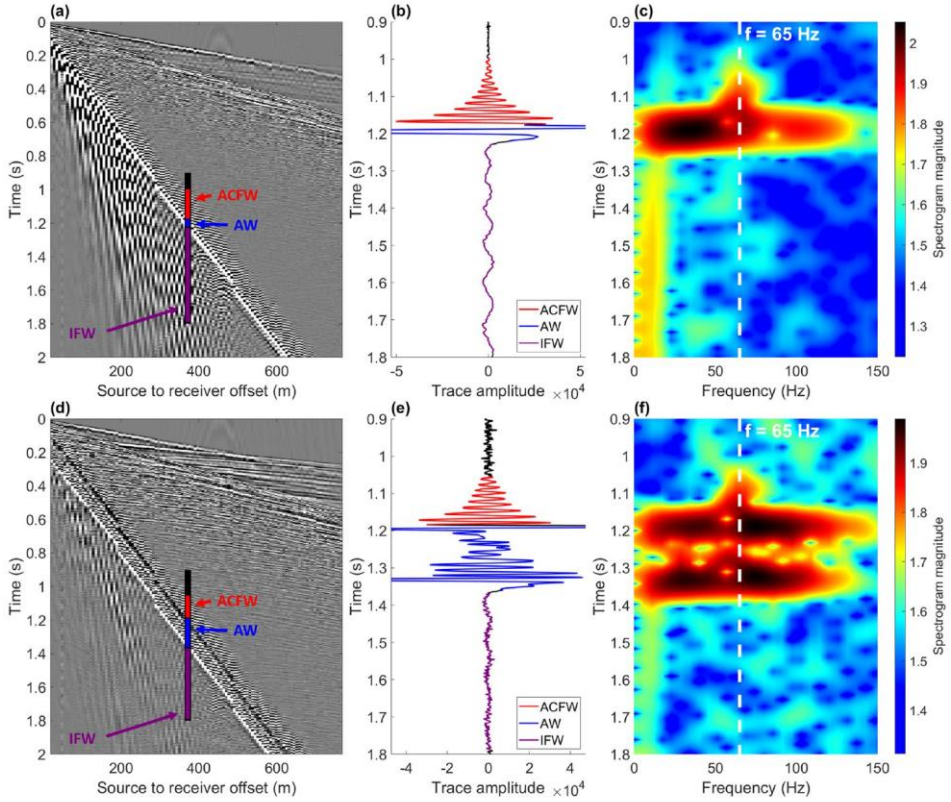


**Figure 5.** Example geophone records for **(a)** a point charge and **(d)** a 50 m long detonating cord line source, **(b)** and **(e)** show illustrative time series enlarged around the air wave (AW) arrival, and **(c)** and **(f)** show spectrograms for the time series **(b)** and **(e)**. The air-coupled flexural wave (ACFW) arrives with a constant frequency of ∼65 Hz in advance of the broadband air wave. The characteristically dispersive ice flexural waves (IFWs) are significantly attenuated due to destructive interference for the line source.

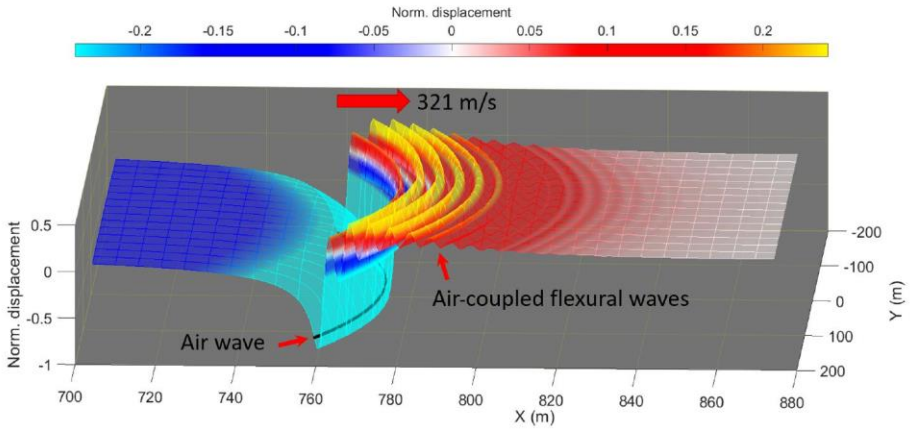


**Figure 6.** Modelled normalized displacement wave field for $h = 74$ cm, $c_{air} = 321\ m\ s^{-1}$ and elastic parameters as in Table 1. The black line marks the position of the load (representing the air wave).

produce a variation of ∼0.3 % in air-coupled flexural frequency, while water depth has no effect for depths > 3.2 m. Temperature variation over the range −20 to +2 °C would cause the speed of sound in air to vary from 318–332 $m\ s^{-1}$, resulting in ∼8 % variation in air-coupled flexural frequency. The apparent speed of sound in air at the measurement location is also affected by horizontal wind velocity, and gusts may lead to a variation of $\pm 5\ m\ s^{-1}$ over timescales of minutes (e.g. Franke and Swenson, 1989). However, as described in Sect. 4.1, we estimate the apparent velocity of the air wave

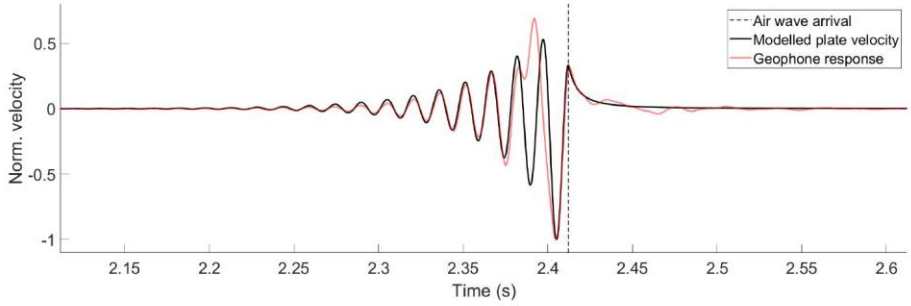


**Figure 7.** Modelled normalized velocity response time series (black curve) at an offset of 759 m compared with the time series recorded by a geophone at the same offset from a point charge fired during the 2013 field season (red curve). The air wave arrival time is indicated by the dashed line.

for each shot, which should ensure that our air-coupled flexural thickness estimates are independent of changes in wind and temperature over time.

The Young's modulus of $2.5 \pm 0.2$ GPa given in Table 1 was constrained by observing that the median air-coupled flexural wave thickness estimate for the 2013 field season would fall outside the range of borehole-measured thicknesses for Young's modulus outside this range. The fact that this Young's modulus gives thickness estimates that fit with borehole measurements across all four field seasons indicates that the bulk, effective elastic properties of first-year sea ice in Van Mijenfjorden are relatively consistent from year to year. A somewhat higher Young's modulus of $\sim 4$ GPa was reported for Van Mijenfjorden by Moreau et al. (2020a), but the deviation from the present study is likely attributable to the protected physical setting of their study site at the estuarine Vallunden lake. It is also important to highlight that all elastic properties we assume represent bulk, apparent values corresponding to the thin isotropic plate assumption, while real floating ice sheets are a composite sandwich material consisting of multiple ice layers of varying strength (Timco and Weeks, 2010).

Here we give a summary of our air-coupled flexural wave ice thickness estimates for each field season and examine them in the context of borehole measurements of ice thickness and prevailing meteorological conditions, as represented by records at the nearby Sveagruva weather station (Norwegian Meteorological Institute, 2020), which was upgraded prior to the 2017 season to include measurement of precipitation. We assume the air-coupled flexural frequency recorded at a given geophone is related to the ice thickness at the location of the geophone as this gave the strongest correlation with borehole thickness measurements.

#### 5.2.1 The 2013 field season

The ice thickness estimates for the 2013 field season are summarized in Fig. 8 and show good agreement with borehole measurements. There is somewhat greater spread in the results on the Y line which is likely related to the fact that the majority of the source positions were inline with the X line and therefore oblique to the Y line (see Fig. 1). The oblique geometry reduces the precision of using the linear Radon transform to estimate the arrival time and velocity of the air wave, which becomes smeared in the transform domain. Air temperatures remained consistently $< 0\,^{\circ}$C, and the thickness estimates are quite similar over the $\sim 3$ d field campaign, though there is some indication of ice growth with time.

#### 5.2.2 The 2016 field season

The results for the 2016 field season are illustrated in Fig. 9. Some outliers are present in the flexural wave thickness estimates which are caused by interference of other spectral components for the extracted time series segments. This interference can be due to, for example, other wave modes such as sub-seabed reflections, snow scooter engine noises or instrument noise due to wind. Despite these outliers, the median thickness estimates agree well with the range of drilled thicknesses (see Table 1), although the along-profile locations of the boreholes was unfortunately not recorded for this field campaign.

#### 5.2.3 The 2017 field season

The thickness estimates for the 2017 field season are shown in Fig. 10. The significant spatial thickness variation observed in boreholes is reasonably well represented by the median air-coupled flexural wave thickness estimates plotted according to geophone position, though the estimates vary more smoothly in space. This indicates that the air-coupled flexural wave varies according to the thickness and flexural rigidity of the ice in the vicinity of the geophone, likely averaged spatially in proportion with the wavelength of flexure. An alternative hypothesis that the air-coupled flexural wave is controlled by the path-averaged ice properties between the source and geophone was tested by plotting the thickness estimates at the midpoint between source and receiver. While we do not include the figure for brevity, the result is a flat profile with estimates ranging from $\sim 45$–$75$ cm and a simi-

**Table 1.** Summary of ice thicknesses ($h$) estimated from air-coupled flexural waves (ACFW) compared to the range of ice thicknesses measured in boreholes drilled through the ice. MAD signifies median absolute deviation.

| Field season | $h$ (cm) median ACFW | MAD (cm) | $h$ (cm) borehole measured | Young's modulus $E$ (GPa) | Poisson's ratio $\sigma$ | $\rho_{ice}$ (kg m$^{-3}$) | $\rho_{water}$ (kg m$^{-3}$) | Water depth $H$ (m) |
|---|---|---|---|---|---|---|---|---|
| 2013 | 76 | 3 | 74–79 | $2.5 \pm 0.2$ | 0.33 | 925 | 1023 | |
| 2016 | 34 | 3 | 30–40 | Timco and Weeks | Timco and Weeks | Timco and Frederking | Skarðhamar and | $> 3.2$ |
| 2017 | 57 | 4 | 30–75 | (2010) give | (2010) give | (1996) give | Svendsen (2010) give | |
| 2018 | 30 | 2 | 20–40 | range of 1.7–5.7 | range of 0.33–0.39 | range of 920–930 | range of 1020–1026 | |

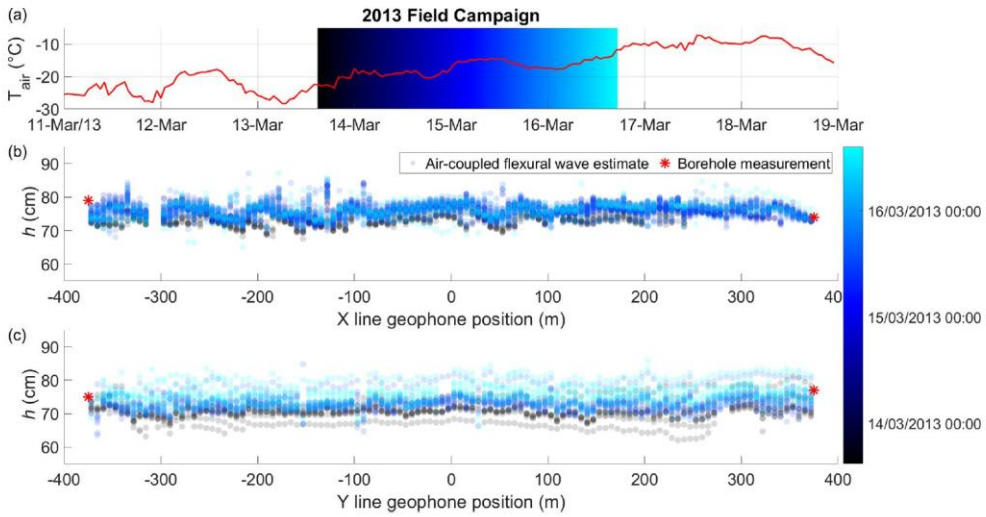


**Figure 8.** The 2013 field campaign air-coupled flexural wave ice thickness estimates (circles), borehole drilled thicknesses (red stars) and air temperature at nearby Sveagruva weather station (red line). The time span of the field campaign is indicated by black–blue–cyan colour gradient. Point estimates are transparent so overlapping repeat tests are indicated by denser colours. Figure 1 shows location of the profiles 2013 X **(b)** and 2013 Y **(c)**.

lar median of $\sim 57$ cm. This does not reflect the real thickness variation recorded by the borehole measurements, leading us to prefer the hypothesis that the frequency of the air-coupled flexural wave is controlled by the ice thickness and flexural rigidity in the vicinity of the geophone. Indeed, we found the borehole-measured spatial variation in ice thickness could only be approximated by assuming the air-coupled flexural wave estimates lie at least 98 % towards the geophone (along the straight line from source to geophone).

We also observe that the air-coupled flexural wave thickness estimates significantly overestimate the ice thickness drilled in the two boreholes closest to land. While further field data would be needed to investigate this phenomenon in detail, it may be attributable to the effect of the land on the lateral boundary condition of the ice sheet (see Appendix A). The infinite ice sheet modelled in the present study does not include a lateral boundary, though it may be possible to heuristically approximate this effect by defining a spatially variable effective elastic modulus that increases near land.

#### 5.2.4 The 2018 field season

The air-coupled flexural wave thickness estimates for the 2018 field season are summarized in Fig. 11. The thickness estimates agree well with the range of ice thickness measured in boreholes (see Table 1), though the along-profile locations of the boreholes were unfortunately not recorded for this field campaign. The most striking feature we observe for the 2018 campaign is an increase in ice thickness of up to $\sim 10$–$15$ cm over the course of the campaign (a period of $\sim 4$ d). This rapid increase in thickness is attributable to the weather event that occurred on 26–27 February, when $> 0\,^{\circ}$C temperatures and rain led to a significant accumulation of freshwater on top of the sea ice. This event was significant enough that fieldwork was not possible on 27 February. The rapid decrease in air temperature on the 28th then promptly caused the accumulated fresh surface water to freeze, a process that occurs much more quickly than basal ice accumulation due to heat loss through the overlying ice layer, salt rejection and eventual freezing of seawater.

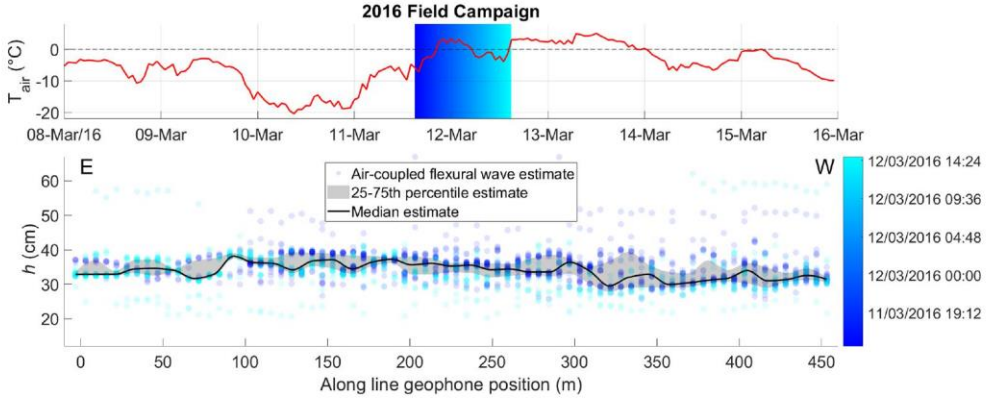


**Figure 9.** The 2016 field campaign air-coupled flexural wave ice thickness estimates (circles) and temperature at nearby Sveagruva weather station (red line). Time span of field campaign is indicated by blue–cyan colour gradient. Point estimates are transparent so overlapping repeat tests are indicated by denser colours. Figure 1 shows location of profile.

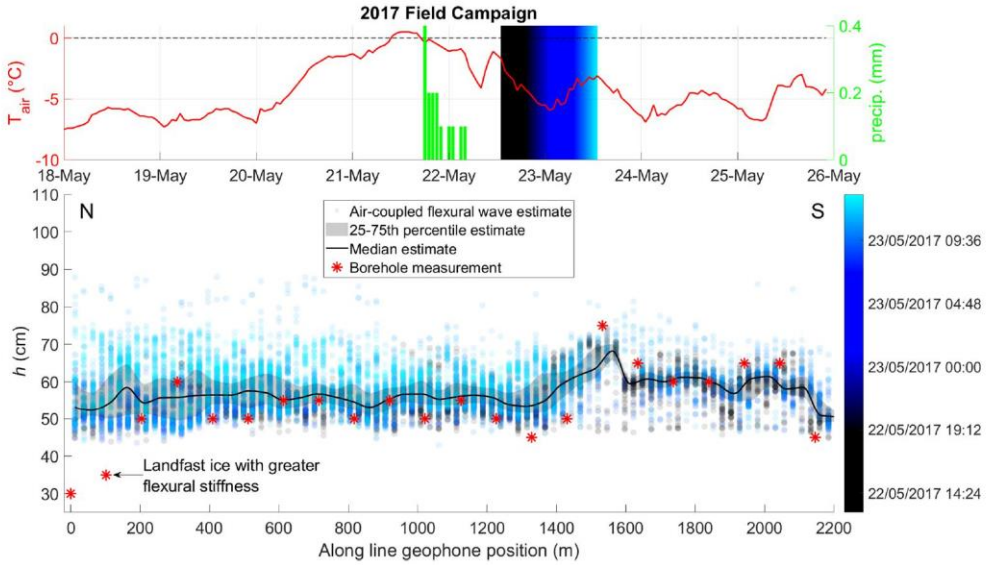


**Figure 10.** Profile 2017 L3 from 2017 field campaign, seaward direction is south (see Fig. 1) showing air-coupled flexural wave ice thickness estimates (circles), borehole drilled thicknesses (red stars), temperature (red line) and precipitation (green bars) at Sveagruva weather station. Timing is indicated by black–blue–cyan colour gradient, and point estimates are transparent so overlapping repeat tests are indicated by denser colours.

## 6 Discussion

It is possible to interpret the origin of the air-coupled flexural waves in several equivalent ways. (1) They are produced by the downward pressure of the air wave moving over the ice surface, i.e., the moving loads on floating plates interpretation as elaborated in Sect. 3. (2) A plate excited by a broadband pulse propagates flexural wave energy at a range of frequencies, but sound transmission from the plate is highest at the coincidence frequency (Bhattacharya et al., 1971) producing a resonance effect. (3) Alternatively, the air-coupled flexural wave can be interpreted as a class of leaky Lamb waves in which flexural wave energy radiates into the air, regulated by the phase matching condition and occurring most efficiently at the grazing angle, where the phase velocity is equal to the speed of sound in air (Brower et al., 1979; Kiefer et al., 2019; Mozhaev and Weihnacht, 2002). The observation of air-coupled flexural waves and absence of dispersive ice flexural waves on the far side of open water leads by Hunkins (1960) is consistent with the interpretation that, for explosive sources on or above the ice, air-coupled flexural waves are generated continuously by the downward pressure exerted by the air wave. The correspondence between experimental data and the solution of the full dynamical model (see Fig. 6) gives further support to this interpretation.

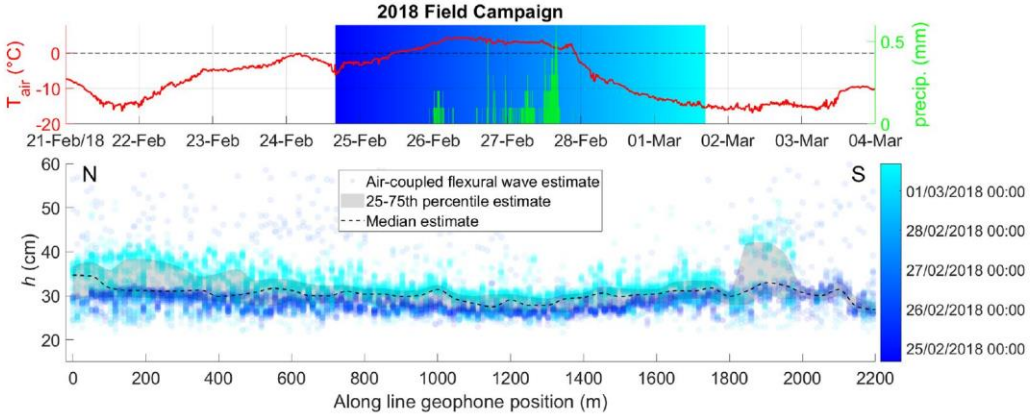


**Figure 11.** The 2018 field campaign air-coupled flexural wave ice thickness estimates (circles), temperature (red line) and precipitation (green bars) at Sveagruva weather station. Timing of experiments is indicated by blue–cyan colour gradient, and point estimates are transparent so overlapping repeat tests are indicated by denser colours. Figure 1 shows location of profile. Median is shown with a dashed line because there are two distinct, temporally separated populations.

Our results indicate that air-coupled flexural waves are affected by spatial (see Fig. 10) and temporal ice thickness variation (see Fig. 11). A high degree of spatial variability in ice thickness has been reported for first-year sea ice in Van Mijenfjorden (Sandven et al., 2010) and in the Arctic in general (Wadhams et al., 2006). Spatial resolution is likely proportional to the air-coupled flexural wavelength, though further field data including high-resolution ground truth measurements would be required to elaborate this proportionality in detail. It is also important to highlight that the air-coupled flexural frequency is affected by the elastic properties of the ice, its flexural rigidity and not just its thickness. By assuming a constant set of elastic parameters our thickness estimates may be considered "effective thicknesses" corresponding to the assumed elastic parameters and subject to the thin isotropic plate assumption. However, we also expect that the "effective thickness" for assumed elastic properties is still highly relevant when assessing the load bearing capacity of floating ice even if it were to deviate from the true thickness.

A small percentage of outliers are present in the thickness estimates that we attribute to spectral contamination caused by the simultaneous arrival of other wave modes with the air-coupled flexural waves. Such interference was minimized by discarding the nearest offsets where high-velocity subseabed reflections arrive at the same time as the air wave (see Fig. 5). However, other noise sources, such as snow scooter traffic, are difficult to avoid in real-world data. In the rare cases that traffic noise is recorded at the same instant as the air-coupled flexural waves, the resulting spectral interference can prevent accurate estimation of the air-coupled flexural frequency. Snow cover also likely decreases the efficiency of coupling between ice and air, though this did not appear to play a major role for the four field seasons investigated, for which gimballed $z$-component geophones were deployed directly on top of the thin snow covers that were present.

## Air-coupled flexural wave data acquisition

In this study, we present data acquired with linear arrays of geophones and active seismic sources that were primarily acquired to test the feasibility of seismic reflection surveying on floating sea ice. It is important to emphasize that it should be possible to employ much simpler equipment to record air-coupled flexural waves. Indeed, from our results we would expect that a simple microphone, sensitive in the relevant frequency range and located in the vicinity of the desired measurement, either above the ice sheet or along the shoreline may be sufficient. In addition to low equipment cost, the potential to monitor ice thickness using a microphone positioned on land could be beneficial from the perspective of environmental monitoring, particularly early in the freezing season when the ice is too thin to be safely traversed.

The use of microphones to record air-coupled flexural waves can be illustrated by a phenomenon that is familiar to the ice-skating community. On thin, floating ice, skates striking or cracking the ice can excite sonorous tones that vary in pitch according to the ice thickness (Lundmark, 2001). These tones correspond to air-coupled flexural waves, simply shifted to higher frequencies because of the thinner, stiffer freshwater ice. We use the audio track from the well-known National Geographic short film "How Skating on Thin Ice Creates Laser-Like Sounds" (Rankin, 2018) to illustrate this. The frequency of the strong monochromatic component corresponding to the air-coupled flexural wave is $\sim 725$ Hz for the scene from 16 s to 33 s, as shown in Fig. 12. Using Eq. (15) we calculate that the ice was $\sim 4.3$ cm thick, assuming Young's modulus of 8.5 GPa, Poisson's ratio of 0.33, water density of 1000 kg m$^{-3}$, ice density of 917 kg m$^{-3}$, water depth of at least 0.3 m and sound speed of 329 m s$^{-1}$ corresponding to an air temperature of $-3.9$ °C. This is in line with the measured ice thickness presented in the film

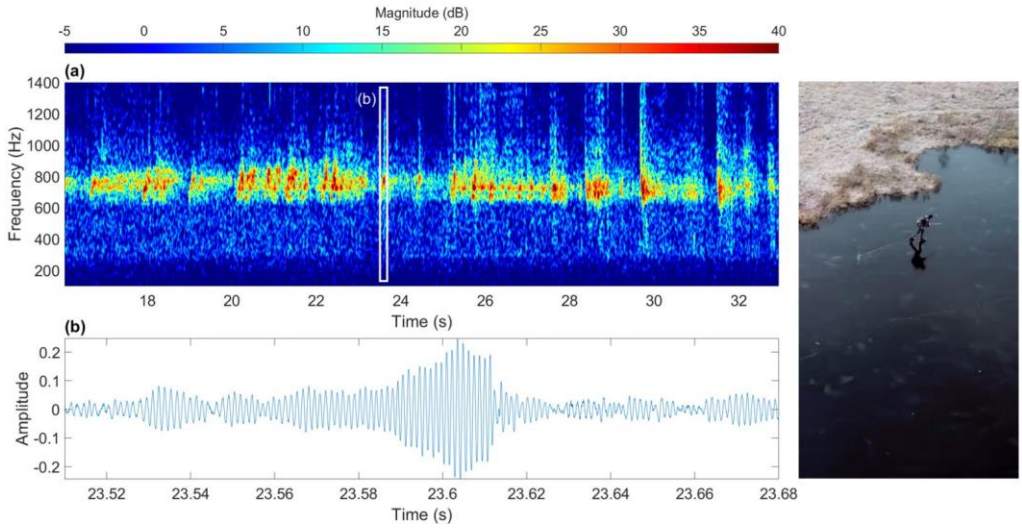


**Figure 12.** **(a)** Spectrogram of audio track from 16 s to 33 s of the National Geographic short film "How Skating on Thin Ice Creates Laser-Like Sounds" (Rankin, 2018) and **(b)** example of waveform dominated by the monochromatic air-coupled flexural wave and broadband impulse at 23.61 s from skate blade cracking ice. Spectrogram is composed of $2^{12}$ sample ($\sim 0.09$ s), 90 % overlapping Kaiser windows with shape parameter $\beta = 10$.

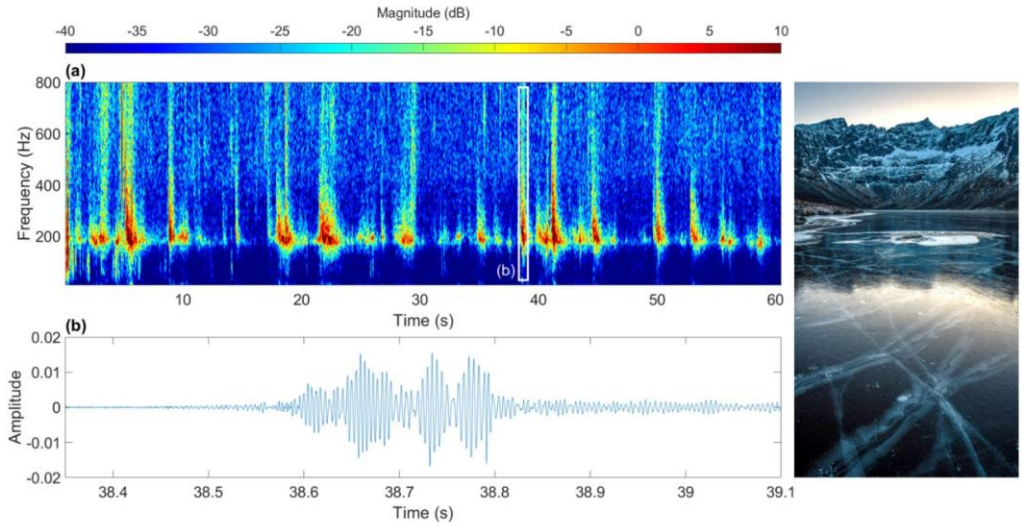


**Figure 13.** **(a)** Spectrogram of natural ice quakes at Storvatnet, Kvaløya (Norway), recorded at midday on 3 January 2021 with the built-in microphone of a Sony a6500 camera at a height of $\sim 1.2$ m above the ice. Spectrogram is composed of $2^{13}$ sample ($\sim 0.17$ s), 90 % overlapping Kaiser windows with shape parameter $\beta = 10$. The waveform of the strong $\sim 190$ Hz monochromatic component corresponding to the air-coupled flexural wave is shown in detail in **(b)**.

and illustrates the potential to use air-coupled flexural waves recorded by a simple microphone to estimate ice thickness.

Detonating cord seismic sources were used for the experiments presented in this study, but other impulsive sources acting on a floating ice sheet also have the potential to excite air-coupled flexural waves. Hammer blows are an alternative active source, while crack propagation is a potential passive source that produces a sudden energy release capable of exciting propagating elastic waves in the plate and acoustic pressure waves in air. Ice quakes produced by the sudden cracking of floating ice are a well-known phenomenon (Kavanaugh et al., 2019; Moreau et al., 2020b; Olinger et al., 2019; Ruzhich et al., 2009) and are typically related to the build-up of stress by thermal, tidal and wind forces. This phenomenon has also been studied from the structural non-destructive testing perspective, for example, by Haider and Giurgiutiu (2018) who model the acoustic emission of axis-

symmetric circular crested Lamb waves excited by crack propagation in a steel plate.

In order to illustrate that ice quakes are capable of producing air-coupled flexural waves, we went out and recorded a series of ice quakes around midday, 3 January 2021, at Storvatnet, Kvaløya (Norway), using the built-in microphone of a Sony a6500 digital camera. This is a relatively low-quality microphone with no shielding from wind noise, but the monochromatic air-coupled flexural waves can still be clearly discerned (in addition to the broadband impulses of the ice crack ruptures). The ice was not drilled, but its thickness was estimated to be 10–20 cm by visual assessment of vertical cracks running through the clear, black ice. The air-coupled flexural frequency of $\sim 195$ Hz indicates the thickness was 16 cm, using the same physical properties for lake ice as introduced earlier. The midday occurrence of these ice quakes, when air temperature was relatively high, suggests they were caused by thermal expansion stresses (Ruzhich et al., 2009). The results of this study and the examples shown in Figs. 12 and 13 suggest that the non-contact, passive recording of air-coupled flexural waves using a single microphone may provide an additional, alternative method of passive flexural wave ice thickness estimation. This complements previously demonstrated passive seismic monitoring methods employing array-based wave field transform approaches (Moreau et al., 2020a) or noise interferometry and Bayesian inversion (Moreau et al., 2020b). The use of inexpensive single, non-contact sensors is an attractive aspect of the air-coupled flexural wave method, particularly the fact that a microphone could be placed on land when the ice is too thin to safely traverse. However, further study is needed to reveal the extent to which the temporal occurrence of ice quakes producing air-coupled flexural waves and reduced air–ice coupling due to thick snow covers may limit the practical acquisition season.

## 7 Conclusion

Air-coupled flexural waves were found to be a robust feature of first-year sea ice excited by explosive sources over a range of ice thicknesses up to $\sim 80$ cm. The physics of these waves can be understood from a theoretical perspective that has largely developed through the study of moving vehicles on floating plates. The dynamical model that we favour is straightforward to understand in terms of linear filter theory, and we derived a closed-form solution of the dispersion relation that relates ice thickness directly to the air-coupled flexural wave frequency and air wave velocity. We tested the proposed closed-form ice thickness estimator extensively on field data from four field seasons and found a remarkably good agreement with in situ borehole measurements. The phenomenon of air-coupled flexural waves is relatively familiar to the wild ice-skating community, in which thin ice produces air-coupled flexural waves that are readily audible. Here we build on the pioneering efforts of Press and Ewing (1951), developing a more accessible theory supported by modern numerical and Fourier transform methods, to show that the same phenomenon also occurs for much thicker sea ice, simply shifted to a lower frequency regime. We have mainly presented data that were acquired for the primary purpose of reflection seismic profiling, but a key benefit of air-coupled flexural waves is that they can also be recorded with very simple equipment, such as a single microphone located either above the ice sheet or along the shoreline. Ice quakes produced by natural cracking excite air-coupled flexural waves for freshwater lake ice, which raises the potential that passive recording of air-coupled flexural waves may also be possible for sea ice.

## Appendix A: Possible effect of land on ice sheet lateral boundary condition

Two outlier points were observed for the 2017 field season, in which ice with drilled thickness of 30–35 cm near land had air-coupled flexural frequency similar to ice of 50 cm drilled thickness further seaward (see Fig. 10). To illustrate that this may be attributable to a lateral boundary condition effect, we approximate an ice sheet of finite extent as a collection of arbitrarily small, uniformly loaded, circular plates. The ice along the shoreline is represented by assuming a clamped boundary condition, while the ice far from shore is considered simply supported by the neighbouring plate elements. We may then find the thicknesses of a simply supported and a clamped plate that lead to equal maximum tangential stresses. From Hearn (1997), the maximum tangential stress, occurring at the centre of the simply supported plate, $\sigma_s$, and the clamped plate, $\sigma_c$, is given by

$$\sigma_s = \frac{3qR^2}{8h_s^2}(3+v) \quad \text{and} \quad \sigma_c = \frac{3qR^2}{8h_c^2}(1+v).$$

Here, $q$ is the uniformly distributed load, $R$ is the plate radius, $v$ is Poisson's ratio, and $h_s$ and $h_c$ are the thicknesses of the simply supported and clamped plates, respectively. Equating the two expressions gives

$$\frac{h_c^2}{h_s^2} = \frac{(1+v)}{(3+v)}$$

so that $h_c \approx 0.63 h_s$ for $v = 0.33$. Therefore, it is anticipated that ice 50 cm thick far from shore will experience the same maximum tangential stress under load as ice that is $0.63 \times 50 = 32$ cm thick at the shoreline (consistent with the outlier points from the 2017 field season). We may similarly equate the maximum deflections of the plates, which also occur at the plate centres. Hearn (1997) gives the relevant expressions for the maximum deflection of the plates as

$$w_s = \frac{3qR^4}{16Eh_s^3}(5+v)(1-v) \quad \text{and} \quad w_c = \frac{3qR^4}{16Eh_c^3}\left(1-v^2\right),$$

where $E$ is the Young's modulus. By equating the two deflections and simplifying we find

$$\frac{h_c^3}{h_s^3} = \frac{\left(1-v^2\right)}{(5+v)(1-v)},$$

which again gives $h_c \approx 0.63 h_s$ for $v = 0.33$. Since both tangential stress and strain are equal for a clamped plate with 63 % of the thickness of a corresponding simply supported plate, the boundary condition effect can also be understood as a change in effective elastic modulus. This supports the heuristic approximation of the lateral boundary condition effect by a spatially variable, effective elastic modulus. While this theoretical description is simplistic since, for example, the fluid loading is ignored, it highlights that the boundary condition of a finite plate can play a significant role. It would be beneficial to explore this effect in greater detail in future studies, particularly with regard to the length scale involved in the transition from clamped to simply supported behaviour. Accurately describing this behaviour would require the collection of more detailed field data in the zone near the shoreline in order to constrain the development of a more complete model, such as a full finite element simulation.

*Code and data availability.* Data and code used to produce this research can be shared upon request to the authors.

*Author contributions.* Development of theory and associated modelling was carried out by RR and AH. The field campaigns were administered and led by TAJ and BOR. Initial data preparation was conducted by BOR, while the air-coupled flexural wave data processing methodology was developed and implemented by RR. RR was responsible for analysing and visualizing the data and writing the manuscript with contributions from all authors.

*Competing interests.* The authors declare that they have no conflict of interest.

*Disclaimer.* Publisher's note: Copernicus Publications remains neutral with regard to jurisdictional claims in published maps and institutional affiliations.

*Acknowledgements.* The authors would like to thank the reviewers for their detailed and constructive comments on the early manuscript versions. These comments were an important foundation that considerably improved the final result.

*Financial support.* This research has been supported by the University of Tromsø (UiT) – The Arctic University of Norway, ARCEx partners and the Research Council of Norway (grant no. 228107). The publication charges for this article have been funded by a grant from the publication fund of UiT – The Arctic University of Norway.

*Review statement.* This paper was edited by Christian Haas and reviewed by Ludovic Moreau and one anonymous referee.

## References

Bhattacharya, M., Guy, R., and Crocker, M.: Coincidence effect with sound waves in a finite plate, J. Sound Vibr., 18, 157–169, 1971.

Brower, N., Himberger, D., and Mayer, W.: Restrictions on the existence of leaky Rayleigh waves, IEEE T. Son. Ultrason., 26, 306–307, 1979.

DiMarco, R., Dugan, J., Martin, W., and Tucker III, W.: Sea ice flexural rigidity: a comparison of methods, Cold Reg. Sci. Technol., 21, 247–255, 1993.

Dinvay, E., Kalisch, H., and Părău, E.: Fully dispersive models for moving loads on ice sheets, J. Fluid. Mech., 876, 122–149, 2019.

Ewing, M. and Crary, A.: Propagation of elastic waves in ice. Part II, Physics, 5, 181–184, 1934.

Ewing, M. and Press, F.: Tide-gage disturbances from the great eruption of Krakatoa, EOS T. Am. Geophys. Un., 36, 53–60, 1955.

Franke, S. J. and Swenson Jr., G.: A brief tutorial on the fast field program (FFP) as applied to sound propagation in the air, Appl. Acoust., 27, 203–215, 1989.

Garrett, C.: A theory of the Krakatoa tide gauge disturbances, Tellus, 22, 43–52, 1970.

Greenhill, A.: Wave motion in hydrodynamics, Am. J. Math., 1886, 62–96, 1886.

Greenhill, G.: I. Skating on thin ice, The London, Edinburgh, and Dublin Philosophical Magazine and Journal of Science, 31, 1–22, 1916.

Griffin, J.: The Magic (and Math) of Skating on Thin Ice without Falling In, Scientific American, available at: https://www.scientificamerican.com/article/the-magic-and-math-of-skating-on-thin-ice-without-falling-in/ (last access: 16 June 2020), 2018.

Haider, M. F. and Giurgiutiu, V.: Analysis of axis symmetric circular crested elastic wave generated during crack propagation in a plate: A Helmholtz potential technique, Int. J. Solids Struct., 134, 130–150, 2018.

Hanssen, A.: Multidimensional multitaper spectral estimation, Signal Process., 58, 327–332, 1997.

Harb, M. S. and Yuan, F.-G.: Air-coupled nondestructive evaluation dissected, J. Nondestruct. Eval., 37, 1–19, 2018.

Harkrider, D. and Press, F.: The Krakatoa Air–Sea Waves: An Example of Pulse Propagation in Coupled Systems, Geophys. J. Int., 13, 149–159, 1967.

Haskell, N. A.: A note on air-coupled surface waves, B. Seismol. Soc. Am., 41, 295–300, 1951.

Hearn, E. J.: Chapter 7 – Circular Plates and Diaphragms, in: Mechanics of Materials 2, 3rd Edn., edited by: Hearn, E. J., Butterworth-Heinemann, Oxford, 1997.

Hinchey, M. and Colbourne, B.: Research on low and high speed hovercraft icebreaking, Can. J. Civil Eng., 22, 32–42, 1995.

Hunkins, K.: Seismic studies of sea ice, J. Geophys. Res., 65, 3459–3472, 1960.

Johansen, T. A., Ruud, B. O., Tømmerbakke, R., and Jensen, K.: Seismic on floating ice: data acquisition versus flexural wave noise, Geophys. Prospect., 67, 532–549, 2019.

Kashiwagi, M.: Transient responses of a VLFS during landing and take-off of an airplane, J. Mar. Sci. Technol., 9, 14–23, 2004.

Kavanaugh, J., Schultz, R., Andriashek, L. D., van der Baan, M., Ghofrani, H., Atkinson, G., and Utting, D. J.: A New Year's Day icebreaker: ice quakes on lakes in Alberta, Canada, Can. J. Earth Sci., 56, 183–200, 2019.

Kiefer, D. A., Ponschab, M., Rupitsch, S. J., and Mayle, M.: Calculating the full leaky Lamb wave spectrum with exact fluid interaction, J. Acoust. Soc. Am., 145, 3341–3350, 2019.

Kozin, V., Zemlyak, V., and Rogozhnikova, E.: Increasing the efficiency of the resonance method for breaking an ice cover with simultaneous movement of two air cushion vehicles, J. Appl. Mech. Tech. Ph.+, 58, 349–353, 2017.

Kozin, V. M. and Pogorelova, A. V.: Submarine moving close to the ice-surface conditions, Proceedings of the Eighteenth (2008) International Offshore and Polar Engineering Conference, 6–11 July 2008, Vancouver, British Columbia, Canada, 630–637, 2008.

Lundmark, G.: Skating on thin ice-And the acoustics of infinite plates, INTER-NOISE and NOISE-CON Congress and Conference Proceedings, The Hague, the Netherlands, 410–413, 2001.

Matiushina, A. A., Pogorelova, A. V., and Kozin, V. M.: Effect of impact load on the ice cover during the landing of an airplane, Int. J. Offshore Polar, 26, 6–12, 2016.

Miles, J. and Sneyd, A. D.: The response of a floating ice sheet to an accelerating line load, J. Fluid Mech., 497, 435–439, 2003.

Moreau, L., Boué, P., Serripierri, A., Weiss, J., Hollis, D., Pondaven, I., Vial, B., Garambois, S., Larose, É., and Helmstetter, A.: Sea ice thickness and elastic properties from the analysis of multimodal guided wave propagation measured with a passive seismic array, J. Geophys. Res.-Oceans, 125, e2019JC015709, https://doi.org/10.1029/2019JC015709, 2020a.

Moreau, L., Weiss, J., and Marsan, D.: Accurate estimations of sea-ice thickness and elastic properties from seismic noise recorded with a minimal number of geophones: from thin landfast ice to thick pack ice, J. Geophys. Res.-Oceans, 125, e2020JC016492, https://doi.org/10.1029/2020JC016492, 2020b.

Mozhaev, V. and Weihnacht, M.: Subsonic leaky Rayleigh waves at liquid–solid interfaces, Ultrasonics, 40, 927–933, 2002.

Nickalls, R. W.: A new approach to solving the cubic: Cardan's solution revealed, Math. Gaz., 77, 354–359, 1993.

Norwegian Meteorological Institute: Norsk Klimaservicesenter – Observations and weather statistics, available at: https://seklima.met.no/ (last access: 14 December 2020), 2020.

Novoselov, A., Fuchs, F., and Bokelmann, G.: Acoustic-to-seismic ground coupling: coupling efficiency and inferring near-surface properties, Geophys. J. Int., 223, 144–160, 2020.

Nugroho, W. S., Wang, K., Hosking, R., and Milinazzo, F.: Time-dependent response of a floating flexible plate to an impulsively started steadily moving load, J. Fluid Mech., 381, 337–355, 1999.

Olinger, S., Lipovsky, B., Wiens, D., Aster, R., Bromirski, P., Chen, Z., Gerstoft, P., Nyblade, A. A., and Stephen, R.: Tidal and thermal stresses drive seismicity along a major Ross Ice Shelf rift, Geophys. Res. Lett., 46, 6644–6652, 2019.

Press, F. and Ewing, M.: Theory of air-coupled flexural waves, J. Appl. Phys., 22, 892–899, 1951.

Press, F. and Oliver, J.: Model study of air-coupled surface waves, J. Acoust. Soc. Am., 27, 43–46, 1955.

Press, F., Crary, A., Oliver, J., and Katz, S.: Air-coupled flexural waves in floating ice, EOS T. Am. Geophys. Un., 32, 166–172, 1951.

Rankin, A.: How Skating on Thin Ice Creates Laser-Like Sounds, short film, National Geographic, available at: https://www.nationalgeographic.com/adventure/article/skating-thin-black-ice-creates-sound-nordic-spd (last access: 23 June 2021), 2018.

Renji, K., Nair, P., and Narayanan, S.: Critical and coincidence frequencies of flat panels, J. Sound Vibr., 205, 19–32, 1997.

Ruzhich, V., Psakhie, S. G., Chernykh, E., Bornyakov, S., and Granin, N.: Deformation and seismic effects in the ice cover of Lake Baikal, Russ. Geol. Geophys.+, 50, 214–221, 2009.

Sandven, S., Hansen, R. K., Eknes, E., Kvingedal, B., Bruserud, K., Nilsen, F., Wåhlin, J., Sagen, H., and Kloster, K.: NERSC Technical Report no. 294, Nansen Environmental Remote Sensing Center, Bergen, Norway, 2010.

Schulkes, R. M. S. M. and Sneyd, A. D.: Time-dependent response of floating ice to a steadily moving load, J. Fluid Mech., 186, 25–46, 1988.

Skarðhamar, J. and Svendsen, H.: Short-term hydrographic variability in a stratified Arctic fjord, Geol. Soc. Lond. Spec. Publ., 344, 51–60, 2010.

Squire, V., Robinson, W., Langhorne, P., and Haskell, T.: Vehicles and aircraft on floating ice, Nature, 333, 159–161, 1988.

Squire, V., Hosking, R. J., Kerr, A. D., and Langhorne, P.: Moving Loads on Ice Plates, Kluwer Academic Publishers, Dordrecht, the Netherlands, 1996.

Sutherland, G. and Rabault, J.: Observations of wave dispersion and attenuation in landfast ice, J. Geophys. Res.-Oceans, 121, 1984–1997, 2016.

Takizawa, T.: Response of a floating sea ice sheet to a steadily moving load, J. Geophys. Res.-Oceans, 93, 5100–5112, 1988.

Thomson, D. J.: Spectrum estimation and harmonic analysis, P. IEEE, 70, 1055–1096, 1982.

Timco, G. and Frederking, R.: A review of sea ice density, Cold Reg. Sci. Technol., 24, 1–6, 1996.

Timco, G. W. and Weeks, W. F.: A review of the engineering properties of sea ice, Cold Reg. Sci. Technol., 60, 107–129, 2010.

Van der Sanden, J. and Short, N.: Radar satellites measure ice cover displacements induced by moving vehicles, Cold Reg. Sci. Technol., 133, 56–62, 2017.

Wadhams, P., Wilkinson, J. P., and McPhail, S.: A new view of the underside of Arctic sea ice, Geophys. Res. Lett., 33, L04501, https://doi.org/10.1029/2005GL025131, 2006.

Wang, K., Hosking, R., and Milinazzo, F.: Time-dependent response of a floating viscoelastic plate to an impulsively started moving load, J. Fluid Mech., 521, 295–317, https://doi.org/10.1017/S002211200400179X, 2004.

Wilson, J. T.: Coupling between moving loads and flexural waves in floating ice sheets, U.S. Army Snow, Ice, and Permafrost Research Establishment, SIPRE technical report no. 34, Corps of Engineers, U.S. Army, Wilmette, Illinois, USA, 1955.

Yang, T. C. and Yates, T. W.: Flexural waves in a floating ice sheet: Modeling and comparison with data, J. Acoust. Soc. Am., 97, 971–977, 1995.

Yeung, R. and Kim, J.: Effects of a Translating Load on a Floating Plate – Structural Drag and Plate Deformation, J. Fluid. Struct., 14, 993–1011, 2000.

Yilmaz, Ö.: Seismic data analysis: Processing, inversion, and interpretation of seismic data, Society of exploration geophysicists, 2nd Edn., 938–942, 2001.

Zhu, J.: Non-contact NDT of concrete structures using air coupled sensors, Newmark Structural Engineering Laboratory, University of Illinois at Urbana, Report No. NSEL-010, 2008.

# 3 Synthesis

## 3.1 Common themes

This PhD thesis is essentially a study in environmental seismology with a particular focus on applications involving floating ice and permafrost and therefore fits neatly under the categorization cryoseismology. Through specific case studies the two main subcategories of environmental seismology defined by Larose et al. (2015) have been explored, i.e., 1) studies of natural seismic vibrations triggered by processes occurring outside of the solid Earth and 2) studies of seismic vibrations whose propagation is controlled or perturbed by environmental external parameters. Natural seismic vibrations triggered by thermal stresses in ice emerged as a common and important theme in this thesis through the studies of frost quakes detailed in Papers 1 and 2. By contrast, from the active seismic experiments conducted on floating sea ice, described in Paper 3, a class of air-coupled flexural waves were isolated whose propagation is largely controlled by environmental parameters, predominantly the ice thickness, its rigidity and to a lesser extent the air temperature.

It is interesting to observe that grouping together a set of contrasting case studies in this thesis highlights that the categorical distinction introduced by Larose et al. (2015) is far from absolute. There is significant overlap and potential for cross pollination between studies focused on seismic vibrations triggered by, e.g., thermal stresses in the cryosphere and those focused on how the environmental physical parameters affect the propagation of seismic waves. In Paper 2 the primary focus was on the source mechanism for frost quakes, which we found could be linked to accumulated thermal stresses in the ground. However, in Paper 1 we also showed that the propagation of the surface waves excited by frost quakes is affected by the layered structure of the ground, in particular the thickness and rigidity/stiffness of these layers and their seasonal variations. The wave propagation effects were illustrated by providing examples of experimental dispersion images and theoretical dispersion spectra calculated by the global matrix method describing wave propagation in layered media.

In the preface to Paper 1, it was also demonstrated that the multimodal surface wave dispersion was better resolved by passively recording frost quakes than by active source experiments utilizing sledgehammer or explosive sources. This serves as a demonstration that the emerging trend in environmental seismology towards continuous, passive recording, which has been driven by technological advancement (Larose et al., 2015), can also deliver high-quality transient signals. This

means that passive source seismic experiments may increasingly overlap with survey applications that were traditionally the domain of active source experiments. An additional benefit of expanding the applications of passive surveying techniques is that the environmental disturbance or footprint of these surveys may be reduced compared to active, artificial source seismic experiments, which is an important ethical consideration within the field of environmental seismology (e.g. Stemland et al., 2019).

In Paper 3, the main focus was on an existing catalogue of active source seismic experiments and developing an understanding of how the propagation of a specific wave mode, the air-coupled flexural wave, is affected by environmental parameters (ice thickness, rigidity, air temperature). Notably, these experiments were not designed with this specific wave mode and application in mind, but provided a rich dataset that proved highly suitable for studying this phenomenon. However, within the broader scope of this thesis and following our work on frost quakes, it was natural to hypothesize that air-coupled flexural waves might also be recorded passively, with naturally occurring ice quakes acting as the seismic source. While this is still a preliminary finding, it was an important result that we were able to go into the field and record examples of air-coupled flexural waves associated with ice quakes resulting from thermal expansion stresses in fresh-water lake ice. That this was possible to observe within a short distance from campus also demonstrates a key benefit of the University of Tromsø as a research institution situated above the Arctic Circle. It follows then that air-coupled flexural wave studies also fit with the paradigm of environmental seismology in that they are both 1) potentially triggered by natural processes outside the solid Earth and 2) their propagation is strongly determined by the environmental parameters of ice thickness, rigidity and air temperature. Had the study leading to Paper 3 been conducted in isolation, removed from the context of the broader thesis, it is not certain that the full picture of the air-coupled flexural wave phenomenon and the potential of ice quakes and passive recording with microphones would have been appreciated.

The effect of temperature changes is of fundamental importance in the cryosphere. In this thesis, stress caused by changing temperature, i.e., thermal stress, emerges as a common theme. In Paper 1, we identified that frost quakes tended to occur during periods of rapidly decreasing temperature, a fact that was already quite well established in the literature (Barosh, 2000; Battaglia et al., 2016; Matsuoka et al., 2018; Nikonov, 2010). This association was further elaborated in Paper 2, where it was developed into the more rigorous concept of thermal stress. While the importance of thermal stress as a trigger for ground fracturing was already known (Mellon, 1997; Okkonen et al., 2020; Podolskiy et al., 2019), the combination of a continuous seismic record and the long term, high-resolution borehole temperature measurements introduced in Paper 2 allowed us to extend the

existing concepts and models to a new level of detail. The concept of thermal stress induced cracks is also important to the potential to passively record the air-coupled flexural waves of floating ice sheets as discussed in Paper 3.

### 3.1.1 Survey design

Survey design plays an intrinsically important role in all seismological studies and survey design considerations also emerge as a common theme of this thesis. An overarching point is that optimal survey design is very difficult to achieve in practice and requires detailed foresight of the dynamic processes to be recorded or measured. It is important to reflect on the topic of survey design because following the work reported on in this thesis, we have improved knowledge of cryoseismological phenomena that can be used to optimize or re-evaluate how future surveys may be conducted.

The studies included in this thesis were, in general, of an exploratory nature, meaning that the survey design was not optimal. For example, the 2D receiver arrays used to record frost quakes as reported in Paper 1 gave quite good spatial/wavenumber sampling, resulting in detailed dispersion imaging of the complex multi-modal pattern of surface wave dispersion. However, constraints of limited battery capacity and logistical challenges of battery swapping severely compromised the time windows that could be surveyed. Having gained a better understanding of the frequencies, wavelengths and propagation velocities of surface waves in the study area, it would be possible to further optimize the array design around the limiting factor of battery capacity or better evaluate the cost/benefit of newer generation recording nodes that would enable longer recording times (e.g. Beker et al., 2016; Dean and Sweeney, 2019). The study reported on in Paper 2 was conceptualized to be complementary to Paper 1. Since the SPITS array is a permanent installation, it was much better suited to study the temporal distribution of frost quakes, even though the reduced number of sensors and coarser spatial and temporal sampling gave poorer resolution of frequencies and wavenumbers of surface waves from individual frost quakes.

Paper 3 developed around the observation of an interesting phenomenon, the air-coupled flexural wave, in a number of existing data sets. The results of the study indicated that similarly useful measurements of air-coupled flexural waves could probably have been made using a radically simplified acquisition setup consisting of microphones and perhaps a thermometer to measure air temperature. This simplified acquisition setup could also be designed as a passive source experiment, using natural ice quakes as the seismic source. This would, in turn, have implications for survey

logistics, cost and the window of time that could be surveyed, in addition to significantly reducing the environmental footprint of the survey. This study is an interesting example where observations were made on real field data, which subsequently drove us to re-examine and improve our understanding of the physical dynamics underpinning the observations. The improved understanding that comes from theory and modelling then ultimately allowed us to hypothesize alternate, potentially more efficient ways of observing the same phenomenon.

### 3.1.2 Selection of simple models

Numerical models constitute an important part of the studies included in this thesis. Models are important because, generally across geophysics, our capacity to measure is very limited given the complexity and scale of the studied phenomena leading to a set of inherently underdetermined problems (e.g. Kleinhans et al., 2010). The construction of models therefore becomes essential to the problem of understanding and generalising from the observed phenomena. Model development proceeds via a two-step process involving 1) conceptualisation of key processes operating in the system and the interaction between system components, and 2) formalising or encoding of the conceptual model with precise mathematical language. Both the conceptualisation of the problem and the choice of mathematical representation then affect the performance of the model (Bokulich and Oreskes, 2017).

An infinite number of models may be conceptualised, but as stated by Box (1979) “all models are wrong, but some are useful”, which highlights that model selection should be a considered choice. As articulated by Oreskes (2003), “the purpose of modelling in science must be congruent with the purpose of science itself: to gain understanding of the natural world”. Simple models can illustrate fundamental dynamical concepts, stimulate new hypotheses and facilitate conceptual understanding (Bokulich and Oreskes, 2017; Stocker and Knutti, 2003). On the other hand, overly complex models can become analytically impenetrable, i.e., the reason for success or failure of the model to explain observational data becomes almost impossible to attribute to specific modelling assumptions (Lenhard and Winsberg, 2011). In this context, the focus throughout this thesis was to develop a set of the simplest possible models that could represent the most essential features or dynamics recorded in the experimental seismic data collected in the field.

In Paper 1, the sub-surface is represented by a highly simplified layer-cake structure, consisting of a small number of flat, horizontal and homogeneous individual layers according to the global matrix

method of Lowe (1995). It was striking to observe that a complex multimodal dispersion pattern, similar to that derived from field recording of frost quakes, could be produced by a simple three-layer model with an anomalously stiff, high-velocity upper layer. This observation points towards the importance of seismic velocity inversion, where the high-velocity layer may act as a partial or complete waveguide. This is an important and fundamental departure from the normal situation where shear-wave velocity increases monotonically with depth that invalidates the assumption that longer wavelengths sample deeper points in the subsurface. This consequently complicates the inversion from observed wave dispersion to inferred S-wave velocity depth profile (e.g. Foti et al., 2018; Ryden and Lowe, 2004).

In Paper 3, the air-ice-water system corresponding to a floating ice-sheet was modelled as a thin plate of infinite horizontal extent, floating on an incompressible, inviscid fluid of finite depth. This is a highly simplified arrangement, but was sufficient to investigate the essential dynamics of the air-coupled flexural wave. It is particularly noteworthy that the dynamics of the air-coupled flexural wave were modelled without the explicit inclusion of an air layer in the model. In this case, the simplest solution was to consider the compressional wave propagating in the air as an external force pushing down on the ice surface, expanding radially at the speed of sound in air. This simplification highlights the similarity of the air-coupled flexural wave with the engineering problem of a moving vehicle on a floating sheet of ice (e.g. Squire et al., 1996). In common with the thermoviscoelastic model introduced in Paper 2, the floating ice is essentially a driven and damped dynamical system. The driver is the pressure pulse of the air wave and the damping is a simple heuristic representation of the viscosity of ice that governs wave attenuation and ensures the system remains numerically stable when driven over time.

By contrast, the thermoviscoelastic dynamical model introduced in Paper 2 is a simple dynamical system driven by thermal stresses resulting from temperature changes. Stress accumulates elastically in the ground as it is simultaneously dissipated viscously, representing slow movement or frost creep. If the stress accumulates faster than it is dissipated, the tensile strength of the ground can be exceeded causing a sudden stress release, or frost quake. This highly simplified model focuses specifically on the thermal contraction mechanism of ground cracking. While other mechanisms of ground cracking might also play a role, such as capillary water migration and ice lens formation at the frozen fringe (e.g. Peppin and Style, 2013), the simple model allows us to directly assess to what degree the single mechanism of thermal contraction can explain the observed dynamics of ground motion.

## 3.2 Broader relevance of the research

The cryosphere is strongly in focus throughout this thesis, with a particular focus on permafrost and the periglacial environment, as well as floating plates of ice on both salt and fresh bodies of water. The case studies included in this thesis give new insights into the dynamics and physics of these aspects of the cryosphere and contribute towards the development of a geophysical toolbox that can be used to monitor changes occurring in response to a warming climate. There is, however, also significant methodological and phenomenological overlap with other research fields, most notably those relating to civil engineering. For example, the stiff top layer resulting from freezing winter air temperatures and elevated ground-ice content that was identified in Paper 1 is directly analogous to a layer of pavement resting on a substrate as exemplified by the study of Ryden and Lowe (2004). Similarly, very large floating structures (VLFS) are under development for applications including floating airports, bridges, docks, storage facilities, wind and solar power farms etc. and behave analogously to floating ice sheets from the perspective of flexural waves (Kakinuma et al., 2012; Ohkusu and Namba, 2004; Wang and Tay, 2011). In these analogous cases, there is significant scope for knowledge transfer between fields, particularly regarding methodology and mathematical theory.

In Paper 2, the dynamics of thermoviscoelastic materials was shown to be an important factor triggering thermal contraction cracking and the release of accumulated elastic stress as frost quakes. This is also an important subject within civil engineering, particularly due to the risk of thermal cracking and material damage. Measuring thermal stress and strain in asphalt can allow optimisation of aggregate and binder components to produce asphalt mixtures that are resistant to thermal contraction cracking under seasonal or diurnal temperature fluctuations (Abu Al-Rub et al., 2011; Alavi et al., 2013; Apeagyei et al., 2008; Pszczola et al., 2019). Pavements constructed of concrete slabs can also be vulnerable to cracking due to freezing temperatures and thermal stresses exceeding the breaking strength (Monismith et al., 1965). The performance of pavement materials can also vary over time due to cyclic temperature loading so that an understanding of the geo-climatic factor is important in order to estimate the expected lifespan of the construction (Merbouh, 2012). Thermal stresses also play an important role in the risk of cracking for newly cast concrete structures, which is of significance to the service lifetime and function of these structures (Harrison, 1981; Larson, 2003; Yuan and Wan, 2002).

The demonstration, in Paper 3, that air-coupled flexural waves are compatible with the theory of moving loads on floating plates highlights the strong physical connection that exists with the important field of moving vehicles on ice. For the case of vehicles, estimation of ice thickness and a physical

understanding of flexural waves is important to ensure that cars, trucks and planes do not break through thin ice or cause it to buckle by exciting large-amplitude flexural waves (Matiushina et al., 2016; Takizawa, 1988; Van der Sanden and Short, 2017; Yeung and Kim, 2000). Other vehicles like icebreaking hovercraft and submarines may seek to do the opposite, i.e., surface through thin ice or cause it to fracture and break apart efficiently by maximising the amplitude of flexural waves they excite (Hinchey and Colbourne, 1995; Kozin et al., 2017; Kozin and Pogorelova, 2008). Common to these applications is that it is critical to understand the physics that govern the air-ice-water dynamical system when it is driven by a load moving across its surface.

The air-coupled flexural waves studied in Paper 3 are also directly analogous to the non-contact, non-destructive measurement of plate properties in engineering applications using guided waves and acoustic emission (Harb and Yuan, 2018). From the cryoseismological standpoint, non-contact estimation of ice thickness may be attractive from a field safety perspective when the ice is too thin to safely traverse. Correspondingly, from an engineering perspective, non-contact guided-wave measurements can have operational benefits that increase testing speed or capacity, by eliminating the need for physical coupling between the sensor and surface. Achieving adequate, repeatable surface coupling can be time consuming for concrete slabs due to the need to polish rough surfaces or problems of limited access (Harb and Yuan, 2018; Zhu, 2008). The concept of coupling between surface or guided flexural waves in solid structures with pressure waves in fluids is also of fundamental importance in the field of structural acoustics (e.g. Everstine, 1997; Hambric, 2006; Ohayon and Soize, 1997). The structures that are studied range from relatively simple cases like concrete slabs (Broyles et al., 2020; Park et al., 2015; Zhu, 2008) to the intricately complicated structure of a violin (Bissinger, 2008). Understanding the coupling between waves in the solid and the air may be leveraged towards design goals such as reduction or amplification of noise, or minimisation of vibration within the solid (Christensen et al., 1998; Hambric, 2006).

The number of researchers working on engineering applications of guided and surface waves far outweighs the number working in the field of environmental seismology, so it is relatively common to discover research results that can be adapted from engineering studies and utilised in environmental seismology. However, it is important to highlight that this synergy is bidirectional such that studies in cryoseismology, which may seem esoteric to some, also have deep physical resonance with other fields and in particular with common engineering applications.

# 4 Conclusion

## 4.1 Thesis statement and contributions

This thesis is devoted to advancing the research field of cryoseismology through specific case studies of frost quakes in periglacial/permafrost systems and flexural waves in sea/lake ice systems. Environmental seismology is an emerging paradigm, underpinned by an expanding focus on passive surveying and/or long-term recording of seismic waves. To an extent, the development of this paradigm is driven by technological improvements in data acquisition and processing, novel aspects of which have been a key focus of this thesis. The cryosphere spans a wide range of environments and dynamic processes relating to ice or frozen ground are both a source of and affect the propagation of seismic waves. Cryoseismology is, correspondingly, an important sub-discipline of environmental seismology. The ability to understand the current state of the cryosphere and the changes resulting from global warming have important implications, both for those who inhabit or traverse the frozen parts of the planet, and globally through climate feedback mechanisms. In line with the goal to better understand the dynamics of the cryosphere through cryoseismology, the principal contributions of this thesis are:

- The demonstration that a complex, multimodal surface wave dispersion structure can be resolved from frost quake signals recorded by a sufficiently dense array of passively recording seismometers.
- The illustration that this complex dispersion structure can be related to a simple arrangement of horizontal layers, with an anomalously high-velocity surface layer is important for the interpretation of seismic surface wave studies in periglacial environments. The observed wave dispersion was interpretable in terms of elevated ground ice content and its seasonal variation, which also hints at the potential for seismic surface wave monitoring of long-term changes and trends in these environments.
- The connection between cryoseisms and thermal stress was explored in greater detail than previously attempted using a long-term, continuous seismic record. Thermal contraction cracking appears to be an important trigger of frost quakes in the periglacial environment, though it is also clear that additional mechanisms may play a role.
- The usefulness of air-coupled flexural waves for estimating the thickness of a floating ice sheet was demonstrated using a multi-year catalogue of field experiments. The work reported in this

thesis may hopefully serve to reinvigorate this topic, which has stagnated since the early investigation period in the 1950's. The simple theoretical framework we implemented unites a wide range of observations in different physical settings and highlights alternative acquisition approaches. Passive recording by relatively low-tech, inexpensive microphones, in particular, may be worthy of further research attention.

In general, this thesis highlights the richness and value of long-term continuous seismic/acoustic records for studying the structure and dynamics of the cryosphere. The high temporal resolution of these records is a key strength common across environmental seismology and provides a valuable complement to other geophysical methods. The richness of seismic observations is borne out by the fact that we were able to use the SPITS array (primarily designed to record regional to teleseismic earthquakes) to study frost quakes and explosive source seismic experiments on sea ice (primarily conceived as reflection seismic profiles) to elucidate the air-coupled flexural wave phenomenon.

## 4.2 Future research

Cryoseismology remains an emerging field that will likely continue to develop both in terms of methodology and scope of application in the future. Additional research and development is, correspondingly, crucial to in order to maximize the potential value of cryoseismology. Following the specific case studies addressed in this thesis, a series of directly related research subjects arise as topics that could be worthy of further attention:

1. **Calibration experiments to better constrain accuracy of estimated frost quake source positions.** As demonstrated in Paper 2, the SPITS array on Janssonhaugen is a fantastic resource, providing a long term, continuous seismic record in an area subject to a range of dynamic periglacial processes. A series of controlled source experiments, using sledgehammer blows or small explosive charges at precisely measured locations, would allow much improved understanding of the accuracy and reliability of estimating the source position using the matched field processing technique. The field logistics to conduct these experiments would be relatively straightforward and could be used as a means of calibration to add value to the existing permanently deployed infrastructure and the historical catalogue of seismic data already recorded. Using a highly repeatable source could also allow issues like spatial seismic velocity heterogeneity in the vicinity of the array to be investigated. This could in turn be used

to address heterogeneities in ground structure, geology or ground ice content. Improved knowledge of the seismic velocity structure around the SPITS array could also be used to improve array-based signal processing of regional or teleseismic earthquake signals, which is the primary application of the permanent recording station (e.g. Michel et al., 2014).

2. **Optimal 2D array design for resolution of multimodal surface wave dispersion.** The fine spatial sampling of the temporary array reported on in Paper 1 provided much better wavenumber resolving power than the relatively sparse, but permanently installed, SPITS array reported on in Paper 2. Given the knowledge gained from the high-resolution temporary array on the multimodal structure of surface wave dispersion, it should be possible to optimize the number and layout of sensors so that future studies focusing on similar frequencies and phase velocities could be carried out more efficiently. Alternatively, additional sensors could be deployed temporarily around and between the permanent SPITS seismometer stations. The temporary deployment could be used to characterize the dispersion of surface waves in detail and build a model of the velocity structure of the subsurface accordingly. This could then act as a base model, which in combination with a forward wave propagation model, could be used to invert for the velocity structure using only the SPITS stations. Moreau et al. (2020b) have shown that using a model-based inversion approach can be highly effective even when the number of sensors is very small. While the Moreau et al. (2020b) study focused on the problem of a floating ice plate, the concept is likely transferrable to the horizontal layers over a solid halfspace that is typically used to represent permafrost and the overlying active layer.

3. **Theoretical and practical study of the flexural stiffness of finite floating plates near their boundary.** In Paper 3, we made the tentative observation that the flexural rigidity of a floating ice sheet is modified in proximity to the lateral boundary that exists at the shoreline. We gave an approximate theoretical justification for this effect based on elementary theory of finite plates in a vacuum. Typically, the more complicated case of ice floating on water has been treated by invoking the approximation of an infinite plate and the problem of the apparent flexural rigidity of a finite floating plate along a pinned or fixed boundary has not been fully elaborated. Experimental data would be of great value in guiding theoretical development and a shoreline-perpendicular profile measuring air-coupled flexural frequencies and borehole ice thicknesses could provide useful insight and constraint. This line of research would also be of relevance to non-destructive testing in industrial or engineering applications, where finite plates are prevalent.

4. **Use of microphones for ice thickness estimation as a tool for improved safety on floating ice.** In Paper 3, we identified the potential to record air-coupled flexural waves using a simple microphone held in the air above a floating ice sheet. The frequency of the air-coupled flexural waves can be used to estimate the ice thickness, in combination with an estimate of the elastic properties and speed of sound in air. We also demonstrated that ice skates striking or cracking the ice surface are capable of exciting air-coupled flexural waves. These observations hint at the possibility that recreational ice skaters (and perhaps other ice users) could potentially utilize the microphones built into their mobile phones to record and estimate the air-coupled flexural frequency of the ice, which could then give an estimate its thickness and warn in the case of dangerously thin ice. Of course, a practical application would require more detailed and rigorous knowledge than is currently available, but this is a potentially interesting avenue for further research.

5. **Effects of snow covers on floating ice sheets and air-coupled flexural waves.** In Paper 3, we were not able to fully elaborate the effects of snow cover on the air-coupled flexural wave phenomenon for a floating ice sheet. We would expect that increasing snow cover would dampen the air-coupled flexural wave by decreasing the efficiency of coupling between ice and air. This effect would likely be frequency dependent and it is uncertain how much damping would be required to render the air-coupled flexural wave indetectable, since snow accumulation on sea-ice in Van Mijenfjorden is generally limited by wind transport. The snow may also act as a thermal insulator, thereby modulating the thermal stresses that develop in the ice and decreasing the probability of natural ice quakes. This effect would be relevant to the potential to passively monitor ice thickness using air-coupled flexural waves and therefore important to elaborate through further research. A seasonal study of ice and snow on a freshwater lake could be a relatively simple and effective way to gain a better understanding of the interaction between snow covers and air-coupled flexural waves.

# Works cited


Abolt, C. J., Young, M. H., Atchley, A. L., & Harp, D. R. (2018). Microtopographic control on the ground thermal regime in ice wedge polygons. *The Cryosphere, 12*(6), 1957-1968. 10.5194/tc-12-1957-2018

Abu Al-Rub, R. K., You, T., Masad, E. A., & Little, D. N. (2011). Mesomechanical modeling of the thermo-viscoelastic, thermo-viscoplastic, and thermo-viscodamage response of asphalt concrete. *International Journal of Advances in Engineering Sciences and Applied Mathematics, 3*(1), 14-33. 10.1007/s12572-011-0028-9

Alavi, M. Z., Hajj, E. Y., Morian, N. E., & Sebaaly, P. E. (2013). Low Temperature Characterization of Asphalt Mixtures by Measuring Visco-Elastic Properties under Thermal Loading. In *ISCORD 2013* (pp. 404-415). Retrieved from https://ascelibrary.org/doi/abs/10.1061/9780784412978.040

Albaric, J., Kühn, D., Ohrnberger, M., Langet, N., Harris, D., Polom, U., . . .Hillers, G. (2021). Seismic monitoring of permafrost in Svalbard, Arctic Norway. *Seismological Society of America, 92*(5), 2891-2904.

Andersen, J. L., Egholm, D. L., Knudsen, M. F., Jansen, J. D., & Nielsen, S. B. (2015). The periglacial engine of mountain erosion - Part 1: Rates of frost cracking and frost creep. *Earth Surf. Dynam., 3*(4), 447-462. 10.5194/esurf-3-447-2015

Apeagyei, A. K., Dave, E. V., & Buttlar, W. G. (2008). Effect of cooling rate on thermal cracking of asphalt concrete pavements. *Asphalt Paving Technology-Proceedings, 77*, 709.

Ardhuin, F., Stutzmann, E., Schimmel, M., & Mangeney, A. (2011). Ocean wave sources of seismic noise. *Journal of Geophysical Research: Oceans, 116*(C9). https://doi.org/10.1029/2011JC006952

Badache, M., Eslami-Nejad, P., Ouzzane, M., Aidoun, Z., & Lamarche, L. (2016). A new modeling approach for improved ground temperature profile determination. *Renewable Energy, 85*, 436-444.

Bandt, C., & Pompe, B. (2002). Permutation entropy: a natural complexity measure for time series. *Physical Review Letters, 88*(17), 174102.

Banville, D. R., Fortier, R., & Dupuis, C. (2016). Objective interpretation of induced polarization tomography using a quantitative approach for the investigation of periglacial environments. *Journal of Applied Geophysics, 130*, 218-233. https://doi.org/10.1016/j.jappgeo.2016.04.019

Barcheck, C. G., Schwartz, S. Y., & Tulaczyk, S. (2019). Icequake streaks linked to potential mega-scale glacial lineations beneath an Antarctic ice stream. *Geology, 48*(2), 99-102. 10.1130/g46626.1

Barosh, P. J. (2000). Frostquakes in New England. *Engineering Geology, 56*(3-4), 389-394.

Barry, R., & Gan, T. Y. (2011). *The global cryosphere: past, present and future*. Cambridge, UK: Cambridge University Press.

Battaglia, S. M., Changnon, D., Changnon, D., & Hall, D. (2016). *Frost quake events and changing wintertime air mass frequencies in southeastern Canada*: Working Paper, Northern Illinois University. doi: 10.13140/RG. 2.2. 22351.48803.

Beaty, K. S., Schmitt, D. R., & Sacchi, M. (2002). Simulated annealing inversion of multimode Rayleigh wave dispersion curves for geological structure. *Geophysical Journal International, 151*(2), 622-631. 10.1046/j.1365-246X.2002.01809.x

Behn, M. D., Goldsby, D. L., & Hirth, G. (2021). The role of grain size evolution in the rheology of ice: implications for reconciling laboratory creep data and the Glen flow law. *The Cryosphere, 15*(9), 4589-4605. 10.5194/tc-15-4589-2021

Beker, M., Campman, X., Van Oven, J., Walk, W., Levell, J., Tang, Z., . . .Koley, S. (2016). Innovations in seismic sensors driven by the search for gravitational waves. *The Leading Edge, 35*(7), 590-593.

Benedict, J. B. (1976). Frost Creep and Gelifluction Features: A Review. *Quaternary Research, 6*(1), 55-76. 10.1016/0033-5894(76)90040-5

Bhattacharya, M., Guy, R., & Crocker, M. (1971). Coincidence effect with sound waves in a finite plate. *Journal of sound and vibration, 18*(2), 157-169.

Bingham, E. C. (1922). *Fluidity and plasticity* (Vol. 2). New York, USA: McGraw-Hill.

Bissinger, G. (2008). Structural acoustics of good and bad violins. *The Journal of the Acoustical Society of America, 124*(3), 1764-1773. 10.1121/1.2956478

Black, R. F. (1976). Periglacial features indicative of permafrost: ice and soil wedges. *Quaternary Research, 6*(1), 3-26.

Bokulich, A., & Oreskes, N. (2017). Models in Geosciences. In L. Magnani & T. Bertolotti (Eds.), *Springer Handbook of Model-Based Science* (pp. 891-911). Cham: Springer International Publishing. Retrieved from https://doi.org/10.1007/978-3-319-30526-4_41

Bonfanti, A., Kaplan, J. L., Charras, G., & Kabla, A. (2020). Fractional viscoelastic models for power-law materials. *Soft Matter, 16*(26), 6002-6020.

Bonnet, P., Yastrebov, V. A., Queutey, P., Leroyer, A., Mangeney, A., Castelnau, O., . . .Montagner, J.-P. (2020). Modelling capsizing icebergs in the open ocean. *Geophysical Journal International, 223*(2), 1265-1287. 10.1093/gji/ggaa353

Bouras, Y., Zorica, D., Atanacković, T. M., & Vrcelj, Z. (2018). A non-linear thermo-viscoelastic rheological model based on fractional derivatives for high temperature creep in concrete. *Applied Mathematical Modelling, 55*, 551-568. https://doi.org/10.1016/j.apm.2017.11.028

Box, G. E. (1979). Robustness in the strategy of scientific model building. In *Robustness in statistics* (pp. 201-236). New York, USA: Academic Press.

Brower, N., Himberger, D., & Mayer, W. (1979). Restrictions on the existence of leaky Rayleigh waves. *IEEE transactions on sonics and ultrasonics, 26*(4), 306-307.

Broyles, J. M., Shepherd, M. R., & Brown, N. C. (2020). Investigation of optimization techniques on structural-acoustical shaped concrete slabs in buildings. *Proceedings of Meetings on Acoustics, 42*(1), 022001. 10.1121/2.0001354

Burtin, A., Hovius, N., Milodowski, D. T., Chen, Y.-G., Wu, Y.-M., Lin, C.-W., . . .Leu, P.-L. (2013). Continuous catchment-scale monitoring of geomorphic processes with a 2-D seismological array. *Journal of Geophysical Research: Earth Surface, 118*(3), 1956-1974. https://doi.org/10.1002/jgrf.20137

Butkovich, T. (1959). Thermal expansion of ice. *Journal of Applied Physics, 30*(3), 350-353.

Cable, S., Elberling, B., & Kroon, A. (2018). Holocene permafrost history and cryostratigraphy in the High Arctic Adventdalen Valley, central Svalbard. *Boreas, 47*(2), 423-442.

Calel, R., Chapman, S. C., Stainforth, D. A., & Watkins, N. W. (2020). Temperature variability implies greater economic damages from climate change. *Nature Communications, 11*(1), 5028. 10.1038/s41467-020-18797-8

Carey, M., McDowell, G., Huggel, C., Marshall, B., Moulton, H., Portocarrero, C., . . .Vicuña, L. (2021). Chapter 8 - A socio-cryospheric systems approach to glacier hazards, glacier runoff variability, and climate change. In W. Haeberli & C. Whiteman (Eds.), *Snow and Ice-Related Hazards, Risks, and Disasters (Second Edition)* (pp. 215-257): Elsevier. Retrieved from https://www.sciencedirect.com/science/article/pii/B9780128171295000184

Carreau, P. J. (1972). Rheological equations from molecular network theories. *Transactions of the Society of Rheology, 16*(1), 99-127.

Chalhoub, M., Bernier, M., Coquet, Y., & Philippe, M. (2017). A simple heat and moisture transfer model to predict ground temperature for shallow ground heat exchangers. *Renewable energy, 103*, 295-307.

Chen, J., Wu, Y., O'Connor, M., Cardenas, M. B., Schaefer, K., Michaelides, R., & Kling, G. (2020). Active layer freeze-thaw and water storage dynamics in permafrost environments inferred from InSAR. *Remote Sensing of Environment, 248*, 112007.

Chillara, V. K., & Lissenden, C. J. (2015). Review of nonlinear ultrasonic guided wave nondestructive evaluation: theory, numerics, and experiments. *Optical Engineering, 55*(1), 011002.

Chmiel, M., Roux, P., & Bardainne, T. (2016). Extraction of phase and group velocities from ambient surface noise in a patch-array configuration. *Geophysics, 81*(6), KS231-KS240.

Christ, M., & Park, J.-B. (2009). Ultrasonic technique as tool for determining physical and mechanical properties of frozen soils. *Cold Regions Science and Technology, 58*(3), 136-142. 10.1016/j.coldregions.2009.05.008

Christensen, S. T., Sorokin, S. V., & Olhoff, N. (1998). On analysis and optimization in structural acoustics — Part I: Problem formulation and solution techniques. *Structural optimization, 16*(2), 83-95. 10.1007/BF01202818

Christiansen, H. H., Etzelmüller, B., Isaksen, K., Juliussen, H., Farbrot, H., Humlum, O., . . .Hjort, J. (2010). The thermal state of permafrost in the Nordic area during the International Polar Year 2007–2009. *Permafrost and Periglacial Processes, 21*(2), 156-181.

Christiansen, H. H., Gilbert, G., Demidov, N., Guglielmin, M., Isaksen, K., Osuch, M., & Boike, J. (2020). Permafrost temperatures and active layer thickness in Svalbard during 2017/2018 (PermaSval). *SESS Report 2019-The State of Environmental Science in Svalbard*.

Christiansen, H. H., Matsuoka, N., & Watanabe, T. (2016). Progress in understanding the dynamics, internal structure and palaeoenvironmental potential of ice wedges and sand wedges. *Permafrost and Periglacial Processes, 27*(4), 365-376.

Coleman, B. D., & Noll, W. (1961). Foundations of Linear Viscoelasticity. *Reviews of Modern Physics, 33*(2), 239-249. 10.1103/RevModPhys.33.239

Cros, E., Roux, P., Vandemeulebrouck, J., & Kedar, S. (2011). Locating hydrothermal acoustic sources at Old Faithful Geyser using matched field processing. *Geophysical Journal International, 187*(1), 385-393.

Currier, J., & Schulson, E. (1982). The tensile strength of ice as a function of grain size. *Acta Metallurgica, 30*(8), 1511-1514.

Curry, J. A., Schramm, J. L., & Ebert, E. E. (1995). Sea ice-albedo climate feedback mechanism. *Journal of Climate, 8*(2), 240-247.
Dammeier, F., Moore, J. R., Haslinger, F., & Loew, S. (2011). Characterization of alpine rockslides using statistical analysis of seismic signals. *Journal of Geophysical Research: Earth Surface, 116*(F4). https://doi.org/10.1029/2011JF002037
Dean, T., & Sweeney, D. (2019). The use of nodal seismic acquisition systems to acquire limited-scale surveys. *First Break, 37*(1), 55-60. https://doi.org/10.3997/1365-2397.n0007
Desprat, N., Richert, A., Simeon, J., & Asnacios, A. (2005). Creep Function of a Single Living Cell. *Biophysical Journal, 88*(3), 2224-2233. https://doi.org/10.1529/biophysj.104.050278
Dietze, M., Mohadjer, S., Turowski, J. M., Ehlers, T. A., & Hovius, N. (2017). Seismic monitoring of small alpine rockfalls – validity, precision and limitations. *Earth Surf. Dynam., 5*(4), 653-668. 10.5194/esurf-5-653-2017
DiMarco, R., Dugan, J., Martin, W., & Tucker III, W. (1993). Sea ice flexural rigidity: a comparison of methods. *Cold regions science and technology, 21*(3), 247-255.
DiMillio, A. F. (1999). *A quarter century of geotechnical research*. McLean Virginia, USA: Turner-Fairbank Highway Research Center.
Ding, Y., Mu, C., Wu, T., Hu, G., Zou, D., Wang, D., . . .Wu, X. (2021). Increasing cryospheric hazards in a warming climate. *Earth-Science Reviews, 213*, 103500. https://doi.org/10.1016/j.earscirev.2020.103500
Dinvay, E., Kalisch, H., & Părău, E. (2019). Fully dispersive models for moving loads on ice sheets. *Journal of Fluid Mechanics, 876*, 122-149.
Dormand, J. R., & Prince, P. J. (1980). A family of embedded Runge-Kutta formulae. *Journal of computational and applied mathematics, 6*(1), 19-26.
Dou, S., & Ajo-Franklin, J. B. (2014). Full-wavefield inversion of surface waves for mapping embedded low-velocity zones in permafrost. *Geophysics, 79*(6), EN107-EN124. 10.1190/geo2013-0427.1
Dou, S., Nakagawa, S., Dreger, D., & Ajo-Franklin, J. (2017). An effective-medium model for P-wave velocities of saturated, unconsolidated saline permafrost. *Geophysics, 82*(3), EN33-EN50.
Draebing, D., & Krautblatter, M. (2012). P-wave velocity changes in freezing hard low-porosity rocks: a laboratory-based time-average model. *The Cryosphere, 6*(5), 1163-1174. 10.5194/tc-6-1163-2012
Droulia, F., Lykoudis, S., Tsiros, I., Alvertos, N., Akylas, E., & Garofalakis, I. (2009). Ground temperature estimations using simplified analytical and semi-empirical approaches. *Solar Energy, 83*(2), 211-219.
Duncan, P. M. (2005). Is there a future for passive seismic? *First Break, 23*(6).
Dypvik, H., Nagy, J., Eikeland, T., Backer-Owe, K., & Johansen, H. (1991). Depositional conditions of the Bathonian to Hauterivian Janusfjellet subgroup, Spitsbergen. *Sedimentary Geology, 72*(1-2), 55-78.
El-Gohary, M., & McNames, J. (2007). Establishing causality with whitened cross-correlation analysis. *IEEE Transactions on Biomedical Engineering, 54*(12), 2214-2222.
Elser, J. J., Wu, C., González, A. L., Shain, D. H., Smith, H. J., Sommaruga, R., . . .Saros, J. E. (2020). Key rules of life and the fading cryosphere: Impacts in alpine lakes and streams. *Global Change Biology, 26*(12), 6644-6656. https://doi.org/10.1111/gcb.15362
Everstine, G. C. (1997). Finite element formulatons of structural acoustics problems. *Computers & Structures, 65*(3), 307-321. https://doi.org/10.1016/S0045-7949(96)00252-0
Ewing, M., & Crary, A. (1934). Propagation of elastic waves in ice. Part II. *Physics, 5*(7), 181-184.
Ewing, M., & Press, F. (1955). Tide-gage disturbances from the great eruption of Krakatoa. *Eos, Transactions American Geophysical Union, 36*(1), 53-60.
Faber, T. J., Jaishankar, A., & McKinley, G. H. (2017). Describing the firmness, springiness and rubberiness of food gels using fractional calculus. Part II: Measurements on semi-hard cheese. *Food Hydrocolloids, 62*, 325-339. https://doi.org/10.1016/j.foodhyd.2016.06.038
Farbotko, C., Dun, O., Thornton, F., McNamara, K. E., & McMichael, C. (2020). Relocation planning must address voluntary immobility. *Nature Climate Change, 10*(8), 702-704. 10.1038/s41558-020-0829-6
Favreau, P., Mangeney, A., Lucas, A., Crosta, G., & Bouchut, F. (2010). Numerical modeling of landquakes. *Geophysical Research Letters, 37*(15). https://doi.org/10.1029/2010GL043512
Fischer, L., Purves, R. S., Huggel, C., Noetzli, J., & Haeberli, W. (2012). On the influence of topographic, geological and cryospheric factors on rock avalanches and rockfalls in high-mountain areas. *Nat. Hazards Earth Syst. Sci., 12*(1), 241-254. 10.5194/nhess-12-241-2012
Forbriger, T. (2003). Inversion of shallow-seismic wavefields: I. Wavefield transformation. *Geophysical Journal International, 153*(3), 719-734. 10.1046/j.1365-246X.2003.01929.x
Fortier, D., & Allard, M. (2005). Frost-cracking conditions, Bylot Island, eastern Canadian Arctic archipelago. *Permafrost and Periglacial Processes, 16*(2), 145-161. https://doi.org/10.1002/ppp.504

Foti, S., Hollender, F., Garofalo, F., Albarello, D., Asten, M., Bard, P.-Y., . . .Di Giulio, G. (2018). Guidelines for the good practice of surface wave analysis: A product of the InterPACIFIC project. *Bulletin of Earthquake Engineering, 16*(6), 2367-2420.

Foti, S., Sambuelli, L., Socco, V. L., & Strobbia, C. (2003). Experiments of joint acquisition of seismic refraction and surface wave data. *Near Surface Geophysics, 1*(3), 119-129. https://doi.org/10.3997/1873-0604.2003002

Fountain, A. G., Campbell, J. L., Schuur, E. A. G., Stammerjohn, S. E., Williams, M. W., & Ducklow, H. W. (2012). The Disappearing Cryosphere: Impacts and Ecosystem Responses to Rapid Cryosphere Loss. *BioScience, 62*(4), 405-415. 10.1525/bio.2012.62.4.11

Franke, S. J., & Swenson Jr, G. (1989). A brief tutorial on the fast field program (FFP) as applied to sound propagation in the air. *Applied Acoustics, 27*(3), 203-215.

Frauenfelder, R., Isaksen, K., Lato, M. J., & Noetzli, J. (2018). Ground thermal and geomechanical conditions in a permafrost-affected high-latitude rock avalanche site (Polvartinden, northern Norway). *The Cryosphere, 12*(4), 1531-1550. 10.5194/tc-12-1531-2018

French, H. M. (2017). *The periglacial environment* (4 ed.). New Jersey, USA: John Wiley & Sons.

Furnish, M. D. (1998). *Measuring Static and Dynamic Properties of Frozen Silty Soils. SAND98-1497* (Sandia National Laboratories). Livermore, California. https://doi.org/10.2172/698

Gajek, W., Trojanowski, J., & Malinowski, M. (2017). Automating long-term glacier dynamics monitoring using single-station seismological observations and fuzzy logic classification: a case study from Spitsbergen. *Journal of Glaciology, 63*(240), 581-592. 10.1017/jog.2017.25

Garrett, C. (1970). A theory of the Krakatoa tide gauge disturbances. *Tellus, 22*(1), 43-52.

Gibbons, S. J., & Ringdal, F. (2006). The detection of low magnitude seismic events using array-based waveform correlation. *Geophysical Journal International, 165*(1), 149-166.

Gibbons, S. J., Schweitzer, J., Ringdal, F., Kværna, T., Mykkeltveit, S., & Paulsen, B. (2011). Improvements to seismic monitoring of the European Arctic using three-component array processing at SPITS. *Bulletin of the Seismological Society of America, 101*(6), 2737-2754.

Gilbert, G. L., Kanevskiy, M., & Murton, J. B. (2016). Recent advances (2008–2015) in the study of ground ice and cryostratigraphy. *Permafrost and Periglacial Processes, 27*(4), 377-389.

Gilbert, G. L., O'neill, H. B., Nemec, W., Thiel, C., Christiansen, H. H., & Buylaert, J. P. (2018). Late Quaternary sedimentation and permafrost development in a Svalbard fjord-valley, Norwegian high Arctic. *Sedimentology, 65*(7), 2531-2558.

Gisnås, K., Westermann, S., Schuler, T. V., Melvold, K., & Etzelmüller, B. (2016). Small-scale variation of snow in a regional permafrost model. *The Cryosphere, 10*(3), 1201-1215. 10.5194/tc-10-1201-2016

Glen, J. W. (1955). The creep of polycrystalline ice. *Proceedings of the Royal Society of London. Series A. Mathematical and Physical Sciences, 228*(1175), 519-538.

Graham, S., Parkinson, C., & Chahine, M. (2010). The water cycle. *NASA Earth Observatory*.

Greenhill, A. (1886). Wave motion in hydrodynamics. *American Journal of Mathematics, 9*(1), 62-96.

Greenhill, G. (1916). I. Skating on thin ice. *The London, Edinburgh, and Dublin Philosophical Magazine and Journal of Science, 31*(181), 1-22.

Griffin, J. (2018). The Magic (and Math) of Skating on Thin Ice without Falling In. *Scientific American*. Retrieved from https://www.scientificamerican.com/article/the-magic-and-math-of-skating-on-thin-ice-without-falling-in/

Gudmestad, O. T. (2020). Technical and economic challenges for Arctic Coastal settlements due to melting of ice and permafrost in the Arctic. *IOP Conference Series: Earth and Environmental Science, 612*, 012049. 10.1088/1755-1315/612/1/012049

Haider, M. F., & Giurgiutiu, V. (2018). Analysis of axis symmetric circular crested elastic wave generated during crack propagation in a plate: A Helmholtz potential technique. *International Journal of Solids and Structures, 134*, 130-150.

Hales, T., & Roering, J. (2009). A frost "buzzsaw" mechanism for erosion of the eastern Southern Alps, New Zealand. *Geomorphology, 107*(3-4), 241-253.

Hales, T., & Roering, J. J. (2007). Climatic controls on frost cracking and implications for the evolution of bedrock landscapes. *Journal of Geophysical Research: Earth Surface, 112*(F2).

Hallet, B., Walder, J., & Stubbs, C. (1991). Weathering by segregation ice growth in microcracks at sustained subzero temperatures: Verification from an experimental study using acoustic emissions. *Permafrost and Periglacial Processes, 2*(4), 283-300.

Hambric, S. A. (2006). Structural acoustics tutorial—Part 1: vibrations in structures. *Acoustics Today, 2*(4), 21-33.

Hanssen, A. (1997). Multidimensional multitaper spectral estimation. *Signal Processing, 58*(3), 327-332.

Hanssen, R. F. (2001). *Radar interferometry: data interpretation and error analysis* (Vol. 2). Drodrecht, Netherlands: Springer Science & Business Media.

Harb, M. S., & Yuan, F.-G. (2018). Air-coupled nondestructive evaluation dissected. *Journal of nondestructive evaluation, 37*(3), 1-19.
Harkrider, D., & Press, F. (1967). The Krakatoa Air—Sea Waves: An Example of Pulse Propagation in Coupled Systems. *Geophysical Journal International, 13*(1-3), 149-159.
Harley, J. B., & Moura, J. M. (2014). Data-driven matched field processing for Lamb wave structural health monitoring. *The Journal of the Acoustical Society of America, 135*(3), 1231-1244.
Harrison, T. A. (1981). *Early-age thermal crack control in concrete*. London: Construction Industry Research and Information Association.
Haskell, N. A. (1951). A note on air-coupled surface waves. *Bulletin of the Seismological Society of America, 41*(4), 295-300.
Hayashi, T., & Inoue, D. (2014). Calculation of leaky Lamb waves with a semi-analytical finite element method. *Ultrasonics, 54*(6), 1460-1469. https://doi.org/10.1016/j.ultras.2014.04.021
Hearn, E. J. (1997). Chapter 7 - Circular Plates and Diaphragms. In E. J. Hearn (Ed.), *Mechanics of Materials 2 (Third Edition)* (pp. 193-219). Oxford: Butterworth-Heinemann. Retrieved from https://www.sciencedirect.com/science/article/pii/B9780750632669500081
Hersbach, H., Bell, B., Berrisford, P., Hirahara, S., Horányi, A., Muñoz-Sabater, J., . . .Thépaut, J.-N. (2020). The ERA5 global reanalysis. *Quarterly Journal of the Royal Meteorological Society, 146*(730), 1999-2049. https://doi.org/10.1002/qj.3803
Herschel, W. (1926). Measurement of consistency of rubber-benzene solutions. *Kolloid-zeitschrift, 39*, 291-298.
Hibert, C., Mangeney, A., Grandjean, G., Baillard, C., Rivet, D., Shapiro, N. M., . . .Crawford, W. (2014). Automated identification, location, and volume estimation of rockfalls at Piton de la Fournaise volcano. *Journal of Geophysical Research: Earth Surface, 119*(5), 1082-1105. https://doi.org/10.1002/2013JF002970
Hibert, C., Mangeney, A., Grandjean, G., Peltier, A., DiMuro, A., Shapiro, N. M., . . .Kowalski, P. (2017). Spatio-temporal evolution of rockfall activity from 2007 to 2011 at the Piton de la Fournaise volcano inferred from seismic data. *Journal of Volcanology and Geothermal Research, 333-334*, 36-52. https://doi.org/10.1016/j.jvolgeores.2017.01.007
Hinchey, M., & Colbourne, B. (1995). Research on low and high speed hovercraft icebreaking. *Canadian Journal of Civil Engineering, 22*(1), 32-42.
Hodson, A., Brock, B., Pearce, D., Laybourn-Parry, J., & Tranter, M. (2015). Cryospheric ecosystems: a synthesis of snowpack and glacial research. *Environmental Research Letters, 10*(11), 110201. 10.1088/1748-9326/10/11/110201
Holm, A. K., & Isaksen, K. (2019). 100 months of above average temperatures on Svalbard (original text in Norwegian: 100 måneder med temperatur over normalen på Svalbard). *The Norwegian Meteorological Institute*. Retrieved from https://www.met.no/nyhetsarkiv/100-maneder-med-temperatur-over-normalen-pa-svalbard
Hu, X.-d., Wang, J.-t., & Yu, R.-z. (2013). Uniaxial compressive and splitting tensile tests of artificially frozen soils in tunnel construction of Hong Kong. *Journal of Shanghai Jiaotong University (Science), 18*(6), 688-692.
Hubbard, S. S., Gangodagamage, C., Dafflon, B., Wainwright, H., Peterson, J., Gusmeroli, A., . . .Wullschleger, S. D. (2013). Quantifying and relating land-surface and subsurface variability in permafrost environments using LiDAR and surface geophysical datasets. *Hydrogeology Journal, 21*(1), 149-169. 10.1007/s10040-012-0939-y
Hudson, T. S., Brisbourne, A. M., Walter, F., Gräff, D., White, R. S., & Smith, A. M. (2020). Icequake Source Mechanisms for Studying Glacial Sliding. *Journal of Geophysical Research: Earth Surface, 125*(11), e2020JF005627. https://doi.org/10.1029/2020JF005627
Humlum, O., Instanes, A., & Sollid, J. L. (2003). Permafrost in Svalbard: a review of research history, climatic background and engineering challenges. *Polar Research, 22*(2), 191-215.
Hunkins, K. (1960). Seismic studies of sea ice. *Journal of Geophysical Research, 65*(10), 3459-3472.
Inoue, D., & Hayashi, T. (2015). Transient analysis of leaky Lamb waves with a semi-analytical finite element method. *Ultrasonics, 62*, 80-88. https://doi.org/10.1016/j.ultras.2015.05.004
Isaksen, K., Holmlund, P., Sollid, J. L., & Harris, C. (2001). Three deep alpine-permafrost boreholes in Svalbard and Scandinavia. *Permafrost and Periglacial Processes, 12*(1), 13-25.
Isaksen, K., Mühll, D. V., Gubler, H., Kohl, T., & Sollid, J. L. (2000). Ground surface-temperature reconstruction based on data from a deep borehole in permafrost at Janssonhaugen, Svalbard. *Annals of Glaciology, 31*, 287-294.
Isaksen, K., Nordli, Ø., Førland, E. J., Łupikasza, E., Eastwood, S., & Niedźwiedź, T. (2016). Recent warming on Spitsbergen—Influence of atmospheric circulation and sea ice cover. *Journal of Geophysical Research: Atmospheres, 121*(20), 11,913-911,931. https://doi.org/10.1002/2016JD025606

Isaksen, K., Sollid, J. L., Holmlund, P., & Harris, C. (2007). Recent warming of mountain permafrost in Svalbard and Scandinavia. *Journal of Geophysical Research: Earth Surface, 112*(F2). https://doi.org/10.1029/2006JF000522

Istomin, A., & Nazarov, T. (2019). Numerical studies of reinforced concrete pile foundations on permafrost soils at low climatic temperatures. *Journal of Physics: Conference Series, 1425*(1), 012082. https://doi.org/10.1088/1742-6596/1425/1/012082

Johansen, T. A., Digranes, P., van Schaack, M., & Lønne, I. (2003). Seismic mapping and modeling of near-surface sediments in polar areas. *Geophysics, 68*(2), 566-573.

Johansen, T. A., Ruud, B. O., Tømmerbakke, R., & Jensen, K. (2019). Seismic on floating ice: data acquisition versus flexural wave noise. *Geophysical Prospecting, 67*(3), 532-549.

Kakinuma, T., Yamashita, K., & Nakayama, K. (2012). Surface and Internal Waves due to a Moving Load on a Very Large Floating Structure. *Journal of Applied Mathematics, 2012*, 830530. 10.1155/2012/830530

Kanevskiy, M., Shur, Y., Fortier, D., Jorgenson, M., & Stephani, E. (2011). Cryostratigraphy of late Pleistocene syngenetic permafrost (yedoma) in northern Alaska, Itkillik River exposure. *Quaternary Research, 75*(3), 584-596.

Kaplar, C. W. (1969). *Laboratory determination of dynamic moduli of frozen soils and of ice*. Hanover, NH: Cold Regions Research and Engineering Lab. https://hdl.handle.net/11681/5722

Kashiwagi, M. (2004). Transient responses of a VLFS during landing and take-off of an airplane. *Journal of marine science and technology, 9*(1), 14-23.

Kavanaugh, J., Schultz, R., Andriashek, L. D., van der Baan, M., Ghofrani, H., Atkinson, G., & Utting, D. J. (2019). A New Year's Day icebreaker: icequakes on lakes in Alberta, Canada. *Canadian Journal of Earth Sciences, 56*(2), 183-200.

Keating, K., Binley, A., Bense, V., Van Dam, R. L., & Christiansen, H. H. (2018). Combined geophysical measurements provide evidence for unfrozen water in permafrost in the adventdalen valley in Svalbard. *Geophysical Research Letters, 45*(15), 7606-7614.

Kell, G. (1967). Precise representation of volume properties of water at one atmosphere. *Journal of Chemical and Engineering data, 12*(1), 66-69.

Kiefer, D. A., Ponschab, M., Rupitsch, S. J., & Mayle, M. (2019). Calculating the full leaky Lamb wave spectrum with exact fluid interaction. *The Journal of the Acoustical Society of America, 145*(6), 3341-3350.

Kleinhans, M. G., Buskes, C. J., & de Regt, H. W. (2010). Chapter 9 - Philosophy of Earth Science. In F. Allhoff (Ed.), *Philosophies of the Sciences: A Guide* (pp. 289-317). New Jersey, USA: John Wiley & Sons.

Knopoff, L. (1964). A matrix method for elastic wave problems. *Bulletin of the Seismological Society of America, 54*(1), 431-438.

Kohnert, K., Serafimovich, A., Metzger, S., Hartmann, J., & Sachs, T. (2017). Strong geologic methane emissions from discontinuous terrestrial permafrost in the Mackenzie Delta, Canada. *Scientific Reports, 7*(1), 5828. 10.1038/s41598-017-05783-2

Kotlyakov, V. M. (1999). The World Atlas of Snow and Ice Resources: A Review. *Mapping Sciences and Remote Sensing, 36*(1), 28-44. 10.1080/07493878.1999.10642105

Kozin, V., Zemlyak, V., & Rogozhnikova, E. (2017). Increasing the efficiency of the resonance method for breaking an ice cover with simultaneous movement of two air cushion vehicles. *Journal of Applied Mechanics and Technical Physics, 58*(2), 349-353.

Kozin, V. M., & Pogorelova, A. V. (2008). *Submarine moving close to the ice-surface conditions.* Paper presented at the The Eighteenth International Offshore and Polar Engineering Conference, July 2008, Vancouver, Canada.

Köhler, A., Nuth, C., Kohler, J., Berthier, E., Weidle, C., & Schweitzer, J. (2016). A 15 year record of frontal glacier ablation rates estimated from seismic data. *Geophysical Research Letters, 43*(23), 12,155-112,164. https://doi.org/10.1002/2016GL070589

Köhler, A., Nuth, C., Schweitzer, J., Weidle, C., & Gibbons, S. J. (2015). Regional passive seismic monitoring reveals dynamic glacier activity on Spitsbergen, Svalbard. *Polar Research, 34*(1), 26178.

Köhler, A., Pętlicki, M., Lefeuvre, P. M., Buscaino, G., Nuth, C., & Weidle, C. (2019). Contribution of calving to frontal ablation quantified from seismic and hydroacoustic observations calibrated with lidar volume measurements. *The Cryosphere, 13*(11), 3117-3137. 10.5194/tc-13-3117-2019

Lachenbruch, A. H. (1962). *Mechanics of thermal contraction cracks and ice-wedge polygons in permafrost* (Special GSA Papers, Volume 70). New York, USA: Geological Society of America.

Lacroix, A. V. (1980). A short note on cryoseisms. *Earthquake Notes, 51*(1), 15-21.

Lai, Y., Zhang, S., & Yu, W. (2012). A new structure to control frost boiling and frost heave of embankments in cold regions. *Cold Regions Science and Technology, 79-80*, 53-66. https://doi.org/10.1016/j.coldregions.2012.04.002

Lamb, H. (1917). On waves in an elastic plate. *Proceedings of the Royal Society of London. Series A, Containing Papers of a Mathematical and Physical Character, 93*(648), 114-128. doi:10.1098/rspa.1917.0008
Lamb, W. F., & Rao, N. D. (2015). Human development in a climate-constrained world: What the past says about the future. *Global Environmental Change, 33*, 14-22. https://doi.org/10.1016/j.gloenvcha.2015.03.010
Landau, L., & Lifshitz, E. (1970). *Theory of Elasticity, 2nd Edition*. Oxford: Pergamon Press.
Langleben, M. P. (1962). Young's modulus for sea ice. *Canadian Journal of Physics, 40*(1), 1-8. https://doi.org/10.1139/p62-001
Lantuit, H., Overduin, P. P., & Wetterich, S. (2013). Recent Progress Regarding Permafrost Coasts. *Permafrost and Periglacial Processes, 24*(2), 120-130. https://doi.org/10.1002/ppp.1777
Larose, E., Carrière, S., Voisin, C., Bottelin, P., Baillet, L., Guéguen, P., . . .Garambois, S. (2015). Environmental seismology: What can we learn on earth surface processes with ambient noise? *Journal of Applied Geophysics, 116*, 62-74.
Larsen, J. N., & Fondahl, G. (2015). *Arctic human development report: Regional processes and global linkages*. Denmark: Nordic Council of Ministers, Rosendahls-Schultz Grafisk.
Larsen, J. N., & Huskey, L. (2015). The Arctic Economy in a Global Context. In B. Evengård, J. Nymand Larsen, & Ø. Paasche (Eds.), *The New Arctic* (pp. 159-174). Cham: Springer International Publishing. Retrieved from https://doi.org/10.1007/978-3-319-17602-4_12
Larsen, P. H., Goldsmith, S., Smith, O., Wilson, M. L., Strzepek, K., Chinowsky, P., & Saylor, B. (2008). Estimating future costs for Alaska public infrastructure at risk from climate change. *Global Environmental Change, 18*(3), 442-457. https://doi.org/10.1016/j.gloenvcha.2008.03.005
Larson, M. (2003). *Thermal crack estimation in early age concrete : models and methods for practical application* (Doctoral thesis). Luleå tekniska universitet, Luleå. Retrieved from http://urn.kb.se/resolve?urn=urn:nbn:se:ltu:diva-25924 DiVA database. (2003:20)
Laruelle, M. (2015). *Russia's Arctic strategies and the future of the Far North* (1 ed.). New York, USA: Routledge.
Lawrence, B. K., Chen, L., & Humphrey, D. N. (2000). *Use of Tire Chip/Soil Mixtures to Limit Frost Heave and Pavement Damage of Paved Roads - NETCR 12* (New England Transportation, Consortium). Retrieved from https://rosap.ntl.bts.gov/view/dot/42253
Le Feuvre, M., Joubert, A., Leparoux, D., & Cote, P. (2015). Passive multi-channel analysis of surface waves with cross-correlations and beamforming. Application to a sea dike. *Journal of Applied Geophysics, 114*, 36-51.
Lenhard, J., & Winsberg, E. (2011). Holism and Entrenchment in Climate Model Validation. In M. Carrier & A. Nordmann (Eds.), *Science in the Context of Application* (pp. 115-130). Dordrecht: Springer Netherlands. Retrieved from https://doi.org/10.1007/978-90-481-9051-5_8
Leung, A. C., Gough, W. A., & Shi, Y. (2017). Identifying frostquakes in Central Canada and neighbouring regions in the United States with social media. In *Citizen Empowered Mapping* (pp. 201-222): Springer.
Lin, S., & Ashlock, J. C. (2014). Multimode Rayleigh wave profiling by hybrid surface and borehole methods. *Geophysical Journal International, 197*(2), 1184-1195. 10.1093/gji/ggu051
Liu, L., Rouyet, L., Strozzi, T., Lauknes, T. R., & Christiansen, H. H. (2018). *Seasonal Thaw Settlement and Frost Heave in Permafrost Regions in the Arctic: A Synthesis of InSAR Observations Using Sentinel-1 SAR Images.* Paper presented at the AGU Fall Meeting Abstracts, Washington, USA.
Lombardi, D., Gorodetskaya, I., Barruol, G., & Camelbeeck, T. (2019). Thermally induced icequakes detected on blue ice areas of the East Antarctic ice sheet. *Annals of Glaciology, 60*(79), 45-56. 10.1017/aog.2019.26
Loranger, B., Kuznetsova, E., Hoff, I., Aksnes, J., & Skoglund, K. A. (2017). Evaluation of Norwegian gradation based regulation for frost susceptibility of crushed rock aggregates in roads and railways. In A. Loizos, I. Al-Qadi, & T. Scarpas (Eds.), *Bearing capacity of roads, railways and airfields* (pp. 2077-2085). London: CRC Press.
Lowe, M. J. (1995). Matrix techniques for modeling ultrasonic waves in multilayered media. *IEEE Transactions on Ultrasonics, Ferroelectrics, and Frequency Control, 42*(4), 525-542.
Lundmark, G. (2001). *Skating on thin ice-And the acoustics of infinite plates*. Paper presented at the INTER-NOISE and NOISE-CON Congress and Conference Proceedings, The Hague, Netherlands.
Lønne, I. (2005). Faint traces of high Arctic glaciations: an early Holocene ice-front fluctuation in Bolterdalen, Svalbard. *Boreas, 34*(3), 308-323.
Ma, W., Zhang, L., & Yang, C. (2015). Discussion of the applicability of the generalized Clausius–Clapeyron equation and the frozen fringe process. *Earth-Science Reviews, 142*, 47-59. https://doi.org/10.1016/j.earscirev.2015.01.003
Mackay, J. R. (1984). The direction of ice-wedge cracking in permafrost: downward or upward? *Canadian Journal of Earth Sciences, 21*(5), 516-524.
Maldonado, J. K., Shearer, C., Bronen, R., Peterson, K., & Lazrus, H. (2014). The impact of climate change on tribal communities in the US: displacement, relocation, and human rights. In J. K. Maldonado, B. Colombi, & R.

Pandya (Eds.), *Climate Change and Indigenous Peoples in the United States: Impacts, Experiences and Actions* (pp. 93-106). Cham: Springer International Publishing. Retrieved from https://doi.org/10.1007/978-3-319-05266-3_8

Maloof, A. C., Kellogg, J. B., & Anders, A. M. (2002). Neoproterozoic sand wedges: crack formation in frozen soils under diurnal forcing during a snowball Earth. *Earth and Planetary Science Letters, 204*(1-2), 1-15.

Mangold, N., Allemand, P., Duval, P., Geraud, Y., & Thomas, P. (2002). Experimental and theoretical deformation of ice–rock mixtures: Implications on rheology and ice content of Martian permafrost. *Planetary and Space Science, 50*(4), 385-401. https://doi.org/10.1016/S0032-0633(02)00005-3

Marks, R., Clarke, A., Featherston, C., Paget, C., & Pullin, R. (2016). Lamb Wave Interaction with Adhesively Bonded Stiffeners and Disbonds Using 3D Vibrometry. *Applied Sciences, 6*(1), 12. Retrieved from https://www.mdpi.com/2076-3417/6/1/12

Masyagina, O. V., & Menyailo, O. V. (2020). The impact of permafrost on carbon dioxide and methane fluxes in Siberia: A meta-analysis. *Environmental Research, 182*, 109096. https://doi.org/10.1016/j.envres.2019.109096

Matiushina, A. A., Pogorelova, A. V., & Kozin, V. M. (2016). Effect of impact load on the ice cover during the landing of an airplane. *International Journal of Offshore and Polar Engineering, 26*(01), 6-12.

Matsuoka, N. (2001). Solifluction rates, processes and landforms: a global review. *Earth-Science Reviews, 55*(1-2), 107-134.

Matsuoka, N. (2008). Frost weathering and rockwall erosion in the southeastern Swiss Alps: Long-term (1994–2006) observations. *Geomorphology, 99*(1-4), 353-368.

Matsuoka, N. (2019). A multi-method monitoring of timing, magnitude and origin of rockfall activity in the Japanese Alps. *Geomorphology, 336*, 65-76.

Matsuoka, N., Christiansen, H. H., & Watanabe, T. (2018). Ice-wedge polygon dynamics in Svalbard: Lessons from a decade of automated multi-sensor monitoring. *Permafrost and Periglacial Processes, 29*(3), 210-227.

Matsuoka, N., Sawaguchi, S.-i., & Yoshikawa, K. (2004). Present-day periglacial environments in central Spitsbergen, Svalbard. *Geographical Review of Japan, 77*(5), 276-300.

McGehee, R., & Lehman, C. (2012). A Paleoclimate Model of Ice-Albedo Feedback Forced by Variations in Earth's Orbit. *SIAM Journal on Applied Dynamical Systems, 11*(2), 684-707. 10.1137/10079879x

Mellon, M. T. (1997). Small-scale polygonal features on Mars: Seasonal thermal contraction cracks in permafrost. *Journal of Geophysical Research: Planets, 102*(E11), 25617-25628.

Melvin, A. M., Larsen, P., Boehlert, B., Neumann, J. E., Chinowsky, P., Espinet, X., . . .Marchenko, S. S. (2017). Climate change damages to Alaska public infrastructure and the economics of proactive adaptation. *Proceedings of the National Academy of Sciences, 114*(2), E122. 10.1073/pnas.1611056113

Merbouh, M. h. (2012). Effect of Thermal Cycling on the Creep-Recovery Behaviour of Road Bitumen. *Energy Procedia, 18*, 1106-1114. https://doi.org/10.1016/j.egypro.2012.05.125

Michalopoulou, Z. H. (1998). Robust multi-tonal matched-field inversion: A coherent approach. *The Journal of the Acoustical Society of America, 104*(1), 163-170.

Michel, C., Edwards, B., Poggi, V., Burjánek, J., Roten, D., Cauzzi, C., & Fäh, D. (2014). Assessment of Site Effects in Alpine Regions through Systematic Site Characterization of Seismic Stations. *Bulletin of the Seismological Society of America, 104*(6), 2809-2826. 10.1785/0120140097

Miles, J., & Sneyd, A. D. (2003). The response of a floating ice sheet to an accelerating line load. *Journal of Fluid Mechanics, 497*, 435-439.

Mino, G. D., Airey, G., Di Paola, M., Pinnola, F. P., D'Angelo, G., & Presti, D. L. (2016). Linear and nonlinear fractional hereditary constitutive laws of asphalt mixtures. *Journal of Civil Engineering and Management, 22*(7), 882-889.

Minsley, B. J., Abraham, J. D., Smith, B. D., Cannia, J. C., Voss, C. I., Jorgenson, M. T., . . .Ager, T. A. (2012). Airborne electromagnetic imaging of discontinuous permafrost. *Geophysical Research Letters, 39*(2). https://doi.org/10.1029/2011GL050079

Monismith, C. L., Secor, G., & Secor, K. E. (1965). *Temperature induced stresses and deformations in asphalt concrete.* Paper presented at the Association of Asphalt Paving Technologists Proceedings (Vol. 34), Minnesota, USA.

Montewka, J., Goerlandt, F., Kujala, P., & Lensu, M. (2015). Towards probabilistic models for the prediction of a ship performance in dynamic ice. *Cold Regions Science and Technology, 112*, 14-28. https://doi.org/10.1016/j.coldregions.2014.12.009

Moreau, L., Boué, P., Serripierri, A., Weiss, J., Hollis, D., Pondaven, I., . . .Helmstetter, A. (2020). Sea ice thickness and elastic properties from the analysis of multimodal guided wave propagation measured with a passive seismic array. *Journal of Geophysical Research: Oceans, 125*(4), e2019JC015709.

Moreau, L., Weiss, J., & Marsan, D. (2020). Accurate estimations of sea-ice thickness and elastic properties from seismic noise recorded with a minimal number of geophones: from thin landfast ice to thick pack ice. *Journal of Geophysical Research: Oceans, 125*(11), e2020JC016492.

Moretti, L., Allstadt, K., Mangeney, A., Capdeville, Y., Stutzmann, E., & Bouchut, F. (2015). Numerical modeling of the Mount Meager landslide constrained by its force history derived from seismic data. *Journal of Geophysical Research: Solid Earth, 120*(4), 2579-2599. https://doi.org/10.1002/2014JB011426

Moretti, L., Mangeney, A., Walter, F., Capdeville, Y., Bodin, T., Stutzmann, E., & Le Friant, A. (2020). Constraining landslide characteristics with Bayesian inversion of field and seismic data. *Geophysical Journal International, 221*(2), 1341-1348. 10.1093/gji/ggaa056

Mozhaev, V., & Weihnacht, M. (2002). Subsonic leaky Rayleigh waves at liquid–solid interfaces. *Ultrasonics, 40*(1-8), 927-933.

Murton, J. B., Peterson, R., & Ozouf, J.-C. (2006). Bedrock fracture by ice segregation in cold regions. *Science, 314*(5802), 1127-1129.

Naskar, T., & Kumar, J. (2017). Predominant modes for Rayleigh wave propagation using the dynamic stiffness matrix approach. *Journal of Geophysics and Engineering, 14*(5), 1032-1041. 10.1088/1742-2140/aa6fe3

Ng, T. S. K., & McKinley, G. H. (2008). Power law gels at finite strains: The nonlinear rheology of gluten gels. *Journal of Rheology, 52*(2), 417-449. 10.1122/1.2828018

Nicholls, R. J., & Cazenave, A. (2010). Sea-Level Rise and Its Impact on Coastal Zones. *Science, 328*(5985), 1517-1520. doi:10.1126/science.1185782

Nickalls, R. W. (1993). A new approach to solving the cubic: Cardan's solution revealed. *The Mathematical Gazette, 77*(480), 354-359.

Nicolle, S., Vezin, P., & Palierne, J. F. (2010). A strain-hardening bi-power law for the nonlinear behaviour of biological soft tissues. *Journal of Biomechanics, 43*(5), 927-932. https://doi.org/10.1016/j.jbiomech.2009.11.002

Nikonov, A. (2010). Frost quakes as a particular class of seismic events: Observations within the East-European platform. *Izvestiya, Physics of the Solid Earth, 46*(3), 257-273.

Nordli, Ø., Przybylak, R., Ogilvie, A. E. J., & Isaksen, K. (2014). Long-term temperature trends and variability on Spitsbergen: the extended Svalbard Airport temperature series, 1898-2012. *Polar Research, 33*(0). 10.3402/polar.v33.21349

Novoselov, A., Fuchs, F., & Bokelmann, G. (2020). Acoustic-to-seismic ground coupling: coupling efficiency and inferring near-surface properties. *Geophysical Journal International, 223*(1), 144-160.

Nugroho, W. S., Wang, K., Hosking, R., & Milinazzo, F. (1999). Time-dependent response of a floating flexible plate to an impulsively started steadily moving load. *Journal of Fluid Mechanics, 381*, 337-355.

NVE. (2021). Ice accidents and incidents (original text in Norwegian: Isulykker og hendelser). *The Norwegian Water Resources and Energy Directorate, 2021*(1/11/2021). Retrieved from https://www.varsom.no/ulykker/isulykker-og-hendelser/

O'Neill, A., Dentith, M., & List, R. (2003). Full-waveform P-SV reflectivity inversion of surface waves for shallow engineering applications. *Exploration Geophysics, 34*(3), 158-173. 10.1071/EG03158

O'Neill, H. B., & Burn, C. R. (2012). Physical and temporal factors controlling the development of near-surface ground ice at Illisarvik, western Arctic coast, Canada. *Canadian Journal of Earth Sciences, 49*(9), 1096-1110.

Ohayon, R., & Soize, C. (1997). *Structural acoustics and vibration: Mechanical models, variational formulations and discretization*. San Diego, USA: Academic Press.

Ohkusu, M., & Namba, Y. (2004). Hydroelastic analysis of a large floating structure. *Journal of Fluids and Structures, 19*(4), 543-555. https://doi.org/10.1016/j.jfluidstructs.2004.02.002

Okkonen, J., Neupauer, R., Kozlovskaya, E., Afonin, N., Moisio, K., Taewook, K., & Muurinen, E. (2020). Frost Quakes: Crack Formation by Thermal Stress. *Journal of Geophysical Research: Earth Surface, 125*(9), e2020JF005616.

Olinger, S., Lipovsky, B., Wiens, D., Aster, R., Bromirski, P., Chen, Z., . . .Stephen, R. (2019). Tidal and thermal stresses drive seismicity along a major Ross Ice Shelf rift. *Geophysical Research Letters, 46*(12), 6644-6652.

O'Neill, H. B., & Christiansen, H. H. (2018). Detection of ice wedge cracking in permafrost using miniature accelerometers. *Journal of Geophysical Research: Earth Surface, 123*(4), 642-657.

Oreskes, N. (2003). The role of quantitative models in science. In C. Canham, J. Cole, & W. Lauenroth (Eds.), *Models in ecosystem science* (pp. 13-31). New Jersey, USA: Princetown University Press.

Pan, L., Chen, X., Wang, J., Yang, Z., & Zhang, D. (2018). Sensitivity analysis of dispersion curves of Rayleigh waves with fundamental and higher modes. *Geophysical Journal International, 216*(2), 1276-1303. 10.1093/gji/ggy479

Pan, Y., Xia, J., Gao, L., Shen, C., & Zeng, C. (2013). Calculation of Rayleigh-wave phase velocities due to models with a high-velocity surface layer. *Journal of Applied Geophysics, 96*, 1-6. https://doi.org/10.1016/j.jappgeo.2013.06.005

Park, C., Miller, R., Laflen, D., Neb, C., Ivanov, J., Bennett, B., & Huggins, R. (2004). Imaging dispersion curves of passive surface waves. In *SEG technical program expanded abstracts 2004* (pp. 1357-1360): Society of Exploration Geophysicists.

Park, C. B., Miller, R. D., & Xia, J. (1998). Imaging dispersion curves of surface waves on multi-channel record. In *SEG Technical Program Expanded Abstracts 1998* (pp. 1377-1380): Society of Exploration Geophysicists.

Park, C. B., Miller, R. D., & Xia, J. (1999). Multichannel analysis of surface waves. *Geophysics, 64*(3), 800-808.

Park, C. B., Miller, R. D., Xia, J., & Ivanov, J. (2007). Multichannel analysis of surface waves (MASW)—active and passive methods. *The Leading Edge, 26*(1), 60-64.

Park, H. S., Oh, B. K., Kim, Y., & Cho, T. (2015). Low-frequency impact sound transmission of floating floor: Case study of mortar bed on concrete slab with continuous interlayer. *Building and Environment, 94*, 793-801. https://doi.org/10.1016/j.buildenv.2015.06.005

Parsekian, A. D., Chen, R. H., Michaelides, R. J., Sullivan, T. D., Clayton, L. K., Huang, L., . . .Schaefer, K. (2021). Validation of Permafrost Active Layer Estimates from Airborne SAR Observations. *Remote Sensing, 13*(15), 2876. Retrieved from https://www.mdpi.com/2072-4292/13/15/2876

Peppin, S. S., & Style, R. W. (2013). The physics of frost heave and ice-lens growth. *Vadose Zone Journal, 12*(1).

Podolskiy, E. A., Fujita, K., Sunako, S., & Sato, Y. (2019). Viscoelastic Modeling of Nocturnal Thermal Fracturing in a Himalayan Debris-Covered Glacier. *Journal of Geophysical Research: Earth Surface, 124*(6), 1485-1515.

Podolskiy, E. A., Murai, Y., Kanna, N., & Sugiyama, S. (2021). Ocean-Bottom Seismology of Glacial Earthquakes: The Concept, Lessons Learned, and Mind the Sediments. *Seismological Research Letters, 92*(5), 2850-2865. 10.1785/0220200465

Podolskiy, E. A., & Walter, F. (2016). Cryoseismology. *Reviews of Geophysics, 54*(4), 708-758. https://doi.org/10.1002/2016RG000526

Press, F., Crary, A., Oliver, J., & Katz, S. (1951). Air-coupled flexural waves in floating ice. *Eos, Transactions American Geophysical Union, 32*(2), 166-172.

Press, F., & Ewing, M. (1951). Theory of air-coupled flexural waves. *Journal of Applied Physics, 22*(7), 892-899.

Press, F., & Oliver, J. (1955). Model study of air-coupled surface waves. *The Journal of the Acoustical Society of America, 27*(1), 43-46.

Pszczola, M., Jaczewski, M., & Szydlowski, C. (2019). Assessment of Thermal Stresses in Asphalt Mixtures at Low Temperatures Using the Tensile Creep Test and the Bending Beam Creep Test. *Applied Sciences, 9*(5), 846. Retrieved from https://www.mdpi.com/2076-3417/9/5/846

Rabiner, L. R., Schafer, R. W., & Rader, C. M. (1969). The chirp z-transform algorithm and its application. *Bell System Technical Journal, 48*(5), 1249-1292.

Rahmstorf, S. (2003). Thermohaline circulation: The current climate. *Nature, 421*(6924), 699-699.

Rahmstorf, S. (2010). A new view on sea level rise. *Nature Climate Change, 1*(1004), 44-45. 10.1038/climate.2010.29

Rankin, A. (2018). How Skating on Thin Ice Creates Laser-Like Sounds. *National Geographic*. Retrieved from https://www.nationalgeographic.com/adventure/activities/winter-sports/skating-thin-black-ice-creates-sound-nordic-spd/

Rankinen, K., Karvonen, T., & Butterfield, D. (2004). A simple model for predicting soil temperature in snow-covered and seasonally frozen soil: model description and testing. *Hydrology and Earth System Sciences, 8*(4), 706-716.

Rayleigh, L. (1885). On Waves Propagated along the Plane Surface of an Elastic Solid. *Proceedings of the London Mathematical Society, s1-17*(1), 4-11. https://doi.org/10.1112/plms/s1-17.1.4

Rempel, A. W. (2010). Frost heave. *Journal of Glaciology, 56*(200), 1122-1128.

Renji, K., Nair, P., & Narayanan, S. (1997). Critical and coincidence frequencies of flat panels. *Journal of sound and vibration, 205*(1), 19-32.

Richart, F. E., Hall, J. R., & Woods, R. D. (1970). *Vibrations of soils and foundations* (Prentice-Hall International Series in Theoretical and Applied Mechanics). New Jersey, USA: Prentice Hall.

Romeyn, R., Hanssen, A., Ruud, B. O., Stemland, H. M., & Johansen, T. A. (2021). Passive seismic recording of cryoseisms in Adventdalen, Svalbard. *The Cryosphere, 15*(1), 283-302. https://doi.org/10.5194/tc-15-283-2021

Rose, J. L. (2004). Ultrasonic guided waves in structural health monitoring. *Key Engineering Materials Conference, 270*, 14-21.

Rosen, P. A., Hensley, S., Joughin, I. R., Li, F. K., Madsen, S. N., Rodriguez, E., & Goldstein, R. M. (2000). Synthetic aperture radar interferometry. *Proceedings of the IEEE, 88*(3), 333-382.

Rouyet, L., Lauknes, T. R., Christiansen, H. H., Strand, S. M., & Larsen, Y. (2019). Seasonal dynamics of a permafrost landscape, Adventdalen, Svalbard, investigated by InSAR. *Remote Sensing of Environment, 231*, 111236.

Rouyet, L., Liu, L., Strand, S. M., Christiansen, H. H., Lauknes, T. R., & Larsen, Y. (2021). Seasonal InSAR Displacements Documenting the Active Layer Freeze and Thaw Progression in Central-Western Spitsbergen, Svalbard. *Remote Sensing, 13*(15), 2977.

Ruzhich, V., Psakhie, S. G., Chernykh, E., Bornyakov, S., & Granin, N. (2009). Deformation and seismic effects in the ice cover of Lake Baikal. *Russian Geology and Geophysics, 50*(3), 214-221.

Ryden, N., & Lowe, M. J. (2004). Guided wave propagation in three-layer pavement structures. *The Journal of the Acoustical Society of America, 116*(5), 2902-2913.

Ryden, N., & Park, C. B. (2004). Surface waves in inversely dispersive media. *Near Surface Geophysics, 2*(4), 187-197. https://doi.org/10.3997/1873-0604.2004016

Ryden, N., & Park, C. B. (2006). Fast simulated annealing inversion of surface waves on pavement using phase-velocity spectra. *Geophysics, 71*(4), R49-R58.

Ryden, N., Park, C. B., Ulriksen, P., & Miller, R. D. (2004). Multimodal approach to seismic pavement testing. *Journal of Geotechnical and Geoenvironmental Engineering, 130*(6), 636-645.

Sandven, S., Hansen, R. K., Eknes, E., Kvingedal, B., Bruserud, K., Nilsen, F., . . .Kloster, K. (2010). *ICESONAR: Monitoring of sea ice thickness from a subsea 4D sonar - NERSC Technical Report no. 294* (Nansen Environmental and Remote Sensing Center). Bergen, Norway.

Santin, I., Colucci, R. R., Žebre, M., Pavan, M., Cagnati, A., & Forte, E. (2019). Recent evolution of Marmolada glacier (Dolomites, Italy) by means of ground and airborne GPR surveys. *Remote Sensing of Environment, 235*, 111442. https://doi.org/10.1016/j.rse.2019.111442

Saramito, P. (2007). A new constitutive equation for elastoviscoplastic fluid flows. *Journal of Non-Newtonian Fluid Mechanics, 145*(1), 1-14.

Scherler, D. (2014). Climatic limits to headwall retreat in the Khumbu Himalaya, eastern Nepal. *Geology, 42*(11), 1019-1022.

Schmidt, H., & Jensen, F. B. (1985). A full wave solution for propagation in multilayered viscoelastic media with application to Gaussian beam reflection at fluid–solid interfaces. *The Journal of the Acoustical Society of America, 77*(3), 813-825.

Schulkes, R. M. S. M., & Sneyd, A. D. (1988). Time-dependent response of floating ice to a steadily moving load. *Journal of Fluid Mechanics, 186*, 25-46.

Schulson, E. M., & Duval, P. (2009). *Creep and fracture of ice*. Cambridge Books Online: Cambridge university press.

Schuur, E. A. G., McGuire, A. D., Schädel, C., Grosse, G., Harden, J. W., Hayes, D. J., . . .Vonk, J. E. (2015). Climate change and the permafrost carbon feedback. *Nature, 520*(7546), 171-179. 10.1038/nature14338

Schweitzer, J., Köhler, A., & Christensen, J. M. (2021). Development of the NORSAR Network over the Last 50 Yr. *Seismological Society of America, 92*(3), 1501-1511.

Schweizer, J., Mitterer, C., Techel, F., Stoffel, A., & Reuter, B. (2020). On the relation between avalanche occurrence and avalanche danger level. *The Cryosphere, 14*(2), 737-750. 10.5194/tc-14-737-2020

Sergeant, A., Chmiel, M., Lindner, F., Walter, F., Roux, P., Chaput, J., . . .Mordret, A. (2020). On the Green's function emergence from interferometry of seismic wave fields generated in high-melt glaciers: implications for passive imaging and monitoring. *The Cryosphere, 14*(3), 1139-1171.

Sergeant, A., Mangeney, A., Yastrebov, V. A., Walter, F., Montagner, J.-P., Castelnau, O., . . .Luckman, A. (2019). Monitoring Greenland ice sheet buoyancy-driven calving discharge using glacial earthquakes. *Annals of Glaciology, 60*(79), 75-95. 10.1017/aog.2019.7

Shearer, P. M. (2009). Surface waves and normal modes. In P. M. Shearer (Ed.), *Introduction to Seismology* (2 ed., pp. 215-240). Cambridge: Cambridge University Press. Retrieved from https://www.cambridge.org/core/books/introduction-to-seismology/surface-waves-and-normal-modes/16DDA65BE376B33D704983D8518892EC

Shiklomanov, N. I., Streletskiy, D. A., Grebenets, V. I., & Suter, L. (2017). Conquering the permafrost: urban infrastructure development in Norilsk, Russia. *Polar Geography, 40*(4), 273-290. 10.1080/1088937X.2017.1329237

Sinha, N. K. (1978). Short-Term Rheology of Polycrystalline Ice. *Journal of Glaciology, 21*(85), 457-474. 10.3189/S002214300003361X

Skarðhamar, J., & Svendsen, H. (2010). Short-term hydrographic variability in a stratified Arctic fjord. *Geological Society, London, Special Publications, 344*(1), 51-60.

Skvortsov, A., Sadurtdinov, M., & Tsarev, A. (2014). Seismic Criteria for Identifying Frozen Soil. *Kriosfera Zemli, 18*(2), 75-80.

Squire, V., Hosking, R. J., Kerr, A. D., & Langhorne, P. (1996). *Moving Loads on Ice Plates* (Solid Mechanics and its Applications Vol. 45). Dordrecht, Netherlands: Kluwer Academic Press.

Squire, V., Robinson, W., Langhorne, P., & Haskell, T. (1988). Vehicles and aircraft on floating ice. *Nature, 333*(6169), 159-161.
Stein, P. J., Euerle, S. E., & Parinella, J. C. (1998). Inversion of pack ice elastic wave data to obtain ice physical properties. *Journal of Geophysical Research: Oceans, 103*(C10), 21783-21793. https://doi.org/10.1029/98JC01269
Stein, S., & Wysession, M. (2009). *An introduction to seismology, earthquakes, and earth structure*. New Jersey, USA: John Wiley & Sons.
Stemland, H. M., Johansen, T. A., & Ruud, B. O. (2020). Potential Use of Time-Lapse Surface Seismics for Monitoring Thawing of the Terrestrial Arctic. *Applied Sciences, 10*(5), 1875. Retrieved from https://www.mdpi.com/2076-3417/10/5/1875
Stemland, H. M., Johansen, T. A., Ruud, B. O., & Aniceto, A. S. (2019). Measured sound levels in ice-covered shallow water caused by seismic shooting on top of and below floating ice, reviewed for possible impacts on true seals. *First Break, 37*(1), 35-42. https://doi.org/10.3997/1365-2397.2018010
Stocker, T. F., & Knutti, R. (2003). Do simplified climate models have any useful skill. *CLIVAR Exchanges, 8*(1), 7-10.
Streletskiy, D. A., Suter, L. J., Shiklomanov, N. I., Porfiriev, B. N., & Eliseev, D. O. (2019). Assessment of climate change impacts on buildings, structures and infrastructure in the Russian regions on permafrost. *Environmental Research Letters, 14*(2), 025003. 10.1088/1748-9326/aaf5e6
Suter, L., Streletskiy, D., & Shiklomanov, N. (2019). Assessment of the cost of climate change impacts on critical infrastructure in the circumpolar Arctic. *Polar Geography, 42*(4), 267-286. 10.1080/1088937X.2019.1686082
Sutherland, G., & Rabault, J. (2016). Observations of wave dispersion and attenuation in landfast ice. *Journal of Geophysical Research: Oceans, 121*(3), 1984-1997.
Sørbel, L., & Tolgensbakk, J. (2002). Ice-wedge polygons and solifluction in the Adventdalen area, Spitsbergen, Svalbard. *Norsk Geografisk Tidsskrift-Norwegian Journal of Geography, 56*(2), 62-66.
Takizawa, T. (1988). Response of a floating sea ice sheet to a steadily moving load. *Journal of Geophysical Research: Oceans, 93*(C5), 5100-5112.
Tanner, T., & Horn-Phathanothai, L. (2014). *Climate change and development* (Routledge Perspectives on Development). UK: Routledge.
Thackeray, C. W., & Hall, A. (2019). An emergent constraint on future Arctic sea-ice albedo feedback. *Nature Climate Change, 9*(12), 972-978. 10.1038/s41558-019-0619-1
The Norwegian Meteorological institute. (2020). Norsk Klimaservicesenter - Observations and weather statistics Retrieved from https://seklima.met.no/observations/. Retrieved 14/12/2020 https://seklima.met.no/observations/
Thomson, D. J. (1982). Spectrum estimation and harmonic analysis. *Proceedings of the IEEE, 70*(9), 1055-1096.
Thomson, W. T. (1950). Transmission of Elastic Waves through a Stratified Solid Medium. *Journal of Applied Physics, 21*(2), 89-93. 10.1063/1.1699629
Timco, G., & Frederking, R. (1996). A review of sea ice density. *Cold regions science and technology, 24*(1), 1-6.
Timco, G. W., & Weeks, W. F. (2010). A review of the engineering properties of sea ice. *Cold Regions Science and Technology, 60*(2), 107-129. 10.1016/j.coldregions.2009.10.003
Timoshenko, S., & Goodier, J. (1951). *Theory of Elasticity* (2 ed. Engineering Societies Monographs). New York: McGraw-Hill book Company.
Timur, A. (1968). Velocity of compressional waves in porous media at permafrost temperatures. *Geophysics, 33*(4), 584-595. 10.1190/1.1439954
Tokimatsu, K., Tamura, S., & Kojima, H. (1992). Effects of Multiple Modes on Rayleigh Wave Dispersion Characteristics. *Journal of Geotechnical Engineering, 118*(10), 1529-1543. doi:10.1061/(ASCE)0733-9410(1992)118:10(1529)
Trnkoczy, A. (2009). Understanding and parameter setting of STA/LTA trigger algorithm. In *New Manual of Seismological Observatory Practice (NMSOP)* (pp. 1-20). Potsdam: Deutsches GeoForschungsZentrum GFZ.
Unakafova, V., & Keller, K. (2013). Efficiently measuring complexity on the basis of real-world data. *Entropy, 15*(10), 4392-4415.
Van der Sanden, J., & Short, N. (2017). Radar satellites measure ice cover displacements induced by moving vehicles. *Cold Regions Science and Technology, 133*, 56-62.
Vaughan, D. G., & Comiso, J. C. (2014). Chapter 4 - Observations: Cryosphere. In T. Stocker (Ed.), *Climate change 2013: the physical science basis: Working Group I contribution to the Fifth assessment report of the Intergovernmental Panel on Climate Change*. New York: Cambridge university press.
Vel'sovskij, A., Karpov, B., & Smirnova, E. (2015). Development of a new method for checking frost heave in roads. *Proceedings of the Institution of Civil Engineers - Civil Engineering, 168*(5), 49-54. 10.1680/cien.14.00036

Vincent, W. F., Callaghan, T. V., Dahl-Jensen, D., Johansson, M., Kovacs, K. M., Michel, C., . . .Sharp, M. (2011). Ecological Implications of Changes in the Arctic Cryosphere. *AMBIO, 40*(1), 87-99. 10.1007/s13280-011-0218-5

Vinh, P. C. (2013). Scholte-wave velocity formulae. *Wave Motion, 50*(2), 180-190. https://doi.org/10.1016/j.wavemoti.2012.08.006

Vogel, S., Eckerstorfer, M., & Christiansen, H. H. (2012). Cornice dynamics and meteorological control at Gruvefjellet, Central Svalbard. *The Cryosphere, 6*(1), 157-171. 10.5194/tc-6-157-2012

Wadhams, P., Wilkinson, J. P., & McPhail, S. (2006). A new view of the underside of Arctic sea ice. *Geophysical Research Letters, 33*(4).

Wahr, J., Liu, L., & Zhang, T. (2008). *InSAR measurements of ground surface deformation due to thaw settlement and frost heave over permafrost on the North Slope of Alaska.* Paper presented at the AGU Fall Meeting Abstracts, San Francisco, USA.

Walder, J., & Hallet, B. (1985). A theoretical model of the fracture of rock during freezing. *Geological Society of America Bulletin, 96*(3), 336-346.

Walter, F., Roux, P., Roeoesli, C., Lecointre, A., Kilb, D., & Roux, P.-F. (2015). Using glacier seismicity for phase velocity measurements and Green's function retrieval. *Geophysical Journal International, 201*(3), 1722-1737.

Wang, C. M., & Tay, Z. Y. (2011). Very Large Floating Structures: Applications, Research and Development. *Procedia Engineering, 14*, 62-72. https://doi.org/10.1016/j.proeng.2011.07.007

Wang, D.-y., Zhu, Y.-l., Ma, W., & Niu, Y.-h. (2006). Application of ultrasonic technology for physical–mechanical properties of frozen soils. *Cold Regions Science and Technology, 44*(1), 12-19. https://doi.org/10.1016/j.coldregions.2005.06.003

Wang, J., Nishimura, S., Okajima, S., & Joshi, B. R. (2019). Small-strain deformation characteristics of frozen clay from static testing. *Géotechnique, 69*(9), 816-827. 10.1680/jgeot.18.P.115

Wang, K., Hosking, R., & Milinazzo, F. (2004). Time-dependent response of a floating viscoelastic plate to an impulsively started moving load. *Journal of Fluid Mechanics, 521*, 295.

Weber, S., Beutel, J., Faillettaz, J., Hasler, A., Krautblatter, M., & Vieli, A. (2017). Quantifying irreversible movement in steep, fractured bedrock permafrost on Matterhorn (CH). *The Cryosphere, 11*(1), 567-583. 10.5194/tc-11-567-2017

Weeks, W. F., & Assur, A. (1967). *The Mechanical Properties of Sea Ice* (Cold Regions Science and Engineering, Part II: Physical Science, Section C: Physics and Mechanics of Ice). Hanover, New Hampshire: Cold Regions Research & Engineering Laboratory.

Weertman, J. (1983). Creep deformation of ice. *Annual Review of Earth and Planetary Sciences, 11*(1), 215-240.

Wilson, J. T. (1955). *Coupling between moving loads and flexural waves in floating ice sheets - SIPRE technical report no. 34.* (U.S. Army Snow, Ice, and Permafrost Research Establishment.). Wilmette, Illinois.

Wu, Y., Nakagawa, S., Kneafsey, T. J., Dafflon, B., & Hubbard, S. (2017). Electrical and seismic response of saline permafrost soil during freeze-thaw transition. *Journal of Applied Geophysics, 146*, 16-26.

Xia, J., Miller, R. D., & Park, C. B. (1999). Estimation of near-surface shear-wave velocity by inversion of Rayleigh waves. *Geophysics, 64*(3), 691-700. 10.1190/1.1444578

Xing, L., & Spitler, J. D. (2017). Prediction of undisturbed ground temperature using analytical and numerical modeling. Part I: Model development and experimental validation. *Science and Technology for the Built Environment, 23*(5), 787-808.

Xu, X., & Hou, J. (2011). A stress relaxation model for the viscoelastic solids based on the steady-state creep equation. *Mechanics of Time-Dependent Materials, 15*(1), 29-39. 10.1007/s11043-010-9122-9

Yang, T. C., & Yates, T. W. (1995). Flexural waves in a floating ice sheet: Modeling and comparison with data. *The Journal of the Acoustical Society of America, 97*(2), 971-977. 10.1121/1.412076

Yeung, R., & Kim, J. (2000). Effects of a Translating Load on a Floating Plate—Structural Drag and Plate Deformation. *Journal of fluids and structures, 14*(7), 993-1011.

Yuan, Y., & Wan, Z. L. (2002). Prediction of cracking within early-age concrete due to thermal, drying and creep behavior. *Cement and Concrete Research, 32*(7), 1053-1059. https://doi.org/10.1016/S0008-8846(02)00743-3

Yuen, K.-V., & Yang, X.-H. (2020). Bayesian Rayleigh wave inversion with an unknown number of layers. *Earthquake Engineering and Engineering Vibration, 19*(4), 875-886. 10.1007/s11803-020-0601-y

Zhang, Z.-D., & Alkhalifah, T. (2019). Wave-equation Rayleigh-wave dispersion inversion using fundamental and higher modes. *Geophysics, 84*(4), EN57-EN65. 10.1190/geo2018-0506.1

Zhankui, Y., Yuanling, Z., & Ping, H. (1998). *Experimental study of Poisson's ratio for frozen soil.* Paper presented at the Proceedings of the 7th International Conference on Permafrost, Yellowknife, Canada.

Zhu, J. (2008). *Non-contact NDT of concrete structures using air coupled sensors* (NSEL Report Series Report No. NSEL-010): Newmark Structural Engineering Laboratory. University of Illinois at Urbana.

Zhu, J., Popovics, J. S., & Schubert, F. (2004). Leaky Rayleigh and Scholte waves at the fluid–solid interface subjected to transient point loading. *The Journal of the Acoustical Society of America, 116*(4), 2101-2110. 10.1121/1.1791718

Øvstedal, E. (2012). *Frost heave in new Norwegian roads - why, and what can be done to avoid this (original text in norwegian: Telehiv på nye norske veger-hvorfor, og hva kan gjøres for å unngå dette?)* (Statens Vegvesens rapporter Nr. 79 1893-1162): Statens Vegvesen. Retrieved from http://hdl.handle.net/11250/2507883